Stress and Structure Evolution During Volmer-Weber Growth of Thin Films

by

Steven Craig Seel

Submitted to the Department of Materials Science and Engineering in Partial Fulfillment of the Requirements for the Degree of

Doctor of Philosophy

at the

MASSACHUSETTS INSTITUTE OF TECHNOLOGY

March 2002
[June 2002]

© Massachusetts Institute of Technology 2002. All rights reserved.

Author..
Department of Materials Science and Engineering
March 14, 2002

Certified by..
Carl V. Thompson
Stavros Salapatas Professor of Materials Science and Engineering
Thesis Supervisor

Accepted by..
Harry L. Tuller
Chairman, Department Committee on Graduate Students

ARCHIVES

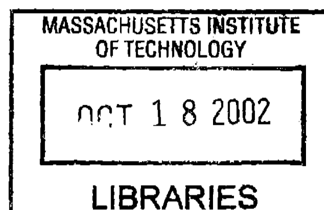
MASSACHUSETTS INSTITUTE OF TECHNOLOGY
OCT 1 8 2002
LIBRARIES

V.1

Stress and Structure Evolution During Volmer-Weber Growth of Thin Films

by

Steven Craig Seel

Submitted to the Department of Materials Science and Engineering on March 14, 2002, in partial fulfillment of the requirement for the degree of Doctor of Philosophy

Abstract

To investigate stress evolution during film deposition, a novel electrical technique for *in situ* thin film stress measurements was developed utilizing piezoresistive silicon microcantilevers, or piezocantilevers. In addition to the thin film stress measurements of Cu made with the piezocantilevers, our collaborators at Sandia National Laboratories have studied thin film growth stresses for Al, Ag, and amorphous Ge (*a*-Ge) films measured using conventional laser deflectometery.

A computer simulation of thin film formation by the Volmer-Weber mechanism was developed to model the nucleation and growth of individual islands that impinge and coalesce to form a continuous film. By including a size-dependent lattice contraction in pre-coalescence islands, the simulation can be used to qualitatively reproduce the measured compressive stress behavior of Al at low film thicknesses. In contrast to Al films that support stress from the very onset of deposition, Ag films exhibit no measurable stress until larger film thickness are achieved. This difference in behavior was attributed to shear occurring at the Ag-SiO_2 interface, which is suppressed at the much stronger Al-SiO_2 interface. Tensile stress generation resulting from island coalescence was modeled analytically and by finite element methods (FEM) as the energetic balance between interfacial energy reduction and strain energy generation resulting from grain boundary formation. The magnitude of the island-coalescence stress calculated using FEM was found to decrease dramatically with decreasing island-substrate contact angle. Using the contact-angle-dependent FEM calculations of island-coalescence stress, simulations closely matched the stress-thickness measurements of Al, by assuming perfect island-substrate traction, and of Ag, by assuming partial island-substrate sliding, over the range of thicknesses prior to film continuity.

The compressive stress evolution during deposition of continuous films and the stress behavior during interrupts of film growth was modeled in terms of a non-equilibrium surface morphology that develops during deposition. For the resulting non-equilibrium grain shapes, the in-plane compressive stress resulting from excess surface stress was calculated using FEM. Model predictions are consistent with observed decreasing compressive stress-thickness with increasing film thickness observed experimentally for Cu and *a*-Ge, as well as the reversible tensile rise behavior observed during growth interrupts of Cu.

Thesis Supervisor: Carl V. Thompson
Title: Stavros Salapatas Professor of Materials Science and Engineering

Acknowledgments

First and foremost, I would like to thank my thesis advisor Carl Thompson, who has provided invaluable guidance during my thesis research and encouragement throughout my years of toil at MIT. Carl gave me the support and freedom to switch projects during the course of my graduate career and ultimately the opportunity to achieve my goals.

I have also had the great fortune to interact with Professor Harold Frost, whose depth of knowledge extends far beyond the field of science. My thanks also extend to my collaborators Jerry Floro and Sean Hearne at Sandia National Laboratories without whom much of the experimental measurements and scientific understanding in the thesis would not have been possible.

Being at work *all the time* would have been (more) tortuous were it not for my fellow rats in the maze. Roland Carel and Brett Knowlton taught me the ropes when I first came to Carl's group and I'm indebted to them for their early guidance. I wish for luck and success for everyone still there at MIT, especially Andrew, Cody, Frank, Ramkumar, Rob, Srikar, and Zung. Special thanks go to Mauro Kobrinsky and Walid Fayad who are both amazing people that I feel fortunate to have had the opportunity to interact with on a daily basis.

Fortunately life does actually exist outside of MIT and to those friends on the *other side*, you've made Boston my home that I'll so sorely miss. Thank you for the dinners together, the parties, the road trips, flying across the country and around the world, and everything in between. I'll miss all of you greatly but especially Carla, whose love and support pushed me through the most difficult years of my thesis.

Finally and with great honor, I'd like to dedicate my thesis to my parents whose unconditional love and unwavering encouragement through out my life are the foundations on which my successes in life have been possible.

Contents

1 Introduction **22**
1.1. Motivation 22
1.2. Objectives of thesis 23
1.3. Origins of stress in thin films 24
1.3.1. Deposition technique 24
1.3.2. Thermal stress 25
1.3.3. Intrinsic stress 25
1.3.4. Other sources of stress 31
1.4. Correlations between thin film stress measurements and film formation 32

2 Experimental techniques **35**
2.1. Overview 35
2.2. Multibeam optical stress sensor (MOSS) 36
2.2.1. *In situ* thin film stress measurement 36
2.3. Piezoresistive microcantilevers (piezocantilevers) 38
2.3.1. Thin film stress and substrate stress 38
2.3.2. Cantilever geometry 41
2.3.3. Piezoresistivity 47
2.3.4. Resistor structures for stress and temperature measurement 50
2.3.5. Measurement sensitivity and stability 54
2.3.6. Calibration 56
2.3.6.1. Stress calibration of Wheatstone bridge structures 57
2.3.6.2. Temperature calibration of Kelvin structures 62
2.3.6.3. Temperature calibration of Wheatstone bridge structures 64
2.3.6.4. Cantilever thickness metrology 66
2.3.7. Correction for thermal stress during deposition 68
2.3.8. Piezocantilever fabrication 69
2.3.9. Piezocantilever packaging and UHV instrumentation 73
2.4. Comparison of MOSS and piezocantilever devices 76

3 Experimental results **79**
3.1. Overview of experimental results 79
3.2. Intrinsic stress measurements of Ag and Al 80
3.3. Intrinsic stress measurements of Ag at different deposition rates and temperatures 84
3.3.1. Influence of deposition rate 84
3.3.2. Influence of deposition temperature 86
3.4. Intrinsic stress measurements of Cu using piezocantilever devices 89
3.4.1. Continuous Cu thin film deposition 90

3.4.2. Cu thin films deposition with growth interrupts 93
3.4.2.1. Thickness dependence of growth interrupt behavior 95
3.4.2.2. Influence of deposition rate on growth interrupt behavior 97
3.4.3. Intrinsic stress measurements of amorphous germanium 100

4 Discussion of continuous deposition results 104
4.1. Overview 104
4.2. Simulation of film growth by the Volmer-Weber mechanism 105
4.2.1. Introduction 105
4.2.2. Thin film growth simulation technique 106
4.2.2.1. Island nucleation rate 106
4.2.2.2. Island radial growth velocity 107
4.2.2.3. Grain boundary algorithm 108
4.2.2.4. Limitations of film growth simulation 111
4.2.3. Simulated substrate coverage compared to experiment 115
4.2.4. Incorporating stress generation/relaxation mechanisms into simulation 116
4.3. Compressive stress generation during island stage growth 117
4.3.1. Introduction 117
4.3.2. Surface stress 117
4.3.3. Lattice contraction measurements 118
4.3.4. Compressive stress generation in islands during thin film growth 119
4.3.4.1. Cammarata lock-down radius model 120
4.3.4.2. Compressive shell model 122
4.3.5. Model comparison with compressive island stress measurements 123
4.4. Tensile stress generation upon island impingement 127
4.4.1. Introduction 127
4.4.2. First order global energetic analysis of tensile stress generation 127
4.4.3. Nix-Clemens model 129
4.4.4. Approximate analytical model of grain boundary zipping 131
4.4.5. Finite element comparison to analytical models 134
4.4.5.1. Plane strain model of island coalescence 134
4.4.5.2. Axisymmetric representation of island coalescence 137
4.4.5.3. Influence of island contact angle on tensile stress generation 139
4.4.5.4. Influence of sliding on tensile stress generation 145
4.4.6. Tensile stress model comparison with stress measurements 148
4.4.6.1. Application of tensile stress models in film growth simulation 148
4.4.6.2. Simulation of tensile stress evolution during Al and Ag thin film growth 150
4.4.6.3. Multiple stress generation/relaxation mechanisms during thin film grow 153
4.5. Stress relaxation during thin film growth 156
4.5.1. Introduction 156
4.5.2. Model for surface Coble creep in the simulation 156
4.6. Summary and conclusions 164

5 Discussion of stress evolution during growth interrupts 168
5.1. Introduction 168
5.2. Experimental evidence for non-equilibrium film growth 169
5.3. Non-equilibrium thin film growth model 171
5.3.1. Partial differential equation (PDE) describing thin film growth 171
5.3.2. Modeling thin film growth of low-mobility materials 174
5.3.3. Modeling thin film growth of high-mobility materials 178
5.4. Compressive stress generation in continuous films 179
5.4.1. Finite element method (FEM) modeling of compressive stress generation 179
5.4.2. FEM model comparison to measured compressive stress evolution 183
5.4.3. Discussion 187
5.5. Stress behavior during growth interrupts 189
5.6. Discussion of other models in the literature 190

6 Conclusions and future work 192
6.1. Conclusions and summary 192
6.2. Future work 196
6.2.1. Piezocantilevers 196
6.2.2. Compressive stress during island stage of thin film growth 197
6.2.3. Film growth simulation 199
6.2.4. Tensile stress generation during grain boundary formation 199
6.2.5. Stress behavior of continuous films during deposition and growth interrupts 200

Appendix A Piezocantilever design and fabrication 202
Appendix B Simulation of Volmer-Weber growth of thin films 228
Appendix C Texture develop. due to grain growth in FCC thin films 267
References 283

List of Figures

1-1 Schematic of the progression of thin film growth by the Volmer-Weber island growth mode 27

1-2 Schematic view of polycrystalline film growth for (left) a high melting point material with columnar grain, and (right) a low melting point material with equiaxed grains 28

2-1 Schematic setup of the multibeam optical stress sensor (MOSS) apparatus used at Sandia National Labs for the *in situ* measurement of thin film stress during deposition 37

2-2 Optical microscope image of the top surface of a piezoresistive microcantilever. The 20-μm thick silicon cantilever terminates into a 475-μm thick supporting wafer on the left side of the image. The white lines in the image are the aluminum metallization that make electrical contact to the underlying silicon. A [110]-oriented resistor with strong piezoresistance and three [001]-oriented resistors with weak piezoresistance are configured in a Wheatstone bridge structure near the end of the cantilever 39

2-3 Finite element method (FEM) mesh of a 5:3 length-to-width (L:w) cantilever (comparable to Fig. 2-2) with a thin film on the top surface. The thickness of the film is 40 times thinner than the substrate thickness. The FEM calculations were performed using the commercial software ADINA 42

2-4 Finite element results for the thin film in-plane stresses resulting from differential thermal expansion between the film and substrate for the system shown in Fig. 2-3. The in-plane stresses calculated by FEM are normalized by the calculated thermal stress. Traces (indicated by arrowed lines) of the stress are shown in Fig. 2-5 43

2-5 The normalized in-plane stresses in the film (a) along the centerline of the cantilever length, (b) across the cantilever at y= 0.8L for the traces indicated in Fig. 2-4 ... 44

2-6 The normalized in-plane stresses in the top surface of the cantilever substrate (a) along the centerline of the cantilever length, and (b) across the cantilever at y= 0.8L for the traces indicated in Fig. 2-4 ... 46

2-7 Plots of the room temperature values of π'_{11} and π'_{12} for p-type doped silicon plotted as a function of crystal direction for orientations in the (a) (100) plane, and (b) (110) plane [Kand 82]. The upper halves of the graphs show the positive-valued π'_{11}, while the lower halves show negative-valued π'_{12}. The units of the piezoresistive coefficients are in 10^{-11} Pa^{-1} ... 48

2-8 The calculated piezoresistive coefficients for p-type silicon (normalized by the value of the piezoresistive coefficient at 25°C) as a function of doping concentration and temperature [Kand 82] ... 50

2-9 The stress monitor consists of one piezoresistive resistor and three nonpiezoresistive resistors. The four resistors are connected in a Wheatstone bridge as shown in (a) a schematic of the fabricated structure similar to Fig. 2-2, and as (b) an electrical circuit diagram. A supply voltage is applied across two of the leads while the voltage response of the bridge is monitored across the other two leads ... 51

2-10 The temperature monitor consists of three nonpiezoresistive resistors connected in a Kelvin structure as shown in (a) a schematic of the fabricated structure, and (b) an electrical circuit diagram. A constant current is supplied across the outer two leads while a voltage drop is monitored across the inner two leads. The dimensions of the resistor are labeled in (a) and are used to calculate the sheet resistance $R_\square$ using the equation shown in (b) ... 53

2-11 Wheatstone bridge voltage response V_{bridge} as a function of time with V_{supply}= 1V at room temperature without any externally applied stress. The non-zero Wheatstone bridge response is most probably due to residual stress from the aluminum metallization and passivation oxide processing. Notice that the signal

is relatively stable over five hours with a standard deviation of approximately 0.7 μV/V.......... 56

2-12 Tip deflection of a cantilever by a tungsten probe controlled by a linear micrometer. The image above was obtained by optical interferometry using a Veeco WYKO commercial system. The WYKO system provides vertical deflection data as a function of position along the cantilever.......... 57

2-13 Vertical deflection along the length of a 600-μm-long cantilever in the unloaded state and with nominal 2, 4 and 6-μm tip deflections. The magnitude of the tip deflection is controlled by translating a tungsten probe attached to a linear micrometer. The vertical deflections as a function of position are measured by optical interferometry using the WYKO system. Note that vertical deflections occur past the base of the fabricated cantilever as a result of support compliance. Fitted curves using Eq. 2.17 are dashed lines that are almost indistinguishable from the measured deflection data.......... 59

2-14 The measured Wheatstone bridge voltage divided by the supply voltage as a function of (a) tip deflection determined by fitting vertical deflection data to Eq. 2.17, and (b) average stress in piezoresistor determined from Eq. 2.15. The slope in (b) is the measured piezoresistive coefficient for the fabricated piezolever devices.......... 61

2-15 The measured sheet resistance as a function of temperature for a Kelvin structure fabricated near the end of a cantilever. Approximately 15 minutes is allowed for the temperature to equilibrate between measurements.......... 63

2-16 The measured Wheatstone bridge voltage as a function of temperature for an uncoated piezocanitlever device (open circles) and for a piezocantilever device coated with a 100 nm Cu film.......... 65

2-17 (a) Comb structure fabricated near to cantilevers used for cantilever thickness calibration. (b) Profilometer scan along the comb structure gives the thickness of the (110) silicon cantilever as a function of position. Because the thickness is relatively consistent over almost 2 mm, the thickness measured at the comb structure gives an accurate estimate of the cantilever thickness.......... 67

2-18 Infrared images of wafer bond between (110) device wafer and (100) handle wafers showing (a) a good wafer bond, and (b) a wafer bond with interface bubbles presumably due to trapped particles between the wafers.................. 70

2-19 Schematic of bonded wafer after ion implantation showing (a) a cross-sectional view, and (b) a top view of the wafer surface. Note that the structures shown are to aid in understanding of the processing procedure, and do not diagram actual structures used in the piezocantilever devices... 71

2-20 Schematic of bonded wafer after aluminum metallization and an oxide passivation showing (a) a cross-sectional view, and (b) a top view of the wafer surface. Note that the structures shown are to aid in understanding of the processing procedure, and do not diagram actual structures used in the piezocantilever devices......... 74

2-21 Schematic of bonded wafer after backside and frontside deep reactive ion etching that releases the silicon cantilever as can be seen in (a) a cross-sectional view, and (b) a top view of the wafer surface... 75

2-22 Sample stage for packaged piezocantilever devices for use in UHV deposition chamber. The pins on the backside of the ceramic package plug into the array of gold-plated receptacles within the PEEK socket. Kapton-coated wires are connected to the backside of the gold-plated receptacles and out to an electrical feedthrough on a vacuum flange (not shown). Both the PEEK and Kapton are plastics compatible with UHV pressures and temperature as high as 200°C. Thermal contact to the backside of the ceramic package is achieved via a thermal finger that extends to the stage.. 77

3-1 Schematic diagram of a measured (a) stress-thickness product versus film thickness curve, and (b) the corresponding average stress, which is the stress-thickness product divided by the film thickness from (a). The film thickness is simply the product of the deposition rate and the deposition time. The instantaneous stress is defined as the slope of the stress-thickness curve at a given film thickness.. 81

3-2 Stress-thickness versus thickness during deposition of Al and Ag on oxidized silicon substrates at 0.2 nm/sec deposition rate at room temperature. The circles

correspond to the TEM micrographs in Fig. 3-3. The measurements were performed at SNL by JAF and SJH.. 82

3-3 Plan-view TEM micrographs of Al films (upper panels) and Ag films (lower panels) deposited on oxidized silicon substrates. The micrographs correspond to the circles indicated on the measured Al and Ag stress-thickness curves in Fig. 3-2. The TEM microscopy was performed at SNL by JAF and SJH................. 83

3-4 Comparison of the stress-thickness evolution during deposition for Al (dash line) and Ag (solid line) on an oxidized silicon substrate at 0.2 nm/sec at room temperature. The scales have been normalized by the values at the tensile peak of each curve in Fig. 3-2.. 84

3-5 (a) Stress-thickness versus film thickness for Ag thin films deposited on oxidized silicon substrates at room temperature at different deposition rates. (b) The same data replotted as average stress (i.e. stress-thickness divided by film thickness) versus film thickness. The measurements were performed at SNL by JAF and SJH.. 85

3-6 Fractional substrate coverage versus film thickness from SEM images during various stages of deposition of Ag at different deposition rates. The SEM images were obtained at SNL by JAF and SJH.. 87

3-7 (a) Stress-thickness versus film thickness for Ag thin films deposited at 0.2 nm/sec on oxidized silicon substrates at different deposition temperatures. Inset is an enlargement of the initial 20 nm of deposition. (b) The same data replotted as average stress (i.e. stress-thickness divided by film thickness) versus film thickness. The measurements were performed at SNL by JAF and SJH........... 88

3-8 Fractional substrate coverage versus film thickness from SEM images during various stages of deposition of Ag at different temperatures. The SEM images were obtained at SNL by JAF and SJH.. 89

3-9 Stress-thickness versus film thickness during deposition of Cu at 0.1 nm/sec at room temperature measured with a piezocantilever device. Note that the sharp tensile rise during the first couple nanometers of thickness (inset) is not observed by other researchers [Aber 85, Shul 96].. 91

3-10 The "adjusted" stress-thickness versus film thickness during deposition of Cu at 0.1 nm/sec at room temperature measured with a piezocantilever device. Note that the sharp tensile rise during the first couple nanometers of thickness observed in Fig. 3-7 has been removed and attributed to a measurement artifact. Several critical features have been labeled above and the corresponding values have been catalogued in Table 3-1 92

3-11 (a) Stress-thickness versus film thickness before and after a growth interrupt during intermittent deposition of Cu measured with a piezocantilever device. (b) The stress-thickness versus time during the growth interrupt of a 25 nm-thick Cu film 94

3-12 (a) Stress-thickness versus time during growth interrupts of an intermittent Cu deposition. The curves have been replotted with common stress-thickness and time origins. (b) The same curves replotted as average stress (i.e. stress-thickness divided by film thickness) versus time 96

3-13 Stress-thickness versus film thickness before and after growth interrupts during intermittent deposition of Cu at different deposition rates. Notice that the instantaneous slope increases with decreasing deposition rate 98

3-14 (a) Stress-thickness versus time during growth interrupts of an intermittent Cu deposition at different film thicknesses. The deposition rate prior to each growth interrupt was different. The curves have been replotted with common stress-thickness and time origins. (b) The same curves replotted as average stress (i.e. stress-thickness divided by film thickness) versus time 99

3-15 Stress-thickness versus film thickness for *a*-Ge films grown at room temperature (solid line) and 270°C (dots). An AFM image from a 7 nm-thick film grown at 270°C is shown inset, where the sides of the image are 212 nm across. The measurements were performed at SNL by JAF and SJH 100

3-16 Growth interrupt behavior for *a*-Ge grown at room temperature showing (a) stress-thickness versus time, and (b) stress-thickness versus film thickness. The solid line is for growth with interrupts, while the dashed lines are uninterrupted growth data. The arrows in (b) indicate the thickness at which the interrupts occurred. The measurements were performed at SNL by JAF and SJH 102

3-17 Growth interrupt behavior for a-Ge grown at 270°C showing (a) stress-thickness versus time, and (b) stress-thickness versus film thickness. The solid line is for growth with interrupts, while the dots are uninterrupted growth data. The arrows in (a) indicate the thickness at which the interrupts occurred. The measurements were performed at SNL by JAF and SJH. 103

4-1 Nucleation rate I as a function of time for a simulation of 500 grains using a nominal rate of I equal to one and a constant radial growth velocity. The nucleation rate is defined as the number of new nuclei per unit time per unit exposed substrate area. The nucleation rate was averaged over 20 nucleation events for each point in the plot. 106

4-2 A time sequence of film growth by the Volmer-Weber mechanism using the simulation with growth conditions of constant nucleation rate and radial growth velocity resulting in the so-called Johnson-Mehl structure. 108

4-3 Grain boundary formation between (a) two growing islands, and (b) three growing islands. A grain boundary is represented as the line of intersection of two impinging circles. Notice in (b) that the three boundaries eventually intersect and form a triple point with the ensemble of three islands. 109

4-4 Schematic of the simulation algorithm for calculating grain boundaries between multiple intersecting island, including (a) calculating the points where circles intersect, (b) determining lines of intersection between points, and (c) calculating triple point locations where three boundaries intersect within an ensemble of three islands. The situation become more complex as growth continues and multiple circles begin overlapping as shown in (d). 110

4-5 The film volume per unit substrate area as a function of time for a constant deposition rate (dotted line) compared to the simulation results (solid curve) under growth conditions of a constant nucleation rate and radial growth velocity for hemispherical islands. Note that the simulation accumulates volume very slowly at early times. 111

4-6 (a) Side view of an island of radius r, and (b) top view of an island of radius r with nucleation-exclusion zone of width δ. 112

4-7 A time sequence of simulated film growth by the Volmer-Weber mechanism with a nucleation-exclusion zone. In the simulation, the nucleation rate is constant and the radial growth velocity depends on both the island radius and the nucleation-exclusion zone width according to Eq. 4.4 114

4-8 A time sequence of simulated film growth by the Volmer-Weber mechanism with island coarsening. When an island smaller than a critical size impinges with a large island, coarsening occurs so that the volume of the small island is incorporated into the larger island 115

4-9 Fractional substrate coverage versus film thickness from SEM images during various stages of deposition of Ag at different temperatures. The lines are from the simulations of microstructural evolution scaled using the measured average grain sizes (listed next to each curve in the plot) 116

4-10 Spherical cap island with contact angle θ between the island surface and substrate, radius of curvature R, and in-plane radius r 121

4-11 (a) Comparison of the Al stress-thickness data (from Fig. 3-2) with calculated curves from the simulation using the Cammarata model (Eq. 4.9) and the compressive shell model (Eq. 4.11). The compressive stresses was calculated in the simulation using f= 1.5 J/m^2 and θ= 50 degrees. (b) Magnification of the first 4 nm of Al deposition 126

4-12 Schematic diagram of a regular array of square parallelpiped islands of thickness h and diameter d on a substrate, each separated by a distance α from its neighbors. When the islands grow to within a critical distance, the separation gap is closed by deforming the islands and a tensile stress is generated in the film 128

4-13 (a) Schematic of the island coalescence process resulting in tensile stress generation. The dashed lines represent the hemicylindrical islands at impingement, while the solid lines represents the deformed surface of the island after coalescence through grain boundary zipping to a height z_0 130

4-14 Finite element model of island coalescence represented by a two-dimensional element under plane strain conditions. The y-axis represents the island-substrate interface where traction was imposed. The z-axis is an axis of mirror symmetry

along which sliding was allowed. The arrowed lines are the series of displacement that represent zipping to a height z_0 of an island of radius r....... 135

4-15 Comparison of the FEM calculations with results from the Nix-Clemens model and the analytical model in section 4.4.4, showing (a) the equilibrium zipping distance $z_{0,eq}$ divided by the island radius r, and (b) the average stress as a function of island radius.. 136

4-16 (a) Contacting of two identical spheres of radius r with cohesive attraction between them. The center of each sphere is constrained not to move. The contact area between the spheres has radius z_0. (b) Hemispherical islands impinging with their neighbors in analogy to the case of contacting two spheres................ 138

4-17 Comparison of the axisymmetric FEM calculations with results from the Freund-Chason model, showing (a) the equilibrium zipping distance $z_{0,eq}$ divided by the island radius r, and (b) the average stress as a function of the island radius..... 140

4-18 Schematic of impingement between identical cylindrical cap islands with contact angle θ. An island was represented in finite element modeling by a two-dimensional element under plane strain conditions with perfect traction at the island-substrate interface. A series of displacements were imposed along the surface to a height z_0 to mimic the zipping process................................ 141

4-19 Finite element calculation of the tensile stress generation resulting from island coalescence for different contact angles showing (a) the equilibrium zipping distance $z_{0,eq}$ divided by the island radius r, and (b) the average stress as a function of the island radius.. 142

4-20 Finite element calculations for island zipping with different contact angles showing (a) strain energy as a function of the in-plane zipping distance y_0 divided by the island radius r, and (b) in-plane strain as a function of y_0/r............... 144

4-21 Schematic of island coalescence showing (a) the (i) first, and (ii) second coalescence of an island with traction at the island-substrate interface. (b) Island coalescence with sliding at the island-substrate interface for the (iii) first, and (iv) second coalescence of an island. In case (iv), the impinging islands are already part of a larger island cluster which inhibits island sliding........................ 146

4-22 (a) The equilibrium zipping distance z_0 divided by the island radius r and (b) the average stress as a function of the island radius from FEM modeling of a two-dimensional element under plane strain conditions for the cases shown in Fig. 4-21 147

4-23 (a) Stress-thickness versus film thickness from experimental results (see Fig. 3-2) and the simulation of tensile stress generation during thin film growth for (a) Al, and (b) Ag. Perfect traction was assumed between the film and substrate...... 151

4-24 Stress-thickness versus film thickness of the Ag experimental data (see Fig. 3-2) and the simulation of tensile stress generation during thin film growth including a critical cluster area to capture stress relaxation due to island shear.............. 153

4-25 Schematic of the stresses distribution within a growing island showing (a) compressive stress during the island stage of growth, (b) localized tensile stress generation due to island coalescence leaving a compressive region, (c) tensile stress assumed by new material inherited from underlying material, (d) possible tensile stress relaxation at grain boundaries cannot relax compressive stress regions........ 154

4-26 Proposed stress relaxation mechanism involving the diffusion of atoms across the surface of the island and down grain boundaries to the strained regions near the grain boundary. Since surface diffusion and grain boundary diffusion occur in series, either process may be rate limiting........ 157

4-27 Simulation of Ag thin films with traction at the film-substrate interface during deposition at different temperatures showing, (a) stress-thickness product versus film thickness, and (b) average stress versus film thickness. Stress generation was modeled using the FEM approach, while stress relaxation was assumed to occur via a microstructure-dependent diffusion mechanism........ 160

4-28 Simulation of Ag thin films with partial sliding at the film-substrate interface during deposition at different temperatures showing, (a) stress-thickness product versus film thickness, and (b) average stress versus film thickness. Impingements between island clusters with an area less than A_{crit} were assumed to not generate tensile stress during coalesence due to island sliding........ 161

5-1 Surface morphology of the film before and after island coalescence. Prior to coalescence, the islands have a circular cap cross-section (dashed line) with an island-substrate contact angle θ. After coalescence, the balance between the surface energy γ_s and grain boundary energy γ_{gb} result in an angle ϕ between the grain surface and the plane of the substrate.. 173

5-2 Schematic of the surface morphology evolution with deposition for (a) hemispherical cap grains that increase in height by Δh linearly with time of deposition, and (b) grains with angle ϕ between the grain surface and the plane of the substrate that increase in height Δh faster at the center of grain than at the grain boundary due differences in curvature. The in-plane grains radius r is shown to increase with the film thickness h as $h^{1/2}$................................. 175

5-3 FEM axisymmetric representation of a grain with in-plane radius r, average film thickness h, and an ellipsoidal grain cap. The aspect ratio of the grain cap is equal to h_{cap}/r where h_{cap} is the height of the grain cap. The x-axis represents the grain-substrate interface where traction is imposed. The y-axis is a rotational axis of symmetry along which sliding is allowed. Sliding along the grain boundary of height h_{gb} is also allowed. The arrowed lines along the grain surface represent the local pressure proportional to the local mean curvature............................ 179

5-4 Schematic diagram showing the origin of the in-plane compressive stress σ_x in the grain due to the action of a reduction in the grain cap surface area. The dark gray block arrows indicate the in-plane stress in the grain cap due to the horizontal components of the "pressure" acting on the opposite surfaces of the grain cap. The symmetric boundary conditions at the grain boundaries prevent a Poisson expansion due to σ_y, which therefore results in an in-plane compressive stress σ_x in the lower portion of the grain as indicated by light gray block arrows........ 181

5-5 FEM calculations of the average in-plane stress as a function of the in-plane grain radius r for grain cap aspect ratios of (a) AR_{cap}= 2, (b) AR_{cap}= 4, and (c) AR_{cap}= 6. For each figure with different grain cap aspect ratio, the aspect ratio of the entire grain h/r was also varied.. 182

5-6 Calculated compressive stress generation during thin film deposition of a continuous a-Ge film for (a) a cluster cap shape at the surface that remains

hemispherical during deposition (see Fig. 5-2(a)), and (b) a cluster cap shape that increases in aspect ratio linearly during deposition (see Fig. 5-2(b)). The average cluster size at the surface was assumed to increase as $h^{1/2}$ 185

5-7 Calculated compressive stress generation during thin film deposition of a continuous Cu film for a grain cap shape that increases in aspect ratio linearly during deposition (see Fig. 5-2(b)). The in-plane grain radius was assumed to increase linearly with film thickness 187

A-1 (a) The ALI mask used to create the alignment mark in the 0.2 μm-thick thermal oxide. The features shown above are enlarged by approximately a factor of ten relative to the other mask in Fig. A.1 to see the detail better. Note that a couple of the labels used in the alignment marks, which correspond to other masks, have been changed. The "ARS" label corresponds to the PHO mask, and the "PAS" label corresponds to the CVD mask 204

(b) The PHO mask used for the phosphorous implant of n++ contacts. The original design was to use arsenic for the contacts, and hence the ARS alignment mark label, but the phosphorous implant was significantly less expensive...... 205

(c) The BOR mask used for the boron implant of the resistors.................... 206

(d) The CCO mask used to create the contacts through to 0.2 μm-thick thermal oxide to the implanted regions in the silicon.. 207

(e) The MET mask for the aluminum metallization. The squares near the edges of the pattern are the bond pads. Gold wire bonding connects the bond pads on the die to the gold bond pads on the ceramic packaging............................... 208

(f) The CVD mask used to pattern the CVD oxide to expose the aluminum bond pads. Note that the name of the mask was changed from PAS to CVD in the alignment mark labels 209

(g) The BSE mask used to etch through the entire wafer thickness of the handle wafer. Note that the pattern is mirrored relative to the other mask layers because the mask is used on the wafer backside but aligned to marks on the front....... 210

(h) The FSE mask used to etch through the device wafer silicon to release the cantilevers. There are four sets of six cantilevers shown above.................. 211

A-2 (a) Schematic of an individual die showing aluminum bond pads around the outside edge and four groups of six cantilevers. (b) The die are patterned across the chrome masks so as not to intersect with the edges of the silicon wafer..... 212

A-3 Schematic of the types of alignment marks used for (a) dark-field masks, and (b) clear-field masks. The patterned etch on the wafer is shown in light gray, while the chrome mask features are shown in dark gray. The touching square pattern is inspected after the expose and develop steps to aid in the photolithography processing... 215

A-4 Target mount pattern of thick photoresist (gray) on the 6" handle wafer. The cleared areas provide a vent path for the resist, which outgases due to heating during the DRIE etch. (b) After mounting the 4" wafer, the long vent path should be painted over with resist to leave only a vent near the top and bottom......... 223

C-1 (a) (111) fiber texture plot for an as-deposited 1.0 μm-thick Ag film deposited at room temperature on an oxidized silicon substrate, and (b) after a 1 hr anneal at 400°C at 1 X 10^{-9} Torr. The Ag film exhibits (111), (200) and random texture components... 274

C-2 Compilation of the (111), (100) and random texture components of as-deposited Ag films and after a 1 hour anneal at 400°C for systematically varied deposition temperature and final film thickness. The bold values are textures that strengthened following the 400°C anneal, while italic values indicate texture components that weakened... 275

C-3 (a) (111) fiber texture plot for an as-deposited 1.0 μm-thick Cu film deposited at room temperature on an oxidized silicon substrate, and (b) after a 1 hr anneal at 450°C at 1 X 10^{-9} Torr. The Cu film exhibits (111), (200), (110) and random texture components.. 276

C-4 Compilation of the (111), (200), (110) and random texture components of as-deposited Cu films and after a 1 hour anneal at 450°C for systematically varied deposition temperature and final film thickness. The bold values are texture components that strengthened following the 450°C anneal, while italic values indicate a weakening of the texture component following the high temperature anneal... 277

C-5 A (111) fiber texture plot of a 0.6 μm-thick Ag film deposited at room temperature on an oxidized silicon substrate for the as-deposited film (solid line), after annealing at 400°C in forming gas (80:20 N_2/H_2) alone (dashed line) and with an additional 0.2% compressive strain applied during annealing using a four-point bending apparatus (dash-dot line). The additional compressive strain results in a slight strengthening of the (111) texture.. 278

C-6 Stress versus temperature measurement during annealing of a 0.5 μm-thick Ag film on oxidized Si in an H_2/N_2 reducing gas ambient. Three thermal cycles were performed in the sequence 1-2-3-2-3-2-3 at a heating/cooling rate of 6°C/min. Grain growth occurred primarily during the first heating........................... 280

List of Tables

2-1 Biaxial moduli [Simm 71] and thermal expansion coefficients [Toul 70] for Cu and Si at room temperature.. 66

2-2 The average cantilever thickness and standard deviation in the measurement for five different die from the same wafer.. 68

3-1 Several critical features of the stress-thickness versus thickness curves of Cu have been labeled in Fig. 3-8 and the corresponding values have been catalogued above to compare the piezocantilever results with the Abermann and Koch data [Aber 85] and the Shull data [Shul 96]. The piezocantilever results were averaged over six different experiments... 93

4-1 Selected materials properties for Ag, Al and Cu at room temperature. The Young's modulus and Poisson ratio are from Simmons and Wang [Simm 1971] and the surface and grain boundary energy are from Murr [Murr 75]............ 137

Chapter 1

Introduction

1.1 Motivation

Thin films are deposited on thick substrates to fabricate devices that exploit the electrical, magnetic, optical, and thermal properties of both the film and substrate materials. The general usage of the term "thin film" refers to a layer of material with a thickness that is orders of magnitude smaller than its lateral dimensions. The term "thick substrate" is used to denote the supporting foundation onto which the film is deposited and which is typically at least an order of magnitude thicker than the film. Depending on the application, the type of thin film can range from a single atomic layer of a pure element to a multilayered composite structure. Thin films can be deposited by a variety of methods including: thermal evaporation, sputtering, chemical vapor deposition, laser ablation, and electrochemical deposition. Each method produces films with different microstructural and mechanical properties as a direct consequence of the technique and condition under which the film material is deposited on the substrate. One important characteristic of deposited films is the level of stress resulting from the deposition process.

The reliability and function of thin film devices depends dramatically on the levels of stress in the film, which in turn depends on the deposition conditions as well as the choice of film and substrate materials. Numerous failures of thin film structures can be attributed to stress-related processes such as film delamination, stress-induced

cracking at interfaces, electromigration-induced voiding, and hillock formation. In addition in polycrystalline thin films, the stresses affect the evolution of the microstructure and texture, which in turn influence the reliability and function of many thin film devices. Therefore, understanding the origins of thin film stress evolution during deposition will inevitably allow for the control of stress levels resulting in increased reliability of thin film devices.

1.2 Objectives of thesis

The main objective of the work described in this thesis is to contribute to the understanding of the origins of stresses in thin films during deposition. Towards that end, a new electrical technique for the *in situ* measurement of stress during deposition was developed as described in Chapter 2. The design and fabrication of these piezoresistive microcantilevers, or piezocantilevers, will be detailed along with the calibration and thermal corrections necessary for accurate measurements of film stress. To supplement our experimental work on copper thin films using the piezocantilevers, we have collaborated with researchers Jerrold A. Floro and Sean J. Hearne at Sandia National Laboratories (SNL) who have used the more conventional laser deflection method for measuring stress during deposition of others materials such as silver, aluminum, and amorphous germanium. In Chapter 3, we present our experimental data and observations for Cu deposited on piezocantilevers as well as supporting data from our collaborators at SNL.

Chapter 4 will explain how the measured thin film stresses relate to the evolving film structure during deposition. In order to model the evolving microstructure during growth, a simulation of thin film growth by the Volmer-Weber mechanism has been developed. The film growth simulation allows modeling of microstructure, temperature, and time-dependent stress generation and relaxation mechanisms using a realistically evolving microstructure. By integrating models for film-substrate traction into the microstructural simulation, the qualitative differences in the stress during deposition for Ag and Al on oxidized silicon are explained. By including a time and temperature-dependent diffusive creep mechanism into the simulation, an explanation for the stress behavior of Ag films deposited at different temperature has been explored.

Even though the qualitative shape of the stress curves during deposition are similar for amorphous Ge and polycrystalline Cu, the stress behaviors during interruptions of the film growth were found to be dramatically different. In Chapter 5, the differences in the Ge and Cu stress behavior will be shown to depend on the shape of the film surface due to non-equilibrium growth conditions.

The summary and conclusion of this work will be detailed in Chapter 6, along with a proposal for future research motivated by the understanding developed during the course of study of thin film growth stresses.

1.3 Origins of stress in thin films

1.3.1 Deposition technique

The deposition conditions during thin film growth can strongly influence the level of stress and consequently the physical properties of the film. Because of the multitude of deposition techniques and possible combinations of film-substrate material systems, the origins of thin film deposition stress are numerous and system specific. Reviews of the proposed origins of stresses in thin films are given by Doerner and Nix [Doer 88], by Koch [Koch 94], and by Windischmann for sputtered films [Wind 92].

In this project, we focus on the stresses that originate during deposition near room temperature for films deposited by thermal evaporation in ultra high vacuum (UHV) onto oxidized silicon substrates. Other deposition techniques could have been used to grow the films considered in this study, however each has disadvantages as detailed below. During sputter deposition, compressive stresses develop during growth due to the atomic peening action of energetic inert gas atoms [D'Heu 70] and are not intrinsically related to the stress resulting from thin film formation but more as a consequence of the deposition environment. Chemical vapor deposition, as well as sputtering, requires a gas ambient during deposition that becomes incorporated into the growing film leading to high impurity and defect densities. Laser ablation is useful for depositing complex compound materials, however the films are deposited under highly non-equilibrium conditions resulting in high defect densities. Finally, electrodeposition requires a conductive substrate and electrodeposited films incorporate high concentrations of impurities from

the electrolyte. In contrast, thermal evaporation in UHV involves low energy evaporant atoms (0.1 eV) deposited in a high purity environment [Ohri 92] and consequently has the fewest complicating factors when considering stresses resulting from the thin film formation process.

1.3.2 Thermal stress

A film and substrate with different thermal expansion coefficients subjected to a change in temperature will experience thermal stresses. Thermal evaporation requires heating of the source material to a temperature high enough to promote evaporation in a UHV environment (or sublimation in the case of materials such as Cr) that is on the order of hundreds to thousands of degrees Celsius. At these high temperatures, the molten source results in a significant amount of radiative heating of the substrate. In addition, the high-energy evaporant atoms are transformed from vapor to solid on the substrate and the heat of condensation increases the substrate temperature. Since the thermal expansion coefficient of the silicon substrate is generally smaller than those of the film materials considered in this study, heating (cooling) produces a compressive (tensile) stress in the film that must be subtracted from the measurements to isolate the stress associated with thin film formation during deposition. In Chapter 2, the method for thermal correction will be explained for a system in which both the film thickness and substrate temperature are changing during deposition.

1.3.3 Intrinsic stress

Those stresses associated solely with the process of film formation during growth, excluding thermal stresses, are called intrinsic stresses. The intrinsic stress otherwise referred to as the growth or residual stress in the literature, develops during deposition as well as after deposition is stopped if the atomic mobility is high enough. Numerous studies have attempted to correlate the developing microstructure during polycrystalline film formation with the evolving intrinsic stress during deposition. However due to the inherent difficulty of *in situ* microscopy, the simultaneous study of microstructure and the measurement of intrinsic stresses during deposition are not well represented in the literature. Typically, *ex situ* microscopy is used to study the microstructure at different stages of film formation. Numerous *in situ* studies of the evolution of surface and/or bulk

structure during growth of a wide variety of thin films have been made using techniques such as low energy electron diffraction [Fan 88], low energy electron microscopy [Baue 94], reflected high energy electron diffraction [Mae 99], and x-ray reflectivity [Chas 97], however simultaneous measurements of stress evolution during deposition were not performed.

For metals deposited on oxidized silicon, thin film formation occurs by the Volmer-Weber island growth mode, as shown schematically in Fig. 1-1. During deposition, clusters of atom nucleate on the surface of the substrate forming isolated islands of film material. Nucleation events continue to occur during deposition as long as exposed substrate area exists. Concurrently, existing islands grow larger in size and begin to impinge with each other eventually coalescing to form a continuous, polycrystalline film. As the film continues to thicken, evaporant atoms attach to existing grains of the polycrystalline film and no further nucleation events are assumed to occur. As shown in Fig. 1-2, film thickening leads to a columnar structure with an increasing grain size with film thickness in the case of high melting point materials, while lower melting points materials tend to form equiaxed grains that span the thickness of the film.

For amorphous materials deposited on oxidized silicon, less experimental data exists in the literature studying the evolution of the film structure during deposition. Reinker *et al.* and Geyer *et al.* used scanning tunneling microscopy (STM) to study amorphous metallic films deposited at room temperature on oxidized silicon substrates [Rein 97, Geye 98]. Before reaching film continuity, island nucleation and growth of isolated amorphous domains occurs much like that associated with the Volmer-Weber mechanism shown in Fig. 1-1. Once the amorphous film is continuous, surface scans by AFM indicate an increasing in-plane diameter of the clearly distinct domains at the surface with increasing film thickness. However, the concept of grain boundaries between domains in amorphous films is not clearly defined and the structure of the film below the film surface has not been studied.

Many *in situ* measurement techniques have been developed over the past thirty years to study intrinsic stress during deposition including: direct observation of substrate deflection by microscopy, microbalance techniques, interferometric methods, beam and diaphragm resonance, capacitance methods, and laser deflection. We have developed a

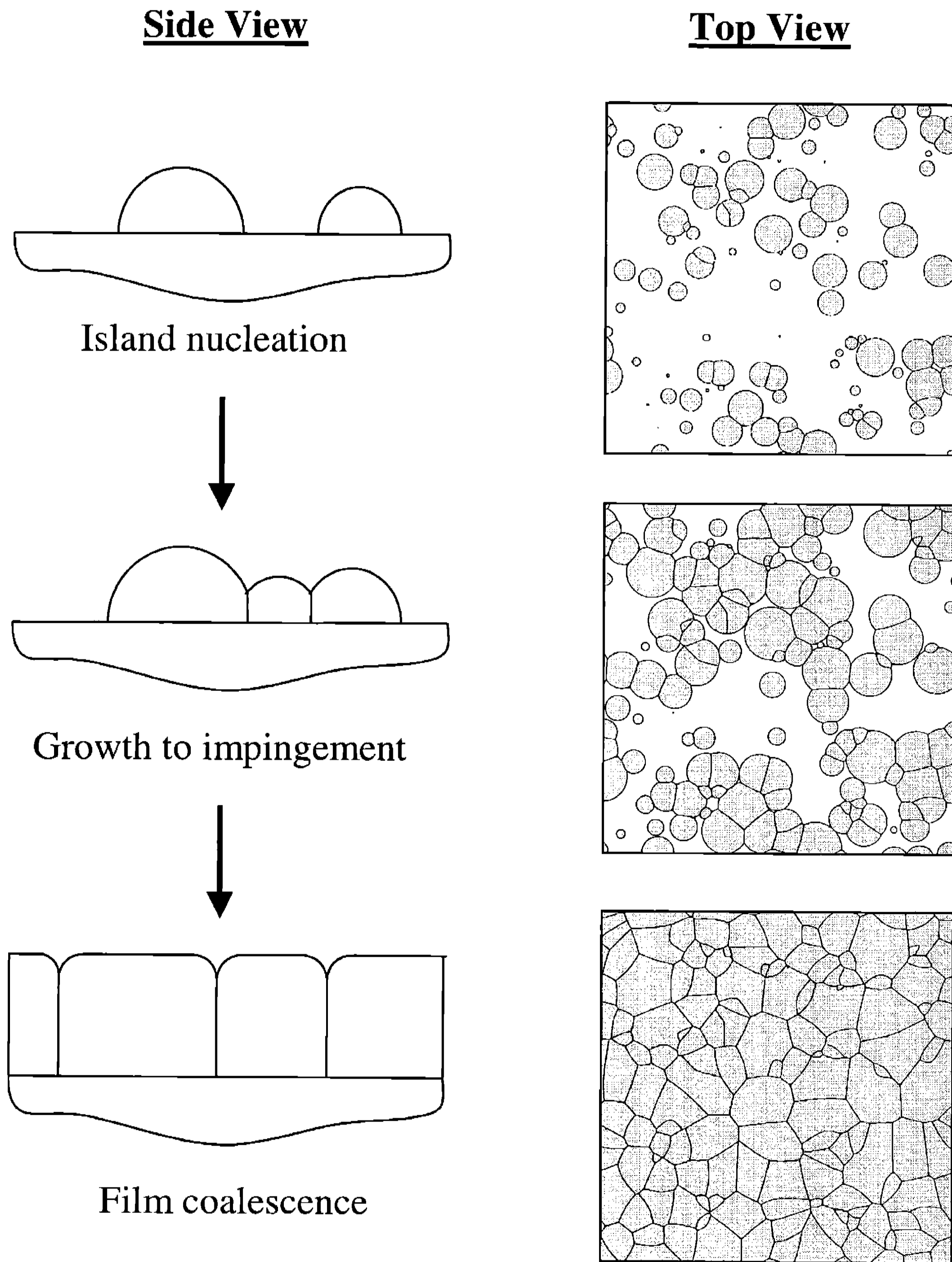

Figure 1-1: Schematic of the progression of thin film growth by the Volmer-Weber island growth mode.

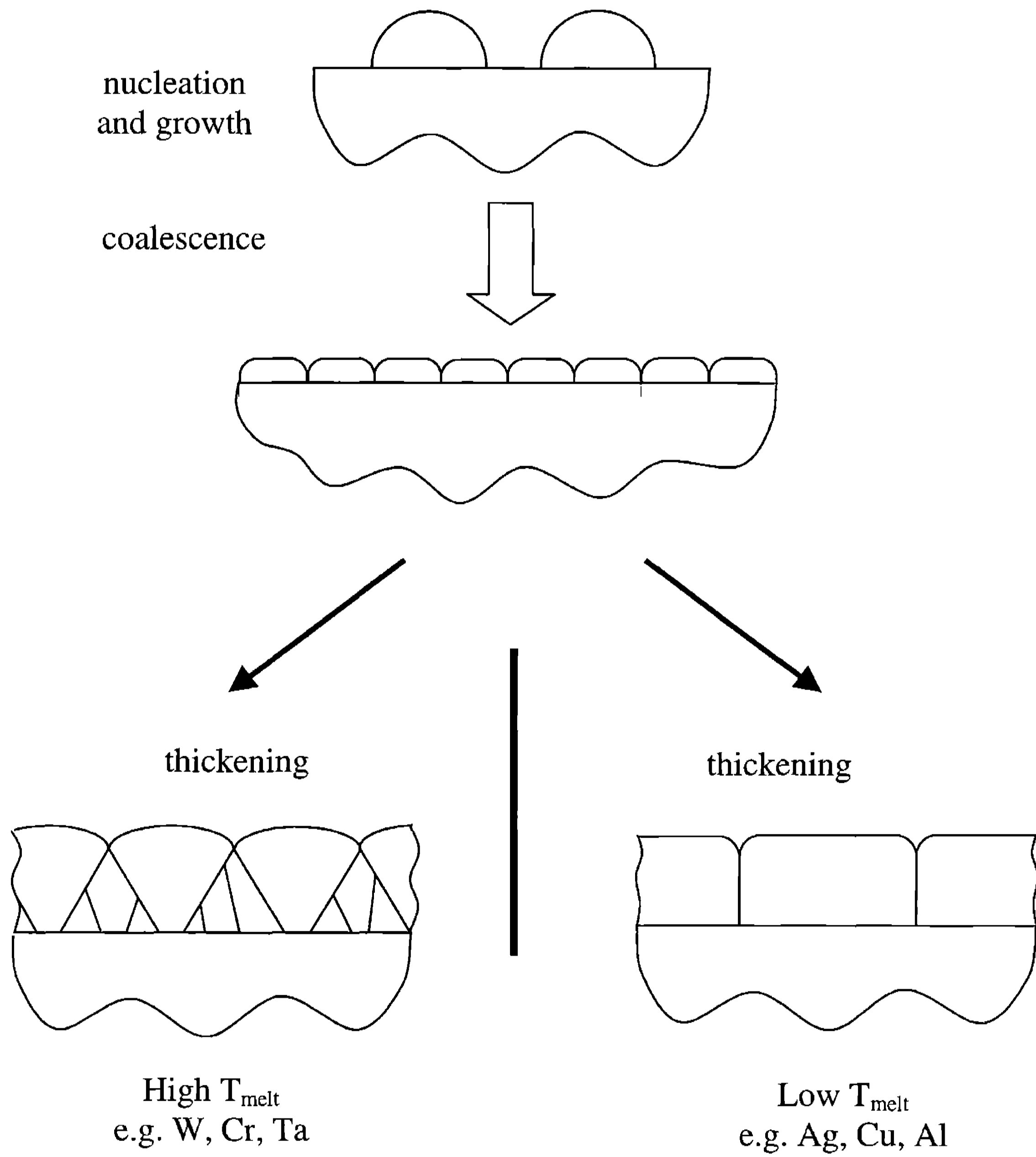

Figure 1-2: Schematic view of polycrystalline film growth for (left) a high melting point material with columnar grain, and (right) a low melting point material with equiaxed grains.

new electrical technique measuring the change in resistance of a piezoresistive element fabricated within a silicon microcantilever, which will be discussed in Chapter 2. However, the majority of measurements in the literature utilize either the capacitance method or the laser deflection technique.

Several early studies of intrinsic stress during deposition revealed important qualitative observations about film growth stresses. However, most measurements were made at only high vacuum (pressures greater than 10^{-7} Torr) and thermal corrections to the measurements were not always considered. Klokholm and Berry [Klok 68] deposited fifteen different metals on glass substrates using electron beam evaporation in the pressure range of 10^{-6} to 10^{-7} Torr. They observed that more refractory metals, such as Ti, Co, and Mn, have larger intrinsic stresses than those of lower melting metals, such as Cu, Ag, and Au. In addition, the refractory metals were found to achieve a constant level of stress at larger thicknesses while softer metals had a broad tensile maximum in the stress. To avoid large changes in temperature during deposition, growth was interrupted every 25Å and therefore the stress measurements during deposition were not truly real time.

Wilcock *et al.* provided early evidence of the correlation between the intrinsic stress and the film structure [Wilc 69]. Silver and gold films were deposited on glass substrate by thermal evaporation at a pressure of 10^{-6} Torr. They found that the maximum tensile stress during deposition was coincident with the film becoming continuous as observed by *ex situ* microscopy. Kinosita *et al.* came to similar conclusion using *in situ* microscopy but for Ag, Au and Cu films deposited on mica (a Stranski-Krastanov growth systems) at 10^{-5} Torr [Kino 67]. Wilcock *et al.* also observed that when deposition was stopped, a tensile rise in the stress was measured and determined to be larger in magnitude than the thermal correction and with a longer time scale than the cooling of the substrate back to room temperature [Wilc 69].

Subsequent research by other groups has reproduced many of the observations made during these early investigations, however several improvements in measurement technique and vacuum technology were necessary for further quantitative study. Abermann *et al.* improved measurement sensitivity by using the differential capacitance technique and were the first to observe an initial compressive stress at the early island

stage of growth for Ag film deposited on MgF_2-coated glass substrate at a vacuum of 10^{-7} Torr [Aber 78]. When using the differential capacitance technique, a cantilever substrate is clamped at one end and displacements of the free end are measured during deposition using capacitance plates above and below the cantilever. Koch *et al.* described the first UHV stress measuring apparatus with a base pressure of better than 5×10^{-10} Torr [Koch 82]. Abermann and Koch were able to reproduce the prior high vacuum intrinsic stress measurements by degrading the vacuum with leaked O_2 [Aber 86].

The subsequent intrinsic stress measurements performed by Abermann, Koch, and co-workers using the differential capacitance technique in UHV revealed several important observations about stress generation during thin films growth. Abermann and Koch deposited Ag, Cu and Au films on MgF_2-coated glass substrates and observed a general trend of stress evolution with film thickness for FCC metals [Aber 85]. Following a small initial compressive transient, tensile stresses develop reaching a broad maximum upon reaching film continuity, similar to the maximum observed in early studies done under only high vacuum. However, subsequent growth led to a decreasing tensile stress that eventually became net compressive.

Initial reports of compressive stresses during thermal evaporation were regarded as experimental error. For metals deposited on glass substrates, heating produces a compressive stress in the film that without proper thermal stress correction would lead to a false compressive intrinsic stress. However, careful experimental work has shown that the thermal stress component is relatively small and can, with confidence, be removed from the intrinsic stress measurements [Koch 86, Shul 96].

Abermann and co-workers have also reproduced earlier observations [Klok 68] that high melting point (low mobility) materials develop large stresses that remain relatively constant with increasing film thickness [Aber 84, Thur 90]. However, Abermann's group also established in these studies that when the substrate temperature was increased, the stress behavior became similar to that described for low melting point (high mobility) materials at room temperature. Similarly, large stresses that remained constant with increasing film thickness were observed for Cu and Ag deposited at 110K [Wina 91]. These results suggest that stress evolution during thin film growth depends solely on the homologous deposition temperature, however results presented in Chapter 3

show that the same trends are not true for amorphous germanium deposited at room temperature.

One final set of observations made by Abermann and co-workers were related to the stress changes that occur during growth interrupts and when growth is resumed. Upon stopping deposition of Ag, Cu, or Au near room temperature, the stress slowly increased in the tensile direction over the period of a few hours [Aber 85]. Any thermal stress contribution due to differential thermal expansion upon cooling were found to be negligible after the relatively short time required for the substrate to cool back to room temperature. When growth was resumed, the stress quickly reversed in the compressive direction and returned to the levels of stress present before the growth interrupt. More recent measurements in the literature confirm these trends for growth interrupts for both Ag and Cu deposited on oxidized silicon substrate [Shul 96, Flor 01]. In Chapter 5, a non-equilibrium growth model will be described to explain this reversible tensile rise during growth interrupts.

1.3.4 Other sources of stress

Especially for semiconductor applications, thin films are grown directly on crystalline substrates and the deposited atoms attempt to maintain registry with the atomic positions of the surface atoms of the substrate. If the lattice constants of the film and substrate are different, the film is deposited under a strain proportional to the difference in the lattice constants. In this project, thin films are deposited on substrates with amorphous surfaces. Because of the lack of a periodic crystal structure of the substrate surface, no lattice mismatch between the film and substrate exists, and therefore, epitaxial stress can be ignored in our study of thin films deposited on oxidized silicon substrates. Reviews of thin film stress evolution during Volmer-Weber epitaxy and Stranksi-Krastanov epitaxy growth are given by Koch [Koch 94].

Especially for high mobility materials, grain growth occurs during thin film deposition on amorphous substrates near room temperature. Early work using *in situ* transmission electron microscopy (TEM) demonstrated that Ag and Au deposited on crystalline MoS_2 substrates have final grains sizes larger than the initial island spacing [Pash 64, Pash 65]. Grain growth during thin film deposition has also been inferred from

ex situ microscopy at different film thicknesses [Aber 85, Lita 99, Thom 90]. Grain growth is a coarsening process by which large grains become larger at the expense of the small grains shrinking. The thermodynamic driving force for grain growth is the excess free energy associated with grain boundaries. Grain boundaries posses an excess volume and are regions of lower than equilibrium density. As grain growth proceeds, the total grain boundary area and the excess volume in the film decreases. If the film is constrained to maintain its macroscopic dimensions due to attachment to the substrate, the elimination of free volume in the film results in the development of a tensile strain ε_{dense} given approximately by [Chau 72]:

$$\varepsilon_{dense} = \Delta a\left(\frac{1}{d_0} - \frac{1}{d}\right), \tag{1.1}$$

where Δa is the excess volume per unit area of grain boundary, d_0 is the starting grain size, and d is the final grain size. For an excess volume per unit area of grain boundary of about 1Å [Hill 65], strains greater than 0.1% are predicted for starting grain diameters of less than 10 nm that eventually grow to much larger final diameters.

Even though film densification due to grain growth results in a tensile stress as described above, grain growth can act as a stress relaxation process as well. The yield stress of thin films has an inverse dependence with grain size [Venk 92, Nix 89], thus grain growth can enhance stress relaxation. Grain growth can also result in the favored growth of strain energy minimizing grain orientations, which have either a lower elastic modulus and/or yield stress, and subsequently results in a film with a lower average stress [Vook 65, Sanc 92, Flor 94].

1.4 Correlations between thin film stress measurements and film formation

Numerous explanations have been proposed as to the origin of the stresses that develop during thin film deposition. Wilcock *et al.* [Wilc 69] and later Abermann *et al.* [Aber 78] suggested that the compressive stress generated during the island stage of growth is due to a size-dependent lattice parameter in agreement with electron diffraction

experiments [Grig 66, Mays 68]. Several studies have subsequently been published following the same general argument as Abermann, but with emphasis on the effects of the free surface stress [Camm 00, Spae 00]. The distinction between surface energy and surface stress is explained in depth by Cammarata *et al.* [Camm 94, Camm 00] and Spaepen [Spae 00], and is briefly reviewed in section 4.2. The importance of film-substrate traction on the magnitude of the early compressive stress has not been addressed in the literature. The difference in the initial compressive stress behavior of Ag and Al deposited on oxidized silicon is discussed in section 4.2 in terms of film-substrate traction.

The correlation between an increasing tensile stress during deposition and island impingement resulting in grain boundary formation has been qualitatively confirmed in many studies and several explanations have been proposed as to the physical origin of the tensile stress generation. In Abermann's research, the tensile stress development was attributed to grain growth densification [Chau 72] as suspected from *ex situ* microscopy showing an increase average grain size with increasing film thickness [Aber 78, Aber 85]. Klokholm and Berry attribute the tensile stress generation to the annealing out of disordered material buried behind the advancing surface of the growing film [Klok 68]. Tensile stress has also been predicted by a model based upon shrinkage of grain boundary voids [Doer 88]. Other researchers have attributed tensile stress generation with the process of grain boundary formation upon island coalescence due to an "island zipping" process, also referred to as grain boundary relaxation [Hoff 76, Doer 88, Nix 99]. Based upon the intuition for stress generation due to grain boundary formation, finite-element methods are used in section 4.3 to calculate the island coalescence stress and are shown to be more consistent with experimentally measured values that the stress calculated using previous analytical models.

The long-term compressive stress measured during deposition once the film is continuous and the reversible tensile rise behavior during growth interrupts have received less attention in the literature. According to Abermann, the capillarity strain at the island stage of growth is propagated into the growing film and therefore gives rise to a respective compressive stress contribution in the continuous film [Aber 85]. Spaepen argues that repulsive step ledges on the growing surface could result in the compressive

stress in the continuous film during deposition [Spae 00]. Based upon *ex situ* microscopy evidence, Abermann and co-workers have attributed the tensile rise upon a growth interrupt to recrystallization [Aber 85]. Similarly, Wilcock *et al.* attributed the tensile rise after deposition was stopped to the annihilation of the excess volume of the grain boundaries resulting from grain coarsening [Wilc 69]. However, the tensile rise behavior is reversible upon resumption of growth while recrystallization is not. Spaepen attributed the reversible tensile rise behavior to a non-equilibrium density of surface ledges during deposition, which partially annihilate by surface diffusion once growth is stopped [Spae 00]. However quantitative predictions are not possible with the repulsive ledge mechanism due to the unknown magnitude of the interaction between surface ledges. Based upon a model for film surface shape evolution due to non-equilibrium growth, both the compressive stress during deposition and the reversible tensile rise behavior can be explained by an argument described in Chapter 5.

Chapter 2

Experimental Techniques

2.1 Overview

During the deposition of a thin film on a thick substrate, stresses are generated as a result of the film growth process, as discussed in detail in Chapter 1. The stresses in the film apply moments on the substrate that induce a change in the substrate curvature. While the substrate bending negligibly relieves the strain in the film, the substrate curvature provides a means of determining the film stress. Therefore, the stress evolution in the film during deposition can be deduced from *in situ* measurements of the substrate curvature. Our collaborators at Sandia National Laboratories (SNL) have measured thin film stresses by monitoring changes in substrate curvature using laser reflectometery, as briefly described in section 2.2.

Alternatively, the stress in the film can be determined by directly measuring the resulting stress in the substrate. We have developed an electrical technique for the *in situ* measurement of stress during thin film deposition utilizing piezoresistive microcantilevers, which will be referred to as piezocantilevers. The stress in the thin film is measured by monitoring the change in resistance of a piezoresistive boron resistor fabricated within a silicon microcantilever onto which the film is deposited. The silicon microcantilevers are fabricated using processing techniques developed for microelectromechanical system (MEMS) device fabrication. The design and fabrication

of the piezocantilevers will be described in section 2.3, along with the calibration required for accurate thin film stress measurements.

2.2 Multibeam optical stress sensor (MOSS)

Thin film stress can be determined by measuring the resulting curvature of the substrate onto which the film is deposited by monitoring the change in position of laser beams reflected off the substrate surface. The most common technique to measure substrate curvature is to scan a single laser beam across the sample and to monitor the deflected beam position on a position sensitive detector [Flin 87]. Another approach is to pass a laser through an etalon that produces multiple output beams that reflect off the substrate and are detected on a charge coupled device (CCD) camera [Flor 97]. A schematic of the multibeam optical stress sensor (MOSS) used by our collaborators at SNL is shown in Fig. 2-1. The relationship between the film stress and substrate curvature and the technique for measuring substrate curvature using MOSS are described below. A more detailed description of the MOSS technique is described elsewhere [Flor 97].

2.2.1 *In situ* film stress measurement

The 100-μm-thick Si (100) wafers used as substrates had either a native oxide or a thermally grown oxide (similar results were obtained for both types of substrates). The substrates were prepared using a solvent clean followed by a 4:1 H_2SO_4:H_2O_2 etch prior to loading in the vacuum chamber. The substrates were outgassed *in vacuo* at 350°C for 1 hour (for metal film deposition) or 750°C for 5 min (for semiconductor film deposition). All films were deposited by electron beam evaporation in ultrahigh vacuum (UHV). Base pressures were 1×10^{-10} Torr, while deposition pressures were in the range 5×10^{-9} – 3×10^{-8} Torr. Deposition rates ranged from 0.01–0.5 nm/s and were controlled using crystal quartz monitors. During deposition, the wafer curvature was measured using the MOSS system and the temperature was monitored using a thermocouple metal bonded to a witness wafer.

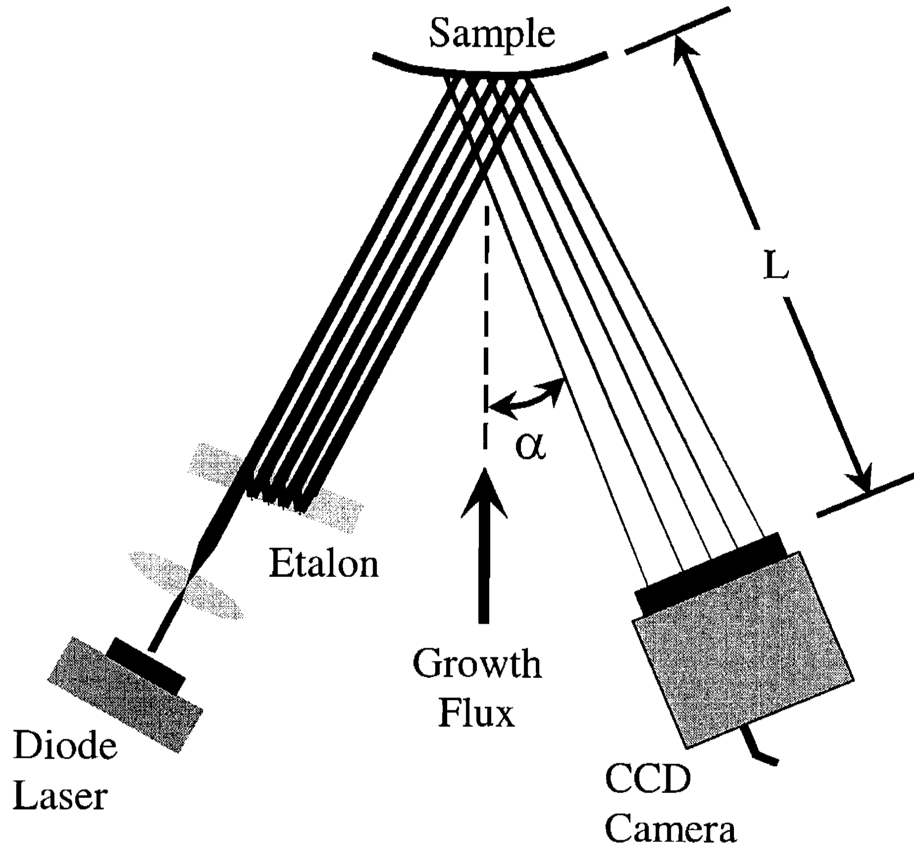

Figure 2-1: Schematic setup of the multibeam optical stress sensor (MOSS) apparatus used at Sandia National Labs for the *in situ* measurement of thin film stress during deposition.

If the thickness of the film is much less than the substrate thickness (i.e. $h_f << h_s$), the product of the average film stress σ_f and film thickness h_f can be related to the substrate curvature κ using Stoney's equation [Ston 09, Flin 87]:

$$\sigma_f \cdot h_f = \frac{E_s h_s^2}{6(1-\nu_s)}\kappa , \tag{2.1}$$

where E_s is the Young's modulus of the substrate and ν_s is the Poisson ratio of the substrate. The substrate curvature κ is determined by measuring the average spacing between adjacent beams normalized by the average initial spacing $<D/D_0>$:

$$\kappa = \frac{\cos\alpha}{2L}\left(1 - \left\langle \frac{D}{D_0} \right\rangle\right), \tag{2.2}$$

where α is the angle of incidence and L is the distance between the sample and CCD camera, as shown in Fig. 2-1. For the 100-μm-thick Si wafers used in the experiments, the stress-thickness measurement sensitivity is approximately 0.05 N/m (i.e. a 50 MPa stress can be resolved for a 1-nm-thick film).

2.3 Piezoresistive microcantilevers (piezocantilevers)

We have developed an electrical technique for the *in situ* measurement of stress during thin film deposition utilizing piezoresistive microcantilevers, or piezocantilevers. Figure 2-2 shows an optical microscope image of the piezocantilever device with the dimensions of the microcantilever and the position of the piezoresistive elements near the end of the cantilever. The 20-μm-thick silicon microcantilever is fabricated from a (110) silicon wafer supported by a 475-μm-thick (100) silicon handle wafer. For (110) surface-normal silicon, a boron resistor fabricated along the [110] in-plane direction has a large piezoresistive response, while a boron resistor fabricated along the [001] in-plane direction has a very small piezoresistive effect. As seen in Fig. 2-2, a Wheatstone bridge structure is fabricated near the end of the cantilever and consists of a single piezoresistive resistor along with three nonpiezoresistive resistors. The stress in a deposited thin film is measured by real-time monitoring of the change in resistance of the piezoresistor fabricated within the silicon microcantilever onto which the film is deposited. The design and theory of operation of the piezocantilevers, as well as the required stress and temperature calibrations, are described below.

2.3.1 Thin film stress and substrate stress

When a thin film is deposited under stress onto the top surface of the cantilever, the film applies moments that result in a stress in the substrate. Because the piezoresistive elements are fabricated within the top surface of the microcantilever, the

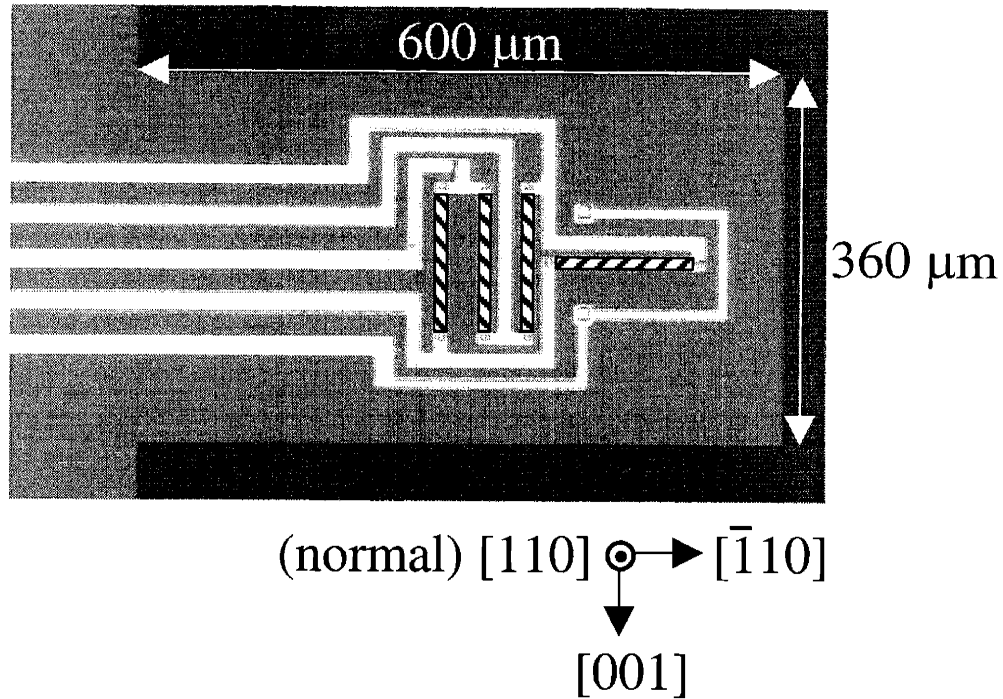

Figure 2-2: Optical microscope image of the top surface of a piezoresistive microcantilever. The 20-μm thick silicon cantilever terminates into a 475-μm thick supporting wafer on the left side of the image. The white lines in the image are the aluminum metallization that make electrical contact to the underlying silicon. A [110]-oriented resistor with strong piezoresistance and three [001]-oriented resistors with weak piezoresistance are configured in a Wheatstone bridge structure near the end of the cantilever.

relationship between the stress in the deposited film and the stress in the top surface of the substrate must be derived.

In order to electrically isolate the piezocantilever device from the deposited thin film, a passivating oxide is deposited on the top surface of the microcantilever. Thin films deposited on amorphous substrates grow with a random in-plane texture [Thom 90]. For a thin film composed of grains with no preferred in-plane texture on a thick substrate, the in-plane stresses in the film are equibiaxial while the shear and film-normal stresses are zero:

$$\begin{aligned}\sigma^f_{xx} &= \sigma^f_{yy} \equiv \sigma_f \\ \sigma^f_{zz} &= \sigma^f_{xy} = \sigma^f_{xz} = \sigma^f_{yz} = 0\end{aligned}, \tag{2.3}$$

where σ_{ij}^f are the components of the stress tensor of the film and σ_f is the biaxial stress in the film. The stress in the film applies moments M_{ij} on the substrate given by:

$$\begin{aligned}M_{xx} &= M_{yy} = h_f \frac{h_s}{2} \sigma_f \equiv M_s \\ M_{xy} &= 0\end{aligned}, \tag{2.4}$$

where h_f is the film thickness and h_s is the thickness of the substrate. The in-plane moments are equal and will be referred to as the moment on the substrate M_s. For an anisotropic plate with greater than orthogonal symmetry, such as for silicon with a cubic diamond structure, the relations between the in-plane stresses in the substrate and the applied moments are given by [Lekh 68]:

$$\sigma^s_{xx} = \sigma^s_{yy} = \frac{12 M_s}{h_s^3}\left(\frac{h_s}{3} - z\right) \equiv \sigma_s, \tag{2.5}$$

where σ_{ij}^s are the components of the stress tensor of the substrate, z is distance from the bottom surface of the substrate, and $h_s/3$ is the position of null stress in the substrate for the case of a thin film on a thick substrate [Town 87]. The in-plane state of stress in the substrate is also equibiaxial and will be referred to as the biaxial stress in the substrate σ_s. By combining Eqs. 2.4 and 2.5, the relationship between the biaxial stress in the film and biaxial stress in the substrate as a function of position is given by:

$$\sigma_s = \frac{6 h_f}{h_s^2}\left(\frac{h_s}{3} - z\right)\sigma_f . \tag{2.6}$$

Since the piezoresistive elements are fabricated within the top surface of the silicon substrate at $z = h_s$ the relation between the stress in the film and the stress at the surface of the substrate σ_s^{top} is desired:

$$\sigma_s^{top} = -\frac{4}{h_s}\sigma_f h_f . \tag{2.7}$$

Therefore the thinner the substrate, the larger is the stress in the top surface of the substrate for a given stress-thickness product $\sigma_f h_f$ in the film.

2.3.2 Cantilever geometry

The mechanical analysis above assumes that the boundary conditions are such that the plate is free to bend. However, the 20-μm-thick silicon cantilever shown in Fig. 2-2 terminates at the base into a 475-μm-thick wafer support. Curvature along the width of the cantilever near the base is constrained by the rigid support. Far from the base, the cantilever is free to deform in both the width and length directions due to the moments applied by the stress in the film. In the transition region from the base towards the end of the cantilever, the stress distribution is non-uniform and difficult to model analytically. For simplicity, the piezoresistive elements were fabricated away from the cantilever base in the region of pure plate bending.

In order to study the influence of the support, finite-element methods were used to study the stress response in a cantilever due to a film under a biaxial stress. An example of the finite element mesh used for a 5:3 length-to-width (L:w) cantilever is shown in Fig. 2-3 (to scale with the 600-μm long cantilever shown in Fig. 2-2). Due to the bilateral symmetry of the cantilever, only half of the cantilever needs to be modeled. The base of the cantilever is assumed to terminate into a fixed, rigid support. In addition, a thin film is present on the top surface of the cantilever with a thickness much less than that of the cantilever ($h_s = 40h_f$). Due to a difference in the thermal expansion coefficient of the film and substrate, changing the temperature imposes a biaxial, thermal strain $\varepsilon_{thermal}$ in the film:

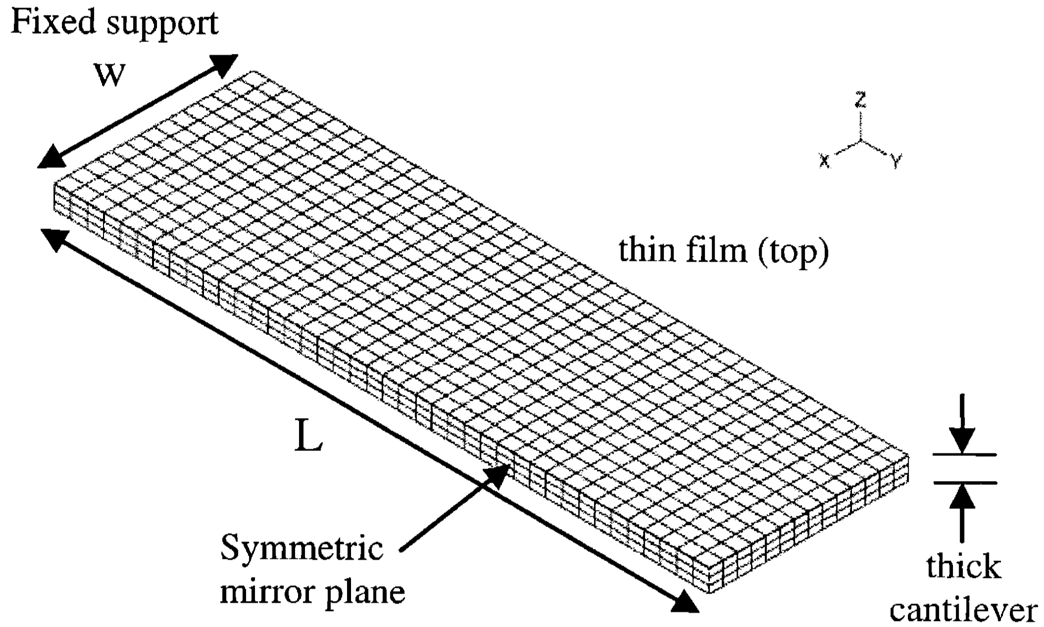

Figure 2-3: Finite element method (FEM) mesh of a 5:3 length-to-width (L:w) cantilever (comparable to Fig. 2-2) with a thin film on the top surface. The thickness of the film is 40 times thinner than the substrate thickness. The FEM calculations were performed using the commercial software ADINA.

$$\varepsilon_{thermal} = (\alpha_s - \alpha_f)\Delta T \,, \tag{2.8}$$

where ΔT is the change in temperature and α_s and α_f are the thermal expansion coefficients of substrate and film, respectively. For convenience, the elastic constants of the film and substrate are assumed to be isotropic.

Near the end of the thick cantilever where substrate deformation is unconstrained by the support, the thermal stress in the thin film σ_f is related to the thermal strain $\varepsilon_{thermal}$ by the biaxial modulus $E_f/(1-\nu_f)$ so that $\sigma_f = [E_f/(1-\nu_f)]\,\varepsilon_{thermal}$ where E_f is the Young's modulus and ν_f is the Poisson ratio of the film. Figure 2-4 shows the in-plane stresses calculated by FEM normalized by the calculated thermal stress as a function of position across the entire cantilever. For clarity, traces of the thin film stress along and across the cantilever are shown in Fig. 2-5 where the positions of the traces are indicated in Fig. 2-4.

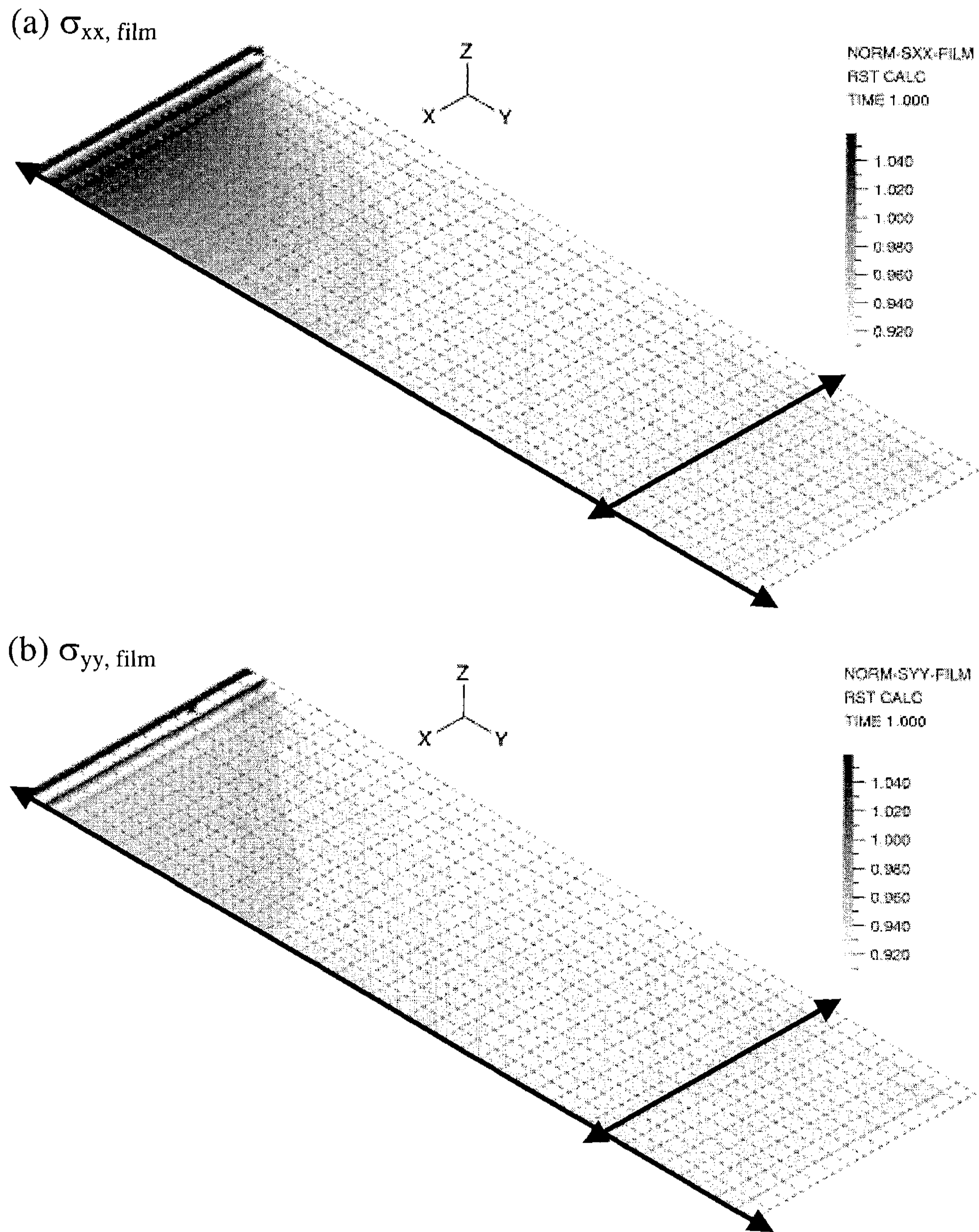

Figure 2-4: Finite element results for the thin film in-plane stresses resulting from differential thermal expansion between the film and substrate for the system shown in Fig. 2-3. The in-plane stresses calculated by FEM are normalized by the calculated thermal stress. Traces (indicated by arrowed lines) of the stress are shown in Fig. 2-5.

(a)

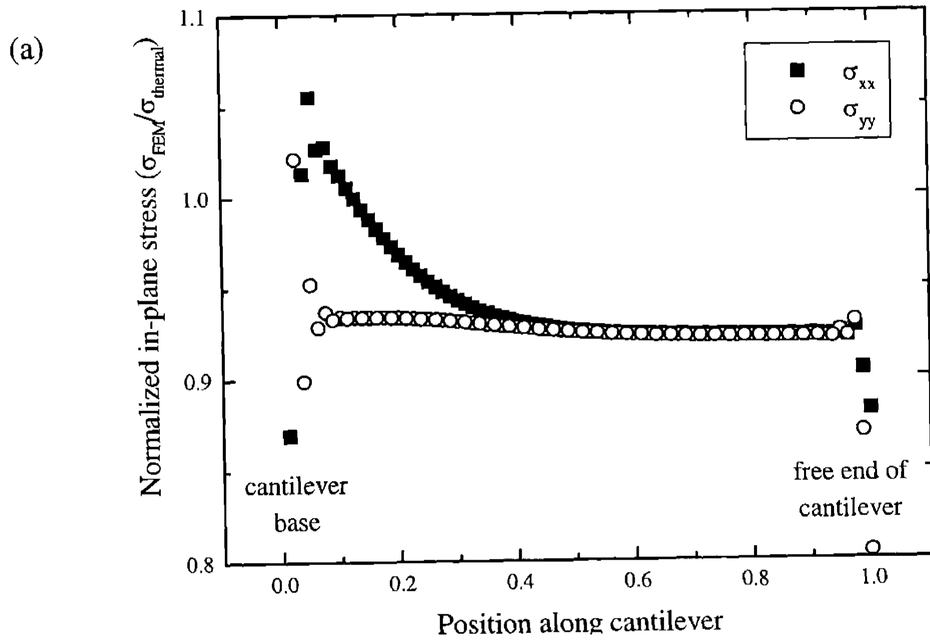

(b)

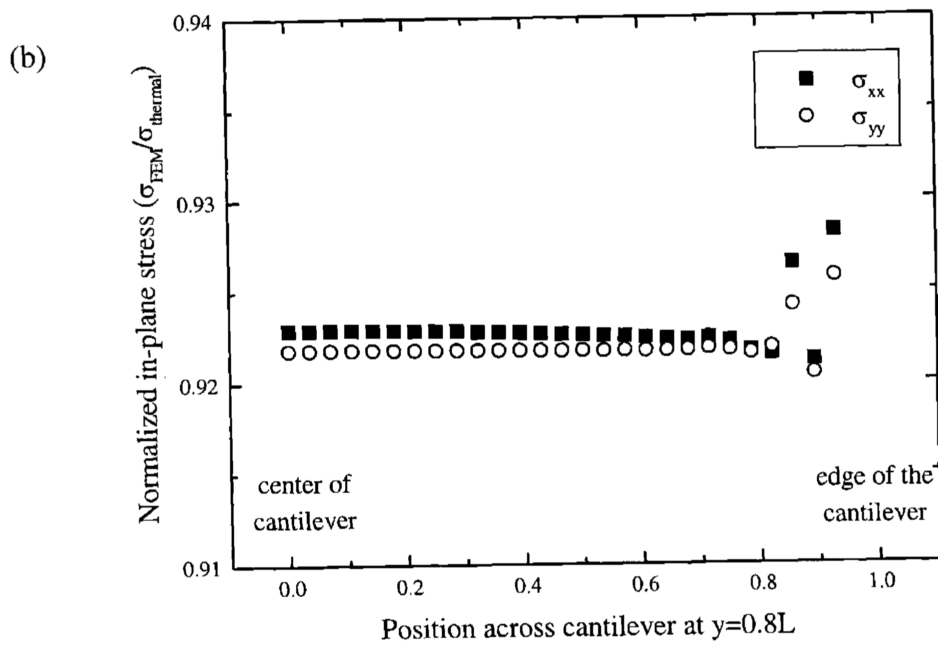

Figure 2-5: The normalized in-plane stresses in the film (a) along the centerline of the cantilever length, (b) across the cantilever at y= 0.8L for the traces indicated in Fig. 2-4.

The normalized in-plane stresses in the film along the centerline of the cantilever length are shown in Fig. 2-5(a), while the normalized in-plane stresses across the cantilever at y= 0.8L are shown in Fig. 2-5(b). As expected, the stresses near the cantilever base are non-uniform, whereas the stresses become uniform and equibiaxial towards the end of the cantilever even for the relatively small 5:3 length-to-width ratio. In addition, the stresses near the free edges of the cantilever are also non-uniform. Note that the normalized stresses in Fig. 2-5 near the end of the cantilever are slightly less than one (by about 8%) because of strain accommodation in the cantilever. Strain accommodation by the substrate becomes even less important for thinner films and is negligible when h_s/h_f is greater than 100. For the 20-μm-thick cantilevers, films of less than 100 nm were typically deposited and therefore strain accommodation by the substrate should be relatively insignificant ($h_s/h_f \approx 200$).

From Eq. 2.7, the ratio of σ_s^{top}/σ_f equals $-4h_f/h_s$ so that in the FEM model for which $h_s = 40h_f$, the magnitude of the stress in the top surface of the substrate should be approximately 10% of the stress in the film. Figure 2-6 shows the in-plane stresses in the top surface of the substrate from FEM divided by the thermal stress in the film along the centerline of the cantilever length (Fig. 2-6(a)), and across the cantilever at y= 0.8L (Fig. 2-6(b)). As expected, the stresses near the cantilever base are non-uniform, whereas the stresses become uniform and equibiaxial towards the end of the cantilever. The stress ratio value σ^{top}_s/σ_f near the end of the cantilever is slightly less in magnitude than 0.10 for the same reason that the normalized stresses in Fig. 2-5 are slightly less than 1.0.

The FEM results in Figs. 2-4 to 2-6 show that the in-plane stresses in both the film and in the top surface of the cantilever are uniform and biaxial near the end of a cantilever with a 5:3 length-to-width ratio. In addition, the stresses become uniform away from the free edges of the cantilever. Consequently, the piezoresistive elements were fabricated near the end of the cantilever, as shown in Fig. 2-2, and experience uniform stresses due to a biaxial stress in the film. Other cantilever geometries were used for the piezocantilever devices but with even greater length-to-width ratios (the cantilever width was always 360 μm with lengths of 600, 900, and 1200 μm), for which the support constraint becomes even less important when the piezoresistive elements are fabricated near the end of the cantilever.

(a)

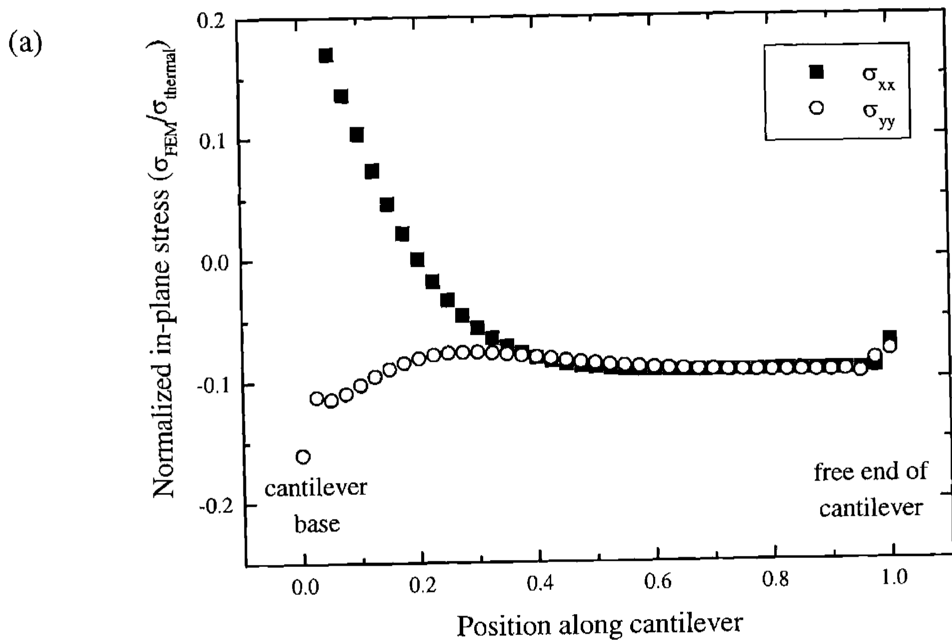

(b)

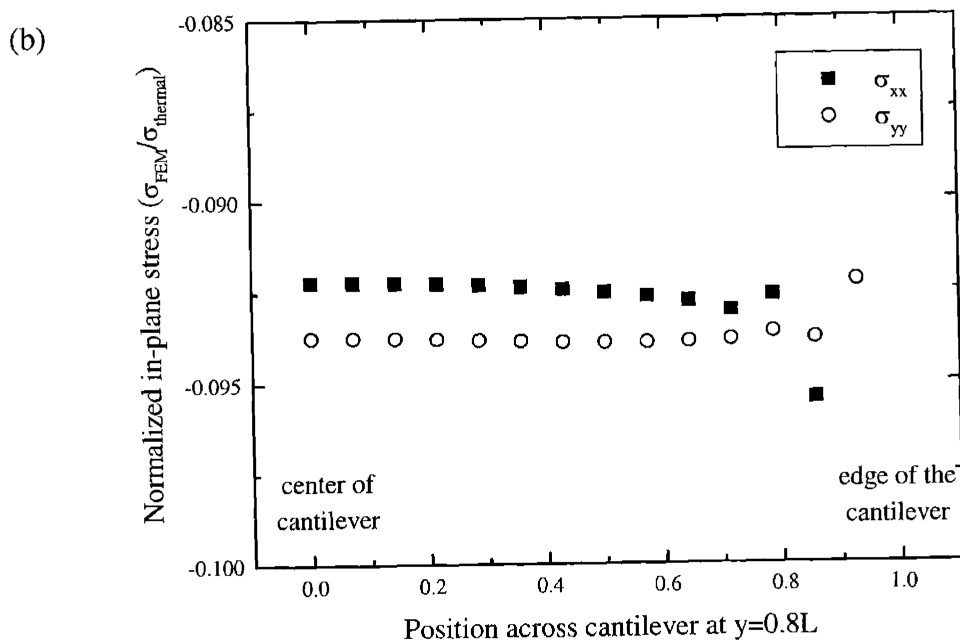

Figure 2-6: The normalized in-plane stresses in the top surface of the cantilever substrate (a) along the centerline of the cantilever length, and (b) across the cantilever at y= 0.8L for the traces indicated in Fig. 2-4.

2.3.3 Piezoresistivity

Since the discovery of the piezoresistance effect in semiconductors having anisotropic energy band structures [Smit 54], it has been used widely for stress and strain sensor applications. The piezoresistance of silicon has been exploited in wide variety of applications including pressure sensors [Eato 97], accelerometers [Royl 79], and for atomic force microscopy [Tort 91, Linn 96]. One of the main reasons for using stress sensors made from silicon is that the piezoresistivity effect is 50−100 times larger than that for conventional metal strain gauges [Kand 91].

Piezoresistance, the linear change in resistivity due to small applied stresses, is expressed by:

$$\Delta\rho_i/\rho_0 = \pi_{ij}\sigma_j, \tag{2.9}$$

where $\Delta\rho_i/\rho_0$ are the components of the tensor expressing the fractional change in resistivity, π_{ij} are the components of the piezoresistance tensor, and σ_j are the components of the stress tensor. In crystals such as Si with cubic symmetry, the fundamental piezoresistive coefficients are π_{11} (longitudinal), π_{12} (transverse), and π_{44} (shear). Considering the general case in Cartesian coordinates for an arbitrary orientation under a biaxial stress, the relative change in the in-plane resistivity is given by:

$$\rho_1/\rho_0 = \pi'_{11}\sigma'_1 + \pi'_{12}\sigma'_2, \tag{2.10}$$

where σ'_1 and σ'_2 are the normal in-planes stresses parallel and perpendicular to the current, respectively. The graphs of the room temperature values of π'_{11} and π'_{12} for p-type doped silicon plotted as a function of crystal direction for orientations in the (100) and (110) planes are shown in Fig 2-7 [Kand 82]. The upper halves of the graphs show the positive-valued π'_{11} piezoresistance coefficients (i.e. the resistivities increase with tensile stress), while the lower halves in the figures show the negative-valued π'_{12} piezoresistive coefficients (i.e. the resistivities decrease with tensile stress). P-doped

(a) (100) Si

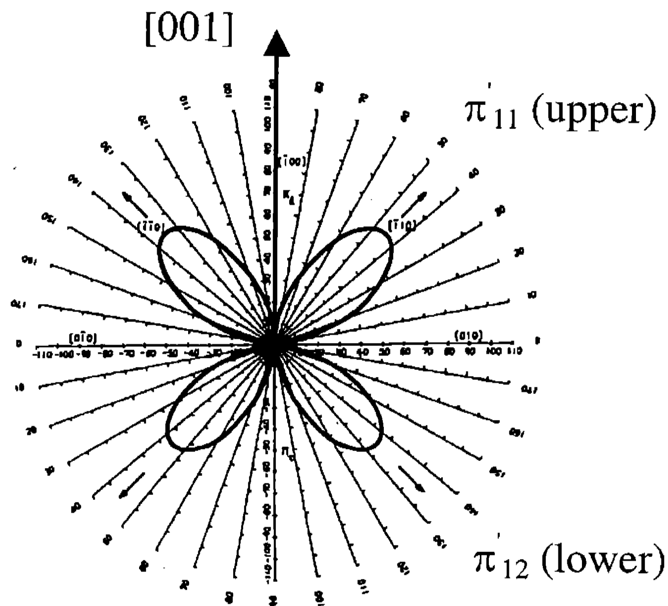

(b) (110) Si

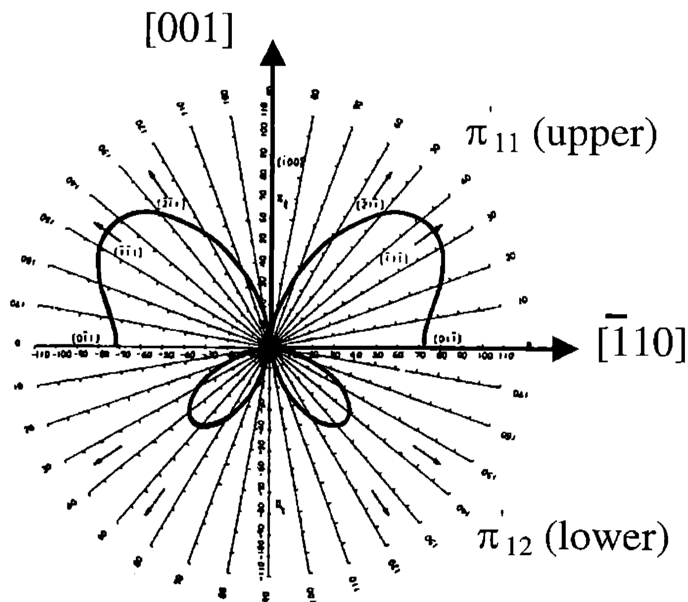

Figure 2-7: Plots of the room temperature values of π'_{11} and π'_{12} for p-type doped silicon plotted as a function of crystal direction for orientations in the (a) (100) plane, and (b) (110) plane [Kand 82]. The upper halves of the graphs show the positive-valued π'_{11}, while the lower halves show negative-valued π'_{12}. The units of the piezoresistive coefficients are in 10^{-11} Pa^{-1}.

silicon was chosen for the piezocantilever devices because it exhibits the largest piezoresistive effect.

As seen in Fig. 2-7(a) for (100) silicon, for all in-plane directions the values of the piezoresistive coefficients are such that $\pi'_{11} + \pi'_{12}$ approximately equals zero. From section 2.3.1, a biaxial film stress results in a biaxial stress in the top surface of the substrate so that σ'_1 equals σ'_2. Therefore according to Eq. 2.10, no appreciable change in resistivity would occur for any in-plane orientation of (100) silicon under a biaxial stress. For (110) silicon, the piezoresistive coefficients are such that $\pi'_{11} + \pi'_{12}$ varies from nearly zero to an advantageously large value depending on the in-plane direction. For (110) silicon in the [110] in-plane direction, the value of $\pi'_{11} = 71.8 \text{ X } 10^{-11} \text{ Pa}^{-1}$ while $\pi'_{12} = -1.1 \text{ X } 10^{-11} \text{ Pa}^{-1}$. Therefore for a p-type doped resistor oriented along the [110] direction in (110) silicon, an equibiaxial stress would result in a large change in resistivity. For (110) silicon in the [001] direction, the value of $\pi'_{11} = 6.6 \text{ X } 10^{-11} \text{ Pa}^{-1}$ while $\pi'_{12} = -1.1 \text{ X } 10^{-11} \text{ Pa}^{-1}$. Therefore for a p-type doped resistor oriented along the [001] direction in (110) silicon, an equibiaxial stress would result in a very small change in resistivity. These two different orientations in (110) silicon were utilized for the resistor structures described in the section 2.3.4.

The calculated doping concentration and temperature dependence of the piezoresistive coefficients for p-type silicon are shown in Fig. 2-8 [Kand 82]. The predicted values in Fig. 2-8 are in general agreement with experimental values of the piezoresistive coefficients of boron as a function of doping level and temperature [Tuft 63]. For the piezocantilevers devices, a doping concentration of 10^{20} cm^{-3} was chosen for two reasons. By choosing a high doping level, the temperature dependence of the piezoresistive coefficients is negligible. Note that the sensitivity of the devices could have been increased by a factor of approximately five by choosing a lower doping concentration but with temperature dependent piezoresistive coefficients. In addition, a high doping concentration also allows for good ohmic contact between the boron-diffused regions and the aluminum metallization.

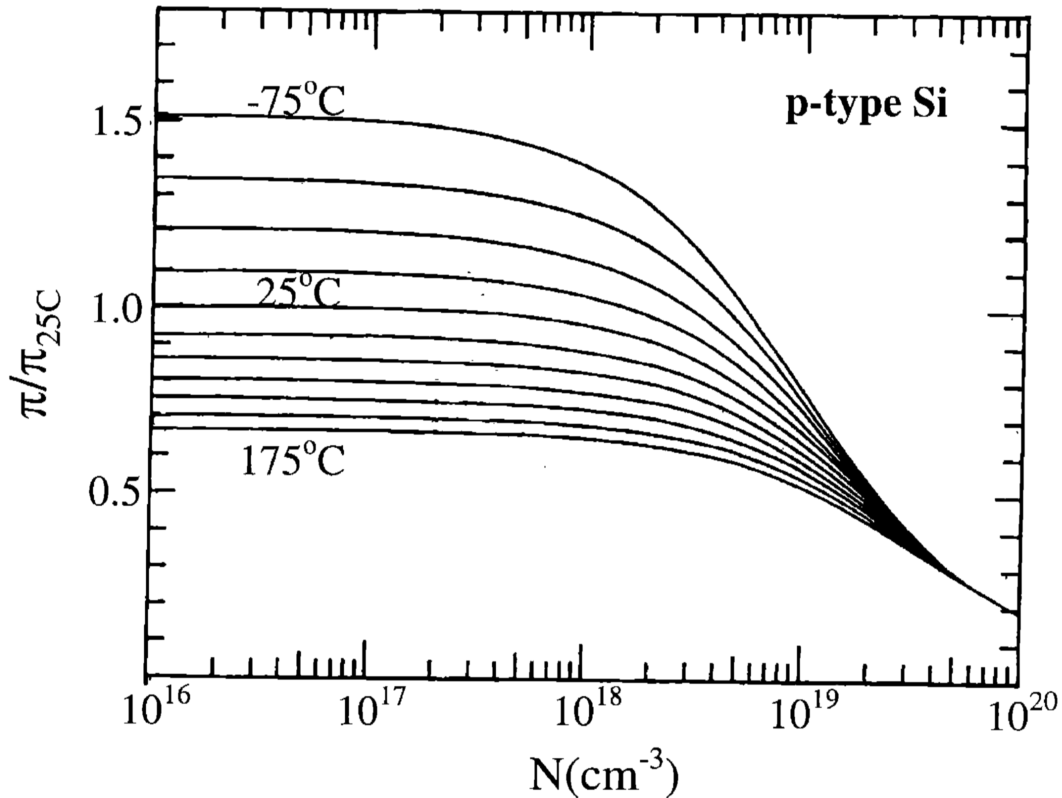

Figure 2-8: The calculated piezoresistive coefficients for p-type silicon (normalized by the value of the piezoresistive coefficient at 20°C) as a function of doping concentration and temperature [Kand 82].

2.3.4 Resistor structures for stress and temperature measurement

Two types of resistor structures were fabricated to monitor stress as well as temperature during deposition. The stress monitor consists of one piezoresistive resistor (piezoresistor) fabricated along the [110] direction, and three nonpiezoresistive resistors (nonpiezoresistors) fabricated along the [001] direction. The four resistors are electrically connected together in a Wheatstone bridge configuration as shown schematically in Fig. 2-9. The same Wheatstone bridge structure can be seen in an image of an actual piezocantilever device in Fig. 2-2. A supply voltage is applied across two of the leads while the voltage response of the bridge is monitored across the other two leads.

(a)

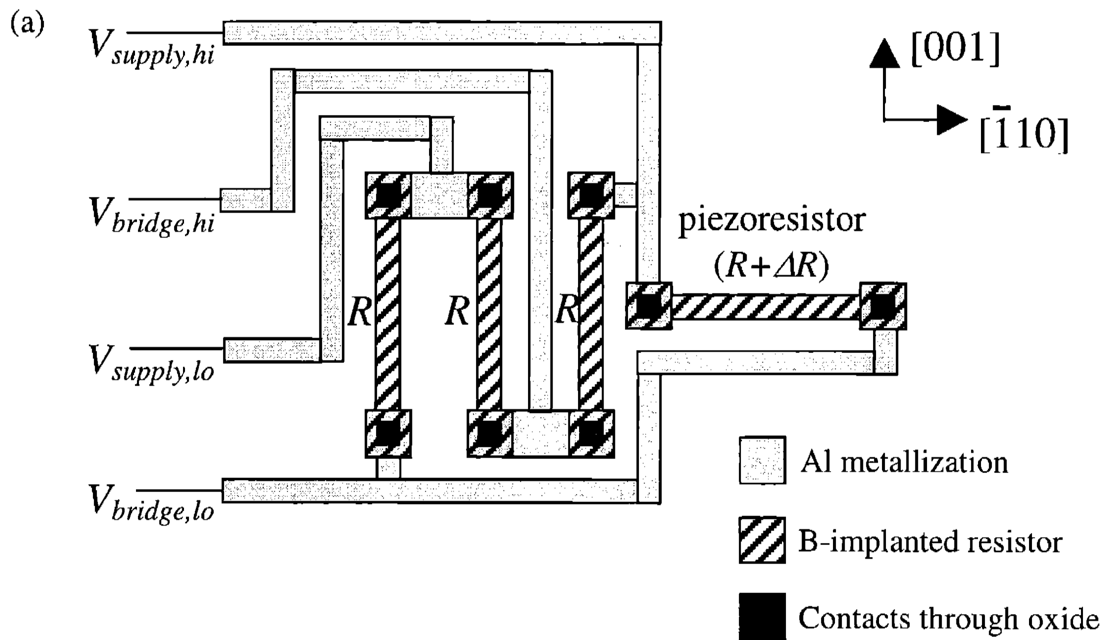

(b)

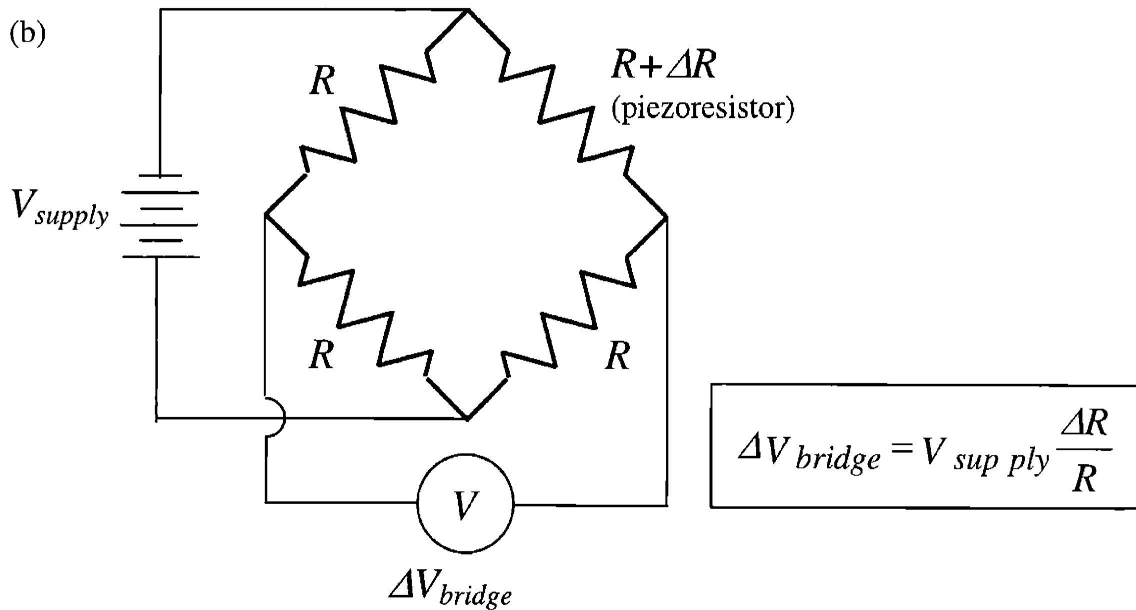

Figure 2-9: The stress monitor consists of one piezoresistive resistor and three nonpiezoresistive resistors. The four resistors are connected in a Wheatstone bridge as shown in (a) a schematic of the fabricated structure similar to Fig. 2-2, and as (b) an electrical circuit diagram. A supply voltage is applied across two of the leads while the voltage response of the bridge is monitored across the other two leads.

The substrate is reverse-biased to electrically isolate the p-type boron resistors from the n-type phosphorous substrate. For a balanced bridge with all four resistances equal, a bridge voltage of zero is measured. When a thin film is deposited on the cantilever, the stress in the film imposed a stress in the top surface of the silicon where the resistors are fabricated. The stress in the silicon results in a change in resistance of the piezoresistor ΔR that is measured as a change in the bridge voltage ΔV_{bridge}:

$$\Delta V_{bridge} = V_{supply} \frac{\Delta R}{R}, \tag{2.11}$$

where V_{supply} is the voltage supplied to the Wheatstone bridge, and R is the resistance of the boron implanted resistors. Since the change in resistance due to dimensional changes is negligible compared to the piezoresistive response, $\Delta R/R \approx \Delta\rho/\rho$ in Eq. 2.11. By combining Eqs. 2.8, 2.10 and 2.11, the relation between the measured Wheatstone bridge voltage and the stress-thickness product of the film can be determined:

$$\Delta V_{bridge} = V_{supply} \left(\pi'_{11} + \pi'_{12}\right) \frac{4}{h_s} \sigma_f h_f \, . \tag{2.12}$$

There are two advantages to using a Wheatstone bridge to measure resistance. A change in temperature results in a change in the resistivity of the boron resistors. However, if all the resistors undergo the same temperature change, the bridge is still balanced. Therefore, the Wheatstone bridge configuration automatically compensates for the temperature dependence of the resistivity. Secondly, only changes in resistivity are measured as opposed to other methods that measure the absolute resistance. Monitoring the absolute resistance would require resolving very small changes of a relatively large resistance value.

The second type of resistor structure is used to monitor changes in temperature during deposition. The temperature monitor consists of three nonpiezoresistors fabricated along the [001] direction as shown in Fig. 2-10(a). The three resistors are

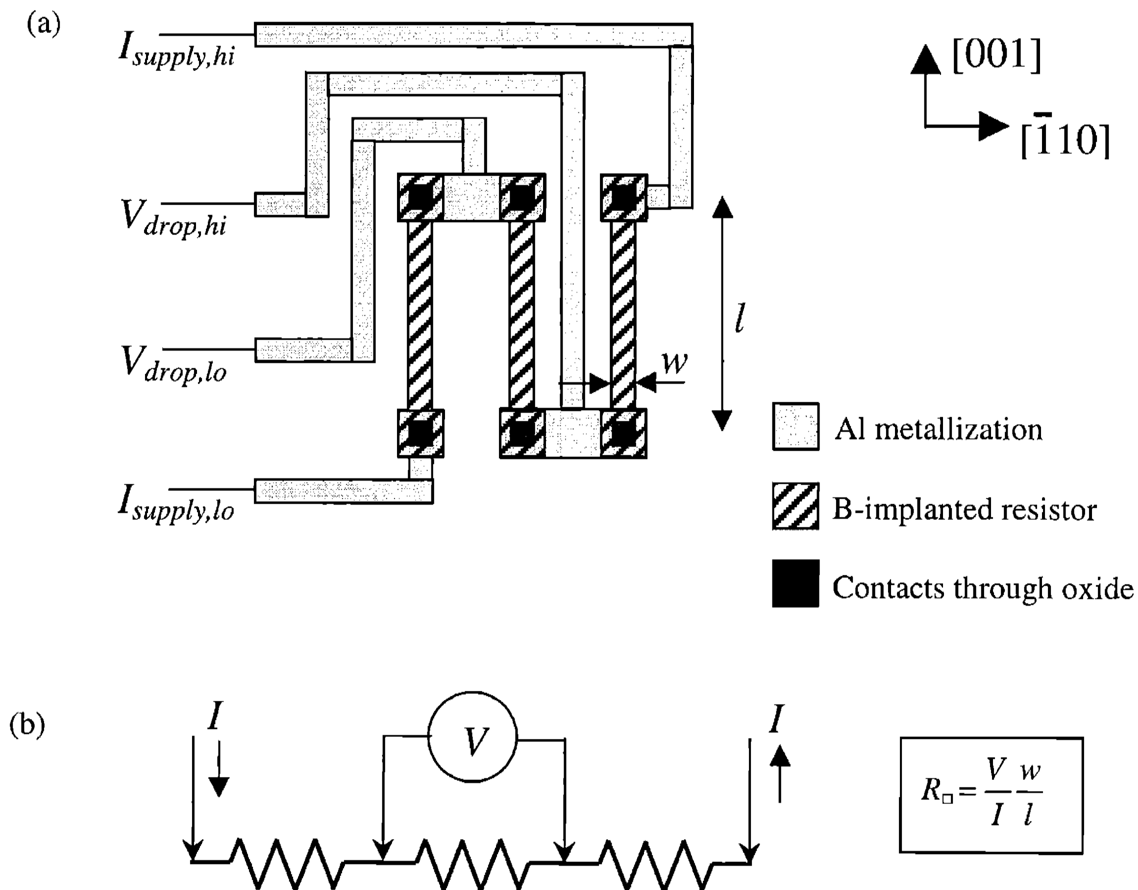

Figure 2-10: The temperature monitor consists of three nonpiezoresistive resistors connected in a Kelvin structure as shown in (a) a schematic of the fabricated structure, and (b) an electrical circuit diagram. A constant current is supplied across the outer two leads while a voltage drop is monitored across the inner two leads. The dimensions of the resistor are labeled in (a) and are used to calculate the sheet resistance $R_{\square}$ using the equation shown in (b).

electrically connected together in Kelvin structure to allow for a four-point resistance measurement, as shown in Fig. 2-10(b). A constant current is applied across the outside leads and a voltage drop is monitored across the inner leads to allow a calculation of the sheet resistance. The substrate is reverse-biased to electrically isolate the p-type boron resistors from the n-type phosphorous substrate. By calibrating the change in resistance

as a function of temperature, the resistance can be measured during deposition to monitor the temperature of the substrate.

The Kelvin structure is fabricated on a separate cantilever from the stress monitor, but a cantilever with the same geometry as the stress monitor cantilever. In addition, the Kelvin structure is positioned near the end of the cantilever much like the Wheatstone bridge structure. Consequently, the Kelvin structure and Wheatstone bridge structure experience the same temperature excursions during deposition. Therefore, using the Kelvin structure to monitor temperature during deposition provides accurate information about the temperature experienced by the Wheatstone bridge during deposition. As will be discussed in section 2.3.7, knowledge of the temperature during deposition allows thermal stress corrections to be applied to the measured thin film stress.

2.3.5 Measurement sensitivity and stability

The sensitivity of the piezoresistive technique for measuring thin film stresses depends on design issues related to device fabrication as well as the noise associated with the electrical measurement setup. The doping species and concentration in the silicon, the orientation of the silicon cantilever, and the cantilever substrate thickness were chosen so as to ensure the highest likelihood of fabricating workable devices with high enough sensitivity to resolve the salient features of stress evolution during thin film deposition. The theoretical piezocantilever device sensitivity will be compared to the MOSS technique described in section 2.2, which is known to have a 0.05 N/m resolution of the film stress-thickness product [Flor 97].

By rearranging Eq. 2.12, the minimum resolvable film stress-thickness product can be expressed in terms of the factors related to the piezocantilever design and the noise in the electrical measurement so that:

$$\left(\sigma_f h_f\right)_{min} = \frac{\Delta V_{bridge}}{V_{supply}} \frac{h_s}{4} \frac{1}{\pi'_{11} + \pi'_{12}}. \qquad (2.13)$$

Due to practical issues related with the micromachining process used to create the cantilevers, a conservative value of h_s= 20 μm was chosen for the device layer thickness.

The wafer thinning process used to create the piezocantilevers is discussed in section 2.3.8, which details the device fabrication. For the piezoresistor fabricated along the [110] direction in the (110) Si wafer, the value of $\pi'_{11} + \pi'_{12}$ equals 14.14 X 10-11 Pa^{-1}. The remaining factor to be considered in Eq. 2.13 is $\Delta V_{bridge}/V_{supply}$, which is related to the signal-to-noise ratio of the Wheatstone bridge resistance measurement.

As discussed in section 2.3.4, for a balanced Wheatstone bridge with equal resistances of all four resistors, the voltage response of the bridge should be zero. However, the as-fabricated piezocantilever structures are not stress free due to residual stress in the aluminum metallization and passivating oxide resulting from the deposition process. For instance, the passivating oxide is deposited at 400°C and then cooled back to room temperature. Due to any differential thermal expansion between the silicon and passivating silicon dioxide, a thermal stress in the oxide results in a residual stress in the silicon cantilever. Therefore, a non-zero bridge voltage is expected even without any externally applied stress. Figure 2-11 shows the Wheatstone bridge voltage as a function of time with a supply voltage of 1 V at room temperature without any externally applied stress. The signal has been corrected for slight temperature variations during the five hour stability test according to the method described in section 2.3.7. Note that the stability of the signal is relatively good over a time span of 5 hrs, which is comparable to the time required for a thin film stress measurement. The standard deviation of the noise of $\Delta V_{bridge}/V_{supply}$ in Fig. 2-11 is about 0.7 μV/V. According to Eq. 2.11, increasing the supply voltage should result in a larger measured bridge voltage for a given $\Delta R/R$ thereby increasing measurement resolution. However, the noise in the measured bridge voltage was found to increase linearly with increasing supply voltage in the range of 1-10 V. Therefore, the standard deviation in the measured Wheatstone bridge response is about 0.7 μV/V, independent of the supply voltage.

Using the experimentally determined signal-to-noise ratio of the Wheatstone bridge electrical measurement, the minimum resolvable film stress-thickness product can finally be calculated according to Eq. 2.13:

$$(\sigma_f h_f)_{min} = \frac{\Delta V_{bridge}}{V_{supply}} \frac{h_s}{4} \frac{1}{\pi'_{11} + \pi'_{12}} = 0.025 \text{ N/m} . \tag{2.14}$$

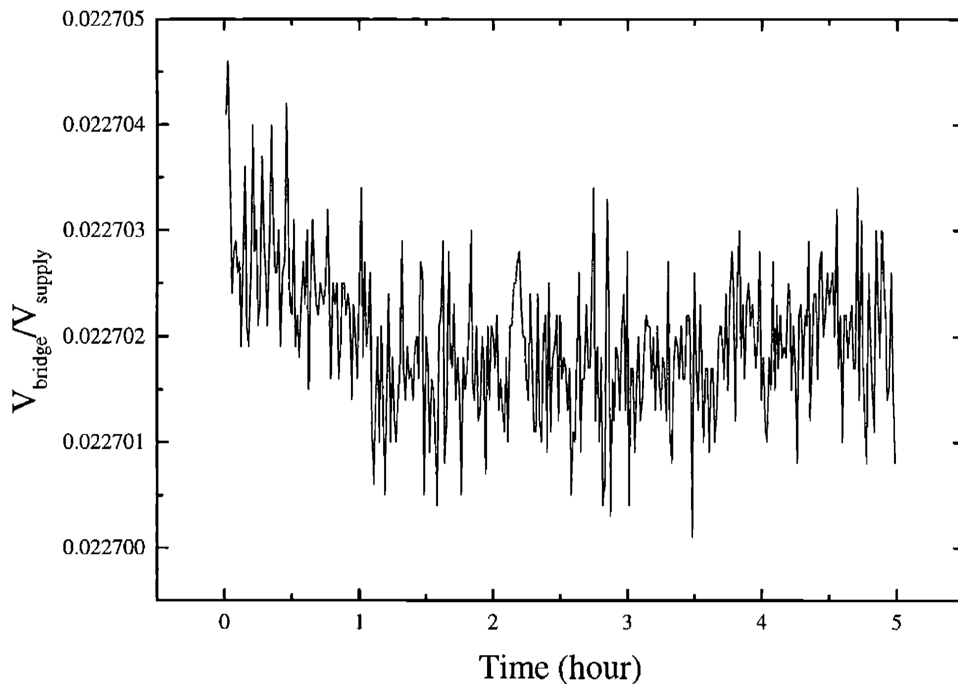

Figure 2-11: Wheatstone bridge voltage response V_{bridge} as a function of time with V_{supply}= 1V at room temperature without any externally applied stress. The non-zero Wheatstone bridge response is most probably due to residual stress from the aluminum metallization and passivation oxide processing. Notice that the signal is relatively stable over five hours with a standard deviation of approximately 0.7 μV/V.

The calculated theoretical sensitivity of the piezocantilever devices is approximately the same, if not better, than the measured sensitivity of 0.05 N/m for the MOSS setup.

2.3.6 Calibration

Calibration of the piezocantilever devices is necessary for accurate *in situ* thin film stress measurements. The stress calibration of the piezocantilever devices relates the measured Wheatstone bridge voltage response to an applied stress. A stress of known magnitude can be applied by deflecting the end of the cantilever with a tungsten probe attached to a linear micrometer. A temperature calibration of the Kelvin structure relates the measured sheet resistance to known changes in temperature. During deposition, the sheet resistance can be monitored and related back to the temperature of the substrate. The temperature of the substrate must be known during deposition to calculate thermal

stresses not associated with the intrinsic stress measurement. Finally, metrology of the cantilever substrate thickness must be done for accurate calibration and thin film stress measurements.

2.3.6.1 Stress calibration of Wheatstone bridge structures

The theoretical sensitivity of the piezoresistive devices was calculated in section 2.3.5 based upon the design of the devices. However, calibration must be performed to measure the Wheatstone bridge voltage response to a known applied stress. By deflecting the end of the cantilever with a tungsten probe as shown in Fig. 2-12, a linear

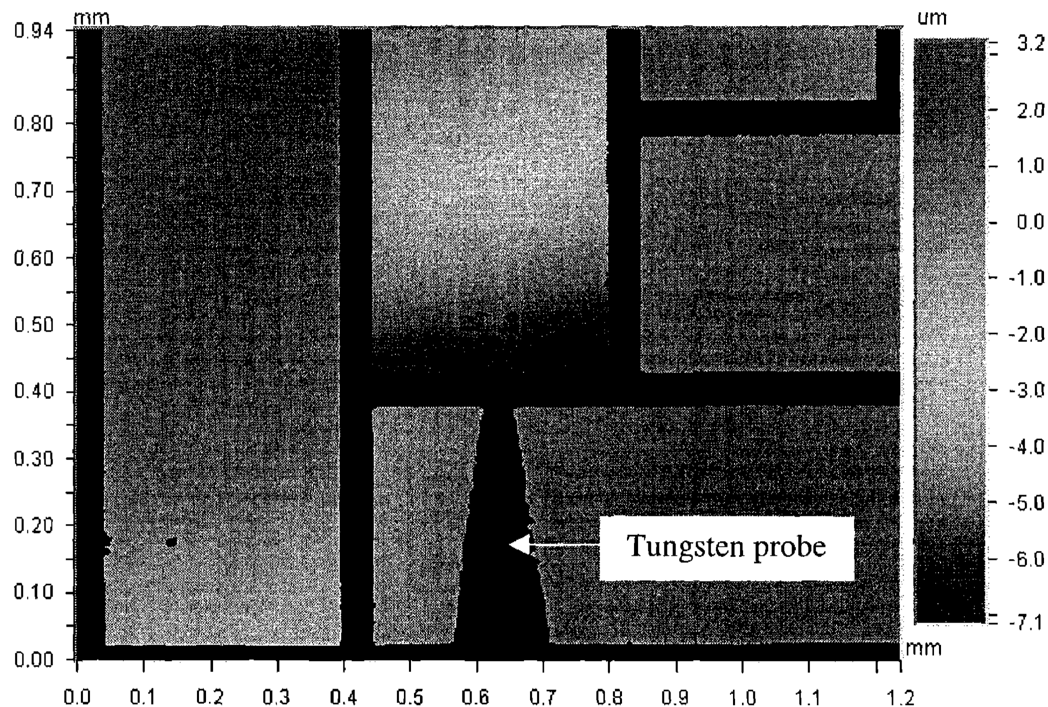

Figure 2-12: Tip deflection of a cantilever by a tungsten probe controlled by a linear micrometer. The image above was obtained by optical interferometry using a Veeco WYKO commercial system. The WYKO system provides vertical deflection data as a function of position along the cantilever.

stress gradient is created along the length of the cantilever. The reference coordinate system is chosen so that the x-direction is along the width of the cantilever, and the y-direction is along the length of the cantilever with the y-origin at the cantilever tip. For a cantilever with a thickness greater than its width, the relation between the tip deflection δ_{tip} and the stress in the top surface of the cantilever as a function of position $\sigma(y)$ is well known [Timo 34]:

$$\sigma(y) = \frac{3}{2} E \frac{h\,\delta_{tip}}{L^3} y, \tag{2.15}$$

where E is the Young's modulus of the cantilever, h is thickness of the cantilever, and L is the cantilever length. However, the silicon piezocantilever devices are not truly cantilevers but plates and have anisotropic elastic properties. Consequently, the Young's modulus in Eq. 2.15 must be substituted by the anisotropic plate modulus so that:

$$\sigma(y) = \frac{3}{2} \frac{E_y}{1 - \nu_y \nu_x} \frac{h\,\delta_{tip}}{L^3} y, \tag{2.16}$$

where E_y is the Young's modulus in the y-direction along the length of the cantilever, and ν_x and ν_y are the Poisson ratios in the x- and y-directions, respectively, where the x-direction is across the width of the cantilever. Anticlastic curvature of the cantilevers due to the tip deflection has been ignored. The (110) silicon cantilevers are fabricated with their length along the [110] direction, and the width in the [100] direction, so the necessary elastic constants are given by [Bran 73]:

$$\begin{aligned} E_{[110]} &= \frac{4}{2 s_{11} + 2 s_{12} + s_{44}} = 1.689 \mathrm{X} 10^{11}\,\mathrm{Pa} \\ \nu_{[110]} &= \frac{-4 s_{12}}{2 s_{11} + 2 s_{12} + s_{44}} = 0.361 \\ \nu_{[100]} &= -\frac{s_{12}}{s_{11}} = 0.279 \end{aligned} \tag{2.17}$$

where s_{ij} are the components of the compliance matrix of silicon, referred to the [001] axes [Simm 71].

Figure 2-13 shows the vertical deflection along the length of a 600-μm-long cantilever in the unloaded state and with nominal 2, 4 and 6-μm tip deflections. The vertical deflections as a function of position are measured by optical interferometry using a commercial system manufactured by WYKO. The magnitude of the tip deflection is controlled by translating a tungsten probe attached to a linear micropositioner. Due to compliance of the tungsten probe arm, the actual amount of tip deflection is not

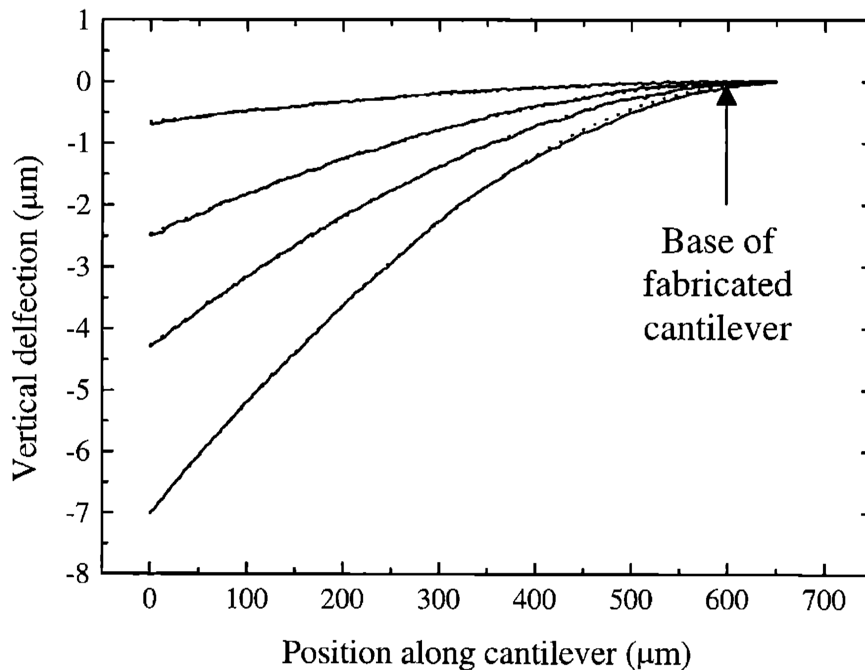

Figure 2-13: Vertical deflection along the length of a 600-μm-long cantilever in the unloaded state and with nominal 2, 4 and 6-μm tip deflections. The magnitude of the tip deflection is controlled by translating a tungsten probe attached to a linear micrometer. The vertical deflections as a function of position are measured by optical interferometry using the WYKO system. Note that vertical deflections occur past the base of the fabricated cantilever as a result of support compliance. Fitted curves using Eq. 2.17 are dashed lines that are almost indistinguishable from the measured deflection data.

necessarily the amount indicated by the linear micropositioner. In addition, note that vertical deflections in Fig. 2-13 occur past the base of the fabricated cantilever as a result of support compliance. The support compliance is due to undercutting during the etch process to fabricate the cantilevers. Fortunately, the optical interferometric scan provides data for the vertical deflection versus position along the cantilever. The vertical deflection data *v(y)* that can be fit to the equation of a deflected plate [Timo 34]:

$$v(y) = \left(\frac{1}{2}\frac{y^3}{L^3} - \frac{3}{2}\frac{y}{L} + 1 \right) \delta_{tip}, \tag{2.18}$$

where L is the length of the cantilever and δ_{tip} acts as the fitting parameter to the deflection data. The distance L is measured between the tungsten probe contact point and the position past the cantilever base at which the slope of the vertical deflection becomes constant (i.e. zero vertical deflection). Once δ_{tip} has been determined, the stress in the top surface of cantilever as function of position can be calculated using Eq. 2.16.

During calibration, the Wheatstone bridge voltage is continuously measured as discrete tip deflections are imposed by moving the tungsten probe attached to the linear micropositioner. Immediately after each incremental tip deflection, an optical interferometric scan is performed to acquire the vertical deflection versus position data, from which the tip deflection δ_{tip} can be determined. Figure 2-14(a) shows the measured Wheatstone bridge response as a function of tip deflection. The tip deflection must be correlated to the stress in the piezoresistive element that spans a finite length along the cantilever. Since the stress varies linearly along the cantilever, the stress also varies linearly over the length of the piezoresistor. Therefore, the average stress in the piezoresistor equals the stress at the position in the middle of piezoresistor. The measured Wheatstone bridge response can then be plotted as a function of the average stress in the piezoresistor, as shown in Fig. 2-14(b). Using Eqs. 2.10 and 2.11 except for uniaxial loading:

$$\frac{\Delta V_{bridge}}{V_{supply}} = \pi'_{11}\sigma_{sub}, \tag{2.19}$$

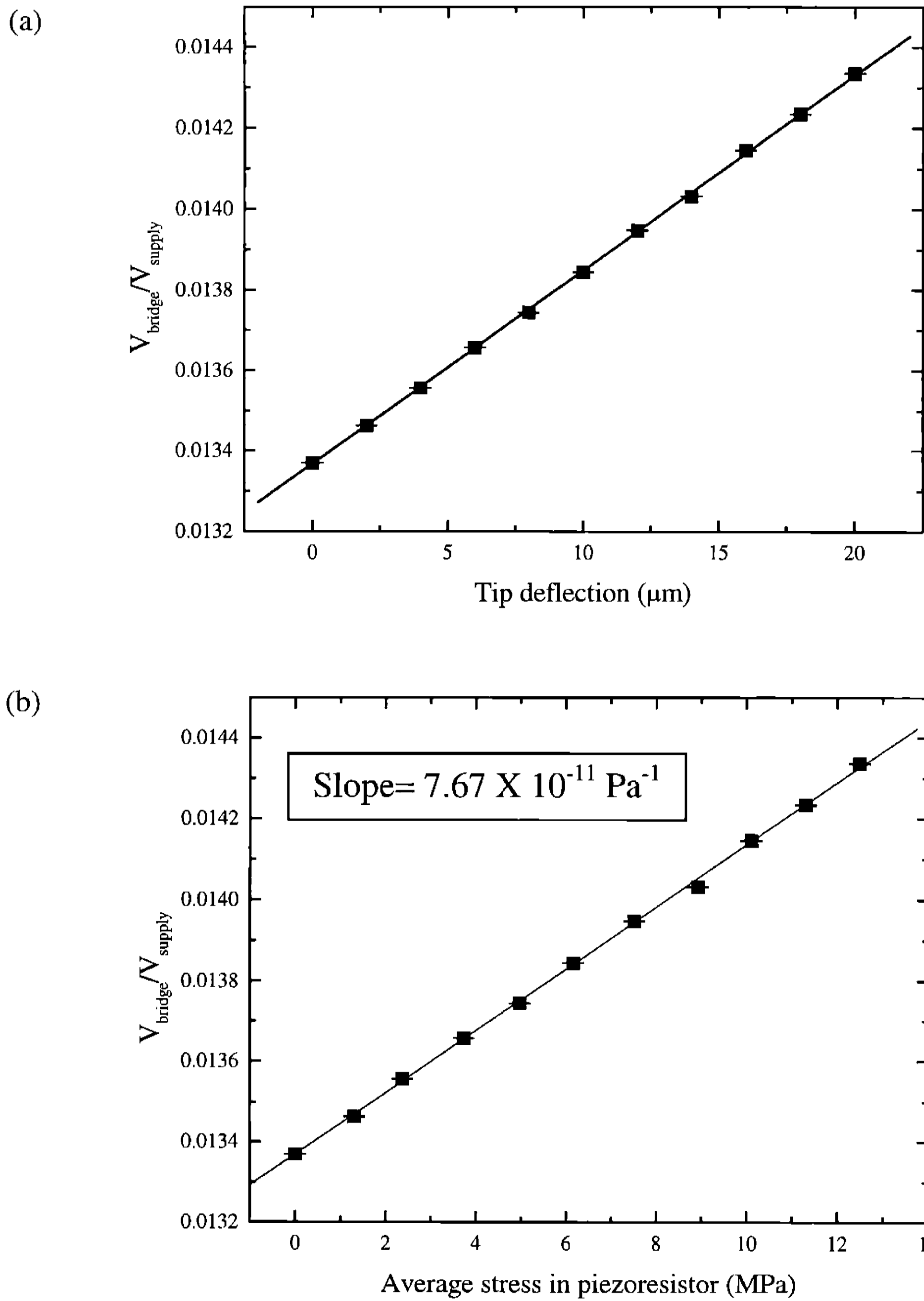

Figure 2-14: The measured Wheatstone bridge voltage divided by the supply voltage as a function of (a) tip deflection determined by fitting vertical deflection data to Eq. 2.17, and (b) average stress in piezoresistor determined from Eq. 2.15. The slope in (b) is the measured piezoresistive coefficient for the fabricated piezolever devices.

where $\Delta V_{bridge}/V_{supply}$ is the measured Wheatstone bridge response and σ_{sub} is the average stress in the piezoresistor. Therefore, the slope from Fig. 2-14(b) gives the experimentally determined value of the piezoresistive coefficient π'_{11}. From the calibration of eight different die from the same wafer, the average value of π'_{11} was 7.7 X 10^{-11} Pa^{-1} with a standard deviation of 0.4 X 10^{-11} Pa^{-1}.

Notice that the experimentally measured π'_{11} = 7.7 X 10^{-11} Pa^{-1} is less than the quoted value in section 2.3.3 of π'_{11}=14.4 X 10^{-11} Pa^{-1} for a [110]-oriented piezoresistor at 10^{20} B/cm^3. In the analysis above, the transverse piezoresistive coefficient π'_{12} was assumed to be small. Therefore, the stress in the transverse direction (i.e. across the width of the cantilever) was ignored in the analysis above. In Fig. 2-3, the piezoresistive coefficient π'_{12} changes quickly at the cusps near the origin. During the wafer-bonding step during fabrication, a 5−10 degree misorientation of the (110) wafer could have occurred. The resistors would consequently be slightly misoriented, which could potentially affect the piezoresistive response of the devices.

2.3.6.2 Temperature calibration of Kelvin structures

The packaging and instrumentation of the piezocantilever devices is necessary for the temperature calibration. In short, the fabricated piezocantilever silicon die is mounted and wire bonded to a ceramic package. The ceramic package is then plugged into a socket to make the necessary electrical connections to the voltage power supply and multimeter. The backside of the ceramic package makes contact to a thermal finger that extends to the hotplate surface. One thermocouple is attached to the hotplate while a second thermocouple is inserted into the thermal finger near the ceramic package. The power supplied to the hotplate is feedback controlled by the thermocouple attached to the substrate. After increasing the temperature of the hotplate by increments of less than 5°C between calibration measurements, approximately 15 minutes is required until the hotplate thermocouple and the thermal finger thermocouple equilibrate to the same temperature.

A Kelvin structure, also referred to as a four-point resistance structure, is used to measure resistance by passing a constant current I across two outer leads and measuring a

voltage drop V across two inner leads, as shown schematically in Fig. 2-10. Because the doping concentration varies with depth through the resistor thickness, the sheet resistance $R_\square$ is typically measured:

$$R_\square = \frac{V}{I}\frac{w}{l}, \tag{2.20}$$

where w is the width and l is the length of the resistor. The sheet resistance was measured as a function of temperature between room temperature and about 50°C as shown in Fig 2-15. For an electrical noise of approximately 0.7 μV/V and using the slope from Fig 2-14, the temperature can be resolved to less than 0.05°C. From the calibration of ten different die from the same wafer, the deviation in the measurements was less than 10%.

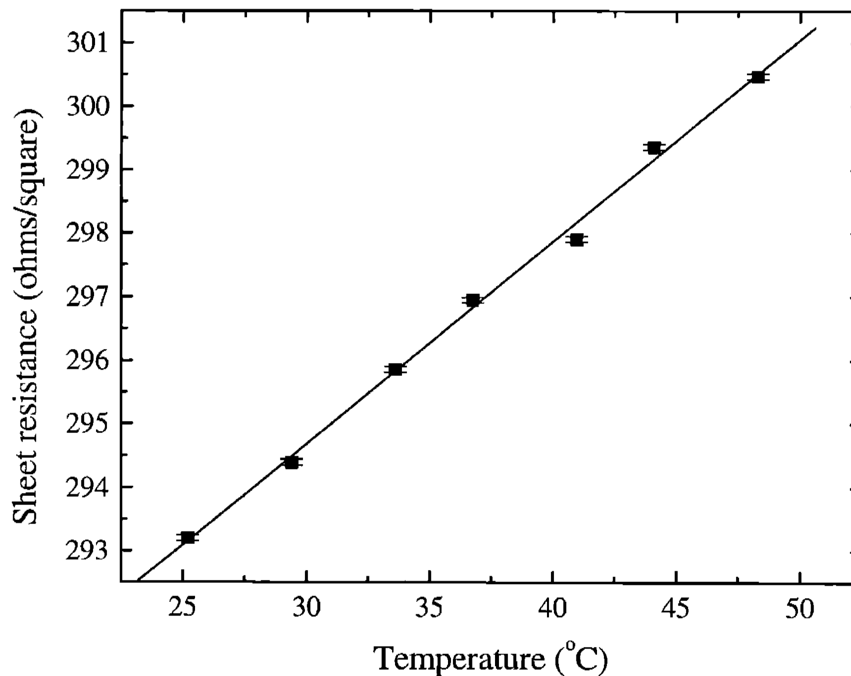

Figure 2-15: The measured sheet resistance as a function of temperature for a Kelvin structure fabricated near the end of a cantilever. Approximately 15 minutes is allowed for the temperature to equilibrate between measurements.

2.3.6.3 Temperature calibration of Wheatstone bridge structure

Two different temperature calibrations of the Wheatstone bridge structure must be performed so that the intrinsic thin film stress measurement can be extracted from the initial experimental data. Stress due to differential thermal expansion must be compensated for and arise from two different contributions. First, due to the aluminum metallization and oxide passivation deposited during piezocantilever fabrication, changes in temperature result in stress in the silicon cantilever due to differential thermal expansion. Second, thermal stresses result from differential thermal expansion between the deposited film and silicon cantilever substrate. Therefore, the Wheatstone bridge voltage as a function of temperature must be measured both before and after thin film deposition in order to subtract any thermal stress component. By monitoring the temperature during deposition, the thermal stress component due to the metallization and passivation layers and the deposited thin film can be compensated for in the intrinsic stress measurement. The method used to correct for thermal stress generation during thin film deposition is described in section 2.3.7.

The same experimental setup and procedure for temperature calibration as described is section 2.3.6.2 is used here. The measured Wheatstone bridge voltage as a function of temperature is shown in Fig. 2-16 both before and after deposition of a thin Cu film. The measured response for the coated piezocantilever is due in part to the Cu film but also as a result of the aluminum metallization and oxide passivation layers. The difference between the two curves in Fig. 2-16 is due to the thermal stress contribution from the differential thermal expansion between the Cu film and silicon substrate alone. The difference in the curves can be converted from Wheatstone bridge voltage to thin film stress using the stress calibration results explained in section 2.3.6.2. The resulting curve is a plot of thin film stress versus temperature. For a thin film on a thick substrate, the thermal stress in the film $\sigma_{thermal}$ is given by:

$$\sigma_{thermal} = \frac{E_f}{1-\nu_f}\left(\alpha_{sub} - \alpha_{film}\right)\Delta T \,. \tag{2.21}$$

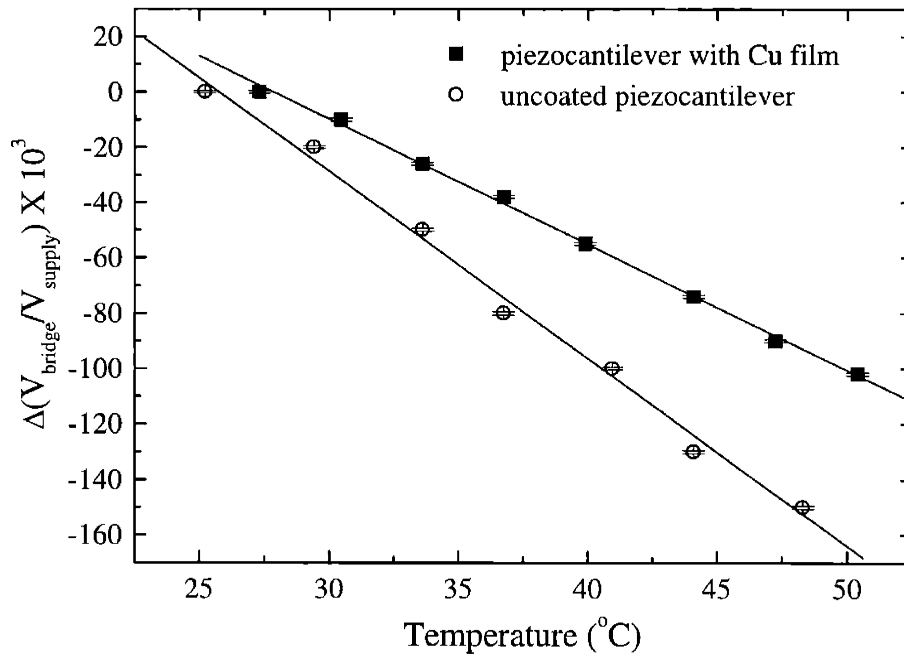

Figure 2-16: The measured Wheatstone bridge voltage as a function of temperature for an uncoated piezocanitlever device (open circles) and for a piezocantilever device coated with a 100 nm Cu film.

The slope of the thin film stress versus temperature curve is the product of the biaxial modulus of the film $E_f/(1-\nu_f)$ times the difference in thermal expansion coefficient between the film and substrate. However, both E_f and ν_f depend on the crystallographic orientation of the film. For most face-centered cubic (FCC) thin films deposited on amorphous substrates such as oxidized silicon, the polycrystalline films are deposited with a strong (111) texture and random in-plane texture [Thom 90]. The thermal expansion coefficient of cubic materials is a diagonal second-rank tensor with all diagonal components equal [Nye 85] and consequently isotropic (i.e. independent of crystallographic orientation). Using known values for the differential thermal expansion coefficients of copper and silicon, the biaxial modulus of the copper film can be calculated.

Material	$[E/(1-\nu)]_{111}$ (GPa)	$[E/(1-\nu)]_{Voigt}$ (GPa)	$[E/(1-\nu)]_{100}$ (GPa)	α ($10^{-6}/^{o}C$)
Cu	266.7	193.5	116.3	16.5
Si	N/A	N/A	180.5	2.6

Table 2-1: Biaxial moduli [Simm 71] and thermal expansion coefficients [Toul 70] for Cu and Si at room temperature.

It should be noted that the measured biaxial moduli of the Cu films in our experiments do not agree with the calculated values for a (111)-textured film when using the thermal expansion coefficients for the Cu film and Si substrate from Table 2-1. If the film is assumed to be comprised of randomly oriented grains under plane strain conditions, as is the case for a thermal strain, the appropriate modulus is the Voigt average, also shown in Table 2.1. The experimentally determined biaxial modulus for Cu lies somewhere between the Voigt average and the in-plane-averaged {111} texture, which is in agreement with other observations [Smal 94, Shul 96].

2.3.6.4 Canitilever thickness metrology

To calibrate the piezocantilever device and to make accurate thin film stress measurements, the thickness of the silicon cantilever must be known. Consequently, a cantilever thickness calibration structure was designed into the piezocantilever devices, as shown in Fig. 2-17(a). Using a Tencor P10 profilometer, the thickness of the (110) silicon device wafer can be measured as function of position along the comb structure as shown in Fig. 2-17(b). Table 2.2 shows the average cantilever thickness and standard deviation in the measurement for five different die from the same wafer. The scatter in the average cantilever thicknesses is rather large, however the standard deviation in the measurements is quite low. Note that the actual thickness of a cantilever is not being measured. However, the thickness measured over almost 2 mm from the calibration structure does not vary significantly. Therefore, the calibration structure gives a representation value of the thickness of the adjacent cantilevers.

(a)

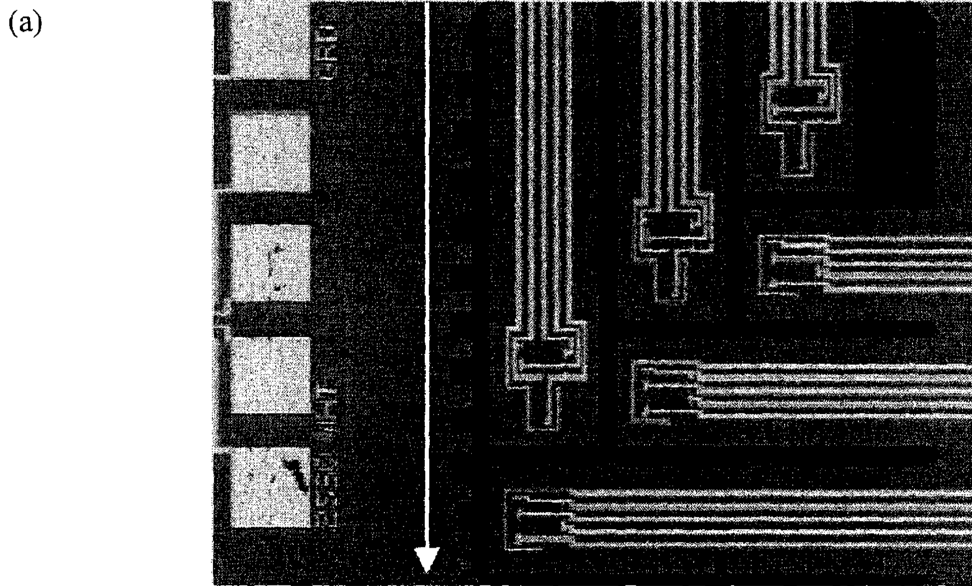

(b)

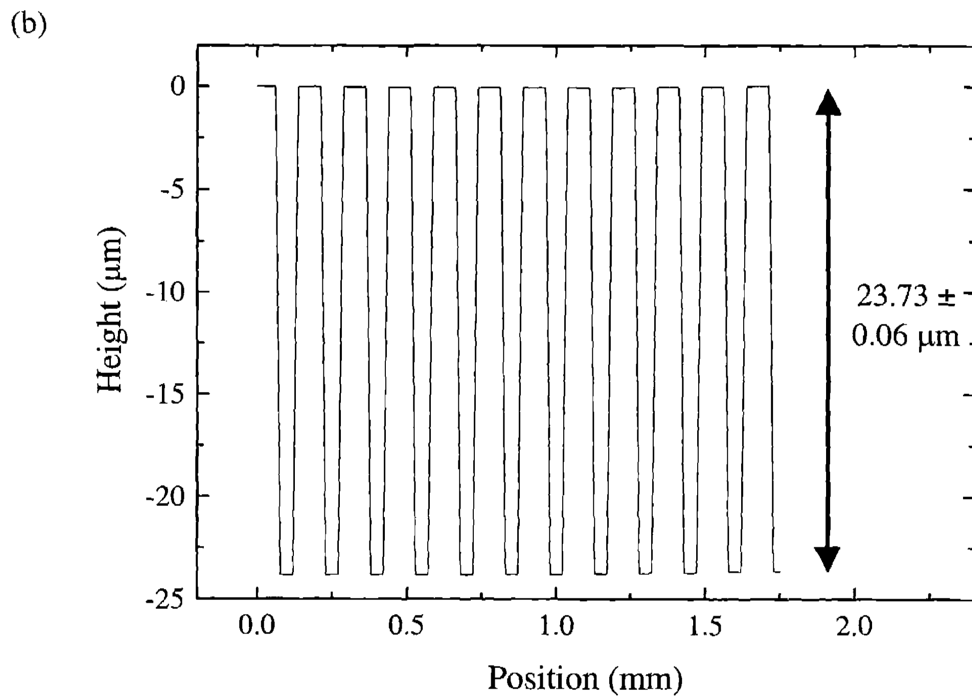

Figure 2-17: (a) Comb structure fabricated near to cantilevers used for cantilever thickness calibration. (b) Profilometer scan along the comb structure gives the thickness of the (110) silicon cantilever as a function of position. Because the thickness is relatively consistent over almost 2 mm, the thickness measured at the comb structure gives an accurate estimate of the cantilever thickness.

Sample#	1	2	3	4	5	Average
average	22.10	22.20	22.65	23.73	23.41	22.8 ± 0.7
deviation	0.07	0.07	0.09	0.06	0.06	0.06 ± 0.03

Table 2-2: The average cantilever thickness and standard deviation in the measurement for five different die from the same wafer.

2.3.7 Correction for thermal stresses during deposition

During thermal evaporation, the melt is radiating heat that results in a temperature rise of the substrate during deposition. Due to the high thermal conductivity of the silicon microcantilevers, temperature gradients across the width and along the length are assumed to be negligible. When the temperature varies during deposition, the thermal strain at a thickness z is given by:

$$\varepsilon_{thermal}(z) = (\alpha_{sub} - \alpha_{film})(T - T_{dep}(z)), \tag{2.22}$$

where T is the final temperature, $T_{dep}(z)$ is the temperature at which the film material at thickness z was deposited, and α_s and α_f are the thermal expansion coefficients of substrate and film, respectively. The average strain in the entire film of thickness h can therefore be calculated as a weighted average integrated over the thickness:

$$\langle \varepsilon_{thermal} \rangle = (\alpha_{sub} - \alpha_{film})\left[T - \frac{1}{h}\int_0^h T_{dep}(z)dz \right]. \tag{2.23}$$

Because the temperature change during deposition is relatively small (i.e. less than 20°C), the thermal strain is accommodated elastically so that the average stress in the film is:

$$\langle \sigma_{thermal} \rangle = \frac{E_f}{1 - \nu_f} \langle \varepsilon_{thermal} \rangle \qquad (2.24)$$

where E_f and ν_f are the Young's modulus and Poisson ratio of the film, respectively, determined from the temperature calibration process described in section 2.3.6.3. The average thermal stress in the film, which depends on both the film thickness and temperature during deposition, is subtracted point wise from the acquired data.

2.3.8 Piezocantilever fabrication

A summary of the fabrication of the piezocantilevers devices is given below, while a complete process flow using the Microsystem Technology Laboratories (MTL) facilities at MIT is given in Appendix A. The eight photolithography masks designed using KIC, a freeware mask layout tool are also included in Appendix A. Because of the complexity and detail of the design and processing, only simplified schematics of cross-sectional and top views of the processing steps are shown.

The specifications for the silicon wafers used for the device and handle wafers must be determined before any processing can occur. The cleanroom facilities at MIT utilize equipment manufactured to handle 4-inch silicon wafers, which have a nominal thickness of around 500 μm. The device wafer from which the 20-μm-thick cantilevers were fabricated is a (110) silicon wafer of standard thickness and double-side polished. The handle wafer that acts as the supporting structure for the thinned (110) wafer was a double-side polished (100) silicon wafer with a low (i.e. less than 2 μm) total thickness variation across the wafer.

A 1-μm-thick oxide was thermally grown on the handle wafer by a sequence of dry-wet-dry oxidation steps in an 1100°C furnace. Both sets of wafers were RCA cleaned prior to wafer bonding to remove all particles on the surface and to create the hydroxyl radical on the surfaces that promote bonding. Immediately after the RCA clean, the device wafer and handle wafer were contacted face-to-face at room temperature and then permanently bonded by annealing at 1100°C in N_2 for 75 minutes. Figure 2-18 shows infrared images of bonded wafers for a "perfect" bond (left) and a bond with an

(a) good wafer bond

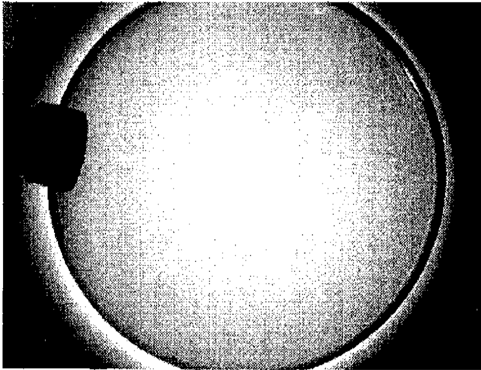

(b) wafer bond with interface bubbles

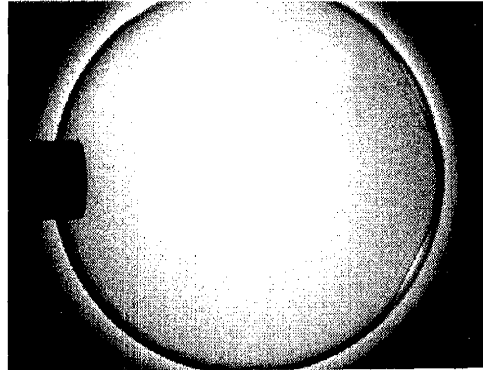

Figure 2-18: Infrared images of wafer bond between (110) device wafer and (100) handle wafers showing (a) a good wafer bond, and (b) a wafer bond with interface bubbles presumably due to trapped particles between the wafers.

interface bubble (right) presumably due to a trapped particle. To achieve a final device wafer thickness of 20 μm, the device wafer was mechanically ground to about a 30-μm thickness then reduced to the final thickness by chemical mechanical polishing to eliminate sub-surface damage due to grinding. The choice of a low thickness variation handle wafer is required because the handle wafer is the reference plane for the grind and polish procedure. At this point in the processing, the bonded wafer stack consists of a 500-μm thick (100) handle wafer bonded to a 20-μm thick (110) device wafer with a 1 μm-thick thermal oxide at the bond interface (see Fig. 2-19).

A conservative value of 20 μm was chosen for the device wafer thickness because the yield of the grind and polish process was better for thicker device wafers. Alternative techniques for creating thin (110) silicon device layers were deemed unsuitable for the piezocantilever devices. Commercial silicon-on-insulator (SOI) wafers are unavailable with devices layers greater than a couple microns in thickness, and the boron etchstop technique is incompatible with the use of boron resistors within the device layer. Decreasing the cantilever thickness to 5 μm would have increased measurement sensitivity of the piezocantilever devices by a factor of four, as can be seen from Eq.

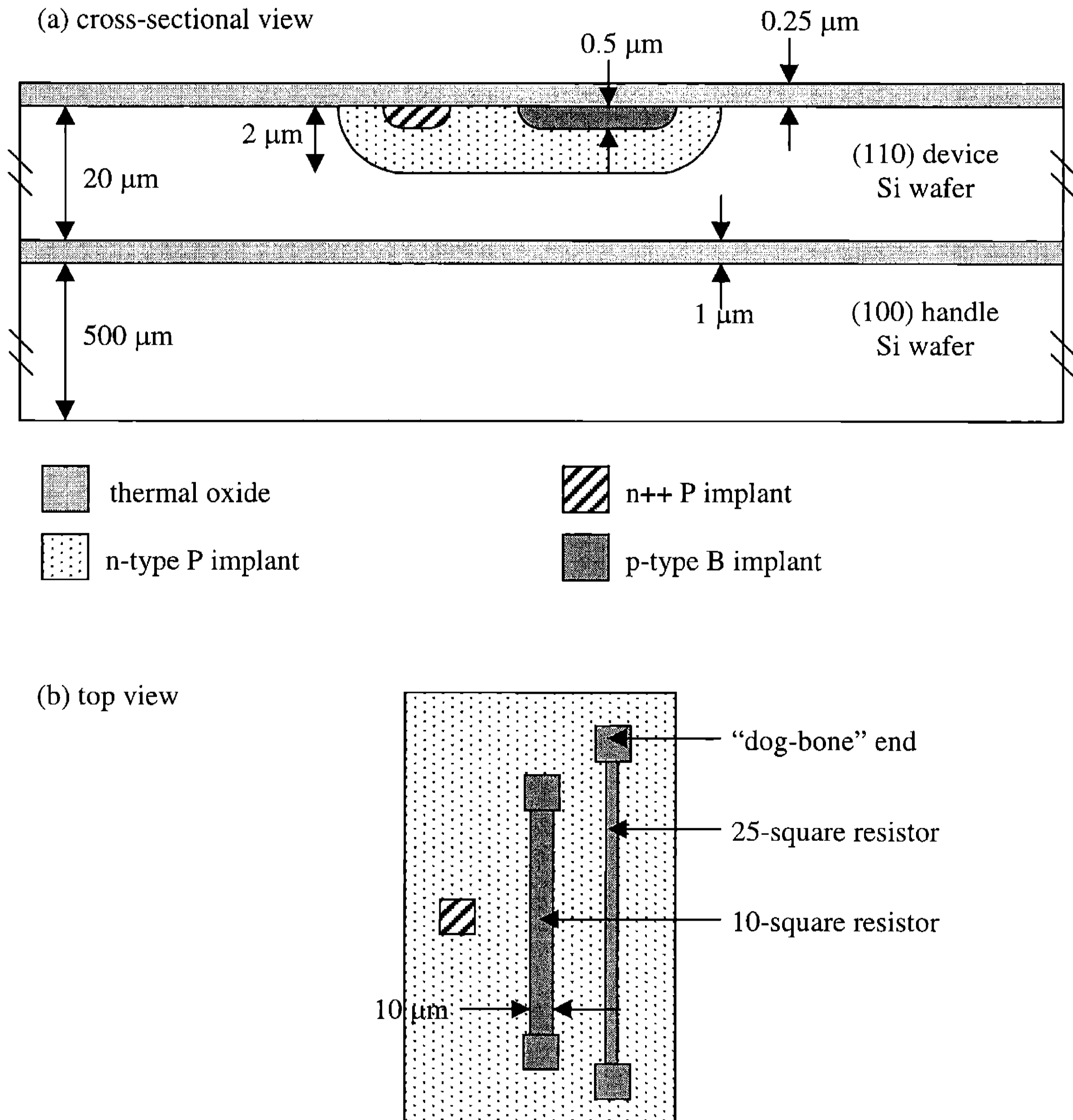

Figure 2-19: Schematic of bonded wafer after ion implantation showing (a) a cross-sectional view, and (b) a top view of the wafer surface. Note that the structures shown are to aid in understanding of the processing procedure, and do not diagram actual structures used in the piezocantilever devices.

2.14. However, the aluminum metallization and oxide layers total 1.0 μm in thickness and are no longer thin compared to the 5 μm-thick substrate and the mechanical response would no longer be dominated by the underlying silicon cantilever alone.

After the bonding and thinning process, a 0.2-μm-thick oxide was thermally grown on the bonded wafer. The oxide layer reduces the amount of damage to the silicon during ion implantation and provides an insulating layer on the top surface of silicon wafer. Three ion implantation steps were performed to create the electrical components in the top surface of the (110) device wafer. Only selected areas of the wafers were ion implanted by masking the surface of the wafer with patterned photoresist. The first implant was a phosphorous implant used to create an n-type region in the top surface of the (110) silicon device layer that was diffused to a depth of about 2 μm by a long drive-in anneal at 1100°C. The second implant was another selected-area phosphorous implant to create n++ contacts to the original phosphorous implant for good ohmic contact with the eventual metallization. The last implant was a selected-area boron implant at a surface concentration of 10^{20} cm^{-3} to create the boron resistors within the top surface of the (110) silicon. A short anneal for 30 min at 1000°C was performed to activate both the boron and n++ phosphorous implanted species. The depth of the metallurgical junction between the p-type boron resistor and the n-type phosphorous region is about 0.5 μm, as confirmed by SUPREM simulations of the implant process. The boron resistors are either 10-square or 25-sqaure resistors with "dog-bone" heads at either end of the resistor where electrical contact is made with the metallization. A cross-section of the bonded wafer and a top view of the wafer surface after the ion implantation steps are shown in Figure 2-19.

Contacts through the 0.2-μm-thick insulating oxide layer were made to the phosphorous and boron regions by selective etching of the oxide in buffered oxide etch (BOE). The usual etch rate for thermal oxide in BOE is about 100 nm/min, but the high concentration of boron in the oxide was found to decrease the etch rate to approximately 50 nm/min. A 0.3-μm thick blanket film of Al was deposited by sputter deposition and then patterned to create the metal interconnects between the silicon layer and bond pads, which provide large areas of Al for wire bonding. A short sinter anneal for 30 mins at 400°C was found to be suitable to create good ohmic contact with the boron region

without "spiking" through to the n-type phosphorous layer. Next, a passivating oxide layer of 0.5-μm thickness was grown over the entire surface of the wafer by chemical vapor deposition of silicon dioxide at 400°C. A cross-section of the bonded wafers and a top view of the wafer surface after the oxide passivation step are shown in Figure 2-20.

The next sequence of steps use silicon micromachining processing techniques to create the 20-μm-thick cantilevers from the continuous (110) device wafer. The backside of the handle wafer is selectively masked with photoresist to create regions that are deep reactive ion etched (DRIE) through the entire handle wafer thickness. The inter-wafer oxide acts as the etch stop layer for the DRIE process. The inter-wafer oxide exposed by the DRIE process is subsequently removed using BOE. After the backside DRIE step, four 20-μm-thick membranes of (110) silicon approximately 2 mm X 2 mm in size have been created in each 10 mm X 10 mm die. From each 2 mm X 2 mm membrane, six cantilevers are fabricated as can be seen in Fig. 2-17. The cantilevers are created by photoresist masking of the device wafer and using DRIE to release the final cantilevers. A cross-section of the bonded wafer with released cantilevers is shown in Fig 2-21.

2.3.9 Piezocantilever packaging and UHV instrumentation

Once the cleanroom processing has been completed and the cantilevers have been released, the wafer must be cut into pieces to separate the individual die. To protect the clean surface of the wafer from silicon dust during wafer dicing, both the frontside and backside of the wafer are coated with photoresist. The full wafers were diced into 10 mm by10 mm die using a diamond-coated die saw yielding approximately 75 die per wafer. The die were subsequently soaked in acetone to remove the protective photoresist and to remove the die saw tape. After cleaning, the die were mounted on a ceramic package using a UHV-compatible lacquer. The mounted die were then gold wire bonded to a pin-grid-array ceramic package.

To make *in situ* measurements using the packaged piezocantilever devices, UHV-compatible instrumentation had to be designed to make both good thermal contact and electrical contacts to the package. Thermal contact to the backside of the ceramic package was achieved via a thermal finger that extends to the UHV sample stage. Only

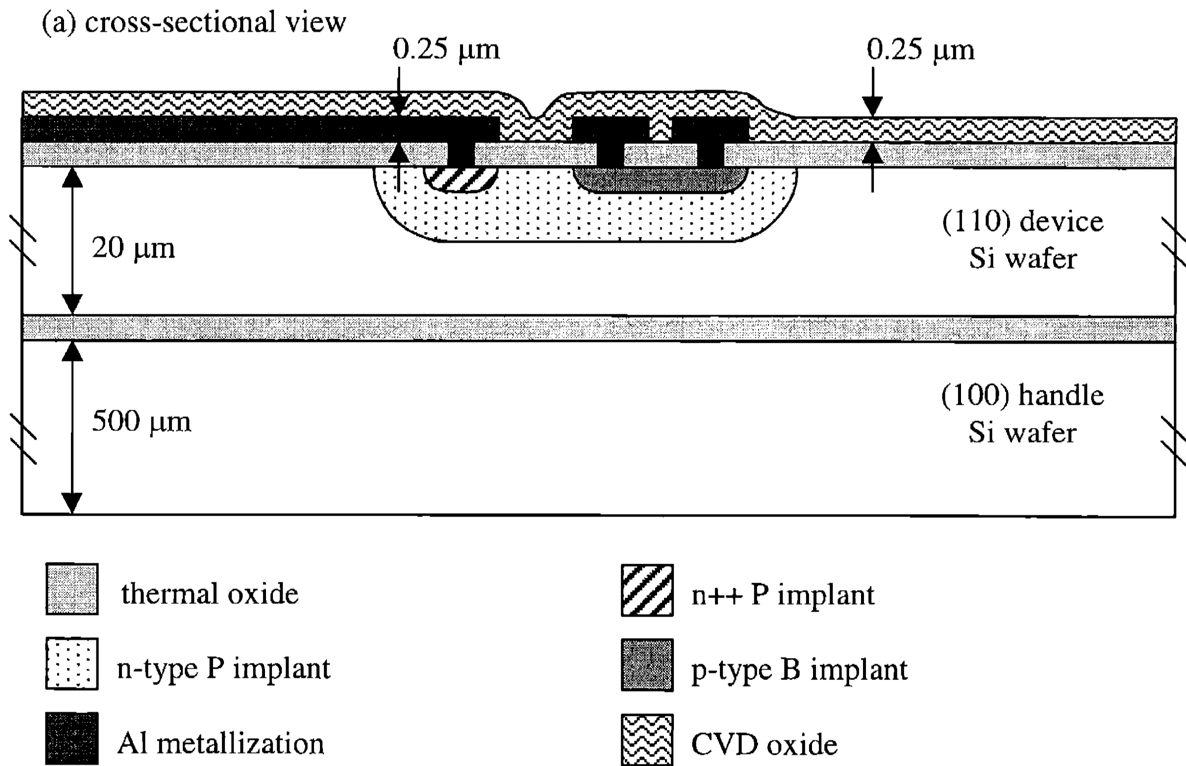

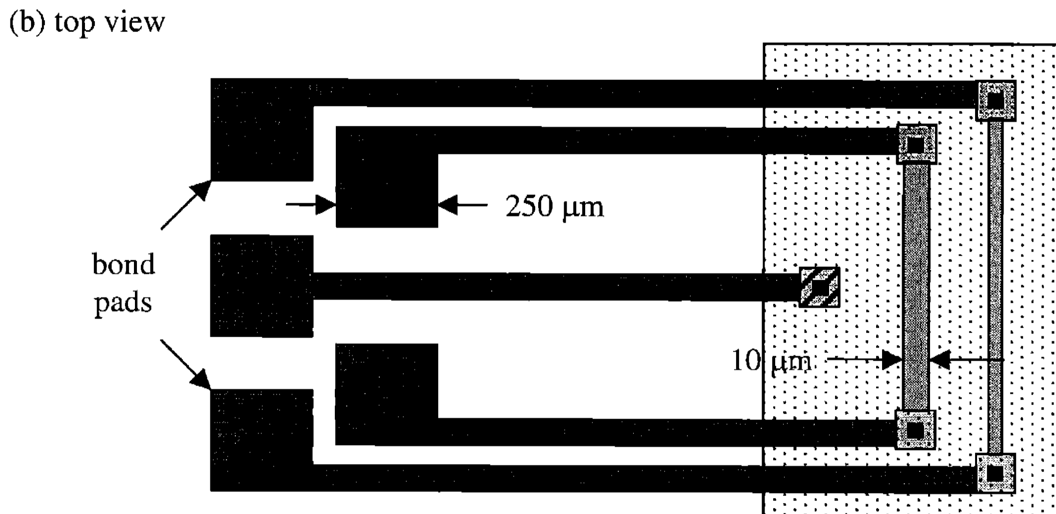

Figure 2-20: Schematic of bonded wafer after aluminum metallization and an oxide passivation showing (a) a cross-sectional view, and (b) a top view of the wafer surface. Note that the structures shown are to aid in understanding of the processing procedure, and do not diagram actual structures used in the piezocantilever devices.

(a) cross-sectional view

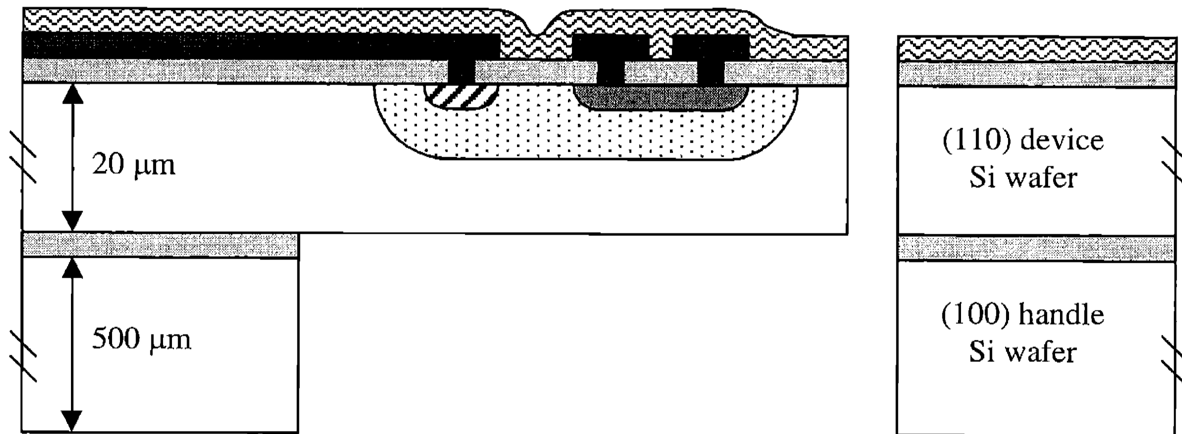

(b) top view

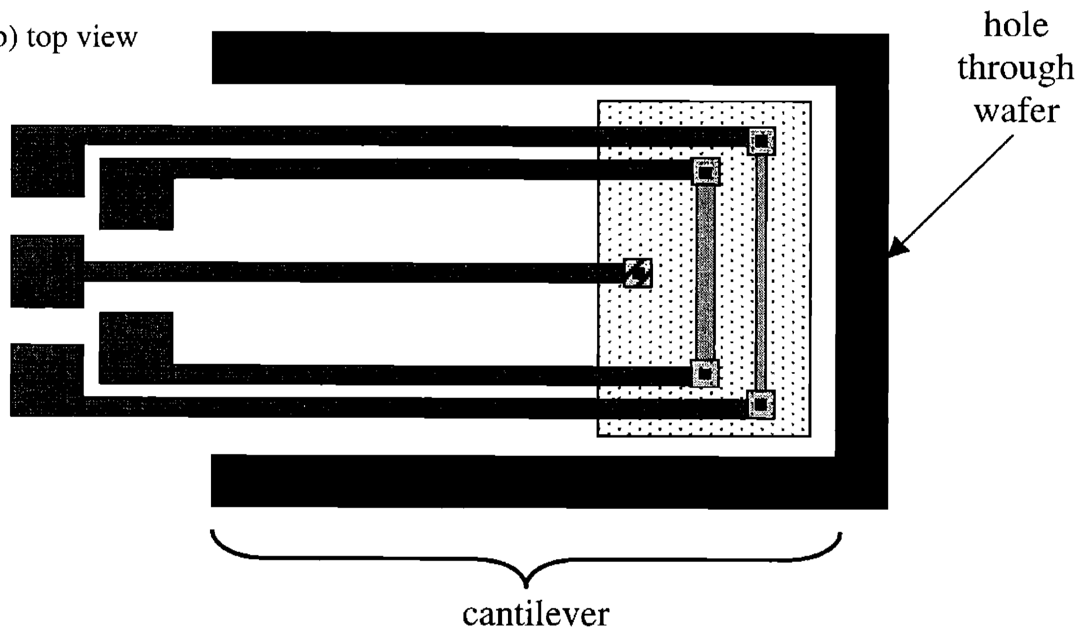

Figure 2-21: Schematic of bonded wafer after backside and frontside deep reactive ion etching that releases the silicon cantilever as can be seen in (a) a cross-sectional view, and (b) a top view of the wafer surface.

conduction is a significant path for heat flow since convection is negligible in vacuum and radiative heat loss is weak at low temperatures. The ceramic package with the piezocantilever devices is plugged into a socket made of PEEK, a plastic compatible with UHV conditions and temperatures as high as 200°C. Within the PEEK socket is an array of gold-plated receptacles that accept the pins on the backside of the ceramic package. Wires are connected to the backside of the gold-plated receptacles and out to an electrical feedthrough vacuum flange. The wires are insulted with Kapton, another plastic material compatible with UHV and temperature as high as 200°C. Figure 2-22 shows a packaged die as well as the UHV sample stage that accepts the packaged die.

2.4 Comparison of MOSS and piezocantilever devices

Laser reflectometry is an established technique for measuring thin film stress by monitoring substrate curvature, although the most widespread use has been for the *ex situ* measurement of thin film stress evolution during thermal cycling [Flin 87]. The application of *in situ* laser reflectometry for measuring stress during thin film deposition has been only recently developed over the last decade [Mart 90, Sche 90]. The unique feature of the MOSS technique is the use of multiple laser beams to take simultaneous deflection measurements, which is less susceptible to vibrational noise than other serial scan techniques [Flor 97].

The piezoresistive microcantilevers described in this thesis provide a new technique for the *in situ* measurement of thin film stress during deposition. As is true with the MOSS technique, mechanical vibration is not an issue with the piezocantilever devices but for different reasons. Since the piezocantilever device is electrical, the time required for a measurement is nearly instantaneous and insensitive to vibration. Furthermore, the stress resulting from vibration is very small near the free end of the cantilever where the piezoresistive element is fabricated. The laser reflectometry technique requires an optical path through the deposition chamber since the laser source and detector are located outside of the chamber. The piezocantilever device only requires an electrical feedthrough on the deposition chamber and very inexpensive power supply and multimeter equipment for measurements. One unique feature of the piezocantilever

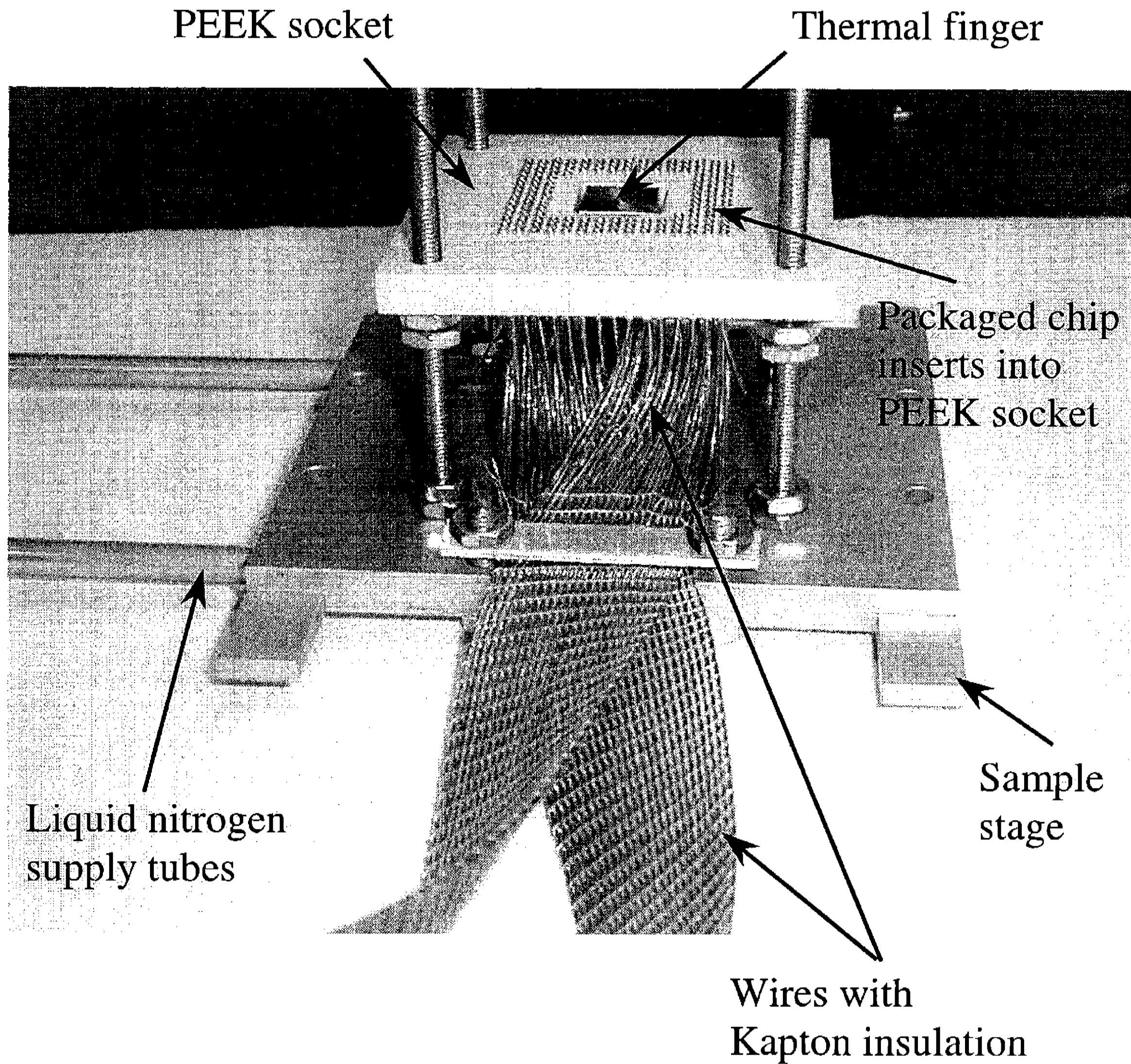

Figure 2-22: Sample stage for packaged piezocantilever devices for use in UHV deposition chamber. The pins on the backside of the ceramic package plug into the array of gold-plated receptacles within the PEEK socket. Kapton-coated wires are connected to the backside of the gold-plated receptacles and out to an electrical feedthrough on a vacuum flange (not shown). Both the PEEK and Kapton are plastics compatible with UHV pressures and temperature as high as 200°C. Thermal contact to the backside of the ceramic package is achieved via a thermal finger that extends to the stage.

devices is the ability to measure stress during chemical vapor deposition, which deposits on both sides of a cantilever and would not result in a change in curvature necessary for a laser reflectometry measurement. If a CVD film is deposited on a cantilever, the cantilever will lengthen in response to the stress in the film and induce a stress in the substrate that can be measured by the piezoresistive technique.

The piezocantilever devices do however have several drawbacks. Since the piezocantilevers are silicon devices relying on electrical isolation by a p-n junction, the operating temperature is limited to below 150°C [Ghan 68]. The operating temperature of the device could be increased by several hundred degrees by using silicon-on-insulator wafers to electrically isolate the boron resistors with an oxide and using Pt metallization. As shown in Appendix A, the cleanroom fabrication of the piezocantilever devices is labor intensive and requires the completion of eight photolithography steps to attain functional devices. However, the inherent batch processing of silicon wafers is advantageous and produces approximately 75 devices from each completed silicon wafer. The one operational drawback to the piezocantilever devices is the required sample calibration as discussed in section 2.3.6, which is not an issue with the laser reflectometry technique. The deviation in the values from calibration is less than 10% between different die on the same wafer and calibration may only be required for the first few die from each wafer if 10% error is acceptable.

Chapter 3

Experimental Results

3.1 Overview of experimental results

The goal of this research is to understand the relation between thin film stress evolution during deposition and the associated process of thin film formation. The differences in behavior resulting from varying deposition conditions and materials systems provide a tool by which to understand and model the stress-structure relationship during thin film deposition. In all experiments, thin films were deposited by electron-beam evaporation (e-beam) in ultrahigh vacuum (UHV) onto oxidized silicon substrate. For all the film materials deposited, the mode of film formation is by the Volmer-Weber mechanism (see Fig. 1-1). In section 3.2, the thin film stress behavior during growth of Ag and Al films is compared for identical deposition conditions. In section 3.3, the influence of deposition rate and temperature on the stress behavior of Ag film is examined. In section 3.4, the stress behavior of Cu during deposition and during interruptions of growth is detailed as a function of film thickness and deposition rate. Finally in section 3.5, the stress during growth of amorphous Ge and during growth interrupts is shown as a function of deposition temperature.

Most of the stress measurement data presented in this chapter will be plotted as the film stress-thickness product as a function of time or film thickness. The stress-thickness is typically reported because it is directly proportional to the experimentally measured quantity: curvature in the case of the substrate curvature method, and the

Wheatstone bridge voltage for the piezocantilever devices. Figure 3-1(a) is a schematic of a measured stress-thickness versus film thickness curve during deposition. The average stress in the film is the stress-thickness product divided by the corresponding film thickness, as shown in Fig. 3-1(b). The reported film thickness, which is somewhat ambiguous for discontinuous films, is the product of the deposition rate and the time of deposition and is often referred to in the literature as the mass-equivalent thickness. The slope of the stress-thickness curve at a given film thickness is referred to as the instantaneous stress. The instantaneous stress at a given film thickness is the sum of the stress associated with adding an infinitesimal layer of new material plus any changes in stress with the bulk of the pre-existing film.

The data presented for the Al, Ag, and amorphous Ge films were collected by our collaborators Jerrold A. Floro (JAF) and Sean J. Hearne (SJH) at Sandia National Labs (SNL). The stress measurements for Cu were made using the piezocantilever devices. These data provide the motivation and supporting evidence for the modeling described in Chapters 4 and 5.

3.2 Intrinsic stress measurements of Ag and Al

Silver and aluminum films were deposited onto 100-μm-thick oxidized silicon wafers at room temperature at a 0.2 nm/sec deposition rate. The stress measurements during deposition were taken using the MOSS system described in section 2.2. During deposition, the temperature was monitored using a thermocouple metal bonded to a witness wafer. The temperature data were used to correct for thermal stresses as described in section 2.3.7. In Fig. 3-2, the film stress-thickness product as a function of film thickness during deposition is shown for the Ag and Al films. The circles on the stress curves correspond to the transmission electron microscopy (TEM) micrographs shown in Fig. 3-3. The TEM micrographs were acquired from graded-thickness samples where a shutter was moved across the wafer during deposition, in order to obtain the full range of evolution in one deposition. While evolution of the microstructure after deposition and upon exposure to air is possible, the basic conclusions drawn from the

(a) generic stress-thickness curve

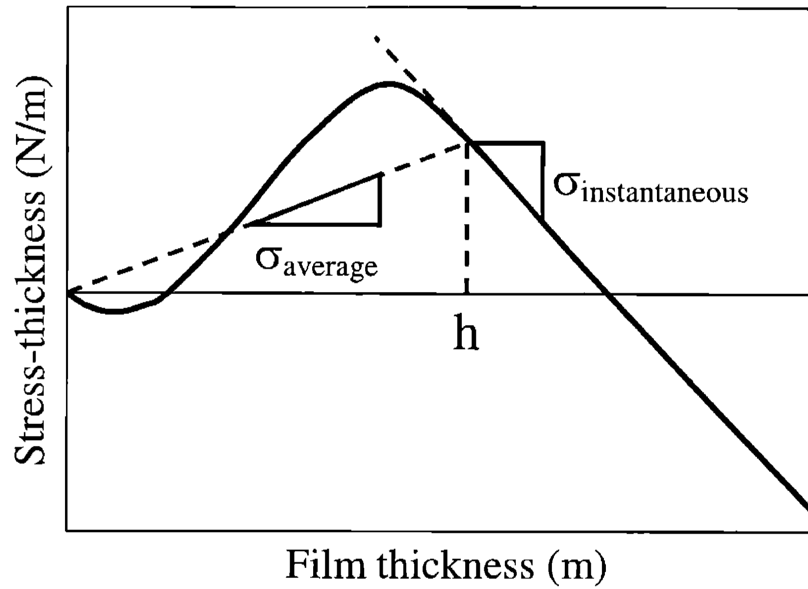

(b) corresponding average stress curve

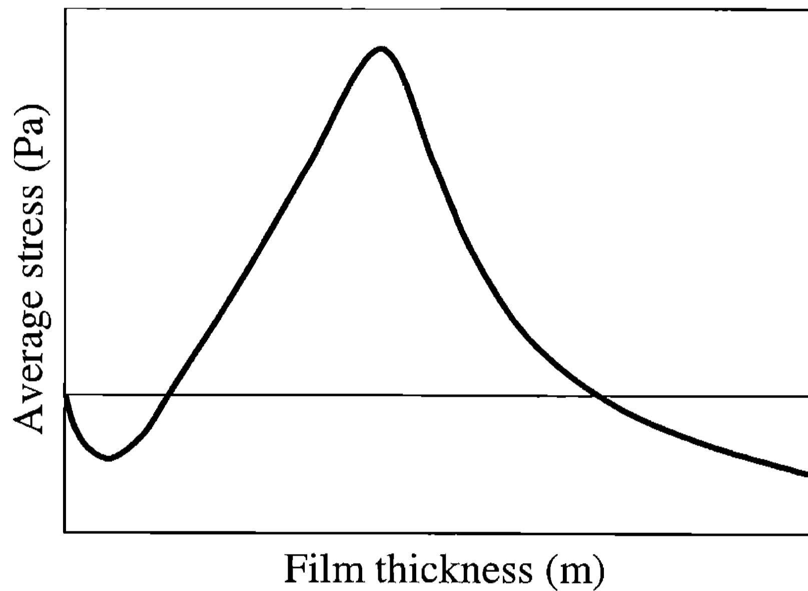

Figure 3-1: Schematic diagram of a measured (a) stress-thickness product versus film thickness curve, and (b) the corresponding average stress, which is the stress-thickness product divided by the film thickness from (a). The film thickness is simply the product of the deposition rate and the deposition time. The instantaneous stress is defined as the slope of the stress-thickness curve at a given film thickness.

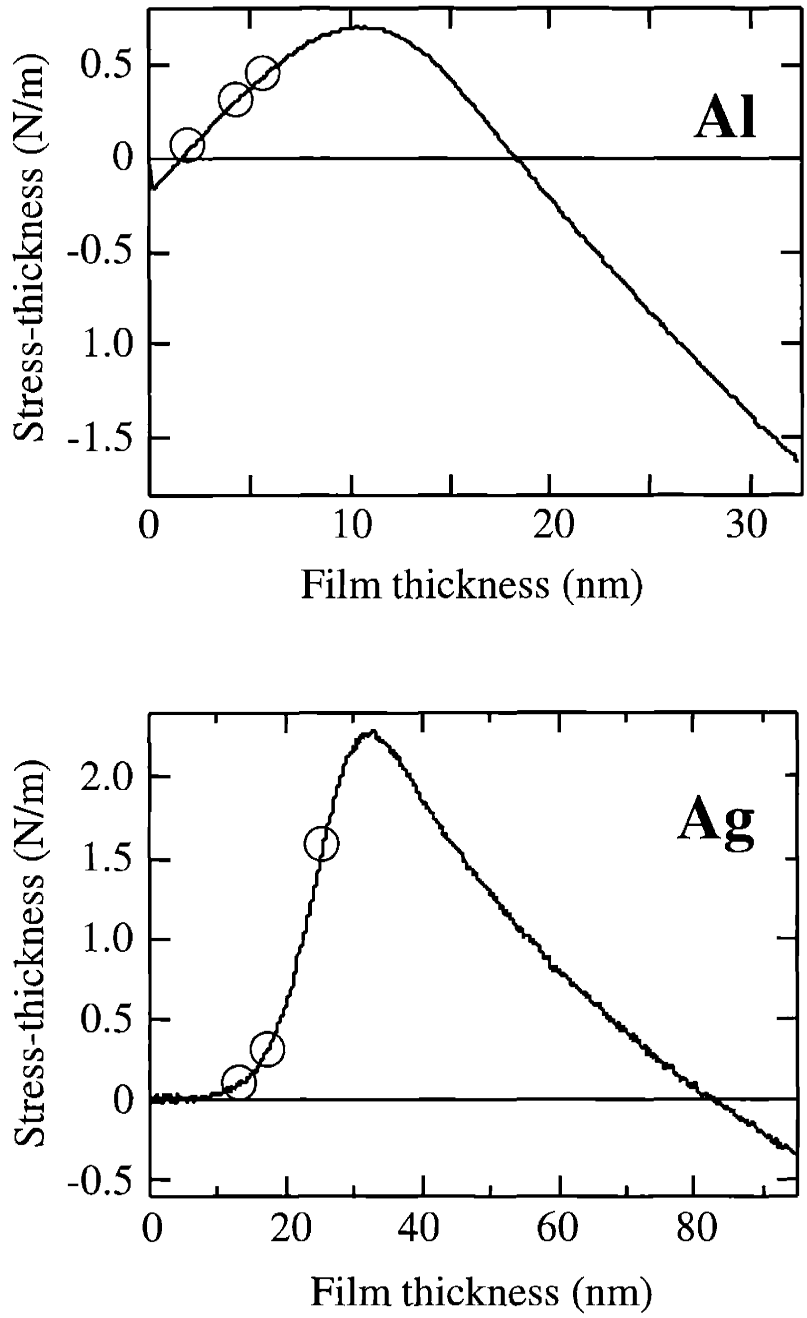

Figure 3-2: Stress-thickness versus thickness during deposition of Al and Ag on oxidized silicon substrates at 0.2 nm/sec deposition rate at room temperature. The circles correspond to the TEM micrographs in Fig. 3-3. The measurements were performed at SNL by JAF and SJH.

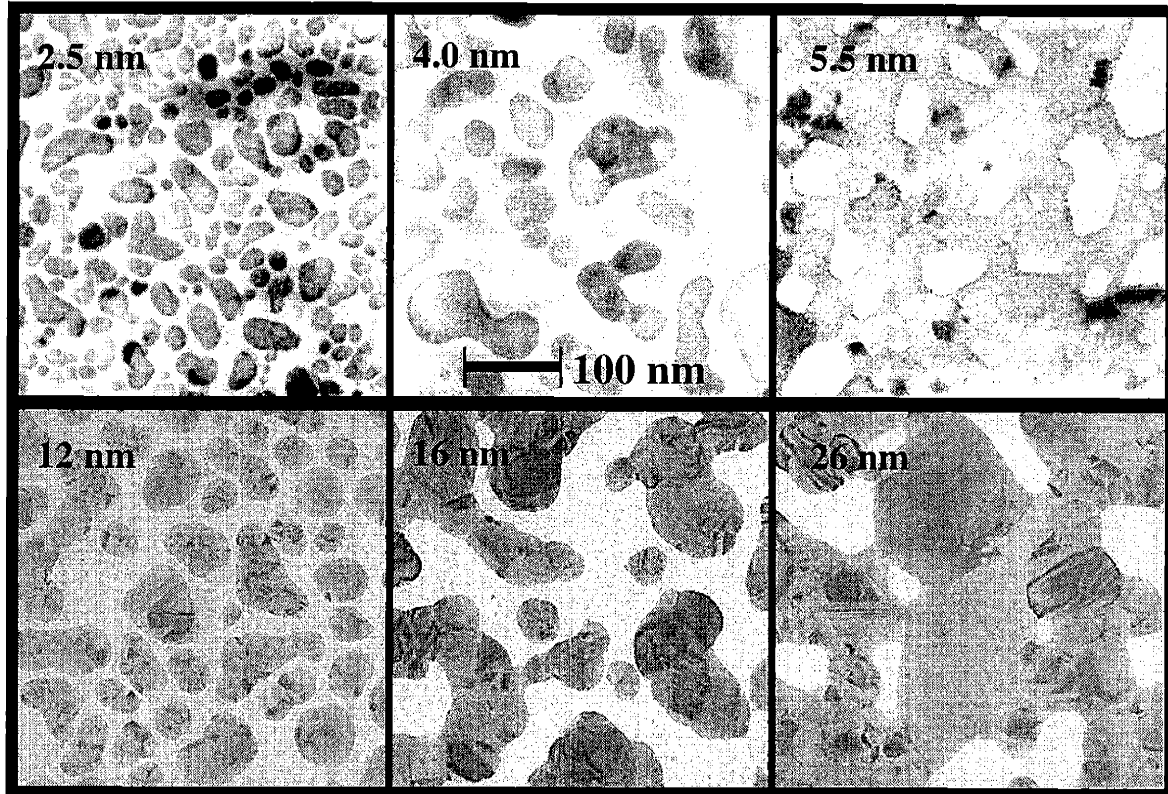

Figure 3-3: Plan-view TEM micrographs of Al films (upper panels) and Ag films (lower panels) deposited on oxidized silicon substrates. The micrographs correspond to the circles indicated on the measured Al and Ag stress-thickness curves in Fig. 3-2. The TEM microscopy was performed at SNL by JAF and SJH.

micrographs should not be affected. Consistent with previous studies [Aber 85, Koch 94], the maximum in the tensile stress-thickness coincides with the late channel stage of growth when the fractional substrate coverage is greater than 0.95.

To compare the Ag and Al data, the curves have been normalized and replotted in Fig. 3-4. The stress-thickness has been normalized by the value of the tensile peak, while the thickness has been normalized by the thickness at which the maximum in the tensile peak occurs. The Ag film shows no measurable stress, either compressive or tensile, until a thickness of approximately 15 nm. By comparison, the Al film supports stress from the earliest stages of thin film growth.

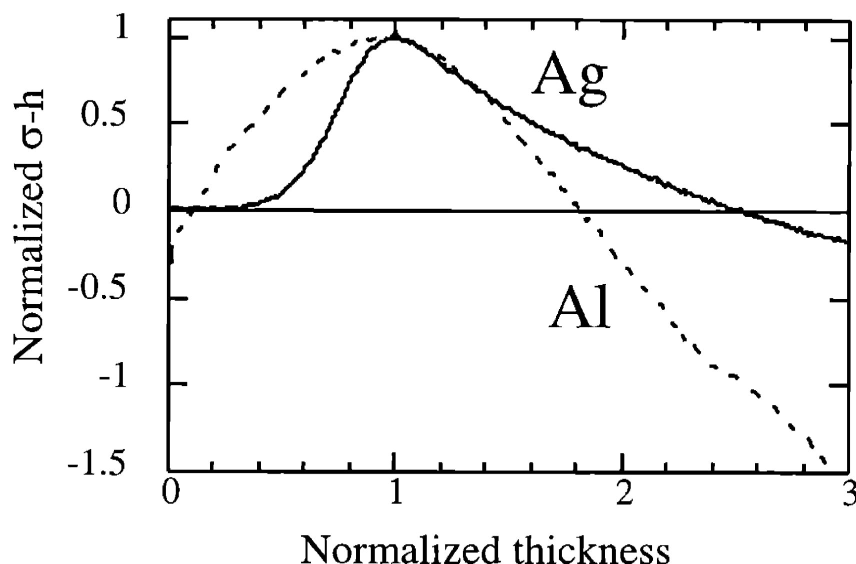

Figure 3-4: Comparison of the stress-thickness evolution during deposition for Al (dash line) and Ag (solid line) on an oxidized silicon substrate at 0.2 nm/sec at room temperature. The scales have been normalized by the values at the tensile peak of each curve in Fig. 3-2.

3.3 Intrinsic stress measurements of Ag at different deposition rates and temperatures

Silver films were deposited onto 100-μm-thick oxidized silicon wafers at different deposition rates and different substrate temperatures. Prior to deposition, the substrate was allowed to equilibrate at the desired growth temperature for at least one hour. The same experimental procedure for measuring stress with the MOSS system was used, as described in section 3.2.

3.3.1 Influence of deposition rate

Silver films were deposited onto 100-μm-thick oxidized silicon wafers at different deposition rates at room temperatures. The measured film stress-thickness versus film thickness curves for three different deposition rates are shown in Fig. 3-5(a). For

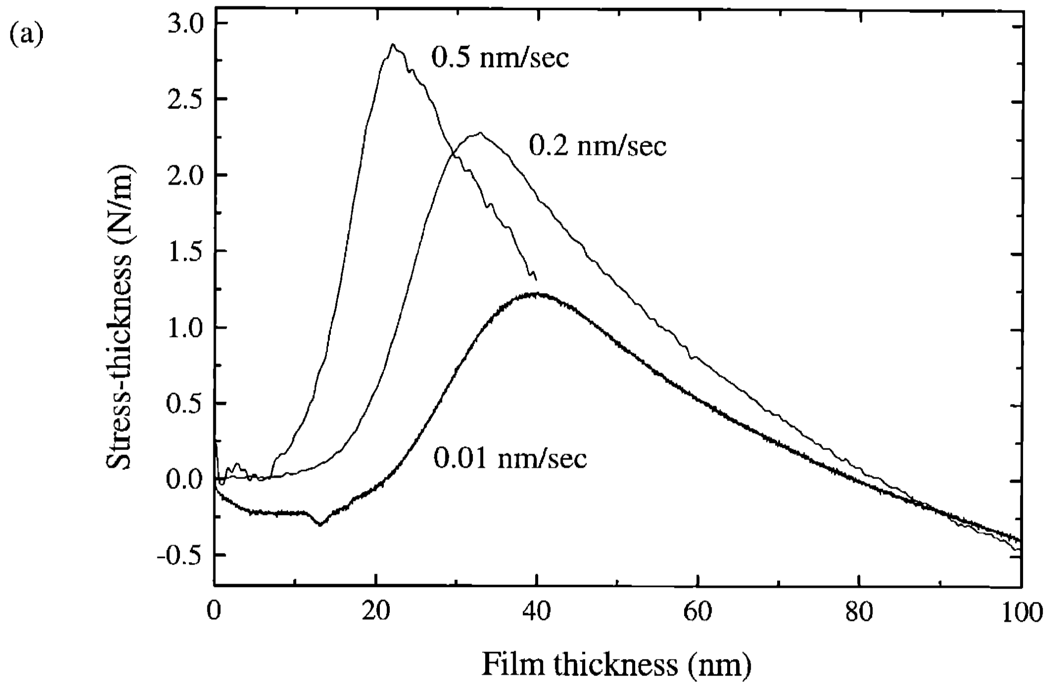

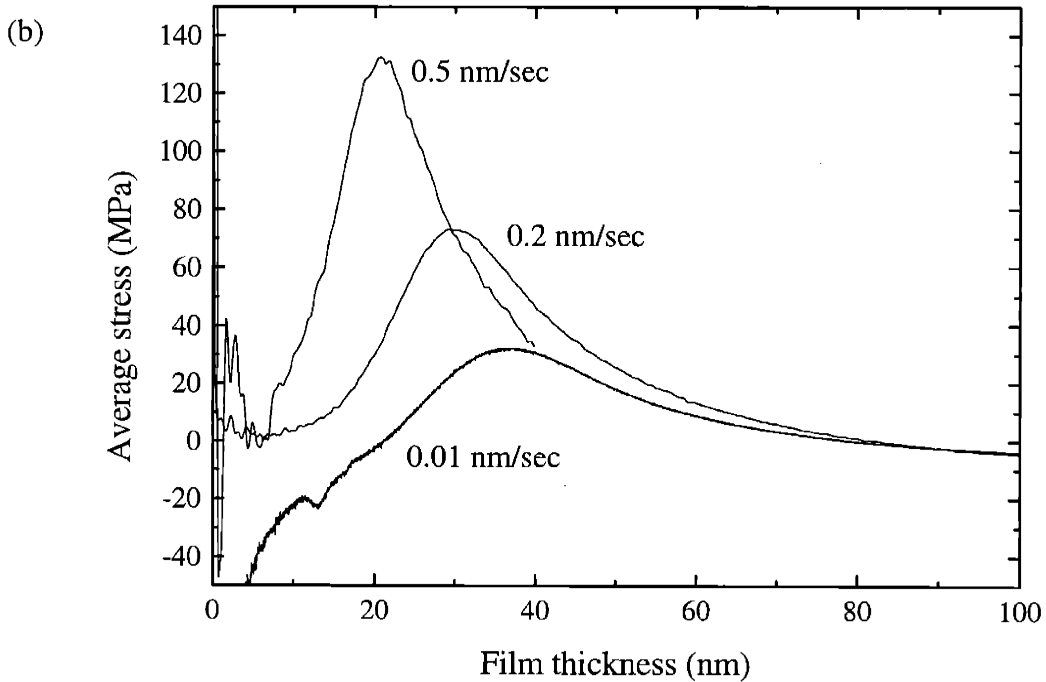

Figure 3-5: (a) Stress-thickness versus film thickness for Ag thin films deposited on oxidized silicon substrates at room temperature at different deposition rates. (b) The same data replotted as average stress (i.e. stress-thickness divided by film thickness) versus film thickness. The measurements were performed at SNL by JAF and SJH.

comparison, the data has been replotted as average stress (i.e. stress-thickness divided by the mass-equivalent thickness) versus film thickness in Fig 3-5(b). Since the sensitivity of the curvature measurements is related to the stress-thickness product, the calculated stress values in Fig. 3-5(b) at small film thicknesses tend to be noisy.

In order to study the evolution of the microstructure, films with a laterally graded thickness were grown by moving a shutter across the wafer during deposition. *Ex situ* plan-view scanning electron microscopy (SEM) images were used to characterize the microstructure as a function of film thickness. From the SEM images for discontinuous Ag films, the fractional substrate coverage versus film thickness was measured for all deposition rates, as shown in Fig. 3-6. For slower deposition rates, the film reaches continuity at a larger film thickness due to a lower nucleation density resulting in a larger average grain size, as confirmed by transmission electron microscopy (TEM).

Figure 3-5(a) shows that the magnitude of the maximum tensile stress-thickness decreased, and the film thickness coinciding with the maximum increased, with decreasing deposition rate. For all deposition rates, the maximum tensile stress-thickness occurred when the film was in the late channel stage just before continuity, as seen in Fig. 3-6. After reaching film continuity, the slope of the stress-thickness curve becomes negative. Note that the slope of the curves decreases in magnitude with decreasing deposition rate. The initial compressive stress measured for the 0.01 nm/sec deposition rate is atypical and not representative of the usual behavior for which neither tensile nor compressive stress is measured during very early deposition times.

3.3.2 Influence of deposition temperature

Silver films were deposited onto 100-μm-thick oxidized silicon wafers at 0.2 nm/sec deposition rate at different temperatures. The measured film stress-thickness versus film thickness curves for three depositions at different substrate temperatures are shown in Fig. 3-7(a). For comparison, the data has been replotted as average stress (i.e. stress-thickness divided by the mass-equivalent thickness) versus film thickness in Fig 3-7(b). Since the sensitivity of the curvature measurements is related to the stress-thickness product, the calculated values in Fig. 3-7(b) at small film thicknesses tend to be noisy.

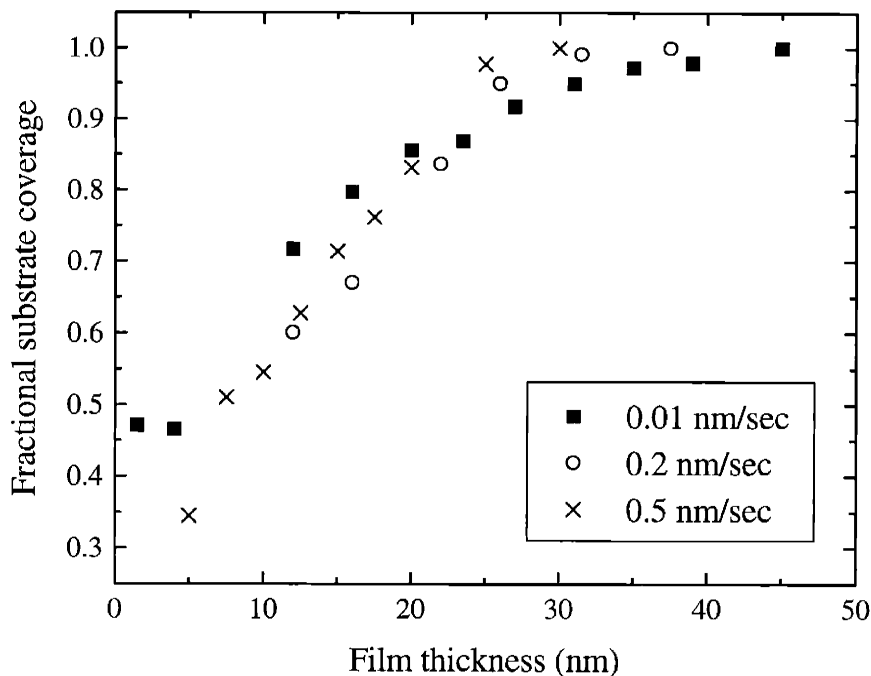

Figure 3-6: Fractional substrate coverage versus film thickness from SEM images during various stages of deposition of Ag at different deposition rates. The SEM images were obtained at SNL by JAF and SJH.

In order to study the evolution of the microstructure, films with a laterally graded thickness were grown by moving a shutter across the wafer during deposition. *Ex situ* plan-view SEM images were used to characterize the microstructure as a function of film thickness. From the SEM images for discontinuous Ag films, the fractional substrate coverage versus film thickness was measured for all deposition temperatures, as shown in Fig. 3-8. As a consequence of enhanced island coarsening and grain growth at higher temperatures, the films deposited at higher temperature reached continuity at a greater film thickness due to a larger average grain size, as confirmed by TEM.

Figure 3-7(a) shows that during early deposition times, no appreciable stress-thickness was measured up to a critical thickness, which increased with increasing deposition temperature. Once tensile stresses developed with further deposition, the magnitude of the maximum tensile stress-thickness decreased, and the film thickness

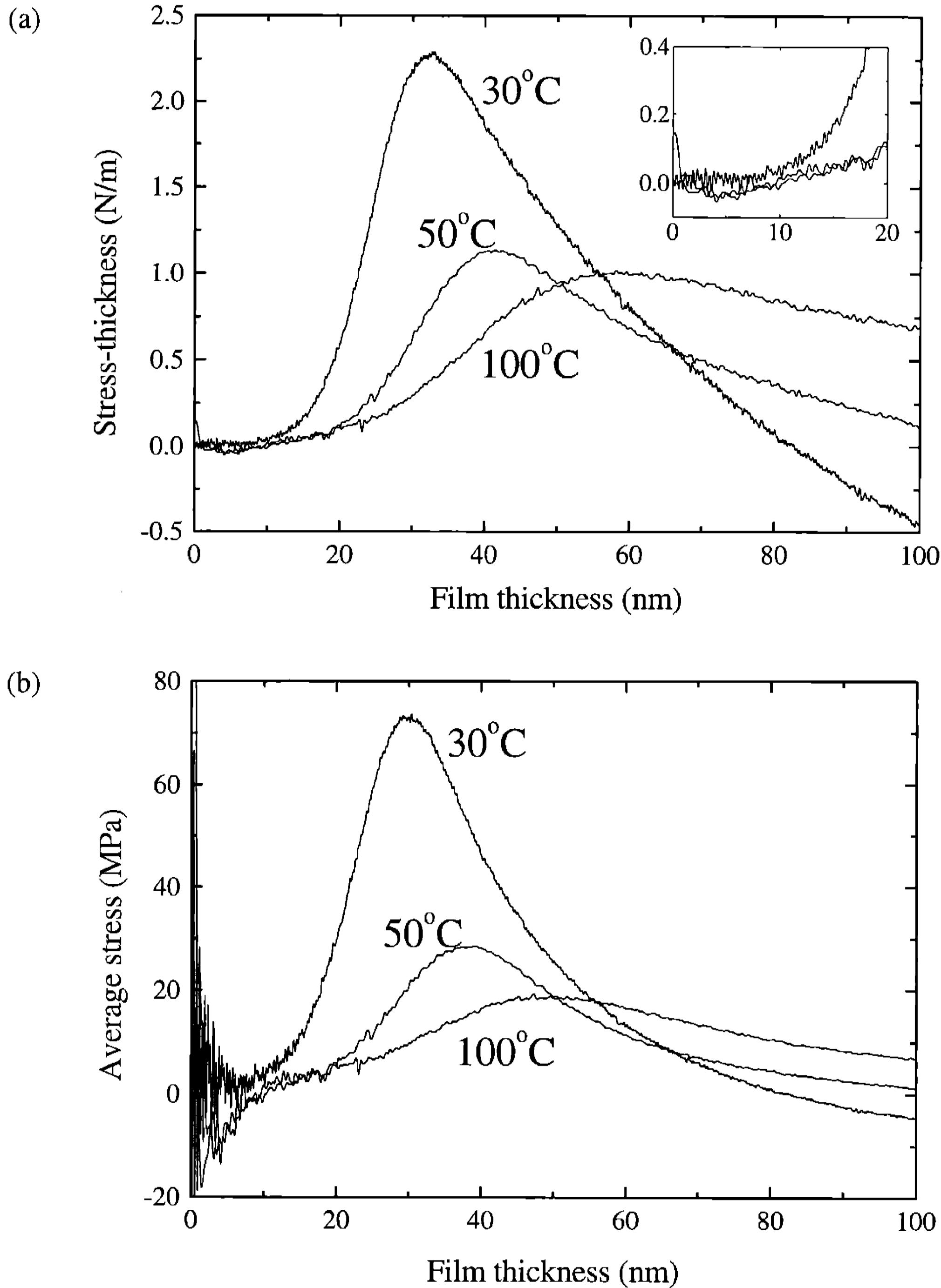

Figure 3-7: (a) Stress-thickness versus film thickness for Ag thin films deposited at 0.2 nm/sec on oxidized silicon substrates at different deposition temperatures. Inset is an enlargement of the initial 20 nm of deposition. (b) The same data replotted as average stress (i.e. stress-thickness divided by film thickness) versus film thickness. The measurements were performed at SNL by JAF and SJH.

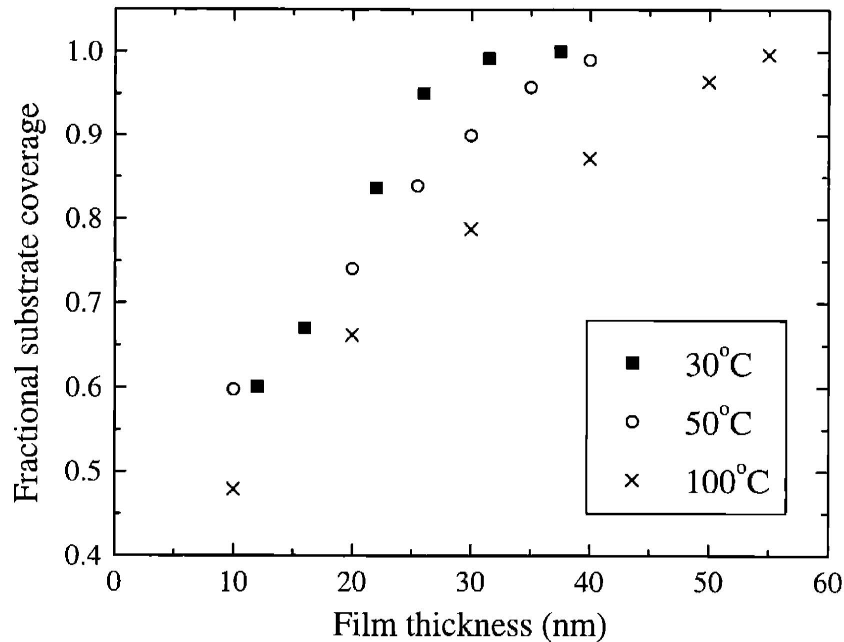

Figure 3-8: Fractional substrate coverage versus film thickness from SEM images during various stages of deposition of Ag at different temperatures. The SEM images were obtained at SNL by JAF and SJH.

coinciding with the maximum increased, with increasing deposition temperature. For all deposition temperatures, the maximum tensile stress-thickness occurred when the film was in the late channel stage just before continuity, as seen in Fig. 3-8. After reaching film continuity, the slope of the stress-thickness curve becomes negative. Note that the slope of the curves is smaller in magnitude for higher deposition temperatures.

3.4 Intrinsic stress measurements of Cu using piezocantilever devices

The intrinsic stress measurements for Cu thin films were collected using the piezocantilever devices. The theory and operation of the piezocantilevers is discussed in detail in section 2.3.

The packaged piezocantilever devices are prepared using a solvent prior to loading in the vacuum chamber. More aggressive cleaning procedures, such as with H_2SO_4:H_2O_2, are not possible because of the exposed aluminum metallization. Once the packaged device is loaded in the chamber, the entire vacuum system is outgassed at

120°C for 12 hours while the sample is heated to 170°C with the use a resistive heating stage. All films were deposited by electron beam evaporation in ultrahigh vacuum (UHV). Base pressures were 1 X 10^{-9} Torr, while deposition pressures were in the range of 3 X 10^{-8} – 8 X 10^{-8} Torr. Deposition rates were controlled using a crystal quartz monitor with feedback control to the electron beam power supply.

The stress during deposition was measured by monitoring the stress-dependent resistivity of a piezoresistive element fabricated within a thin silicon cantilever. The temperature during deposition was monitored by measuring the temperature-dependent resistivity of a nonpiezoresistor fabricated within a thin cantilever of the same geometry. The temperature data were used to correct for thermal stresses generated during deposition as described in sections 2.3.6 and 2.3.7. Films were deposited at 0.1 nm/sec at room temperature unless otherwise noted.

3.4.1 Continuous Cu thin film deposition

Because the piezocantilever technique is a new method for measuring intrinsic stress during deposition, a comparison will be made between the Cu results using the piezocantilever and those found in the literature. Care must be taken when making quantitative comparisons because of differences in the experimental conditions including: the stress measurement technique, the substrate surface, and the deposition rate. When using the piezocantilevers, Cu thins films were deposited by e-beam evaporation at room temperature at 0.1 nm/sec deposition rate onto the piezocantilever devices, which are passivated with a CVD oxide. Abermann and Koch deposited Cu by thermal evaporation onto MgF_2-coated glass substrates at room temperature at a deposition rate of 0.1 nm/sec [Aber 85]. Cantilever deflection during deposition was measured by a differential capacitance technique. Shull deposited Cu by thermal evaporation onto oxidized silicon substrates at room temperature at a deposition rate of 0.01 nm/sec [Shul 96], which is an order of magnitude slower than both the piezocantilever data and the Abermann and Koch data. In Shull experiments, the cantilever deflection during deposition was measured by laser deflectometery using a scanning laser technique.

Figure 3-9(a) is an intrinsic stress measurement using the piezocantilever device

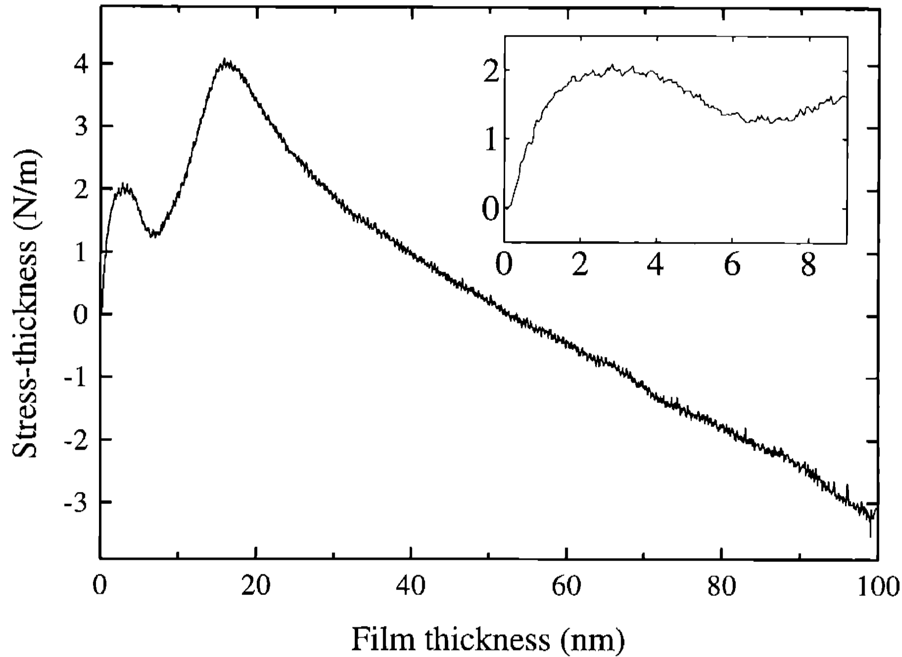

Figure 3-9: Stress-thickness versus film thickness during deposition of Cu at 0.1 nm/sec at room temperature measured with a piezocantilever device. Note that the sharp tensile rise during the first couple nanometers of thickness (inset) is not observed by other researchers [Aber 85, Shul 96].

for a Cu film deposited at 0.1 nm/sec at room temperature. Qualitatively, the piezocantilever results are very similar to both the Abermann and Koch data and the Shull data except for a consistently observed sharp tensile rise in the first 2 nm of deposition seen in Fig. 3-9(a). According to the temperature calibration of the uncoated piezocantilever devices discussed in section 2.3.6.3, the sharp tensile rise would be consistent with an increase in temperature of 5°C in the first 2 nm (i.e. 20 sec) of deposition. However, the measured temperature increase was about 0.1°C in the first 2 nm of deposition and only a 6°C temperature increase was measured during the entire 100 nm deposition. To confirm that electrical noise from the e-beam source was not interfering with the measurement, a deposition was performed with a glass slide over the piezocantilever device and a sharp tensile rise was not observed. One possibility is that charged ions from the evaporation source are deposited on the insulating surface of the cantilever, thereby accumulating charge on the surface, and resulting in a misleading

electrical measurement. A conductive ground path for the accumulated charge does not exist during the island stage of deposition when the film is still discontinuous. If the first couple nanometers of deposition are regarded as a measurement artifact, the "adjusted" piezocantilever results, shown in Fig. 3-10, are very similar to both the Abermann and Koch data and the Shull data. As shown in Fig. 3-10, several critical features have been labeled and the corresponding value have been catalogued in Table 3-1 to compares the piezocantilever results with those obtained by Abermann and Koch and by Shull. The piezocantilever results were averaged over six different experiments with nominally the same deposition conditions.

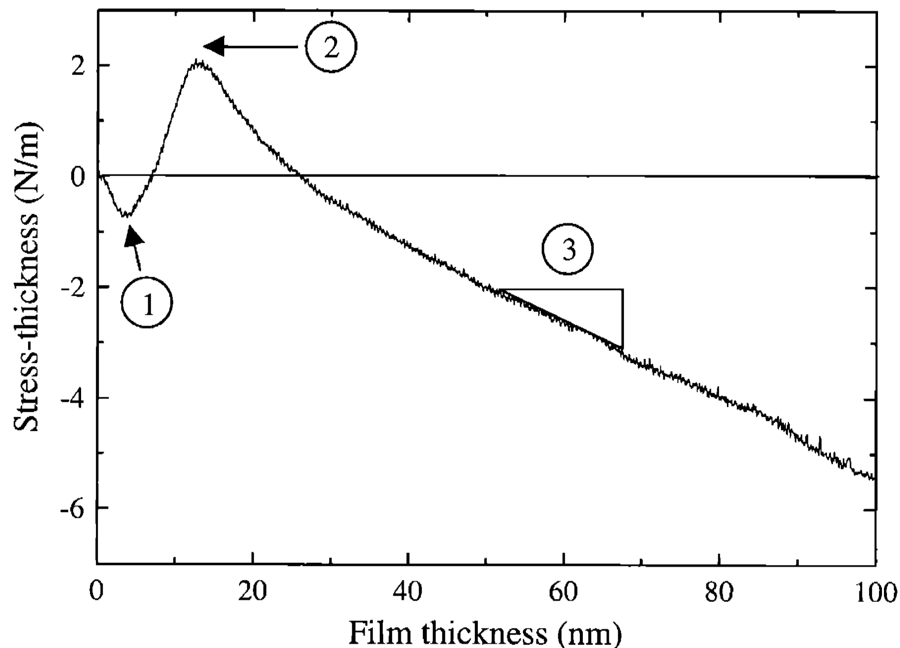

Figure 3-10: The "adjusted" stress-thickness versus film thickness during deposition of Cu at 0.1 nm/sec at room temperature measured with a piezocantilever device. Note that the sharp tensile rise during the first couple nanometers of thickness observed in Fig. 3-7 has been removed and attributed to a measurement artifact. Several critical features have been labeled above and the corresponding values have been catalogued in Table 3-1.

Transition point		Piezocantilever	Aber 85	Shul 96
1	h (nm)	2.1 ± 1.1	Not visible	1.6 ± 0.5
	σ-h (N/m)	-0.43 ± 0.23	Not visible	-0.34 ± 0.17
	σ_{avg} (MPa)	-200	Not visible	-210
2	h (nm)	11.5 ± 2.2	13	12.8 ± 1.8
	σ-h (N/m)	2.0 ± 0.6	3	1.78 ± 0.44
	σ_{avg} (MPa)	175	230	140
3	σ_{inst} (MPa)	-107 ± 33	-80	-260 ± 25

Table 3-1: Several critical features of the stress-thickness versus thickness curves of Cu have been labeled in Fig. 3-8 and the corresponding values have been catalogued above to compare the piezocantilever results with the Abermann and Koch data [Aber 85] and the Shull data [Shul 96]. The piezocantilever results were averaged over six different experiments.

3.4.2 Cu thin films deposition with growth interrupts

To elucidate the origins of any stress relaxation process operating during deposition, film growth was interrupted and the stress evolution with time at a given film thickness was observed. All of the growth interrupts consider in this section involve Cu films greater than 25 nm in thickness, which are fully continuous as confirmed from TEM micrographs. Growth interrupt experiments for Cu have been studied by other researchers [Aber 85, Shul 96] and the experimental trends detailed below using the piezocantilevers are in general agreement with the previous work. The qualitative observations of stress evolution during growth interrupts will be used as the motivation for the modeling described in Chapter 5.

The stress-thickness versus film thickness during and after a growth interrupt of an intermittent deposition of Cu is shown in Fig. 3-11(a). Deposition was interrupted at a film thickness of 25 nm, at which point the Cu film is fully continuous, and the evolution of the stress-thickness versus time over the 120 min hold is shown in Fig. 3-11(b).

(a)

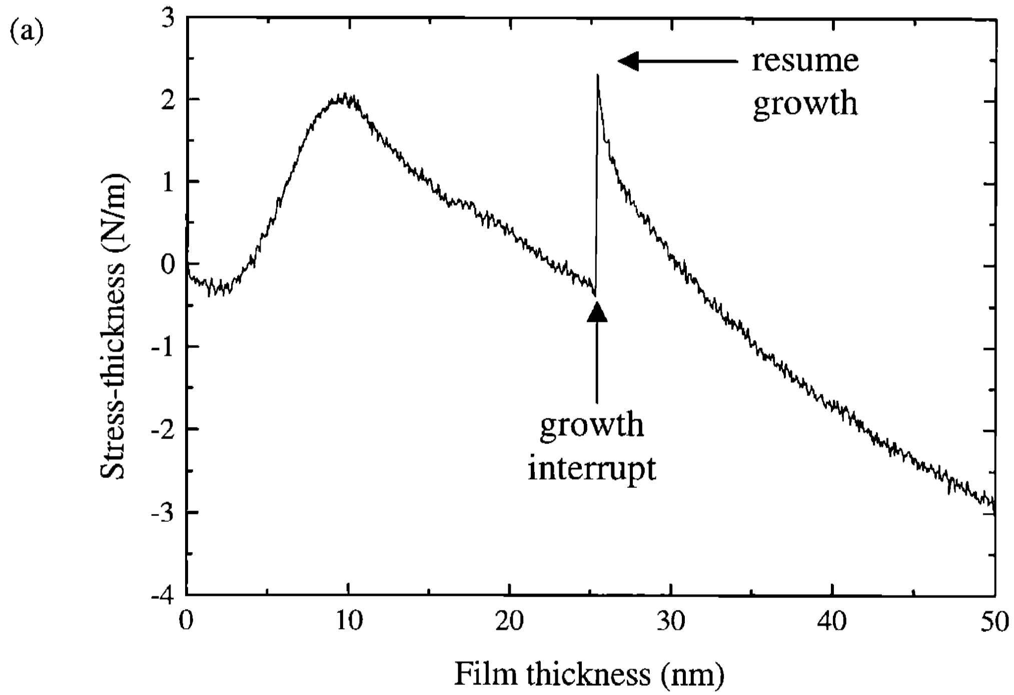

(b)

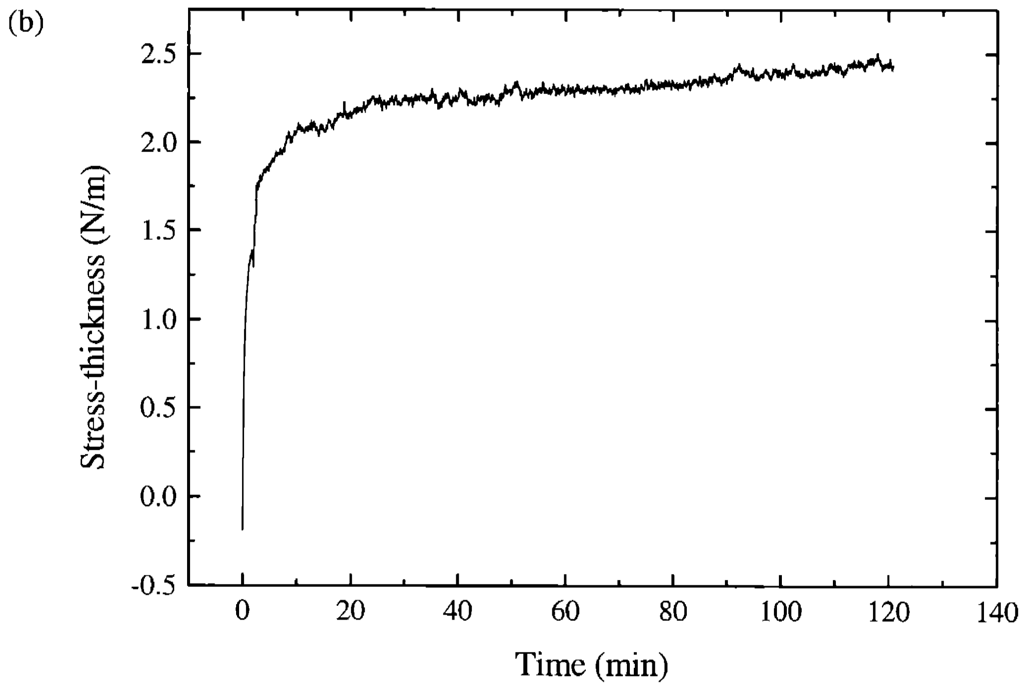

Figure 3-11: (a) Stress-thickness versus film thickness before and after a growth interrupt during intermittent deposition of Cu measured with a piezocantilever device. (b) The stress-thickness versus time during the growth interrupt of a 25 nm-thick Cu film.

Immediately prior to the growth interrupt, the instantaneous stress (i.e. slope of the stress-thickness versus film thickness curve) is nominally constant. After deposition was stopped, the stress-thickness increased in the tensile direction. The post-deposition change in stress-thickness is consistent with a decrease in the substrate temperature as would be expected when the evaporative source is turned off. However, the magnitude of the tensile rise is greater than the calculated thermal component of stress. In addition, the stress-thickness continued to evolve after the temperature of the substrate had equilibrated. A tensile rise during growth interrupts has been observed by several researchers for different thin film materials [Aber 85, Shul 96, Flor 01]. When growth was resumed, the stress-thickness decreased in the compressive direction and resumed the constant instantaneous stress (i.e. slope) that existed before the growth interrupt as consistent with previous observations [Aber 85, Shul 96, Flor 01].

With the piezocantilever measurements, the instantaneous stress after a growth interrupt of a continuous film was sometimes greater (i.e. a steeper slope) when growth was resumed. Larger instantaneous stresses during deposition of continuous films have been observed in Ag resulting from growth interrupts during the discontinuous stage of film growth [Flor 01]. The greater instantaneous stress was attributed to tensile stress relaxation due to island shear during the growth interrupt of the discontinuous film. However for growth interrupts of continuous films, the instantaneous slope has typically been reported to return to the same value as prior to the growth interrupt [Aber 85, Shul 96, Flor 01].

3.4.2.1 Thickness dependence of growth interrupt behavior

The thickness dependence of the stress evolution during growth interrupts of Cu was examined using the piezocantilever devices. Fig. 3-12(a) shows the evolution of the stress-thickness with time for films of different thickness where the curves have been replotted with common stress-thickness and time origins. The magnitude of the tensile rise in the stress-thickness increases with increasing film thickness, in agreement with previous work [Su 93, Shul 96]. Fig. 3-12(b) is the same data as in Fig. 3-12(a) but replotted as the average stress (i.e. stress-thickness divided by film thickness). The

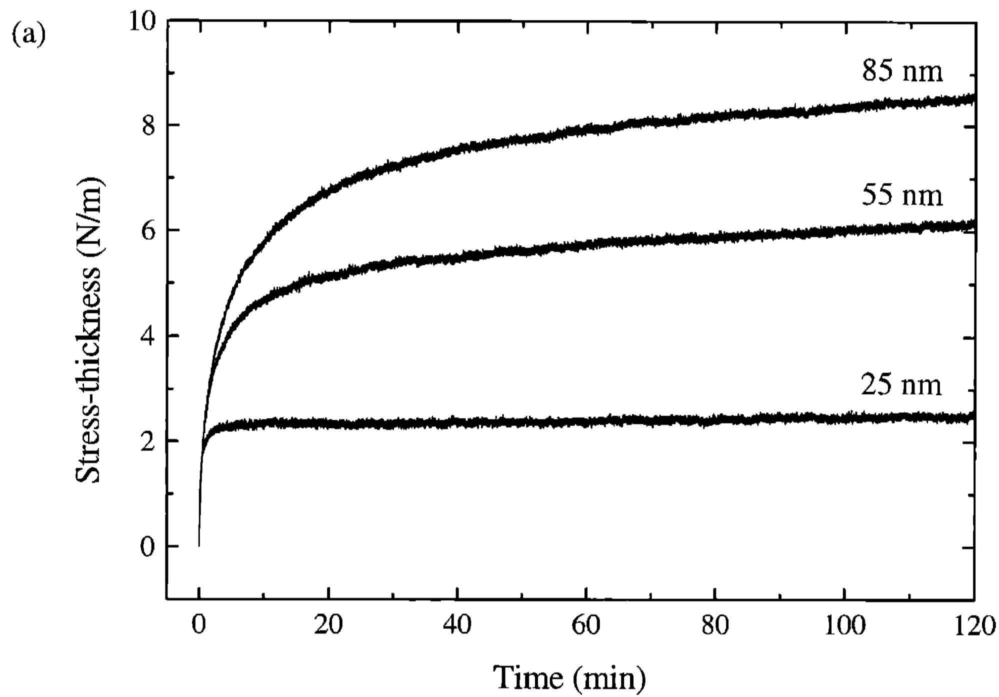

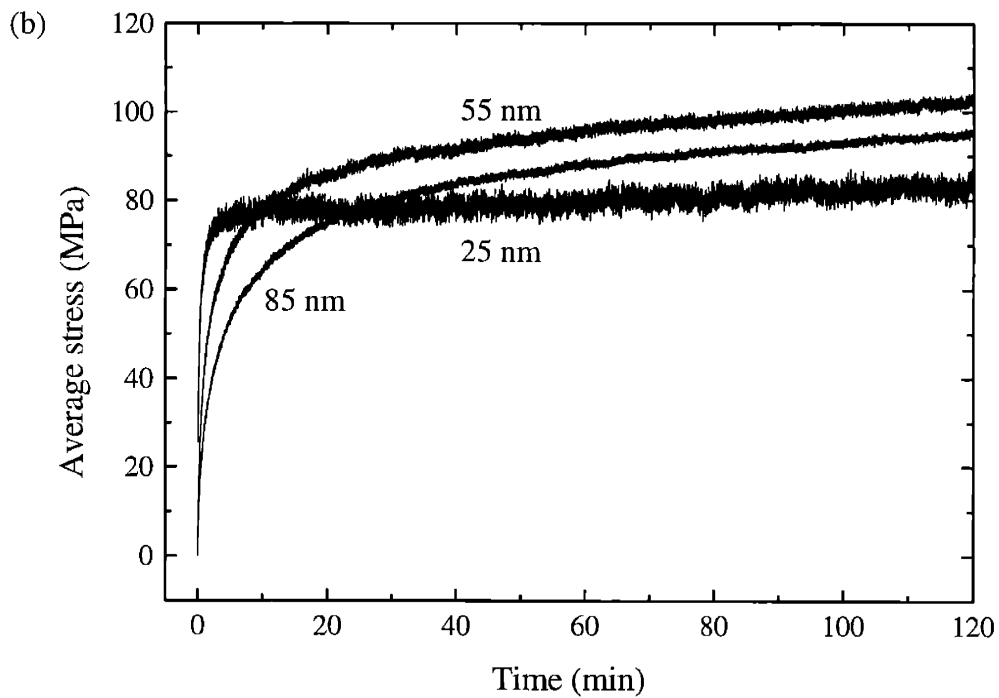

Figure 3-12: (a) Stress-thickness versus time during growth interrupts of an intermittent Cu deposition. The curves have been replotted with common stress-thickness and time origins. (b) The same curves replotted as average stress (i.e. stress-thickness divided by film thickness) versus time.

tensile rise in the average stress during the growth interrupt is between 80-100 MPa and relatively independent of the film thickness. The time scale required for the tensile rise to saturate increases with increasing film thickness, in agreement with previous work [Su 93, Shul 96]. Shull found that the tensile rise of the average stress during growth interrupts was approximately 100 MPa for Cu deposited at 0.01 nm/sec over a range of thicknesses from 10-60 nm [Shul 96]. Although the thickness dependence of the tensile rise was not reported, Abermann and Koch measured a tensile rise of approximately 65 MPa for a 100 nm-thick Cu film deposited at 0.1 nm/sec onto MgF_2-coated glass substrates. As mentioned previously, when film growth is resumed, the stress-thickness curve assumes a constant slope after a finite thickness (see Fig. 3-9(a)). The additional film thickness required to resume a constant instantaneous stress was found to increase with increasing film thickness at which the growth interrupt was performed in agreement with the data of Shull.

3.4.2.2 Influence of deposition rate on growth interrupt behavior

The influence of deposition rate on the stress evolution of Cu during growth interrupts was examined using the piezocantilever devices. As described in section 3.3.1, the deposition rate can influence the microstructure during film formation. The slower the deposition rate, the greater the film thickness required to reach film continuity and the larger the final grain size once the film becomes continuous. To minimize film thickness and grain size effects, an initial 25 nm-thick Cu film was deposited at the usual 0.1 nm/sec deposition rate to establish the initial microstructure. After a one hour anneal at room temperature, growth was resumed at a lower deposition rate of 0.05 nm/sec and 30 nm of Cu was deposited. After another one hour anneal at room temperature, growth was resumed at 0.03 nm/sec and another 30 nm of Cu was deposited. The measured stress-thickness versus film thickness for the intermittent Cu deposition is shown in Fig. 3-13. Notice that the instantaneous slope during deposition *increases* with decreasing deposition rate. Fig. 3-14(a) shows the evolution of the stress-thickness with time during the growth interrupts, where the curves have been replotted with common stress-thickness and time origins. Fig. 3-14(b) is the same data as in Fig. 3-14(a) but replotted

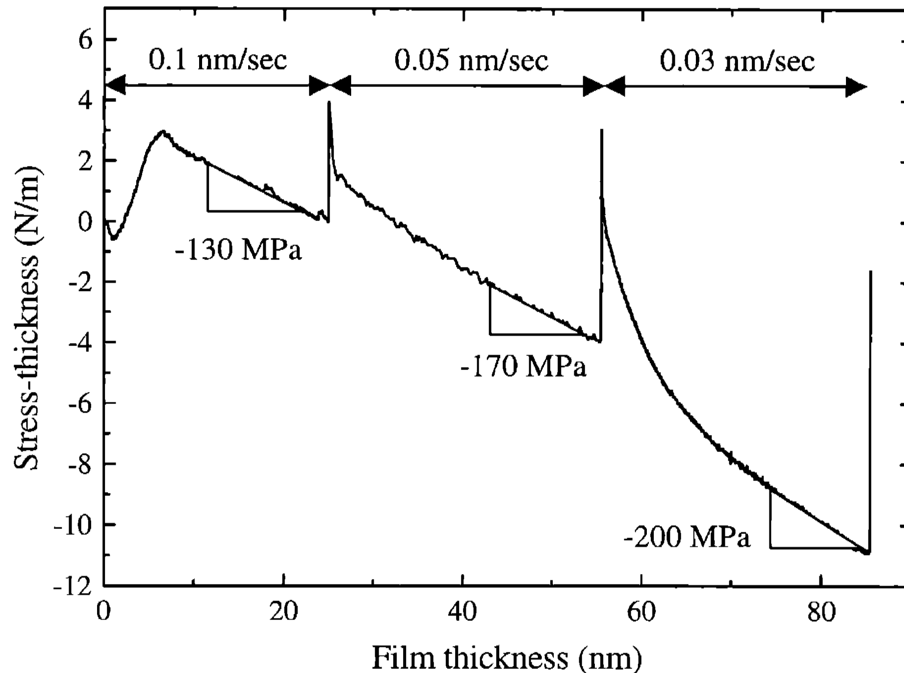

Figure 3-13: Stress-thickness versus film thickness before and after growth interrupts during intermittent deposition of Cu at different deposition rates. Notice that the instantaneous slope increases with decreasing deposition rate.

as the average stress (i.e. stress-thickness divided by film thickness). Similar to the case for which the deposition rate was kept constant between growth interrupts (see section 3.4.2.1), the magnitude of the tensile rise in the stress-thickness increases with increasing film thickness. From Fig. 3-14(b), the time scale required for the tensile rise to saturate also increases with increasing film thickness. When the deposition rate between growth interrupts was maintained constant as in section 3.4.2.1, the magnitude of the rise in the tensile stress during growth interrupts was mostly independent of the film thickness. From Fig. 3-14(b), the magnitude of the rise in the tensile stress during the growth interrupts decreases with decreasing deposition rate.

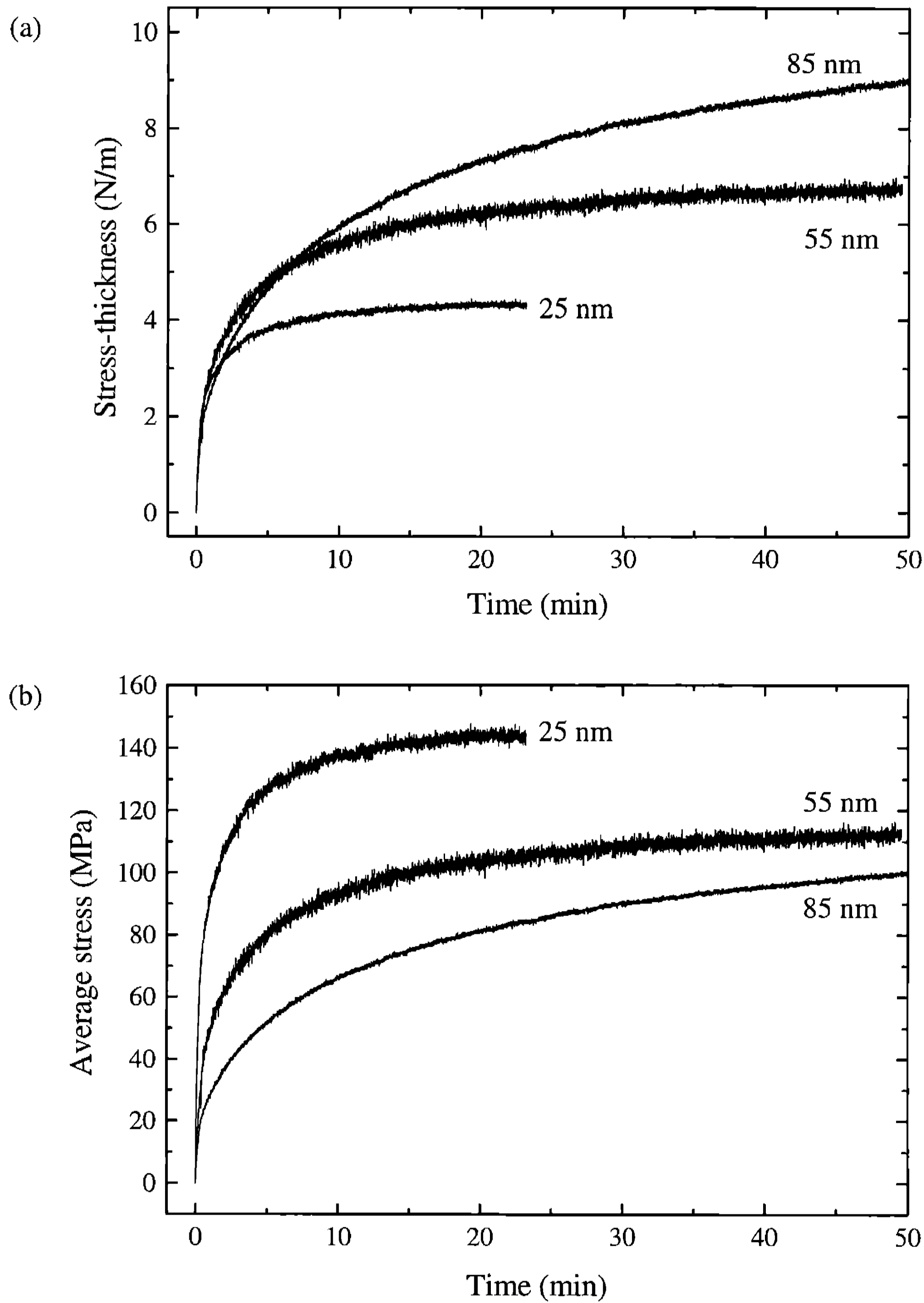

Figure 3-14: (a) Stress-thickness versus time during growth interrupts of an intermittent Cu deposition at different film thicknesses. The deposition rate prior to each growth interrupt was different. The curves have been replotted with common stress-thickness and time origins. (b) The same curves replotted as average stress (i.e. stress-thickness divided by film thickness) versus time.

3.4.3 Intrinsic stress measurements of amorphous germanium

Amorphous germanium (*a*-Ge) films were deposited onto 100-μm-thick oxidized silicon wafers at room temperature and 270°C. The stress measurements during deposition were taken using the MOSS system described in section 2.2. Figure 3-15 shows the stress evolution for *a*-Ge deposited at room temperature (solid line) and at 270°C (dotted line). Reflected high-energy electron diffraction (RHEED) patterns obtained during growth confirmed the lack of long-range order. The typical compressive-tensile-compressive evolution of stress associated with Volmer-Weber growth was observed during the growth of *a*-Ge [Flor 01]. A non-contact AFM image of a 7 nm-thick a-Ge film deposited at 270°C is shown inset in Fig. 3-15 that confirms the island growth mode. Studies of amorphous metallic films investigated by scanning

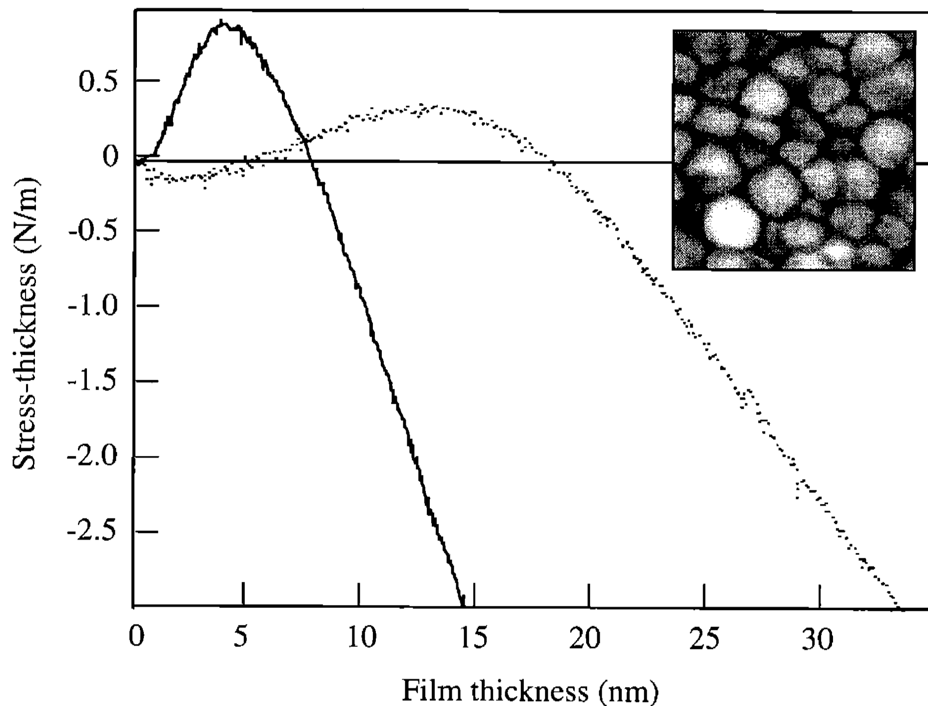

Figure 3-15: Stress-thickness versus film thickness for *a*-Ge films grown at room temperature (solid line) and 270°C (dots). An AFM image from a 7 nm-thick film grown at 270°C is shown inset, where the sides of the image are 212 nm across. The measurements were performed at SNL by JAF and SJH.

tunneling microscopy exhibit similar morphologies during growth [Rein 97; Geye 98]. The same qualitative stress evolution as shown in Fig. 3-15 has subsequently been observed in metallic amorphous thin films deposited on oxidized silicon substrates [Mayr 01].

In order to examine relaxation kinetics, growth interrupts were performed during the growth process, both before and after film continuity occurred. Figure 3-16 shows the behavior for *a*-Ge deposited at room temperature. Fig. 3-16(a) shows the stress-thickness versus time, which explicitly demonstrates the relaxation kinetics, while Fig. 3-16(b) shows the stress-thickness versus film thickness. Absolutely no relaxation was observed during the growth interrupts at room temperature, either before or after continuity, over time scales comparable to those of the deposition. Fig. 3-17 shows the growth interrupt behavior for *a*-Ge deposited at 270°C as a function of both time and thickness. Prior to film continuity, a clear relaxation of the tensile stress is observed as can be seen in Fig. 3-17(b). Furthermore, the stress actually goes into net compression after about 200 sec of annealing.

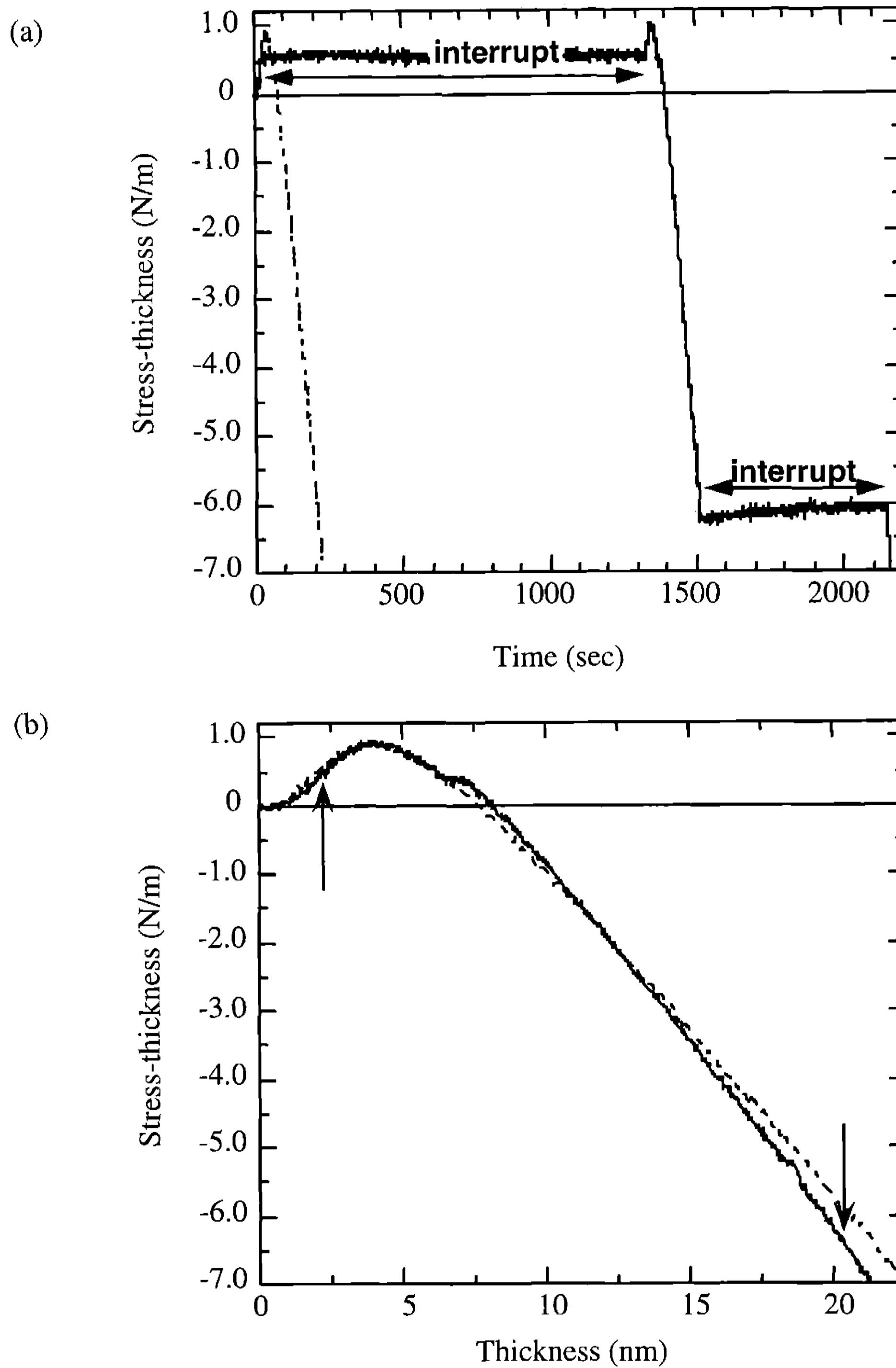

Figure 3-16: Growth interrupt behavior for *a*-Ge grown at room temperature showing (a) stress-thickness versus time, and (b) stress-thickness versus film thickness. The solid line is for growth with interrupts, while the dashed lines are uninterrupted growth data. The arrows in (b) indicate the thickness at which the interrupts occurred. The measurements were performed at SNL by JAF and SJH.

Chapter 4

Discussion of continuous deposition results

4.1 Overview

The experimental results presented in Chapter 3 consist of stress measurements made during deposition as a function of film thickness, and stress measurements during growth interrupts as a function of time for a given film thickness. This chapter will focus on the stress measurements made during continuous film deposition without growth interrupts. The first part of the chapter will detail a simulation tool developed to model the evolution of the film structure during Volmer-Weber type growth. Analytical models and finite element method (FEM) calculations are used to describe compressive and tensile stress generation mechanisms, as well as stress relaxation mechanisms, that are responsible for the measured stress behavior during thin films growth. Modifications to the models for stress generation and relaxation are made to incorporate them into the film growth simulation, which more realistically represents an evolving microstructure during deposition than the idealized models. The simulation provides a tool to study the importance of the different stress models, which depend on island/grain size and film thickness, as well as their kinetics, which are influenced by the deposition rate and temperature, for a microstructure that changes with increasing film thickness during

deposition. Calculations of the stress evolution during deposition from the thin film growth simulation are compared to the experimental measurements.

4.2 Simulation of film growth by the Volmer-Weber mechanism

4.2.1 Introduction

In order to model microstructure evolution during thin film growth, a computer simulation was developed to represent deposition by the Volmer-Weber mechanism [Seel 00]. The aim of the simulation is to reproduce the size and time dependence of the island nucleation and growth process occurring during thin film deposition. With the ability to reproduce a realistically evolving microstructure, models for stress generation and relaxation that depend on size and time can be implemented and compared to experimental results. The C code for the film growth simulation is given in Appendix B. Beside the comments within the code, descriptions are provided that describe the general structure of the code and practical information about its use.

The growth of thin films by the Volmer-Weber mechanism involves the nucleation and growth of individual islands that impinge and coalesce to form a continuous film, as shown in Fig. 1-1. Thin film growth was modeled in a two-dimensional front-tracking simulation with periodic boundary conditions by considering the nucleation and growth of circles, which represent the intersection of islands with the substrate. Nucleation was assumed to occur continuously during deposition at a constant rate, so that the number of new nuclei added per unit time per unit exposed substrate area was constant. The nucleated islands grow with a constant radial growth velocity proportional to the deposition rate. As isolated islands grow larger, island impingement and coalescence results in grain boundary formation at their line of intersection. As growth continues and more grain boundaries form, triple points are formed where grain boundaries meet within an ensemble of three islands or grains. Eventually, all grain boundaries terminate at triple points when the film is fully continuous. Continued deposition results in film thickening with no further nucleation and a constant average grain size. Modifications to the simulation are discussed below to account for non-

idealities associated with the simple growth conditions of a constant nucleation rate and radial growth velocity.

4.2.2 Thin film growth simulation technique

4.2.2.1 Island nucleation rate

A constant nucleation rate I is defined such that the number of new nuclei added per unit time per unit exposed substrate area is constant. To achieve a constant nucleation rate of I_0 for a substrate of area A, the time between nucleation *attempts* is calculated as a random number whose average value is one divided by the product of I_0 times A. The position of the new nucleus is chosen at a random position on the substrate. Nucleation is only successful if an existing island does not currently occupy the randomly chosen nucleus position. Figure 4-1 is a plot of the nucleation rate as a function of time for a simulation of approximately 500 grains growing under conditions of a constant radial growth velocity and a nucleation rate of one. Even though the nucleation rate is

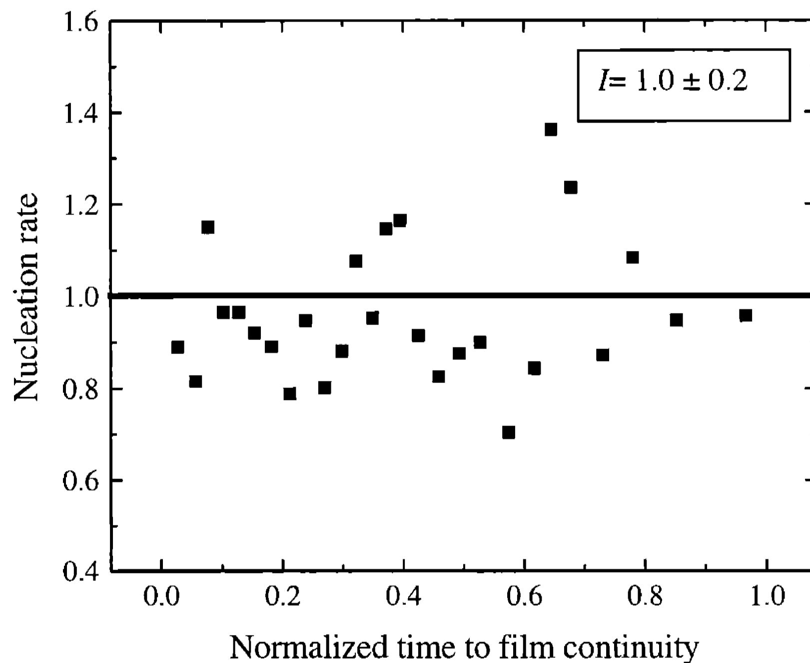

Figure 4-1: Nucleation rate I as a function of time for a simulation of 500 grains using a nominal rate of I equal to one and a constant radial growth velocity. The nucleation rate is defined as the number of new nuclei per unit time per unit exposed substrate area. The nucleation rate was averaged over 20 nucleation events for each point in the plot.

constant, the number of new nuclei per unit time is decreasing with time and reaches zero once the film is continuous. In this model, only one nucleus can be formed in a given time step so that simultaneous nucleation is not possible.

4.2.2.2 Island radial growth velocity

Assuming a constant radial growth velocity is based upon a simplified model of island growth for which only the deposition flux that directly impinges on the growing island contributes to its volume. If the atomic deposition flux is normal to substrate surface, the change in volume of an isolated island per unit time *dV/dt* is given by $D\pi r^2$, where D is the deposition rate in units of length per unit time and r is the in-plane island radius. For a hemispherical island, the volume is given by $(2/3)\pi r^3$ so that *dV/dr* is simply $2\pi r^2$. Using the two previous expressions for *dV/dt* and *dV/dr*, the radial growth velocity *dr/dt* is given by:

$$\frac{dr}{dt} = \frac{1}{2} D \, . \qquad (4.1)$$

Using Eq. 4.1 provides a simple relation between the experimental deposition rate and the radial growth velocity of an isolated hemispherical island. A similar expression can be derived for the more general case of a spherical cap island with only the difference of a geometric factor [Thom 99]:

$$\frac{dr}{dt} = \frac{\sin^3\theta}{(1-\cos\theta)^2(2+\cos\theta)} D \, , \qquad (4.2)$$

where θ is the contact angle that the island surface makes with the substrate. Under conditions of a constant radial growth velocity and constant nucleation rate, the average grain area A in the continuous film is given analytically by [Thom 99, Fros 97]:

$$A = 1.1371 \left(\frac{\sin^3\theta}{(1-\cos\theta)^2(2+\cos\theta)} \frac{D}{I} \right)^{2/3} , \qquad (4.3)$$

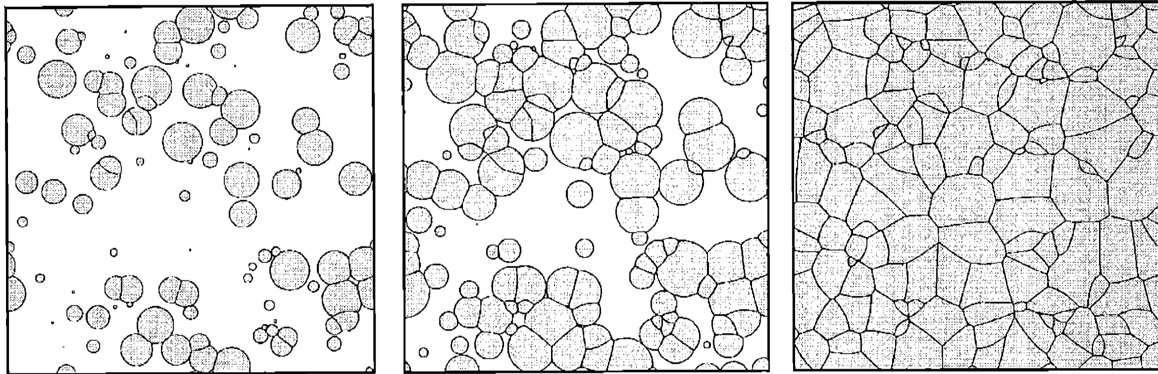

Figure 4-2: A time sequence of film growth by the Volmer-Weber mechanism using the simulation with growth conditions of constant nucleation rate and radial growth velocity resulting in the so-called Johnson-Mehl structure.

where the resulting grain structure is the so-called Johson-Mehl structure, as shown in a time sequence from the simulation in Fig. 4-2. The simulation matches the average grain area calculated using Eq. 4.3 to within less than 3% error.

4.2.2.3 Grain boundary algorithm

For a thin film grown on an amorphous substrate, the in-plane crystallographic orientation of the growing islands is random [Thom 90]. Therefore when growing islands impinge with each other, the surface of intersection is typically a high-angle grain boundary. In the simulation, the line of intersection between impinging circles represents the grain boundary between intersecting islands. The lines of intersection must be calculated at each time step as new islands impinge and existing boundaries lengthen. In the simplest case, either two or three islands intersect and form boundaries that lengthen with time, as shown in Fig. 4-3. For the case with three islands in Fig. 4-3, notice that the three boundaries eventually intersect and form a triple point with the ensemble of three islands. The situation becomes more complex as growth continues and multiple circles begin intersecting, as shown in Fig. 4-4 for five intersecting grains. The general algorithm for calculating lines of intersection between growing islands is given below:

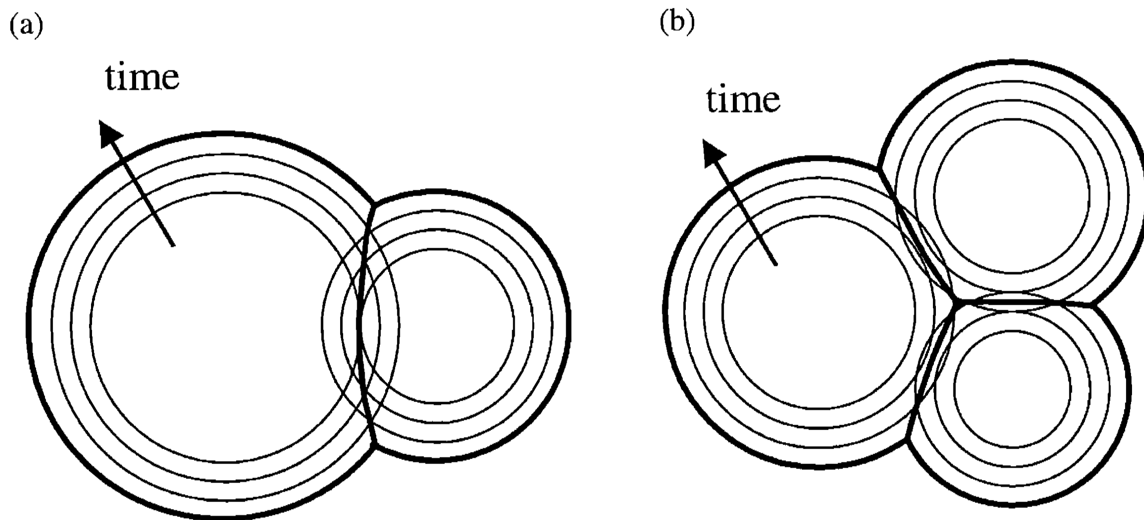

Figure 4-3: Grain boundary formation between (a) two growing islands, and (b) three growing islands. A grain boundary is represented in the simulation as the line of intersection of two impinging circles. Notice in (b) that the three boundaries eventually intersect and form a triple point with the ensemble of three islands.

(1) For each circle, create a neighbor list of intersecting circles.

(2) For each pair of interesting circles, calculate the pair of intersection points.

(3) For each point of intersection, create a list of all circles containing the intersection point within its radius.

(4) If the list contains only two of circles, then the point is a valid intersection point.

(5) If the list contains three circles, calculate the line of intersection between each pair of circles in the list and calculate the triple point at which the three boundaries intersect and store as a valid intersection point.

(6) If the list contains more than three circles, calculate the line of intersection between each pair of circles in the list. Next, calculate the position and time of formation for all triple points formed between intersecting boundaries. The triple point that formed the earliest is the only valid triple point from the list of potential triple points calculated. In addition, the intersection points associated with invalid triple points can be eliminated.

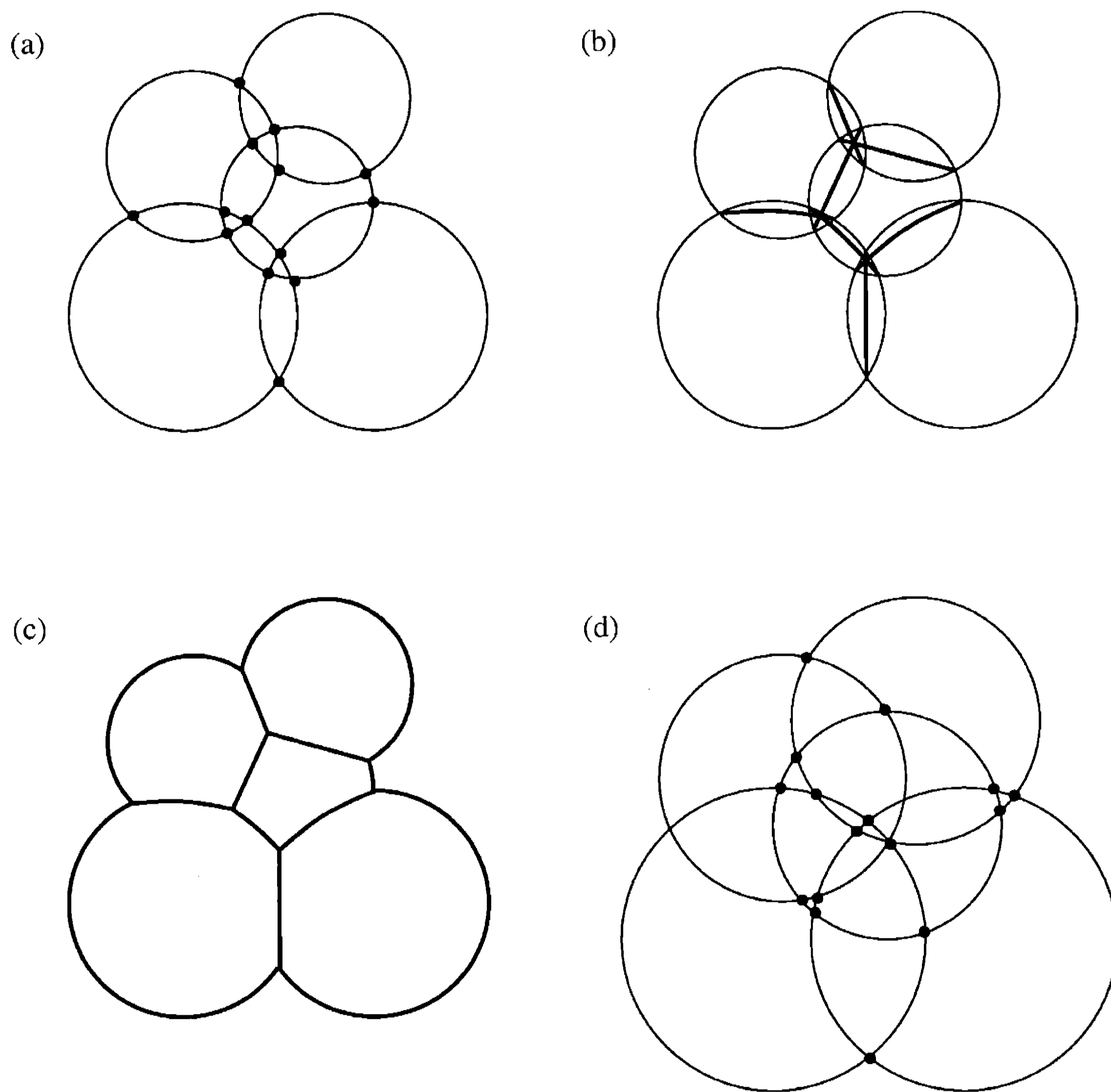

Figure 4-4: Schematic of the simulation algorithm for calculating grain boundaries between multiple intersecting island, including (a) calculating the points where circles intersect, (b) determining lines of intersection between points, and (c) calculating triple point locations where three boundaries intersect within an ensemble of three islands. The situation become more complex as growth continues and multiple circles begin overlapping as shown in (d).

(7) Calculate the boundaries between intersecting circles using the valid intersection point and triple point locations calculated above.

(8) Repeat for all circles in the simulation during the current time step.

The algorithm above was found to be robust and appropriately handles the complexity that arises at later times when multiple circles begin overlapping as shown in Fig. 4-4(d). The actual C code for the algorithm above is supplied in Appendix B.

4.2.2.4 Limitations of film growth simulation

For a constant deposition rate, the volume of material deposited per unit area of substrate per unit time is constant and equal to the deposition rate. Figure 4-5 is a plot of

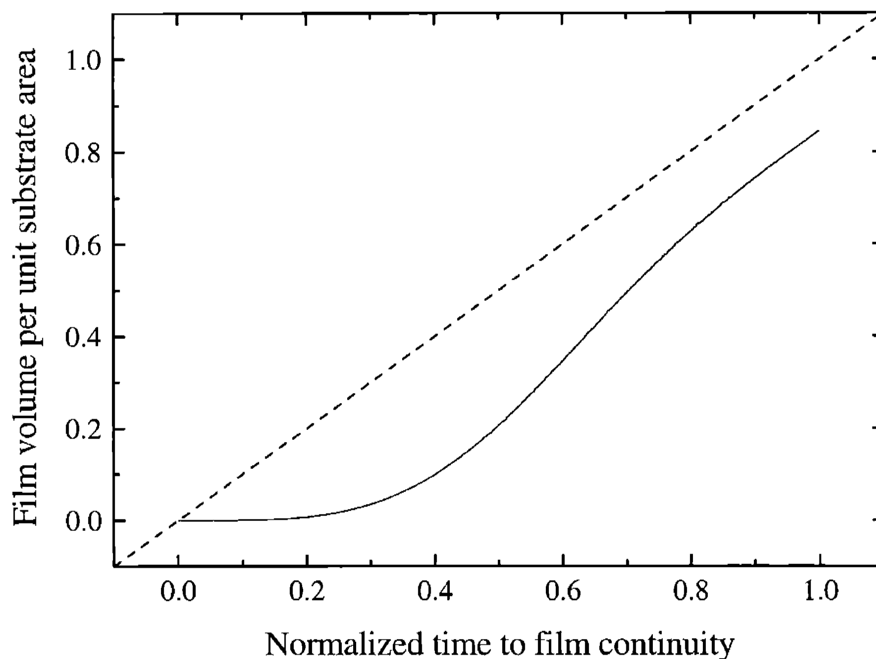

Figure 4-5: The film volume per unit substrate area as a function of time for a constant deposition rate (dotted line) compared to the simulation results (solid curve) under growth conditions of a constant nucleation rate and radial growth velocity for hemispherical islands. Note that the simulation accumulates volume very slowly at early times.

island volume per unit substrate area as a function of time in the simulation for a deposition rate of one. Note that the simplified method of volume calculation in the simulation overestimates the volume of a hemispherical cap by a factor of 1/3 but is acceptable for demonstrative purposes. The dashed line in Fig. 4-5 is the expected accumulation of film material for a constant deposition rate of one. Especially at early times, the simulated behavior demonstrates an accumulation of material much slower than expected for a constant deposition rate. In the simulation, only the material impinging on existing islands contributes to the volume of the film and the volume consumed by nucleation events is very small. One way in which to rationalize this simulation behavior is to assume that the sticking coefficient for the deposited material is one on existing island and nearly zero on the substrate.

Modifications to the simplified model for film growth described above were studied to improve the volume conservation of the system. If substrate surface diffusion is appreciable, atoms adsorbed on the substrate within a distance δ of a growing island can become incorporated by diffusion, as shown in Fig. 4-6. The addition of material due

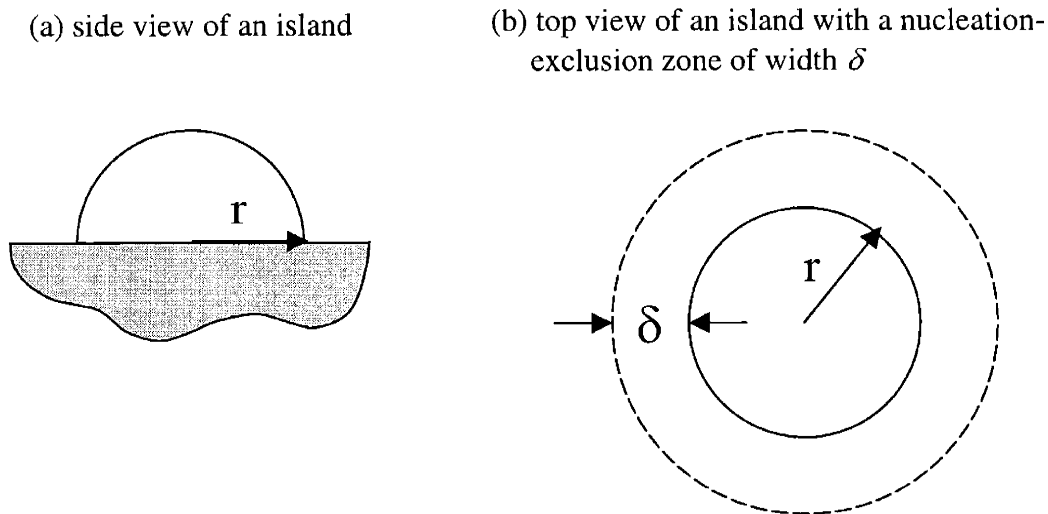

Figure 4-6: (a) Side view of an island of radius r, and (b) top view of an island of radius r with nucleation-exclusion zone of width δ.

to diffusion can occur by a random walk process so that δ is a characteristic diffusion distance for an absorbed atom. Alternatively, any nuclei that form in the diffusion zone will become incorporated into the larger island by diffusion due to a difference in chemical potential. The diffusion zone is therefore also a nucleation-exclusion zone. For a growing island with a nucleation-exclusion zone of width δ, the radial growth velocity is given by [Thom 99]:

$$\frac{dr}{dt} = \frac{\sin^3\theta}{(1-\cos\theta)^2(2+\cos\theta)} D\left(1+\frac{\delta}{r}\right)^2. \qquad (4.4)$$

Note that the radial growth velocity now depends on the radius of the growing island, in contrast to the constant radial growth velocity in Eq. 4.1. The expression for the radial growth velocity is only strictly valid for isolated islands and becomes less ideal once nucleation-exclusion zones begin to overlap. Better volume conservation is achieved since a larger fraction of the material impinging on the substrate is incorporated into the growing islands. However, absolute volume conservation can only be achieved if the entire substrate surface consists of overlapping nucleation exclusion zones. Under these conditions, the simulated microstructure consists of grains with a monomodal grain size distribution [Fros 87], as shown in Fig. 4-7, which is not consistent with typical as-deposited microstructures.

Another approach to improving volume conservation in the simulation is to assume that any material not impinging on an existing island must be involved in nucleation. For physical vapor deposition under vacuum conditions, the critical number of atoms required for nucleation is two from experimental measurements [Vena 84] and the calculated critical radius for nucleation is on the order of an atomic radius [Thom 95]. Therefore, a large number of nuclei must form at early times to conserve volume during deposition. Extremely high island densities have been observed during deposition of Ag and Au using *in situ* TEM, however, the grain size in the continuous films were observed to be greater than the initial island spacing indicating that coarsening of the microstructure occurred during film growth [Pash 65, Pash 64]. From the *ex situ* TEM

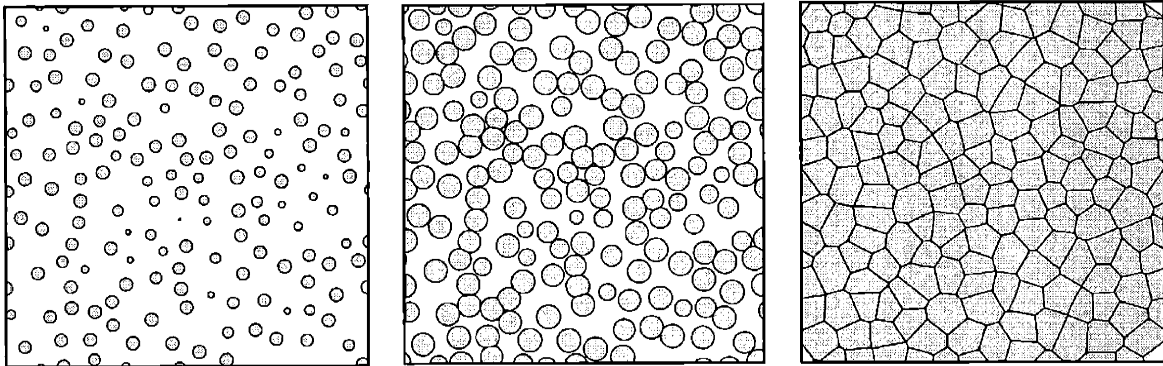

Figure 4-7: A time sequence of simulated film growth by the Volmer-Weber mechanism with a nucleation-exclusion zone. In the simulation, the nucleation rate is constant and the radial growth velocity depends on both the island radius and the nucleation-exclusion zone width according to Eq. 4.4.

micrographs in Fig. 3.3, coarsening of the microstructure is apparent for both the Al and Ag films as the film thickness increases. A heuristic model was implemented in the simulation to capture island coarsening during growth. When an island smaller than a critical size impinges with a large island, coarsening occurs so that the volume of the small island is incorporated into the larger island. Using a high nucleation rate along with island coarsening, the simulation results in a film with grain sizes larger than the initial island spacing, as shown in Fig. 4-8, and better conservation of volume of the deposition flux. To perfectly conserve volume would require nucleation of an extremely large number of islands since the critical number of atoms for nucleation is know to be on the order of a couple atoms. Tracking the number of nuclei required to conserve volume from the deposition flux is not currently possible due to limitations of the computer memory at our disposal.

Because only marginal improvements to the non-idealities could be made with the modification to the simulation suggested above, the remainder of the chapter assumes thin film growth conditions using a constant nucleation rate and a constant radial growth velocity.

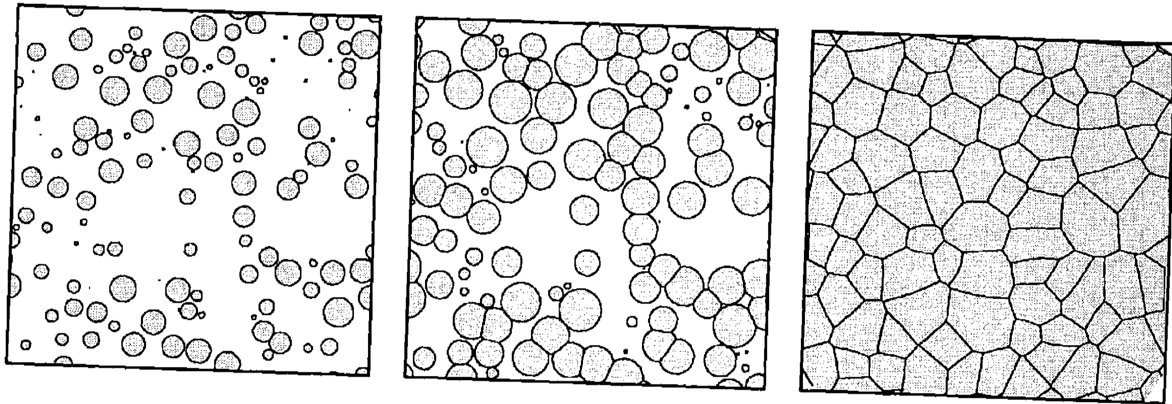

Figure 4-8: A time sequence of simulated film growth by the Volmer-Weber mechanism with island coarsening. When an island smaller than a critical size impinges with a large island, coarsening occurs so that the volume of the small island is incorporated into the larger island.

4.2.3 Simulated substrate coverage compared to experiment

The physical dimensions of the simulation are unitless so a scaling factor must be defined that relates the microstructural dimensions of the real film to the simulated structure. From TEM images of continuous Ag films deposited at different temperatures, the average grains size was measured and used to scale the average grains size from the unitless simulation. In addition, the simulation should capture the evolution of the grain size *during* deposition. From SEM images of discontinuous Ag films, the fractional substrate coverage versus film thickness was measured as a function of deposition temperature, as shown in Fig. 4-9. At higher temperatures, island coarsening is faster and results in larger island sizes during growth and therefore a greater film thickness to reach continuity. Using the scaling factor from the average grain size measurements, the simulated microstructural captures the evolution of the measured substrate coverage versus film thickness, as shown in Fig. 4-9. Note that the simulation did not include island coarsening, but was still able to qualitatively match the evolution of the measured substrate coverage versus film thickness.

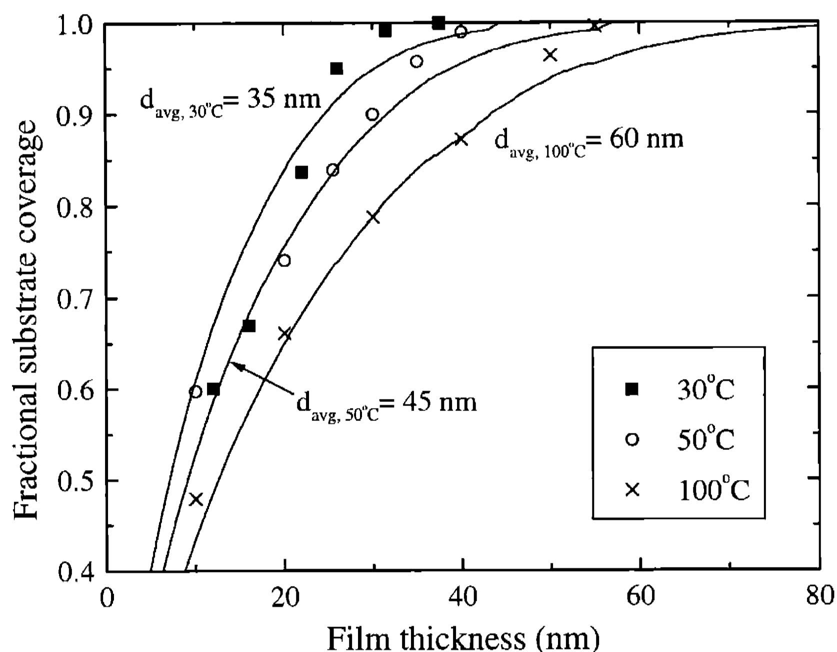

Figure 4-9: Fractional substrate coverage versus film thickness from SEM images during various stages of deposition of Ag at different temperatures. The lines are from the simulations of microstructural evolution scaled using the measured average grain sizes (listed next to each curve in the plot).

4.2.4 Incorporating stress generation/relaxation mechanisms into simulation

The simulation of Volmer-Weber-type thin film growth generates a distribution of island sizes that develop during deposition as a function of film thickness and time. The microstructural simulation can be used as a tool to study stress generation and relaxation process that are length-scale dependent, temperature-dependent, and/or time-dependent. In the remainder of the chapter, experimental results will be compared to simulation results for thin film growth by the Volmer-Weber mechanism using length-, time-, and temperature-dependent models for stress generation and relaxation. The methods by which analytical models were incorporated into the simulation will be discussed in detail in the following sections.

4.3 Compressive stress generation during island stage growth

4.3.1 Introduction

The existence of a compressive stress during the island stage of thin film growth of FCC metals has been experimentally confirmed by several researchers [Aber 78, Shul 96, Flor 01]. Wilcock *et al.* and later Abermann *et al.* have suggested that the compressive stress that develops during the island stage of growth is the result of the dependence of the lattice parameter on the island size [Wilc 69, Aber 78]. The size dependence of the lattice parameter results from the surface stress, which has greater influence when the surface area to volume ratio of the island is high. The origins of thin film stress related to surface stress have recently been reviewed in the literature [Camm 00, Spae 00]. A brief overview of the theory will be given below, along with comparisons between the models and the experimental measurements of stress during the island stage of Al and Ag film growth.

4.3.2 Surface stress

Two thermodynamic quantities characterize the surface of a solid. The surface energy γ of a solid surface is a scalar quantity that represents the reversible work dW to create new surface of area dA (i.e. by increasing the number of atoms at the surface) so that $dW=\gamma dA$. The surface stress f_{ij} is a tensor quantity associated with the reversible work per unit area required to elastically strain a surface by $d\varepsilon_{ij}$. The change in total energy associated with the surface stress is given by $d(\gamma A)=Ad\gamma + \gamma dA=Af_{ij}d\varepsilon_{ij}$. Since $dA=A\delta_{ij}d\varepsilon_{ij}$, where δ_{ij} is the Kronecker delta, then $f_{ij}= \gamma\delta_{ij} + d\gamma/d\varepsilon_{ij}$. For a surface possessing three-fold or higher rotational symmetry, the surface stress is represented by a scalar quantity:

$$f = \gamma + \frac{d\gamma}{d\varepsilon}. \tag{4.5}$$

The term $d\gamma/d\varepsilon$ is Eq. 4.5 is non-zero when forces between atoms in the surface are different than those in the interior. The atoms at the surface have fewer nearest neighbors

than atoms in the interior and therefore would prefer to change their interatomic distance to reduce the energy associated with the free bonds. However, the surface atoms are constrained due to coherency with the underlying material and therefore exert lateral forces across the surface. In the case of a liquid surface, the term $d\gamma/d\varepsilon$ is zero because a liquid cannot support elastic shear stresses and therefore the surface stress and surface energy are equivalent.

The layer of surface atoms can be thought of as a strained membrane that results in a strain in the interior of the solid. The displacements that occur at the surface due to the strained membrane can be represented by a pressure on the surface that results in the same displacements (i.e. the same boundary conditions result from either loading condition). For a finite-size solid, the net pressure ΔP, called the Laplace pressure, results in a change in volume dV and an amount of work ΔPdV. The ΔPdV work must balance the work performed against the surface stress fdA so that:

$$\Delta P = f\frac{dA}{dV}. \tag{4.6}$$

For a spherical solid body of radius r, $\Delta P=2f/r$ where ΔP is a hydrostatic pressure that results in a uniform elastic strain. For $f > 0$, the pressure is positive and results in a compressive stress in the solid body.

4.3.3 Lattice contraction measurements

A lattice parameter that scales proportionally with the inverse of particle size has been reported by many researchers [Mays 68, Wass 70, Wass 72, Apai 79, Wolt 81, Soll 85]. The experimental techniques for measuring lattice contraction and the limitations of these technique for measuring surface stress are discussed in detail in reviews by Marks [Mark 94] and Henry [Henr 98]. Diffraction methods provide reciprocal space lattice information for a collection of islands, typically varying in size, and yields an average lattice contraction. Scattering of electron waves within a cluster of atoms allows for calculation of the average interatomic distance, however the data analysis is rather complicated and not as established as the diffraction technique. Finally, scanning probe

techniques such as scanning tunneling microscopy and atomic force microscopy allow direct imaging, however deconvolution of the imaging tip and sample can be troublesome. Experimental parameters such as surface contamination, cluster-substrate interaction, and surface faceting make interpretation of the experimental results difficult. For instance, Mays *et al.* deposited gold nuclei of radius 3.5 to 12.5 nm onto amorphous carbon substrates and measured a lattice contraction by electron diffraction [Mays 68]. Solliard and Flueli used high-energy electron diffraction to measured lattice contraction of small particles of gold with mean sizes ranging from 3 to 40 nm deposited on carbon films [Soll 85]. For nominally similar measurements for Au, Mays *et al.* determine a value of surface stress f less than the surface energy γ, while Solliard and Flueli find the opposite. Lattice contraction has been measured in other materials including Al [Wolt 81], Ag [Wass 70], Cu [Wass 72, Apai 79], Ni [Apai 79], and Pt [Wass 72]. Even though uncertainty exists in the magnitude of the surface stress, the experimental evidence indicates that a lattice contraction in small volumes resulting in a compressive stress that is inversely proportional to the radius of the particle.

Positive values for surface stress have been obtained by first principles calculations and empirical potential calculations for materials such as Al [Need 90, Pogo 01], Pb [Mans 90], Ir, Pt, and Au [Need 89], and Ni, Cu, Ag, Pt, and Au [Gumb 91]. Calculated surface stresses are performed for surfaces with specific crystallographic orientations, typically (111) and (100) surfaces, whereas in experiments, no specific crystallographic plane forms the entire island surface.

4.3.4 Compressive stress generation in islands during thin film growth

During thin film growth, islands form by nucleation and increase in radius via the deposition flux. Due to excess surface stress energy, a compressive stress in the island will result, whose magnitude depends on the island radius. In thin film stress measurements, the substrate curvature, or substrate stress in the case of the piezocantilevers, is being monitored and must be related back to the stress in the film. Substrate curvature results from forces applied by islands that undergo a *change* in stress. Forces are applied across the island-substrate interface and therefore the influence of the traction between the island and substrate must be considered. If perfect sliding exists for

an island on a substrate, the island cannot exert any forces on the substrate and zero substrate curvature will result even if the lattice parameter of the island is changing. If perfect traction exists between the island and substrate, then changes in stress in the island will apply moments resulting in substrate curvature. In section 4.3.5, the importance of island-substrate traction is used to understand the difference in compressive stress behavior for Al and Ag during the island stage of growth.

4.3.4.1 Cammarata lock-down radius model

The following section outlines an argument for compressive stress generation during the island stage of thin film growth promoted by Cammarata *et al.* [Camm 00]. An extension of the model has been derived to account for the influence of the contact angle between the island surface and substrate.

Consider a cluster of a few atoms that form as a nucleus on the substrate surface. For such a small cluster of atoms, the concept of lattice parameter and stress are somewhat nebulous, but for discussion assume that the island is obeying continuum behavior. Due to excess surface stress energy, the nucleus will experience a Laplace pressure given by Eq. 4.6. For such a small island, any stress supported by traction with the substrate can easily be relieved by shearing along the island-substrate interface and the lattice parameter will adjust to the equilibrium value dictated by the Laplace pressure. Note that after shearing, the island will not longer be applying any force on the substrate and zero substrate curvature will result even though the island is under a compressive stress. Provided that shearing at the island-substrate interface is "fast", the lattice parameter of the growing island will constantly attempt to adjust to the equilibrium value and will not apply any forces on the substrate. However as the island becomes larger, shearing will become more difficult as the area of the island-substrate interface increases. The in-plane lattice spacing of the island will no longer be able to adjust to the equilibrium value and the lattice parameter is effectively frozen-in. The island size at which the shear rate becomes slower than the rate of compressive stress generation is defined as the "lock-down" radius r_{LD}. The lock-down radius depends on the strength of the island-substrate bonding and will be larger for weaker bond strength. As the island grows larger, the equilibrium lattice parameter changes according to the Laplace pressure

but the actual lattice parameter is dictated by the radius at which the island became locked down. Therefore a stress develops in the island that depends on the equilibrium lattice parameter, which is a function of the island radius, and the lock-down radius. For a hemispherical island or radius r, the lock-down stress σ_{LD} is given by:

$$\sigma_{LD} = 2f\left(\frac{1}{r} - \frac{1}{r_{LD}}\right), \tag{4.7}$$

where f is the surface stress. As the island grows larger the equilibrium lattice parameter continually increases and $1/r$ approaches zero, so that the asymptotic value for σ_{LD} is $-2f/r_{LD}$. For f=1 J/m^2 and r_{LD} =1-10nm, the compressive stress σ_{LD} is on the order of 100-1000 MPa. Note that this analysis ignores changes in area of the interface between the island and substrate due to a change in the island radius, or equivalently that the surface stresses of the substrate and island-substrate interface are assumed to be equal.

The contact angle that the island surface makes with the substrate also affects the Laplace stress. For a spherical cap with a contact angle θ as shown in Fig. 4-10, the volume is given by $V=(\pi/3)R^3(1-\cos\theta)^2(2+\cos\theta)$ so that $dV/dR=\pi R^2(1-\cos\theta)^2(2+\cos\theta)$, and the surface area is given by $A=2\pi R^2(1-\cos\theta)$ so that $dA/dR=4\pi R(1-\cos\theta)$, where R is

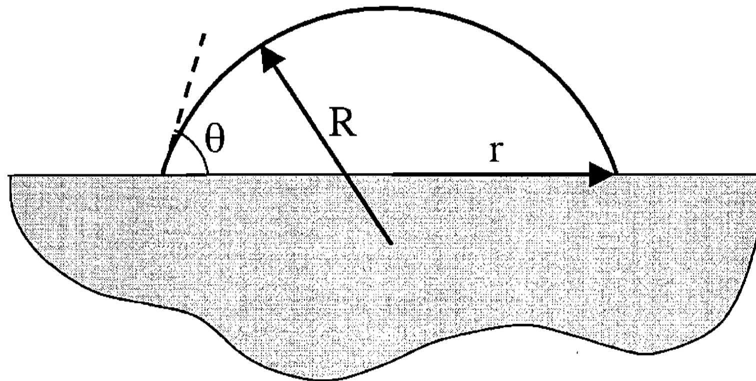

Figure 4-10: Spherical cap island with contact angle θ between the island surface and substrate, radius of curvature R, and in-plane radius r.

the radius of curvature of the island. Using Eq. 4.6 and substituting that R equals $r/sin\theta$, the Laplace pressure for a spherical cap is given by:

$$\Delta P = f\frac{dA}{dV} = \frac{4f}{r}\frac{sin\theta}{(1-cos\theta)(2+cos\theta)}. \tag{4.8}$$

The geometric term $sin\theta/[(1-cos\theta)(2+cos\theta)]$ increases with decreasing contact angle as expected since the surface to volume ratio follows the same trend. In the limit of θ=0, the surface to volume ratio of a finite volume of material is infinite and therefore the geometric term blows up. An expression similar to Eq. 4.7 for the lock-down stress as a function of contact angle can be derived so that:

$$\sigma_{LD} = 4f\frac{sin\theta}{(1-cos\theta)(2+cos\theta)}\left(\frac{1}{r}-\frac{1}{r_{LD}}\right). \tag{4.9}$$

For f=1 J/m^2 and r_{LD} =10 nm, the asymptotic limit of the compressive stress is approximately 400 MPa for θ=40°, 200 MPa for θ=90°, and 100 MPa for θ=150°. Comparison between the predictions of the model and experimental results are discussed in section 4.3.5.

4.3.4.2 Compressive shell model

In the Cammarata model, the lattice parameter does not change after the island becomes larger than the lock-down radius. The experimental measurements of lattice contraction from section 4.3.3 demonstrate a lattice parameter that scales proportionally with the inverse of the island radius. The discrepancy between the Cammarata model and the lattice contraction measurements may occur because of the kinetic argument for the lock-down radius. Given enough time for shear to occur, the actual lattice parameter of the island may relax to the equilibrium lattice parameter and conform to the measured inverse island radius dependency of the lattice contraction.

Alternatively, this conflict can also be resolved by considering a different model for the implementation of the Laplace pressure. Assume that each new layer of material

added to an existing island is deposited at the equilibrium lattice parameter dictated by the radius-dependent Laplace pressure. As the island radius increases during growth, the inner layers of material, which were deposited with lattice parameters smaller than the equilibrium lattice parameter dictated by the island radius, experience pressures that increase towards the center of the island. For a spherical-cap island of radius r_{island}, the stress in a shell of material at a radius r is given by:

$$\sigma_{shell}(r) = 4f\frac{\sin\theta}{(1-\cos\theta)(2+\cos\theta)}\left(\frac{1}{r_{island}}-\frac{1}{r}\right). \tag{4.10}$$

The average stress in the island is the volume average of the stress contribution from each layer so that:

$$\sigma_{shell} = -\frac{2f}{r_{island}}\frac{\sin\theta}{(1-\cos\theta)(2+\cos\theta)}. \tag{4.11}$$

Using this model, the average stress in the island increases with decreasing island radius, which is consistent with the experimentally measured lattice contraction. Shear at the island-substrate interface may relax compressive stress generation attributed to the compressive shell model when islands sizes are small, as discussed in more detail in section 4.3.4.1. Both the Cammarata model and the compressive shell model described in the previous sections will be compared to the experimental measurements of compressive stress during the island stage of growth.

4.3.5 Model comparison with compressive island stress measurements

During the island stage of growth, Ag and Al deposited on oxidized silicon substrates exhibit significantly different behavior (see Fig 3-2). The Al films are compressive from the very beginning of deposition and remain compressive until a thickness of approximately 2 nm. In contrast, the Ag films do not display any compressive regime during the island stage of growth and a measurable stress occurs only above a thickness of 10 nm. Although aluminum oxide formation at the Al-SiO_2

interface may complicate the comparison, Abermann observed similar behavior for Ag and Al on MgF_2–coated substrates [Aber 90]. The inability of Ag islands to support compressive stresses during the island stage of growth suggests that shear occurs easily at the Ag-SiO_2 interface. Interfacial shear is more effective in weakly bonded film-substrate systems and Ag-SiO_2 bonding is expected to be much weaker than the Al-SiO_2 interface, given the much stronger oxidation potential of Al. To confirm these metal-SiO_2 bonding trends, stud-pull adhesion tests were performed for Ag and Al films on oxidized Si substrates [Flor 01]. The Ag films delaminated from the substrates at an average force of 3.3 lbs. By contrast, the Al films failed to delaminate from the SiO_2 until the Si wafer shattered. Abermann and Koch have also suggested that sliding may occur for Ag on MgF_2-coated substrates [Aber 85]. During deposition of Al, shear at the island-substrate interface is not able to relax compressive stress generation at the island stage of growth. The stress measurement during Al deposition will be compared to the analytical models for compressive stress generation detailed in section 4.2.4 implemented in the thin film growth simulation.

During the island stage of thin film growth, a distribution of island sizes is present in the film that evolves during deposition. The simulation of thin film growth by the Volmer-Weber mechanism provides a tool by which to study the stress evolution with islands that increase in size during deposition. During each time step in the simulation, the radius of each island increases and the compressive stress in each island is recalculated using either Eq. 4.9 (Cammarata model) or Eq. 4.11 (compressive shell model). The average stress in the film is calculated as the volume average over all islands in the film, and the average stress-thickness is the average stress times the mass-equivalent film thickness. The inputs to Eqs. 4.9 and 4.11 used to calculate the compressive stress include (1) a material property, the surface stress f, (2) the contact angle θ, which depends on the film-substrate system, (3) the lock-down radius r_{LD}, which depends on the film-substrate system as well as the deposition rate and temperature, and (4) the radius of the island during deposition, which will depend on the film growth conditions such as deposition rate and temperature.

The surface stress of Al calculated from first principles calculations yields values of 1.4 J/m^2 for a (111)-oriented surface and 1.9 J/m^2 for a (001)-oriented surface [Pogo

01]. In another study, the surface stress of a (111)-oriented surface of Al was calculated as 1.25 J/m^2. [Need 89]. For islands in the shape of a spherical cap, no specific crystallographic plane forms the island surface, therefore an approximate average value for the surface stress f for Al will be assumed to be 1.5 J/m^2. For reference, the surface energy for Al at room temperature is approximately 1.15 J/m^2 [Murr 75]. From TEM micrographs of Al during the island stage of growth (e.g. see Fig. 3-3), the island contact angle θ can be estimated to be approximately 50 degrees by assuming that the islands are spherical-cap volumes. In the simulation, the evolving distribution of island sizes during growth can be modeled for the Al film by matching the grain size ($r_{final} \approx 15$ nm) estimated from TEM micrographs of continuous Al films to the simulated structure. When using the Cammarata model (Eq. 4.9) to calculate the compressive stress during deposition, the lock-down radius is an adjustable parameter used to achieve the best fit to the experimental measurements.

Figure 4-11 shows the measured Al stress-thickness data from Fig. 3-2 along with the simulated curves of compressive stress generation during deposition. Two of the simulated curves were calculated using the Cammarata model (Eq. 4.9) with different lock-down radii. The remaining simulated curve was calculated using the compressive shell model (Eq. 4.11). The calculations using the compressive shell model and the Cammarata model with a 5 nm lock-down radius yield an appreciable compressive stress for the very beginning of deposition in agreement with the experimental results. The larger lock-down radius of 10 nm delays the onset of an appreciable compressive stress until at least a thickness of 1 nm.

The simulation dramatically over predicts the compressive stress after a couple nanometers of thickness for the Al film deposition. Especially early in the deposition when islands are small, interfacial shear probably relaxes a significant fraction of the compressive stress generated during growth. The magnitude of the compressive stress in the island stage of growth should depend on both the deposition rate and temperature, which will affect the rate of stress relaxation compared to the rate of stress generation. A slower deposition rate or higher deposition temperature should result in a smaller compressive stress during the island stage of growth. The deposition conditions also

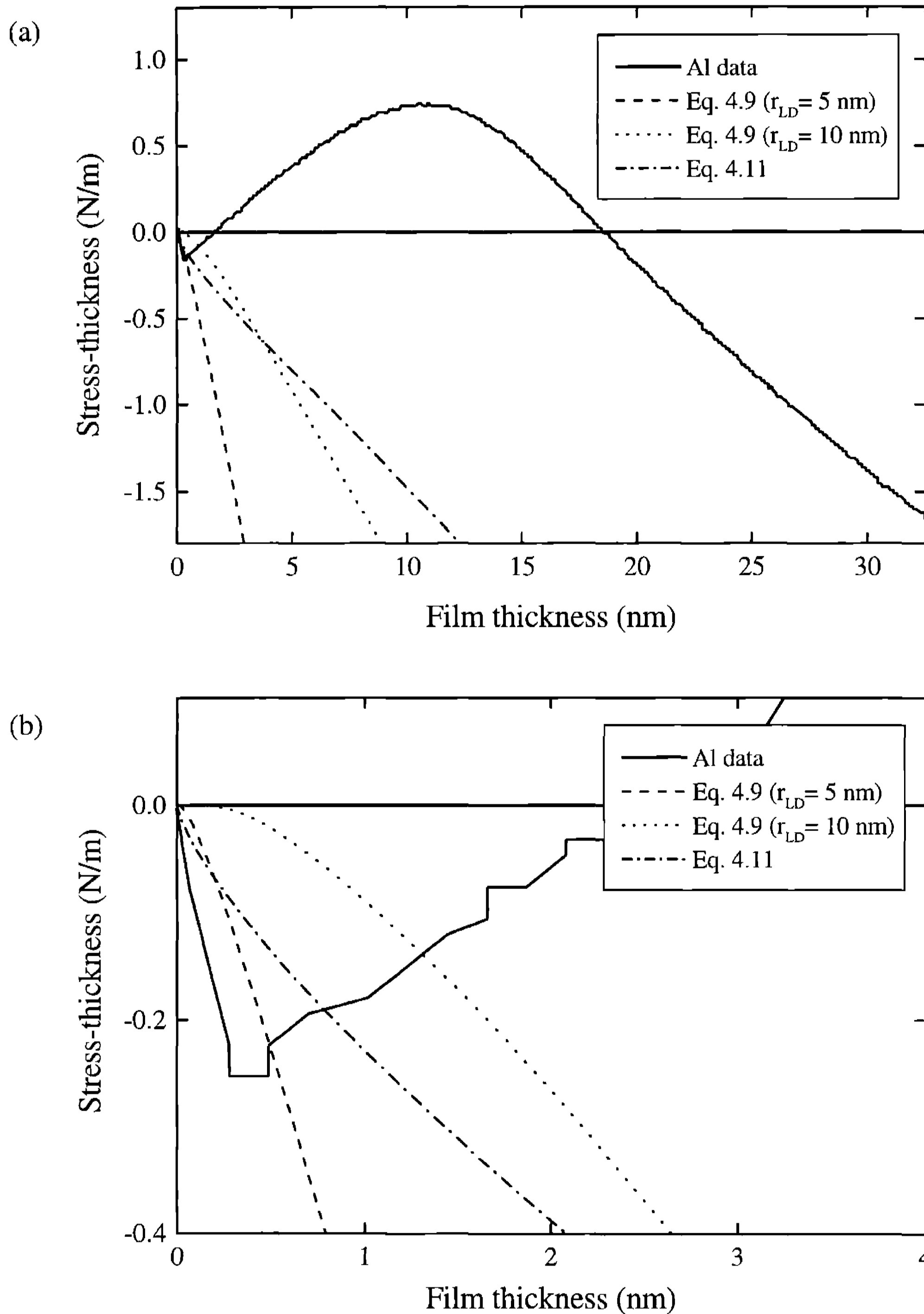

Figure 4-11: (a) Comparison of the Al stress-thickness data (from Fig. 3-2) with calculated curves from the simulation using the Cammarata model (Eq. 4.9) and the compressive shell model (Eq. 4.11). The compressive stresses was calculated in the simulation using f= 1.5 J/m^2 and θ= 50 degrees. (b) Magnification of the first 4 nm of Al deposition.

influence the island size at a given film thickness due to changes in substrate surface diffusion that affects the nucleation rate and island coarsening during deposition. Experimental study of the kinetics of stress relaxation during the island stage of growth is difficult because the deposition conditions affect the microstructure, which in turn affects the kinetics of stress relaxation.

By a thickness of two nm for the Al film, substrate coverage is greater than 40 percent and impingement between growing islands has begun. As described in the next section, grain boundary formation upon island impingement results in tensile stress generation that dominates the stress behavior as the film thickens.

4.4 Tensile stress generation upon island impingement

4.4.1 Introduction

The correlation between an increasing tensile stress during deposition and island impingement resulting in grain boundary formation has been qualitatively confirmed in many experimental studies [Maki 69, Wilc 69, Aber 85]. As two islands impinge and form a grain boundary at their intersection, part of the free surface of each island is eliminated, resulting in a significant energy reduction. Hoffman postulated that if neighboring islands are within close proximity, they stretch towards each other to form a grain boundary to reduce the interfacial energy at the expense of an associated strain energy [Hoff 76]. Implicit to this argument is that no diffusive processes are occurring and that grain boundary formation results from a straining process rather than by diffusion of material to the grain boundary. Even with this simple intuition, the physical process of stress generation due to grain boundary formation and the methods by which to model this process are a matter of debate in the literature.

4.4.2 First order global energetic analysis of tensile stress generation

Hoffman argues that when growing islands impinge with each other, their relative positions are offset (i.e. a non-integer atomic distance) so that non-equilibrium grain boundaries are formed. By assuming a specific potential energy function for the non-equilibrium atoms at the grain boundary sites, the attractive forces between atoms are greater than the repulsive forces and a tensile results as the atoms find equilibrium

positions. The Hoffman argument has been reinterpreted using a simple model diagramed in Fig. 4-12 [Nix 99, Freu 01, Shel 01]. The growing islands are represented by a periodic array of square parallelepipeds with thickness h and diameter d with inter-island spacing of distance α. As the growing island approach each other and α reaches a critical value, the islands will strain an amount α/d to create one grain boundary with energy γ_{gb} for every two surfaces with energy γ_s. The change in energy per island is the sum of the change in interface energy plus the change in strain energy:

$$\Delta E_{island} = \frac{1}{2}(\gamma_{gb} - 2\gamma_s)(4hd) + \left(\frac{E}{1-\nu}\right)\frac{\alpha^2}{d^2}(h\,d^2), \tag{4.12}$$

where $E/(1-\nu)$ is the biaxial modulus of the film, and the ½ in front of the first term on the right hand sides of the equation is necessary because one-half of the interface energy is associated with each of the islands. The critical value of the inter-island spacing α can be

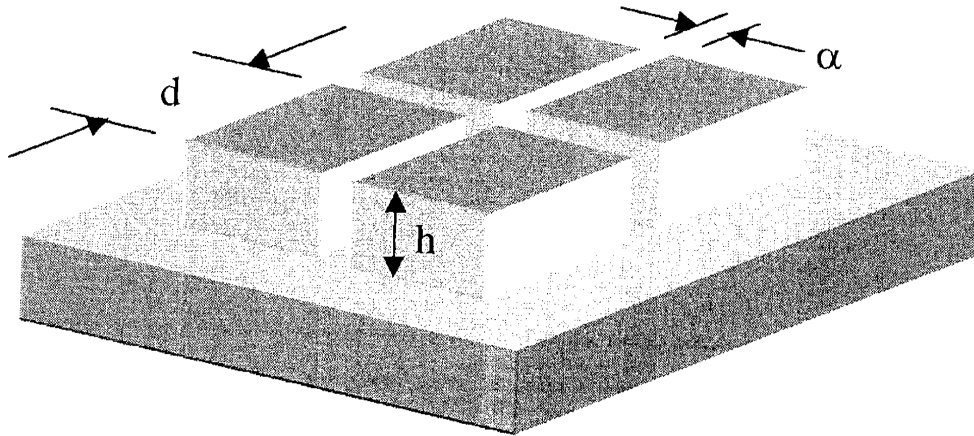

Figure 4-12: Schematic diagram of a regular array of square parallelpiped islands of thickness h and diameter d on a substrate, each separated by a distance α from its neighbors. When the islands grow to within a critical distance of each other, the separation gap is closed by deforming the islands and a tensile stress is generated in the film.

solved by setting ΔE_{island} in Eq. 4.12 equal to zero. By using the critical value of α, the resulting biaxial stress in the film σ is given by:

$$\sigma = \frac{E}{1-\nu}\frac{\alpha}{d} = \left[\frac{E}{1-\nu}\frac{(2\gamma_s - \gamma_{gb})}{r}\right]^{1/2}, \tag{4.13}$$

where r is one-half of the island diameter d. Using typical values for $E/(1-\nu)$ of 100 GPa, γ_s of 2 J/m^2 and γ_{gb} of 1 J/m^2, and grain sizes r in the range of 10-100 nm, the resulting stresses are in the range of 2-5 GPa. This model predicts tensile stresses that are significantly higher than those observed in experiments partly due to the oversimplification of the island geometry shown in Fig. 4-12. One intrinsic shortcoming of this model geometry is that some degree of sliding must occur along the island-substrate interface in order for the islands to stretch across the island gap α. However, the presence of sliding at the island-substrate interface would also allow stress relaxation in the film.

4.4.3 Nix-Clemens model

Nix and Clemens considered a more realistic geometry consisting of an array of two-dimensional islands with hemicylindrical shapes that coalesce to form a surface with a cycloid shape, as shown in Fig. 4-13. The cusps at the surface of the islands were treated like cracks that allowed for a crack-like analysis similar to the Griffith criterion [Nix 99]. Crack closure stops when the strain energy generation per unit crack length G balances the associated decreases in interfacial energy given by $2\gamma_s - \gamma_{gb}$. The strain energy generation per unit crack length G can be calculated for a plane strain crack as $G=(1-\nu^2)K^2/E$, where K is the stress intensity factor. For a cycloid surface with a periodic array of surface cusps under a uniform tensile stress σ, the stress intensity factor K is given by $\sigma(\lambda/2)^{1/2}$ where λ is the periodic cusp spacing [Chiu 93]. Nix and Clemens used a similar expression to described the cycloid surface of the coalesced islands so that $K= \langle\sigma\rangle r^{1/2}/(1+\nu)$ where $\langle\sigma\rangle$ is the average stress in the island, r is the island radius, and ν

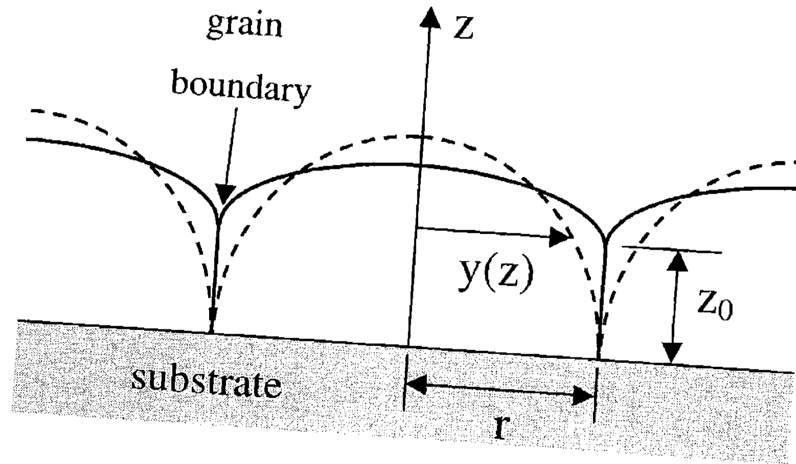

Figure 4-13: (a) Schematic of the island coalescence process resulting in tensile stress generation. The dashed lines represent the hemicylindrical islands at impingement, while the solid lines represents the deformed surface of the island after coalescence through grain boundary zipping to a height z_0.

is the Poisson ratio of the film. By substitution and rearrangement of the equations above, the average stress resulting from the crack closure process (i.e. island zipping) can be solved as:

$$\langle\sigma\rangle = \left[\left(\frac{1+\nu}{1-\nu}\right)E\frac{2\gamma_s-\gamma_{gb}}{r}\right]^{1/2}, \tag{4.14}$$

which is very similar in form to Eq. 4.13 using the simplified Hoffman model for island coalescence. The height of the grain boundary resulting from coalescence is called the zipping distance or z_0. The equilibrium zipping height $z_{0,eq}$ for a hemicylindrical island was given by an approximate expression:

$$z_{0,eq} = \left[\frac{36(1-\nu)(1+\nu)^3(2\gamma_s-\gamma_{gb})}{E}\right]^{1/4} r^{3/4}. \tag{4.15}$$

Using typical values for $E/(1-\nu)$= 100 GPa, ν= 1/3, γ_s= 2 J/m^2, γ_{gb}= 1 J/m^2, and grain sizes r in the range of 10-100 nm, the resulting stress using this model are in the range of 2-6 GPa, which are significantly higher than those observed experimentally. As mentioned by Freund and Chason, the inaccuracy of the model stems from an assumptions in the analysis for the behavior of coalescing islands [Freu 01]. In the Nix-Clemens analysis, a Griffith condition is applied to determine a critical average stress in the island at which the strain energy generated by forming additional grain boundary balances the reduction in interfacial energy. The reduction in interfacial energy per unit increase in grain boundary length is a constant. However, the strain generation per unit increase in grain boundary length is *not* constant. The strain required to create additional grain boundary length increases with increasing zipping height since the gap between the islands increases in the z-direction. Therefore, a global energy balance of the zipping process must be considered because of the changing stress conditions with formation of grain boundary.

4.4.4 Approximate analytical model of grain boundary zipping

An approximate model of the stress resulting from the zipping process can be derived by considering a global energy balance using the same island geometry as considered in the Nix-Clemens model, as shown in Fig. 4-13. Impingement occurs between two infinitely long cylinders with semicircular cross sections of radius r that form grain boundary along their length to a zipping height z_0. The equation for a circle with reference to the coordinate system given in Fig. 4-13 is given by:

$$y(z) = r\sqrt{1-(z/r)^2}, \qquad (4.16)$$

so that the average in-plane strain ε_y as a function of height z is given approximately by:

$$\varepsilon_y(z) = \frac{r - y(z)}{r} = 1 - \sqrt{1-\left(\frac{z}{r}\right)^2} \approx \frac{1}{2}\left(\frac{z}{r}\right)^2. \qquad (4.17)$$

For the plane strain geometry, $\varepsilon_{xy}=\varepsilon_{xz}=\varepsilon_{xx}= 0$, and since the top surface of the island is unconstrained, σ_{zz} is assumed to be small. The shear components ε_{yz} and σ_{yz} are non-zero, but considered negligible in the following calculation. For the plain strain geometry, the in-plane strain ε_y is given by:

$$\varepsilon_y = \frac{1}{E}\left[\left(1-\nu^2\right)\sigma_y - \nu\left(1-\nu\right)\sigma_z\right] \approx \frac{1-\nu^2}{E}\sigma_y . \tag{4.18}$$

The strain energy density is also a function of the height in the z-direction and is approximately equal to ½ $\sigma_y(z)\varepsilon_y(z)$, where only the contribution from the in-plane stress and strain are considered. After zipping and forming grain boundary along the length of the island to a height z_0, the volume of the continuous portion of the island per unit length (i.e. cross-sectional area) can be approximated as $2rz_0$. Therefore, the total strain energy per unit length E_ε in the continuous portion of the island can be estimated as:

$$\begin{aligned} E_\varepsilon &= \frac{1}{2}\int_0^{z_0}(2r)\sigma_y\varepsilon_y dz = r\frac{E}{1-\nu^2}\int_0^{z_0}\left[\frac{1}{2}\left(\frac{z}{r}\right)^2\right]^2 dz \\ E_\varepsilon &= \frac{1}{20}\frac{E}{1-\nu^2}\frac{z_0^5}{r^3} \end{aligned} \tag{4.19}$$

The interfacial energy reduction per island per unit length $E\gamma$ due to island zipping is given by $E_\gamma = (2\gamma_s-\gamma_{gb})z_0$. Therefore, the total energy resulting from the zipping process is given by:

$$E_{tot} = E_\varepsilon - E_\gamma = \frac{1}{20}\frac{E}{1-\nu^2}\frac{z_0^5}{r^3} - \left(2\gamma_s - \gamma_{gb}\right)z_0 . \tag{4.20}$$

The energy minimizing zipping distance $z_{0,eq}$ can be solved by setting dE_{tot}/dz_0 equal to zero so that:

$$z_{0,eq} = \left[4\frac{1-\nu^2}{E}\left(2\gamma_s - \gamma_{gb}\right)\right]^{1/4} r^{3/4} , \tag{4.21}$$

which is very similar in form to Eq. 4.15 from the Nix-Clemens model but *smaller* by exactly a factor of two when using ν=1/3. In addition, approximations made in this analysis to simplify the algebra tend to result in an underestimation of the strain energy in the island, which would result in an overestimation of $z_{0,eq}$. For instance, the contributions to the strain energy due to the shear and the film normal stress components have been ignored in this analysis. Another important factor to consider is that average in-plane stresses and strains were used to calculate the strain energy in the island. In reality, the strains are larger than the average near the grain boundary and smaller than the average towards the center of the grain. The large strains near the grain boundary contribute significantly to the total strain energy of the island, and therefore using average stresses and strain would tend to underestimate the strain energy. Finally, only the strain energy in the continuous portion of the island was considered in the calculation. The top portion of the island above z_0 is continuous with the underlying material and would experience tensile strains due to the zipping process that contribute to the strain energy in the island. Therefore, the analytical model above over predicts $z_{0,eq}$ because of an underestimation of the strain energy in the island due to grain boundary formation.

The average tensile stress in the continuous portion of the film can be estimated as [Nix 99]:

$$\begin{aligned}\langle\sigma\rangle &= \frac{E}{1-\nu^2}\frac{1}{z_0}\int_0^{z_0}\varepsilon(z)dz = \frac{E}{1-\nu^2}\frac{1}{z_0}\int_0^{z_0}\frac{1}{2}\left(\frac{z}{r}\right)^2 dz \\ \langle\sigma\rangle &\approx \frac{E}{1-\nu^2}\frac{1}{6}\left(\frac{z_0}{r}\right)^2\end{aligned} \tag{4.22}$$

The equilibrium average stress in the continuous portion of the film can be calculated using the equilibrium zipping height $z_{0,eq}$ from Eq. 4.21:

$$\langle\sigma\rangle = \left[\frac{1}{9}\left(\frac{E}{1-\nu^2}\right)\frac{(2\gamma_s-\gamma_{gb})}{r}\right]^{1/2} \tag{4.23}$$

which is very similar in form to Eq. 4.14 from the Nix-Clemens model but *smaller* by exactly a factor of four when using ν=1/3. Using typical values for $E/(1-\nu)$= 100 GPa, ν= 1/3, γ_s= 2 J/m^2, γ_{gb}= 1 J/m^2, and grain sizes r in the range of 10-100 nm, the resulting stress using this model are in the range of 0.5-1.5 GPa, which are more similar to experimentally observed stress levels than those predicted by the Nix-Clemens model.

The assumptions in the analytical model tend to result in an overestimation of the magnitude of the stress due to the grain boundary zipping process. As stated earlier, the assumptions used to calculate the equilibrium zipping height in the analytical model overestimate the value of $z_{0,eq}$. From Eq. 4.22, an overestimation of $z_{0,eq}$ would result in a larger than expected stress due to grain boundary zipping. In addition, the stress calculated using Eq. 4.23 was derived by averaging over the continuous portion of the film up to a height z_0 and ignores the volume of material above z_0. Due to continuity between the island cap and the continuous film, the portion of the film above z_0 will experience strain, albeit less than those in the continuous portion of the film. Therefore, the calculated stress in the island would be smaller if averaged over the entire island.

4.4.5 Finite element comparison to analytical models

4.4.5.1 Plane strain model of island coalescence

The accuracy of the Nix-Clemens model and the analytical approach detailed in section 4.4.4 were examined by performing finite element method (FEM) calculations using the commercial software ADINA [Seel 00]. An island is represented by a two-dimensional element under plane strain conditions and with perfect traction at the island-substrate interface, as shown in Fig. 4-14. The plane strain conditions implies that impingement is occurring between two infinitely long hemicylinders, similar to the Nix-Clemens model geometry. A series of displacements were imposed along the surface to a height z_0 to mimic the zipping process. For a given island radius, the positive strain energy from the FEM modeling and the associated reduction in interfacial energy were calculated as a function of the zipping distance. The sum of these two energies represents the change in energy of the system and the negative-valued minimum corresponds to the equilibrium value of the zipping distance. Because the FEM results are used later for

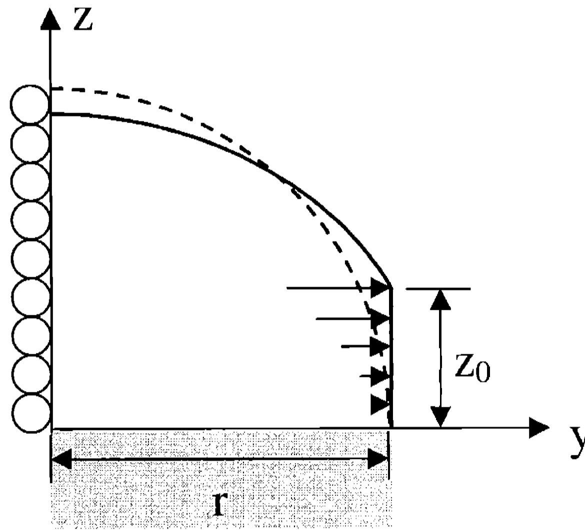

Figure 4-14: Finite element model of island coalescence represented by a two-dimensional element under plane strain conditions. The *y*-axis represents the island-substrate interface where traction was imposed. The *z*-axis is an axis of mirror symmetry along which sliding was allowed. The arrowed lines are the series of displacement that represent zipping to a height z_0 of an island of radius *r*.

comparison with experimental data, material constants for Ag were used in the calculation using values shown in Table 4-1. The equilibrium zipping distance $z_{0,eq}$ and average stress versus island radius from the FEM modeling are shown in Fig. 4-15, along with the predictions from the Nix-Clemens model and the analytical model derived in section 4.4.4. From the FEM model, $z_{0,eq}$ decreases with the island radius raised to the 0.675 power, compared to the 0.75 dependence in both the Nix-Clemens model and analytical model. The FEM calculations yield an average stress with an exponential dependence of –0.814 on the island radius, compared to the inverse square root dependence in both the Nix-Clemens model and analytical model.

The FEM model of island coalescence uses the same physical model of island zipping as the Nix-Clemens model and the analytical model of section 4.4.4, however the finite element method produces straightforward numerical solutions for the tensile stress

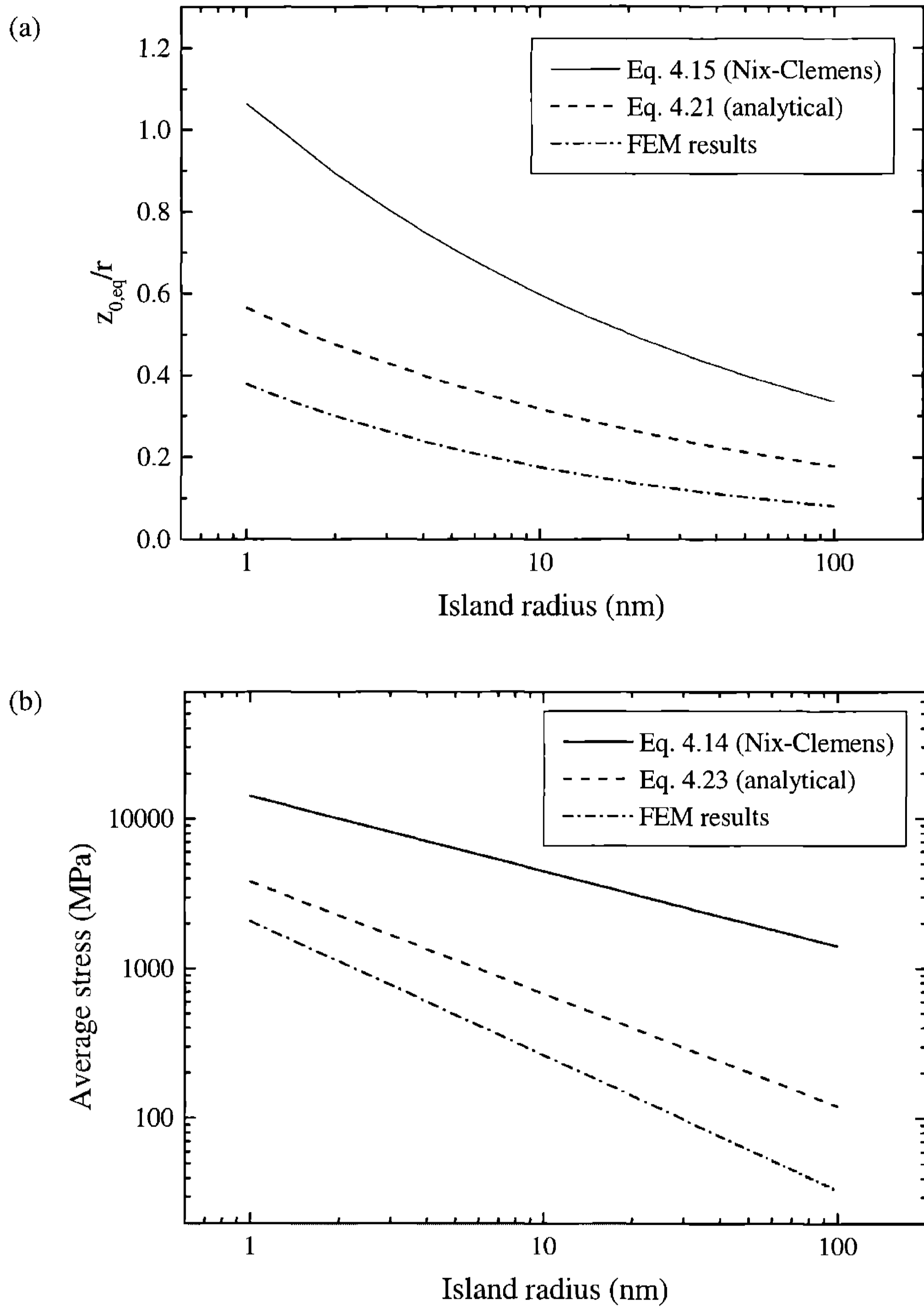

Figure 4-15: Comparison of the FEM calculations with results from the Nix-Clemens model and the analytical model in section 4.4.4, showing (a) the equilibrium zipping distance $z_{0,eq}$ divided by the island radius r, and (b) the average stress as a function of island radius.

Material	Youngs Modulus, E (GPa)	Poisson Ratio, ν	Surface Energy, γ_s (J/m^2)	Grain Boundary Energy, γ_{gb} (J/m^2)
Ag	87.3	0.354	1.50	0.470
Al	70.8	0.348	1.15	0.375
Cu	127.7	0.340	2.23	0.715

Table 4-1: Selected materials properties for Ag, Al and Cu at room temperature. The Young's modulus and Poisson ratio are from Simmons and Wang [Simm 1971] and the surface and grain boundary energy are from Murr [Murr 75].

generation due to island zipping. The FEM results predict stresses that are more consistent with experimental observations than the extremely large stresses predicted by the Nix-Clemens model. In addition, the FEM results confirm that the simplified analytical model derived in section 4.4.4 tends to overestimate both the equilibrium zipping distance and the tensile stress resulting from the island zipping process. However even acknowledging that the analytical model overestimates the average stress, it still predicts stresses closer to the FEM results than those of the Nix-Clemens model.

4.4.5.2 Axisymmetric representation of island coalescence

A potentially more accurate representation of the geometry of island coalescence uses an axially symmetric coalescence analogous to contacting two spheres with cohesive forces between them, as shown in Fig. 4-16(a). It should be noted that the axisymmetric representation conflicts with the boundary conditions of perfect traction at the island-substrate interface. The islands attempt to zip towards each other in the plane of the substrate but are prevented from doing so by the traction with the substrate. If the constraint of the substrate is assumed to be negligible, then contacting sphere can be thought of as analogous to contact hemispheres on a substrate as shown in Fig 4-16(b). Freund and Chason have modeled island zipping for a two-dimensional array of hemispherical island using Hertz contact theory with cohesive attraction [Freu 01]. The calculated average stress in the hemispheres due to island coalescence is given by:

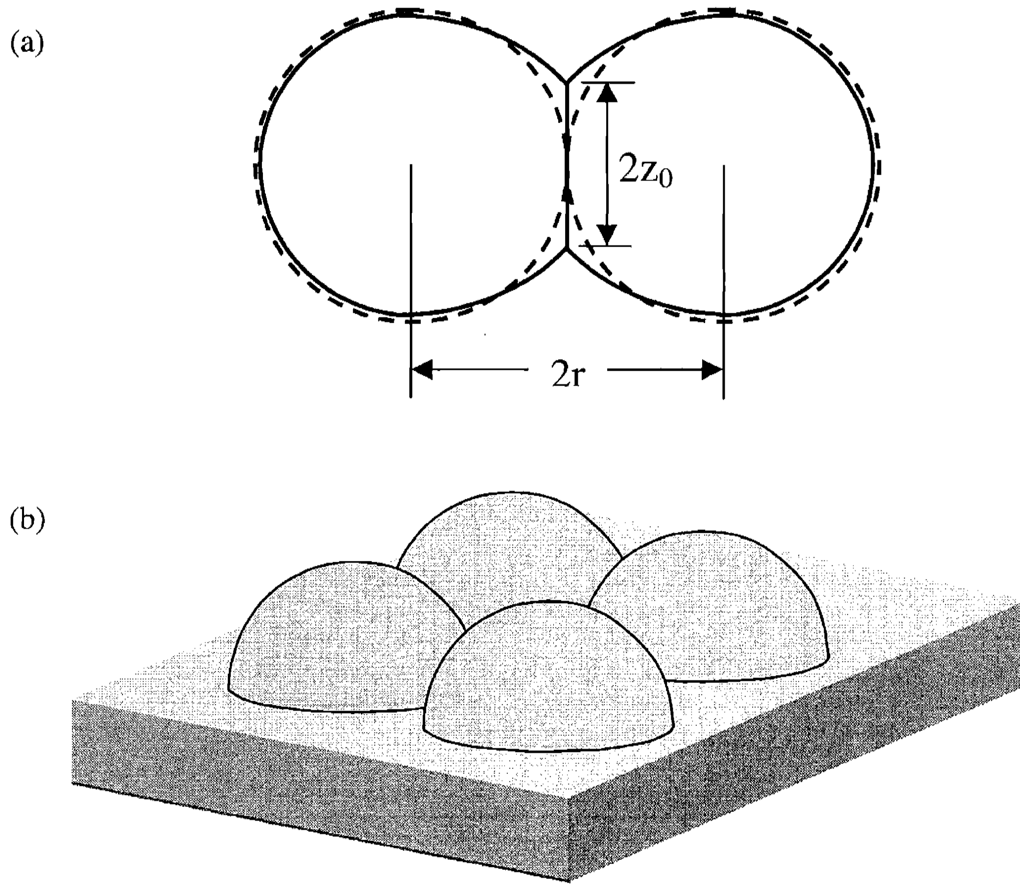

Figure 4-16: (a) Contacting of two identical spheres of radius r with cohesive attraction between them. The center of each sphere is constrained not to move. The contact area between the spheres has radius z_0. (b) Hemispherical islands impinging with their neighbors in analogy to the case of contacting two spheres.

$$\sigma = \frac{2(2\gamma_s - \gamma_{gb})}{r}, \tag{4.24}$$

which surprisingly is independent of the elastic properties of the islands. Using typical values for γ_s= 2 J/m^2, γ_{gb}= 1 J/m^2, and grain sizes r in the range of 10-100 nm, the resulting stress using this model are in the range of 100-1000 MPa. An analytical expression is given for the radius of the contact area z_0, which is analogous to the equilibrium zipping height $z_{0,eq}$:

$$z_{0,eq} = \left[4\pi \frac{1-\nu^2}{E} \left(2\gamma_s - \gamma_{gb} \right) \right]^{1/3} r^{2/3}. \tag{4.25}$$

The accuracy of the Freund-Chason model was examined by performing finite element method (FEM) calculations using the commercial software ADINA. An axisymmetric element was used to represent the impinging spheres, shown in Fig. 4-16(a). The centers of the sphere are constrained to be fixed and a series of displacements were imposed along the surface to a height z_0 to mimic the zipping process. The material constants for Ag were used in the calculation for values shown in Table 4-1. The equilibrium zipping distance $z_{0,eq}$ and average stress versus island radius from the FEM calculations are shown in Fig. 4-17, along with the analytical predictions of the Freund-Chason model. From the FEM model, $z_{0,eq}$ decreases with the island radius raised to the 0.63 power, compared to the 2/3 dependence in the Freund-Chason model. The FEM calculations yield an average stress with an exponential dependence of –0.97 on the island radius, compared to the inverse radial dependence in the Freund-Chason model.

The radial dependence of both $z_{0,eq}$ and the average stress agree well between the FEM results and the Freund-Chason model. The models agree in magnitude within a factor of two as seen in Fig. 4-17, however the origin of the discrepancy is unknown. Perhaps the specific choice of displacements used to represent the zipping process in the FEM calculations is not the optimal path by which to create a grain boundary of height z_0 (i.e. do not minimize the strain energy generation). Note that the average stress calculated by FEM for both the axisymmetric geometry and the plane strain geometry considered in section 4.3.5.1 are very similar in magnitude.

4.4.5.3 Influence of island contact angle on tensile stress generation

The contact angle between the island surface and the substrate has a strong influence on the magnitude of the stress resulting from island coalescence. Consider an array of two-dimensional cylindrical cap islands with radius of curvature R, in-plane radius r and contact angle θ as shown in Fig. 4-18. Using the finite element package

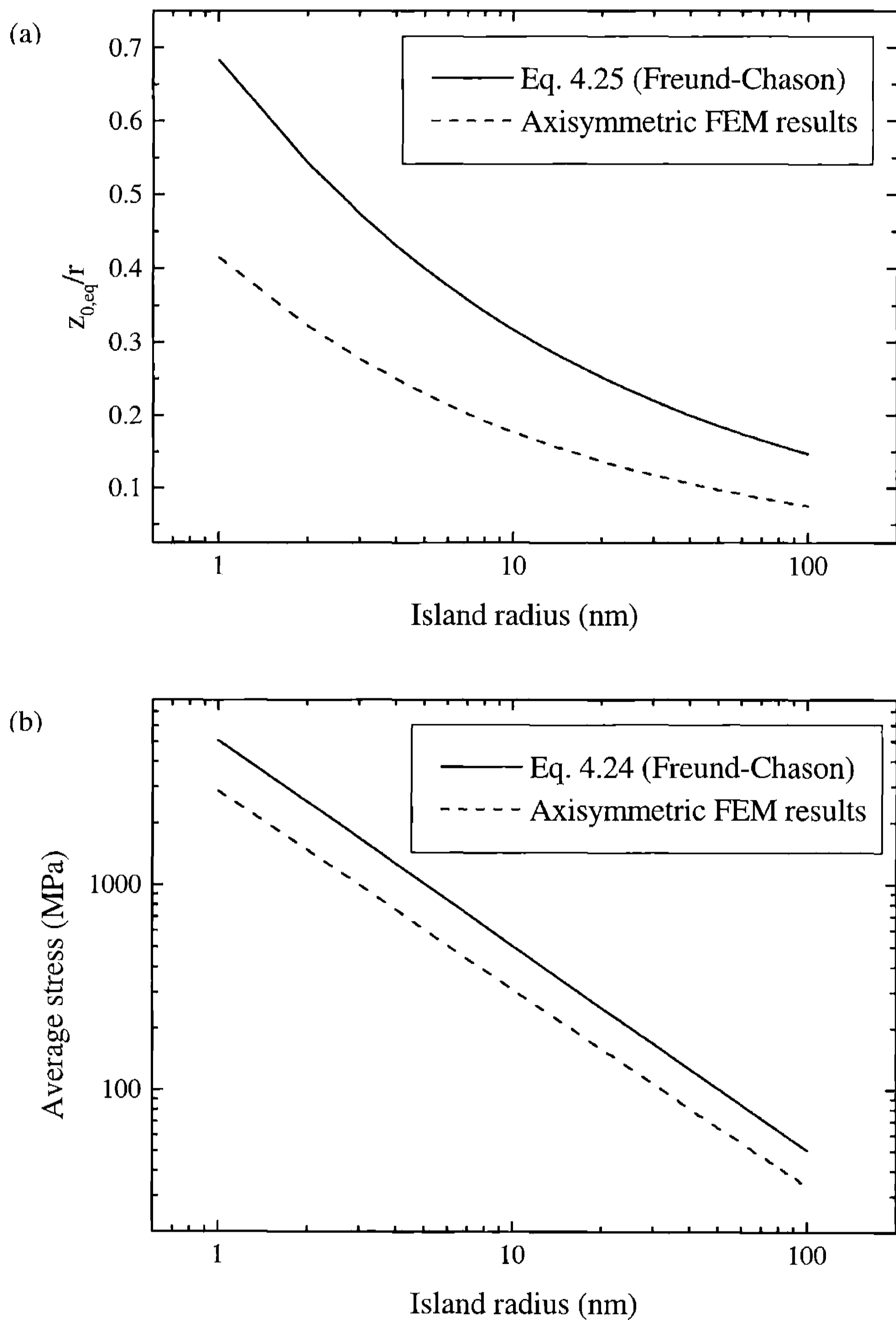

Figure 4-17: Comparison of the axisymmetric FEM calculations with results from the Freund-Chason model, showing (a) the equilibrium zipping distance $z_{0,eq}$ divided by the island radius r, and (b) the average stress as a function of the island radius.

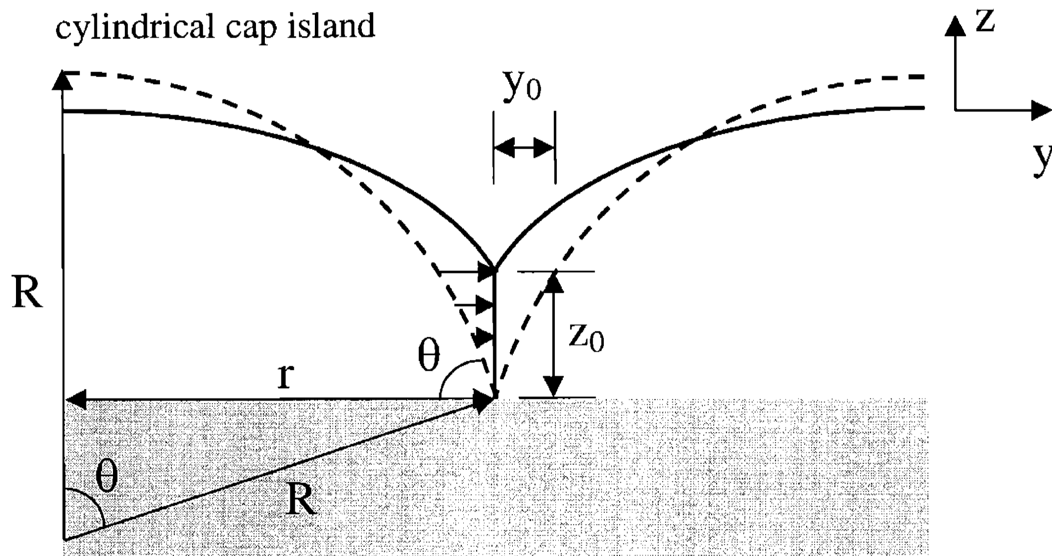

Figure 4-18: Schematic of impingement between identical cylindrical cap islands with contact angle θ. An island was represented in finite element modeling by a two-dimensional element under plane strain conditions with perfect traction at the island-substrate interface. A series of displacements were imposed along the surface to a height z_0 to mimic the zipping process.

ADINA, an island was represented by a two-dimensional element under plane strain conditions with perfect traction at the island-substrate interface. The plane strain conditions imposed in the yz-plane implies that impingement is occurring between two infinitely long cylinders with circular cap cross sections. The material constants for Ag were used in the calculation for values shown in Table 4-1. The equilibrium zipping distance $z_{0,eq}$ and average stress versus island radius and contact angle from the FEM calculations are shown in Fig. 4-19.

For a given value of z_0, the magnitude of the decrease in interfacial energy per unit length of grain boundary is independent of the contact angle and equal to $(2\gamma_s-\gamma_{gb})\, z_0$. However, the amount of strain required to close the gap between islands to a height z_0 increases with decreasing contact angle (see Fig. 4-18). Since the strain energy increases quickly as a function of z_0 for a smaller contact angle, the equilibrium zipping distance

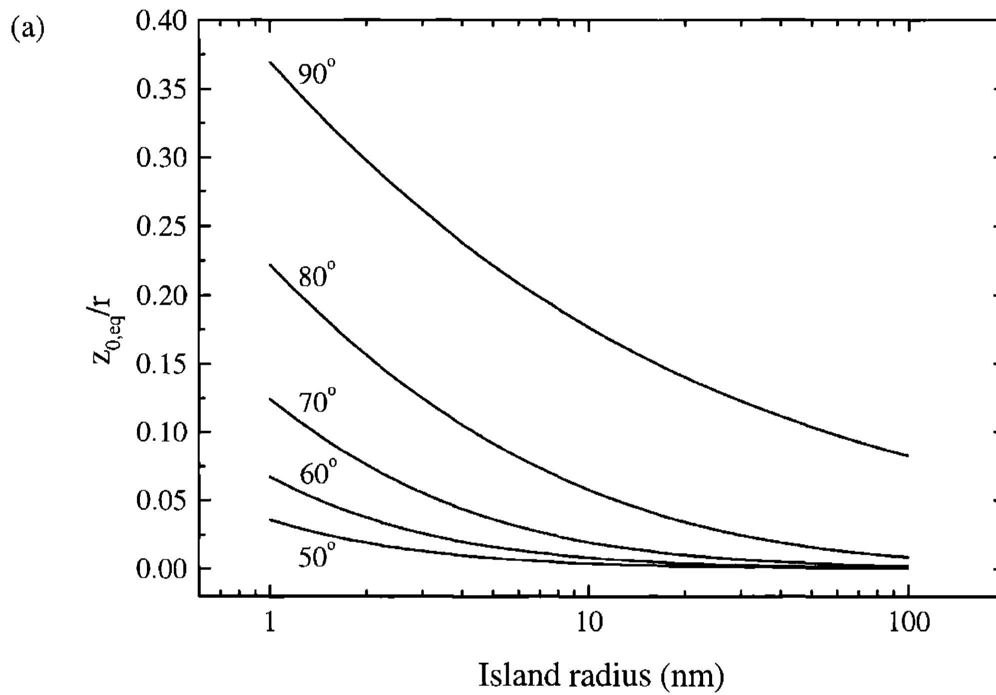

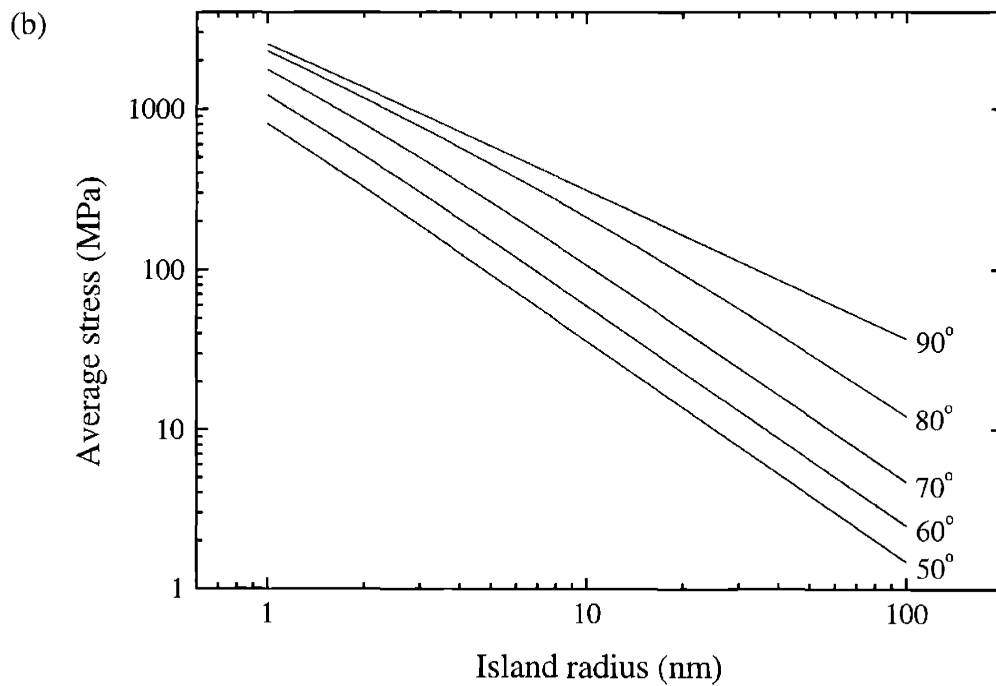

Figure 4-19: Finite element calculation of the tensile stress generation resulting from island coalescence for different contact angles showing (a) the equilibrium zipping distance $z_{0,eq}$ divided by the island radius r, and (b) the average stress as a function of the island radius.

$z_{0,eq}$ for a given island radius is smaller for decreasing contact angle, as shown in Fig. 4-19(a). The intuition for the smaller average stress as a function of contact angle, shown in Fig. 4-19(b), is similar.

Unfortunately, simple analytical expressions for the equilibrium zipping distance $z_{0,eq}$ and average stress resulting from island zipping, similar to Eqs. 4.21 and 4.23 for a hemicylindrical island, could not be derived for the cylindrical cap island geometry. For the cylindrical cap geometry, the expression for the total energy, similar to Eq. 4.20, is a fourth-order polynomial with cumbersome solutions. However, empirical fits to the FEM results provide fortuitously simple expressions for the strain energy and average stress as a function of the zipping distance. Rather than the zipping height z_0, the more useful variable to consider is y_0, the in-plane zipping distance as defined in Fig. 4-18. Provided that $y_0/r << 1$, the *total* strain energy resulting from zipping an amount y_0 is independent of the contact angle and the island radius, as shown in Fig. 4-20(a), and approximately given by $E_\varepsilon = \frac{1}{2} E y_0^2$. Therefore, the total energy per island per unit length of grain boundary resulting from island coalescence is approximately:

$$
\begin{aligned}
E_{tot} &= \frac{1}{2} E\, y_0^2 - (2\gamma_s - \gamma_{gb}) z_0 \\
E_{tot}(y_0) &= \frac{1}{2} E\, y_0^2 - (2\gamma_s - \gamma_{gb}) \left(\sqrt{\frac{r^2}{\sin^2\theta} - (r - y_0)^2} + r\frac{\cos\theta}{\sin\theta} \right),
\end{aligned}
\tag{4.26}
$$

where E is the Young's modulus of the island material. The equilibrium in-plane zipping distance $y_{0,eq}$ can be solved numerically by determining the energy minimizing y_0. The empirical expression for the in-plane strain as a function of y_0 is also independent of the contact angle, as shown in Fig. 4.20(b). The empirical expressions exists for the average in-plane strain ε_{yy} and stress σ_{yy} resulting from island coalescence are given by:

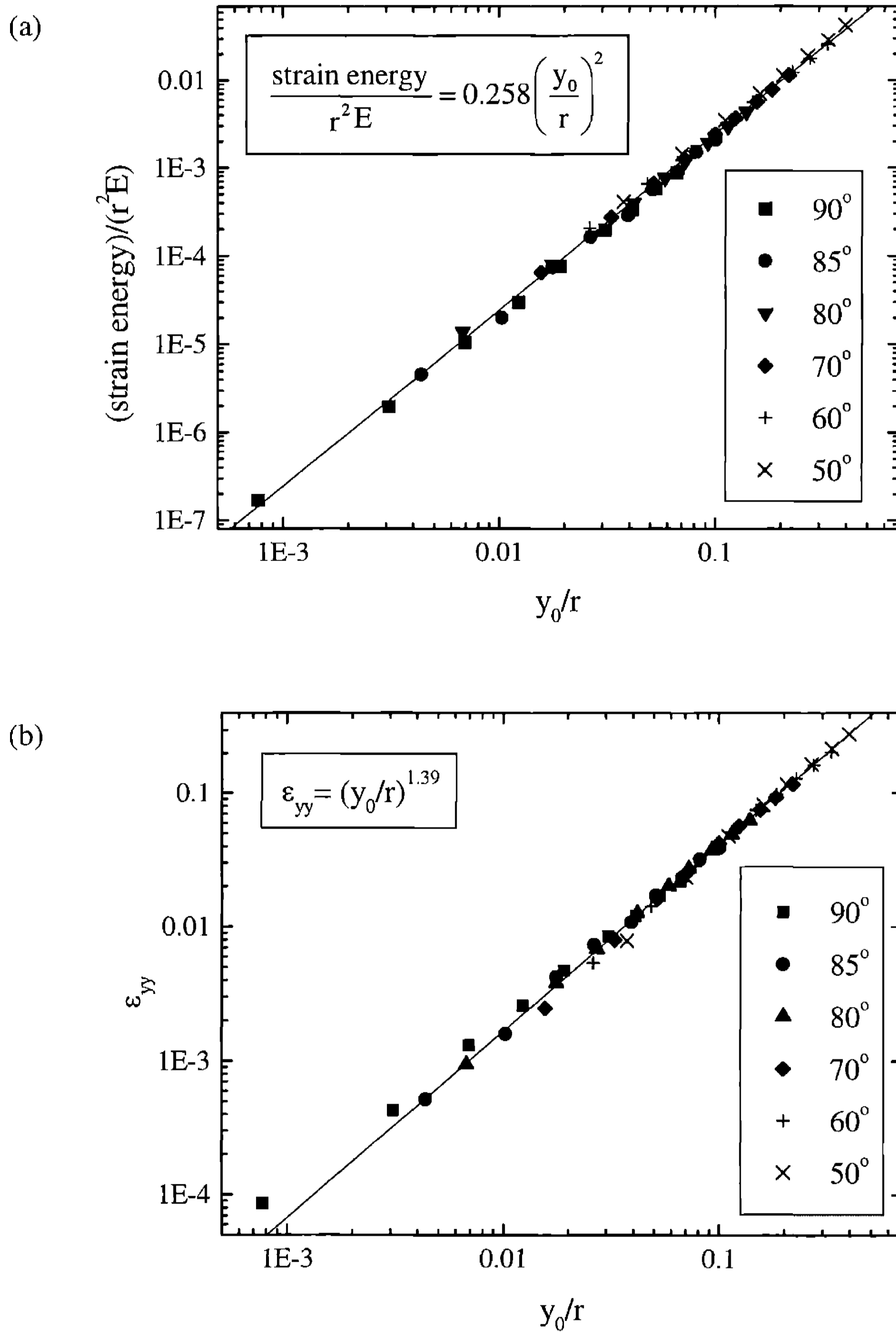

Figure 4.20: Finite element calculations for island zipping with different contact angles showing (a) strain energy as a function of the in-plane zipping distance y_0 divided by the island radius r, and (b) in-plane strain as a function of y_0/r.

$$\varepsilon_{yy} = \left(\frac{y_0}{r}\right)^{1.4}$$

$$\sigma_{yy} = \frac{E}{1-\nu^2}\left(\frac{y_0}{r}\right)^{1.4} \tag{4.27}$$

where ν is the Poisson ratio of the film material. The empirical expressions from Eqs. 4.26 and 4.27 are utilized in the thin film growth simulation to calculate island coalescence stresses as discussed in section 4.4.6.

4.4.5.4 Influence of sliding on tensile stress generation

During the growth of a real film, impingement does not occur simultaneously within a periodic array of islands as assumed in the models. At low substrate coverage, island impingement will typically involve only two islands that have not yet impinged with any other islands. To model the first coalescence of an island using FEM, an island was represented as a plane strain, two-dimensional element with either traction at the island-substrate interface [island (i) in Fig. 4-21(a)] or with sliding at the island-substrate interface [island (iii) in Fig. 4-21(b)]. The zipping due to the single coalescence was represented by displacements imposed along only one side of the island. The equilibrium zipping distance [Fig. 4-22(a)] and average stress [Fig. 4-22(b)] versus island radius resulting from a single coalescence are shown for both the cases of traction and sliding at the island-substrate interface. If traction was imposed at the substrate, the coalescing island stretched towards the forming grain boundary to eliminate part of its surface. Since island movement was constrained due to traction, tensile stresses were generated in the island. If sliding was allowed along the substrate, the island moved its center towards the forming grain boundary during zipping, resulting in a very small, compressive mean stress. However, without traction, no load transfer between the island and substrate can occur, so the stress will not results in a measurable substrate curvature.

At higher substrate coverage, an impinging island most likely will have already coalesced with other islands forming what will be referred to as an island cluster. The second coalescence of an island was modeled using a plane strain element with one edge

(a) island-substrate traction

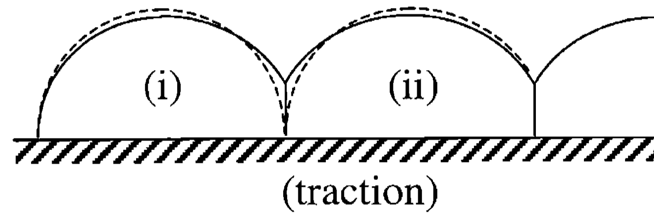

(b) island-substrate sliding

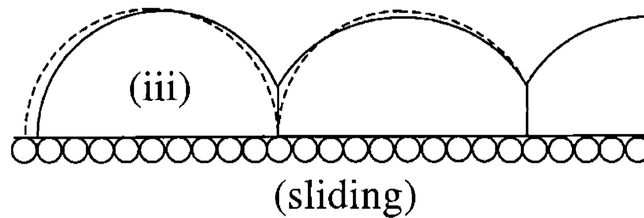

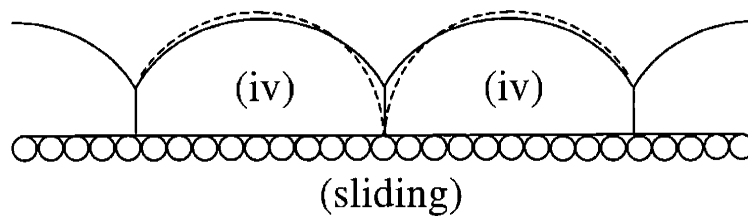

Figure 4-21: Schematic of island coalescence showing (a) the (i) first, and (ii) second coalescence of an island with traction at the island-substrate interface. (b) Island coalescence with sliding at the island-substrate interface for the (iii) first, and (iv) second coalescence of an island. In case (iv), the impinging islands are already part of a larger island cluster which inhibits island sliding.

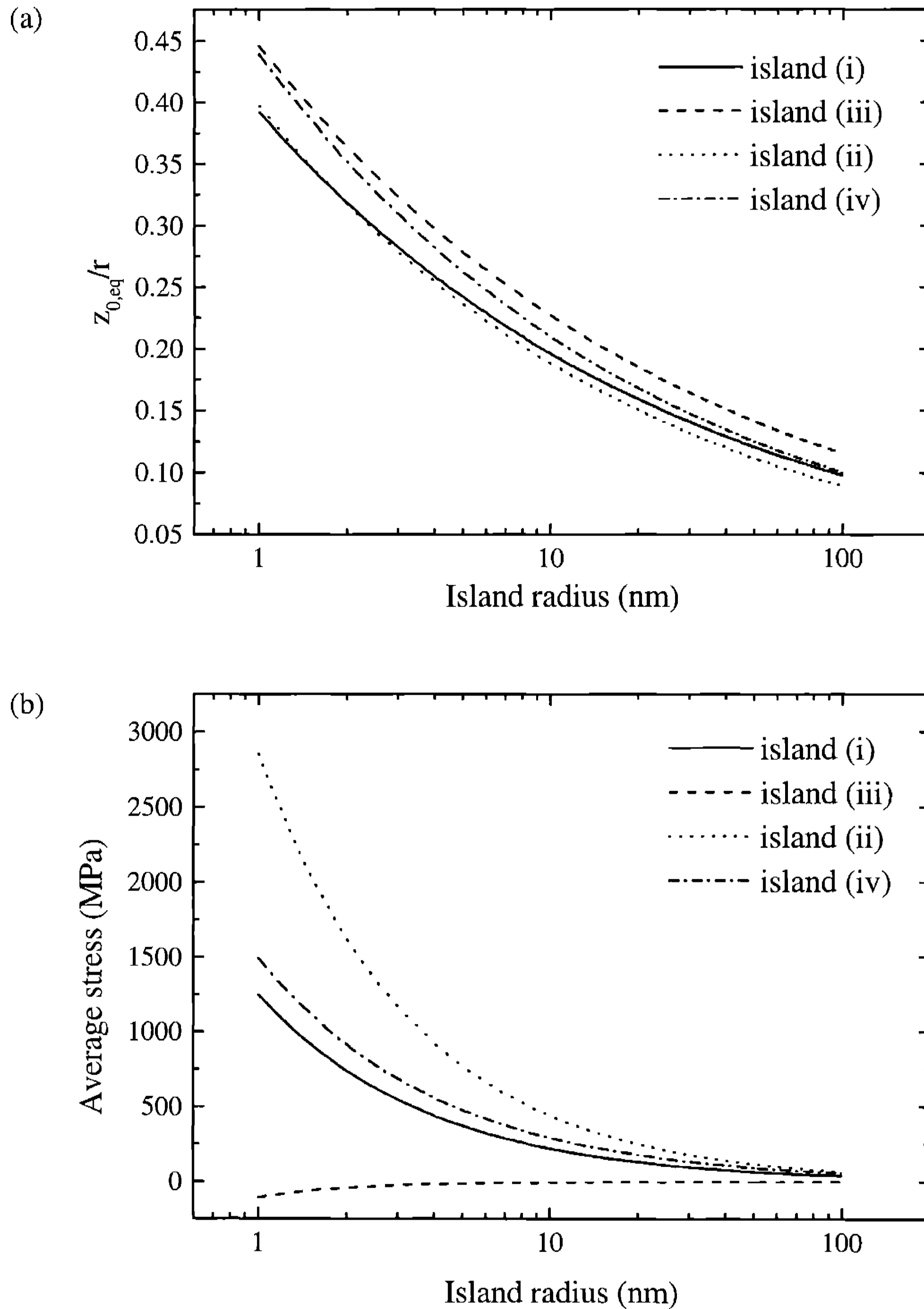

Figure 4-22: (a) The equilibrium zipping distance z_0 divided by the island radius r and (b) the average stress as a function of the island radius from FEM modeling of a two-dimensional element under plane strain conditions for the cases shown in Fig. 4-21.

pinned and displacements imposed along the opposite edge to mimic zipping to a height z_0. For the case with traction at the island-substrate interface, the second coalescence [see island (ii) in Fig. 4-21(a)] approximately doubled the average stress in the island, as shown in Fig. 4-22(b). If sliding at the island-substrate interface is allowed, the consequence of subsequent impingements is less obvious. If the entire island cluster is able to slide, then island coalescence will result in a slightly compressive stress, as shown previously. However, sliding of an island may become inhibited after a few coalescence events, as discussed in the following paragraph. If sliding is allowed along the island-substrate interface but is constrained along the opposite edge [see island (iv) in Fig. 4-21(b)], the second coalescence generates tensile stresses similar in magnitude to the first coalescence of an island with traction, as shown in Fig. 4-22(b).

The mechanism responsible for island sliding must be examined more closely to understand how load transfer between the film and substrate can occur even with interface sliding. When islands coalesce, large shear stresses are generated near the grain boundary due to the displacements resulting from zipping. These shear stresses can drive the movement of dislocation-like entities along the film-substrate interface away form the grain boundary [Gao 99]. Island sliding will result if the "dislocation" can travel across the entire island. As the substrate coverage increases, most islands have coalesced with other islands. The movement of the dislocation-like entities across the entire island will be opposed by shear stresses from previous coalescence events. Consequently, sliding of an island will become inhibited after the island has coalesced with other islands. If island sliding is inhibited, subsequent coalescence of an island will generate tensile stress in the film, as shown in Fig. 4-22(b). Since traction now exists between the island and substrate, the tensile stress generation will result in substrate curvature. If perfect sliding occurs at the island-substrate interface, no load transfer can occur between the film and substrate and consequently no substrate curvature will be measured.

4.4.6 Tensile stress model comparison with stress measurements

4.4.6.1 Application of tensile stress models in film growth simulation

Modifications to the idealized geometry of the tensile stress models must be made to utilize them for calculating stress resulting from island coalescence within the realistic

microstructure in the simulation. The plane-strain FEM results with variable island-substrate contact angle (see section 4.4.5.3) is the basis for the stress calculations in the simulation. The FEM calculations assume a plane-strain geometry so that impingement occurs between infinitely long cylinders with contact angle θ between the island and substrate surface. In a real microstructure, islands are better represented by spherical caps with contact angle θ. Fortunately, the plane-strain geometry and axisymmetric geometry give quantitatively similar results for the stress resulting from island coalescence(see Figs. 4-15 and 4-17), so that the plane-strain FEM results can be used with confidence for the spherical-cap islands in the simulation.

During deposition, islands with different radii impinge and behave differently than the symmetric geometry considered in the models. The energy minimizing z_0 is determined for the coalescence of islands with dissimilar sizes using the FEM calculations of strain energy (see Eq. 4.26). The boundary of the smaller island will zip more than if it had coalesced with an island of the same size. Consequently, the stress in a smaller island impinging with a larger island is greater than if it had coalesced with an island of the same size. The opposite trends are true for the larger island. The tensile stress that results from island coalescence is directional and the components of the stress in the in-plane directions contribute to the average equibiaxial stress in the film.

During the late stages of film growth, each island has coalesced with several other islands. In the simulation for each new coalescence of an island, the average stress calculated using the FEM results was simply added to any existing stress in the island. The principle of superposition states that two strains may be combined by direct superposition, with the order of application having no effect on the final strain of the body. However, for subsequent coalescence events, the calculation of the strain energy, used to determine the equilibrium zipping distance and the corresponding stress, neglected the existing stress in the island. For the first few coalescence, this approximation is valid because typically the stress fields do not overlap significantly since the stress as a function of position decays exponentially away from the grain boundary formed by coalescence. However as the film approaches continuity, the pre-exiting stress within the island will inhibit island zipping since increasing the tensile stress in the island will dramatically increase the total strain energy. Therefore, ignoring

the pre-existing stress in the islands resulted is an overestimation of the island-coalescence stress in the simulation.

Once coalescence between two islands occurred, further lengthening of the grain boundary was assumed to generate no additional stress due to island zipping. However, continued deposition was specified to occur "epitaxially" so that new material inherited the stress of the underlying layer [Dolj 72]. The first assumption has been questioned recently in the literature as a consequence of new experimental evidence. For chemical-vapor deposited diamond films, the tensile stress has been observed to continue increasing significantly after films become continuous [Shel 01]. In addition for low-temperature Ag deposition, the tensile stress does not reach a steady state value until after film continuity [Flor 02]. Tensile stress generation due to island zipping is thought to occur continuously during deposition as step edges in adjacent grains across the grain boundary stretch towards each other due to short-range attractive forces [Shel 01, Flor 02].

4.4.6.2 Simulation of tensile stress evolution during Al and Ag thin film growth

The simulation of tensile stress evolution during thin film deposition is based upon the nucleation and growth simulation coupled with the FEM results for tensile stress generation. The compressive stress generation resulting from a Laplace pressure (see section 4.3) is not included in the stress calculations in this section. In the simulation, the tensile stress resulting from island coalescence during film growth is calculated according to methodology described in the previous section. The materials constants for Ag and Al used in the simulation are shown in Table 4-1. From TEM micrographs, the island contact angle is approximately 50 degrees for Al and 80 degrees for Ag. The contact angle affects both the radial growth rate of the island (see Eq. 4.2) and the magnitude of the island coalescence stress (see Fig. 4-19). In the simulation, the evolving distribution of island sizes during growth was modeled during deposition by matching the grain size from TEM micrographs of continuous films to the simulated structure. The final average grain size was estimated to be 15 nm for Al and 18 nm for Ag. For the first set of simulations shown in Fig. 4-23, perfect traction was assumed between the film and substrate.

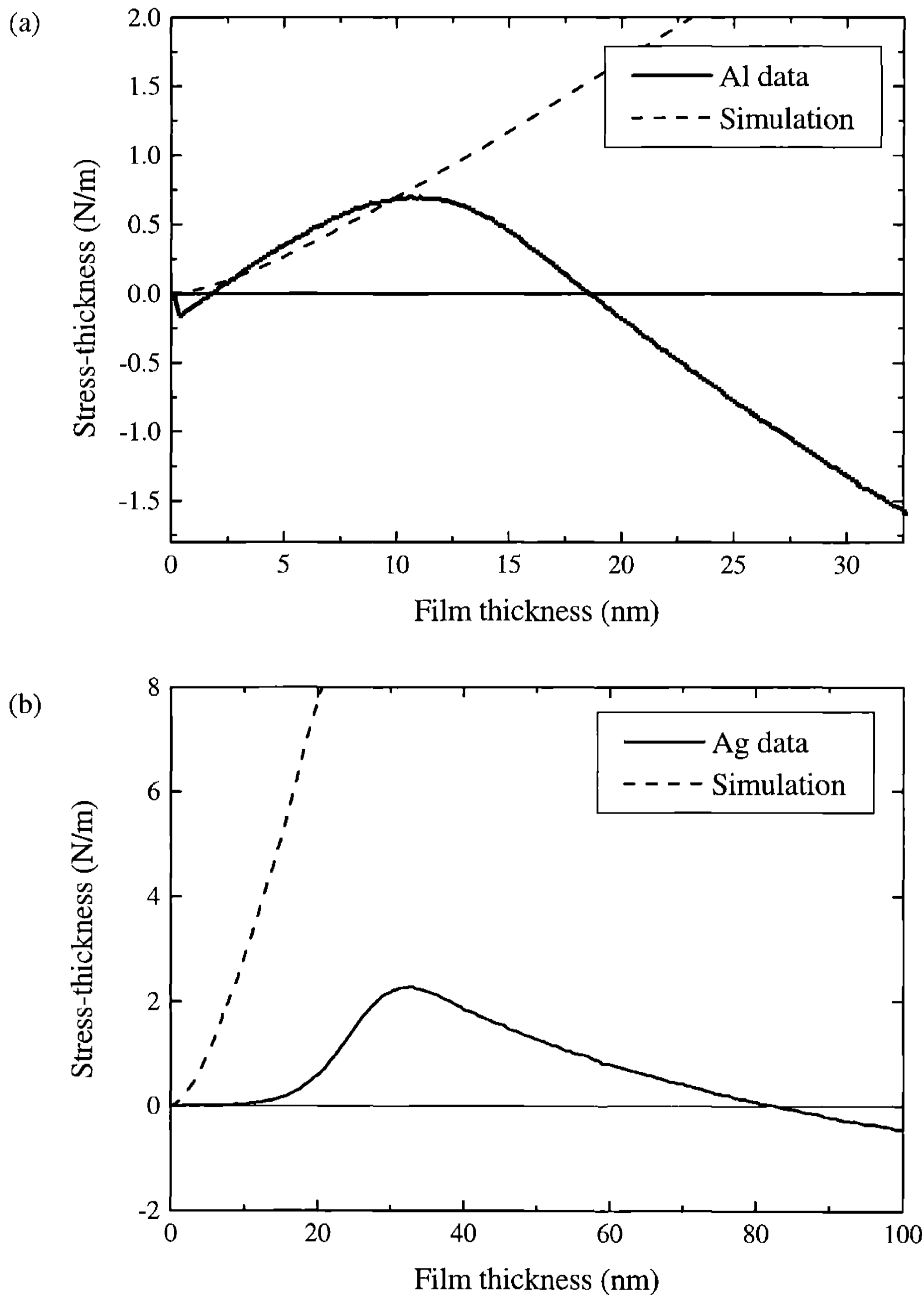

Figure 4-23: (a) Stress-thickness versus film thickness from experimental results (see Fig. 3-2) and the simulation of tensile stress generation during thin film growth for (a) Al, and (b) Ag. Perfect traction was assumed between the film and substrate.

Figure 4-23(a) shows the stress-thickness versus film thickness measurement for Al (see Fig. 3-2) along with the stress calculated with the film growth simulation. Once the film is continuous (around 10 nm film thickness), island coalescence no longer occurs and tensile stress generation ceases. However as mentioned previously, new material is assumed to inherit the stress of the underlying layer. In terms of the plot of stress-thickness versus film thickness, a constant stress with increasing film thickness appears as a line with constant, positive slope. The simulation results and the measured stress-thickness for Al are in fair agreement over the range of thickness for which the film is discontinuous (i.e. until the tensile peak in the stress-thickness curve).

The same calculation of tensile stress generation has been performed in a simulation of Ag thin film growth. Figure 4-23(b) shows the stress-thickness versus film thickness measurement for Ag (see Fig. 3-2) along with the stress calculated from the film growth simulation. The simulation predicts tensile stress generation starting at a much smaller film thickness than observed experimentally in Ag. The adhesion between Ag and the oxidized Si substrate is relatively weak, and shear at the island-substrate interface can result in relaxation of the tensile stress resulting from island coalescence [Flor 01]. As large clusters of islands form during later growth, island sliding will become inhibited as shear must be accommodated across a larger island-substrate area. A discussion of partial island sliding has been given in detail in section 4.4.5.4 above. These concepts can be incorporated into the simulation by defining a critical island cluster area A_{crit}. If either island (or island cluster) has an area smaller than the critical area A_{crit}, then sliding occurs upon island coalescence and no tensile stress is generated. If both members in an impingement event have an area greater than A_{crit}, then island sliding is inhibited and island coalescence results in tensile stress generation. As shown in Fig. 4-24, the simulation more closely matches the experimental data for Ag by including a critical cluster area to capture stress relaxation due to island shear.

The calculated tensile stress evolution from the simulation and the experimental data, as shown in Fig. 4-23(a) for Al and Fig. 4-24 for Ag, show reasonable agreement during the discontinuous film stage of growth (i.e. until the tensile peak in the stress-thickness curve). After film continuity, the measured stress begins to decrease and

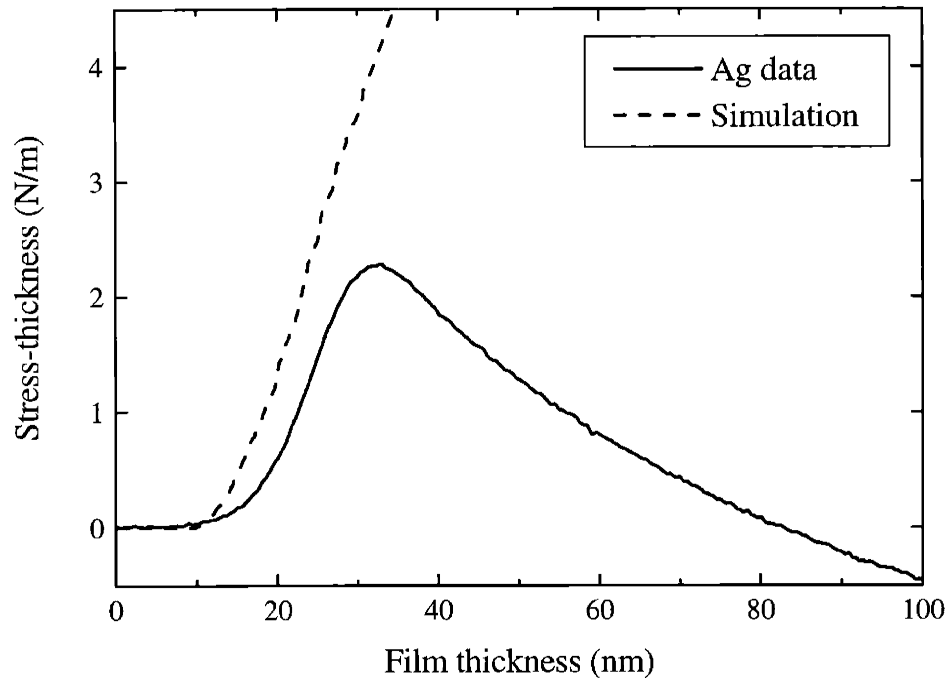

Figure 4-24: Stress-thickness versus film thickness of the Ag experimental data (see Fig. 3-2) and the simulation of tensile stress generation during thin film growth including a critical cluster area to capture stress relaxation due to island shear.

become net compressive at greater thicknesses. However, the simultaneous action of the compressive stress generation during the early island stage of growth (see section 4.3) and the tensile stress generation due to island coalescence has been neglected so far. A discussion of both stress generation mechanisms operating simultaneously during thin film growth is addressed in the following section. In addition, the importance of diffusive stress relaxation during film growth resulting in the observed decreasing tensile stress levels will be discussed in section 4.5.

4.4.6.3 Multiple stress generation/relaxation mechanisms during thin film growth

In section 4.3.5, models for compressive stress generation due to a Laplace pressure were compared to experimental data for Al and Ag during the early island stages of growth. In section 4.4.6.2, an FEM-based model for tensile stress generation due to island coalescence was compared to experimental data for Al and Ag from the onset of

growth until film continuity (i.e. the tensile peak of the stress-thickness curve). A simple superposition of the calculated compressive and tensile stresses neglects the complex nature of the interactions between the mechanisms. Figure 4-25 shows the expected stress distribution within a growing island starting from the island stage, through island coalescence, and after film continuity. Each stage of growth show in Fig. 4-25 is discussed in detail below.

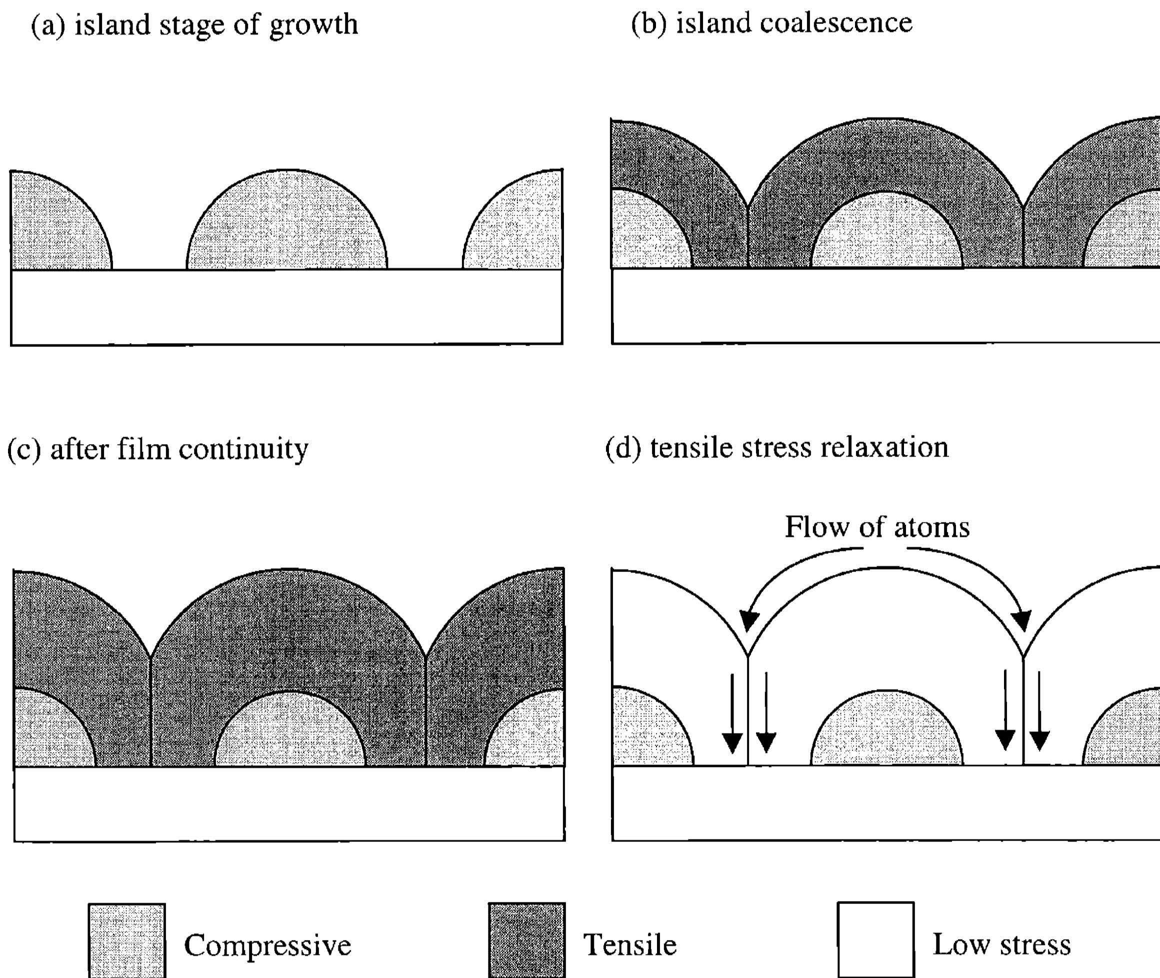

Figure 4-25: Schematic of the stresses distribution within a growing island showing (a) compressive stress during the island stage of growth, (b) localized tensile stress generation due to island coalescence leaving a compressive region, (c) tensile stress assumed by new material inherited from underlying material, (d) possible tensile stress relaxation at grain boundaries cannot relax compressive stress regions.

During the isolated island stage of growth, a compressive stress exists within the island due to a Laplace pressure as shown in Fig. 4-25(a). The compressive stress requires traction between the island and substrate and can be relaxed by shear at the island-substrate interface or by inclined shear of dislocations. Upon island coalescence, tensile stresses are generated that are balanced by the reduction in interfacial energy upon creating grain boundary. In the island coalescence models considered in the previous sections, the calculation of strain energy ignored any contribution from pre-existing stresses within the island. For an island under a compressive stress, any creation of tensile stress due to grain boundary zipping will actually decrease the total strain energy in the island. As the zipping height increases and larger tensile stresses are created, the strain energy will begin to increase and eventually balance the interfacial energy reduction at the equilibrium zipping height. Therefore, the average stress after coalescence will be net tensile even for an island starting with a pre-existing compressive stress.

The stress distribution within an island after coalescence results from the process by which grain boundary zipping occurs. In the coalescence model, the surfaces of two island strain towards each other to create the grain boundary. Consequently, the resulting tensile stress is mostly localized near the grain boundary and decays exponentially in magnitude with distance away from the boundary. In addition if traction is assumed between the island and substrate, zero tensile strain results at the island-substrate interface after island zipping because of the assumed boundary conditions. Therefore for an island originally under compression, a region of compressive stress will remain after island coalescence that is located towards the center of the grain, which is away from the grain boundary, and near the island-substrate interface, where zero tensile strain results from island zipping. The resulting stress distribution after coalescence of an island under compression is shown schematically in Fig. 4-25(b).

As discussed previously, newly deposited material is assumed to inherit the stress of the underlying layer. Therefore once the film is continuous, continued deposition will inherit the tensile stress present at the surface of the island as shown in Fig. 4-25(c). However, the experimental evidence shows that the tensile stress begins to decrease after film continuity and actually becomes net compressive at large film thicknesses. One

proposal is that the tensile stresses near the grain boundary are relaxed during deposition due to diffusion of material down the grain boundary, which "exposes" the core compressive region within the center of the island, as shown in Fig. 4-25(d). The inclusion of a stress relaxation mechanism into the film growth simulation allows for an examination of this proposal in the following section.

4.5 Stress relaxation during thin film growth

4.5.1 Introduction

The maximum tensile stress measured during deposition of high mobility films is typically an order of magnitude lower than that for low mobility materials [Koch 94]. However if low mobility materials are deposited at higher temperatures, they behave much like high mobility materials [Thur 90]. Conversely, high mobility materials deposited at lower temperatures exhibited large intrinsic stresses similar to low mobility materials [Wina 91]. These observations are consistent with the existence of a diffusive stress relaxation mechanism with a strong dependence on temperatures. Since the microstructural scale during deposition can be on the order of 10 nm, diffusion distances along surfaces and grain boundaries are short so that significant stress relaxation may occur during deposition.

As shown in Fig. 3-7, Ag deposited at different temperatures exhibit significantly different behavior. As described in detail below, the influence of a diffusive stress relaxation mechanism is studied using the film growth simulation and compared to the Ag films deposited at different temperatures.

4.5.2 Model for surface Coble creep in the simulation

Tensile stress generation resulting from island coalescence occurs due to the localized displacements at the grain boundary. One possible mechanism by which the tensile stress can relax is through transport of matter to the strained region within the grain boundary as shown schematically in Fig. 4-26. A fast diffusion path for atoms is along the island surface, which acts as a source of atoms, and down the grain boundary.

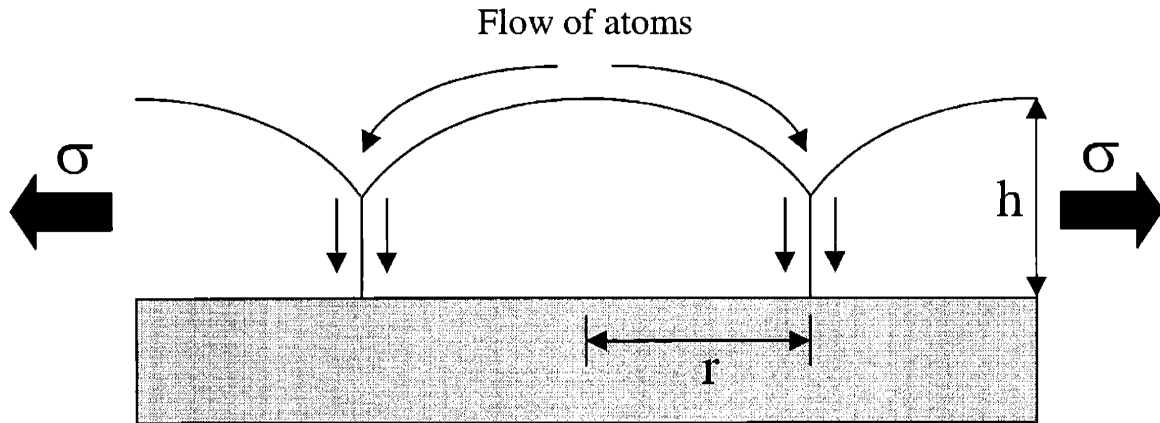

Figure 4-26: Proposed stress relaxation mechanism involving the diffusion of atoms across the surface of the island and down grain boundaries to the strained regions near the grain boundary. Since surface diffusion and grain boundary diffusion occur in series, either process may be rate limiting.

Since both surface and grain boundary diffusion are required in series, either diffusive mechanism may be rate limiting. With or without sliding at the film-substrate interface, the stress relaxation rate $\dot{\sigma}$ will take the form [Turl 92, Thou 93, Kobr 01]:

$$\dot{\sigma} = -\frac{C_0}{h^3}\sigma\, exp(-Q/kT), \qquad (4.28)$$

where C_0 is a material-dependent, temperature- and stress-independent constant, σ is the average stress in the film, h is the film thickness, k is Boltzmann's constant, T is temperature in Kelvin, and Q is the activation energy for the rate-limiting diffusive process, either grain boundary or surface diffusion. Implicit in this expression is that the grain size scales with the film thickness. Unlike the uniform strains associated with lattice mismatch or thermal expansion mismatch, the strains created by island coalescence results from localized surface displacements due to island zipping. Consequently, matter diffusing to the grain boundaries can relax all of the tensile stress generated by island coalescence. Since the diffusion distance along the surface and grain

boundary is very short, this diffusive process may be an important stress relief mechanism even at low temperatures.

In the simulation, stresses generated by island coalescence were assumed to relax by a microstructure-dependent diffusive stress relaxation mechanism, similar to that described by Eq. 4.28. The proposed expression for stress relaxation is the most appropriate for continuous films since the stresses are approximately equibiaxial and the grains have formed boundaries on all sides. However, after a single coalescence, an island has only one grain boundary and the stresses are not equibiaxial. Nonetheless, the form of the stress relaxation rate given by Eq. 4.28 was used in the simulation with the film thickness term replaced by the island height, and using the average stress in the island. This implementation implies that stress relaxation in each individual island can be treated independently. These approximations are not expected to significantly affect the results of the simulation.

The simulation of stress evolution during thin film deposition is based upon the nucleation and growth simulation coupled with the FEM results for tensile stress generation and the analytical model for the microstructure-dependent stress relaxation mechanism. The experimental inputs to the simulation were the deposition rate and temperature, which both affect the rates of stress generation and relaxation. The physical dimensions of the simulation are unitless so a scaling factor must be defined that relates the microstructural dimensions of the real film to the simulated structure. From SEM images of discontinuous Ag films, the fractional substrate coverage versus film thickness was measured for all deposition conditions. For each deposition temperature, a scaling factor was determined that gave reasonable agreement between the simulated microstructure and the measured coverage versus film thickness, as shown in Fig. 4-9. The scaling factor influences both the island-size-dependent stress generation model and the microstructure-dependent stress relaxation model. In addition, a diffusivity for the rate-limiting diffusive process of the stress relaxation mechanism must be supplied. An activation energy of 0.3 eV and a pre-exponential factor of an appropriate magnitude were chosen to best match the simulation to the experimentally measured stress-thickness versus thickness curves at different deposition temperatures. For each deposition temperature, results were averaged over approximately 2500 islands/grains from ten

simulations using different random starting seeds. Assuming traction at the island-substrate interface, the average stress-thickness versus thickness and average stress resulting from simulations of Ag films deposited at different temperatures are shown in Fig. 4-27.

In another set of simulations, the equilibrium zipping distance and average stress were calculated using the FEM results with partial sliding at the island-substrate interface. Contrary to the case with traction, two different types of coalescence events can occur. If either island (or island cluster) has an area smaller than the critical area A_{crit}, then sliding occurs upon island coalescence and no tensile stress is generated. If both members in an impingement event have an area greater than A_{crit}, then island sliding is inhibited and island coalescence results in tensile stress generation. A larger A_{crit} will delay the onset of the rise of the tensile stress until a greater film thickness. The tensile stress was assumed to relax via the proposed diffusive mechanism. Otherwise, the simulations were run under exactly the same conditions as the case with island-substrate traction. Under conditions of island-substrate sliding, simulations of the stress-thickness versus thickness and average stress versus thickness were performed for Ag films deposited at different temperatures as shown in Fig. 4-28.

The measured stress-thickness versus film thickness for Ag deposited at different temperatures, shown in Fig 3-7, exhibit four distinct regimes at different film thicknesses. During early deposition times, no appreciable stress-thickness was measured up to a critical thickness, which increased with increasing deposition temperature. From TEM micrographs, the island density was initially very high but decreased with increasing film thickness, indicating the presence of island coarsening by surface diffusion and/or grain growth. If neighboring islands have different radii then the gradient in chemical potential may be sufficient to drive island coarsening by surface diffusion, especially at higher temperatures. However, if islands are approximately the same size or once islands are large, the gradient will be smaller and impinging islands will form grain boundaries rather than undergoing coarsening. The simulation of film growth does not include island coarsening so all island impingements resulted in stress generation. In the simulation with traction at the island-substrate interface, the onset of an appreciable stress-thickness occurred at a much smaller film thickness than was observed in the experiments.

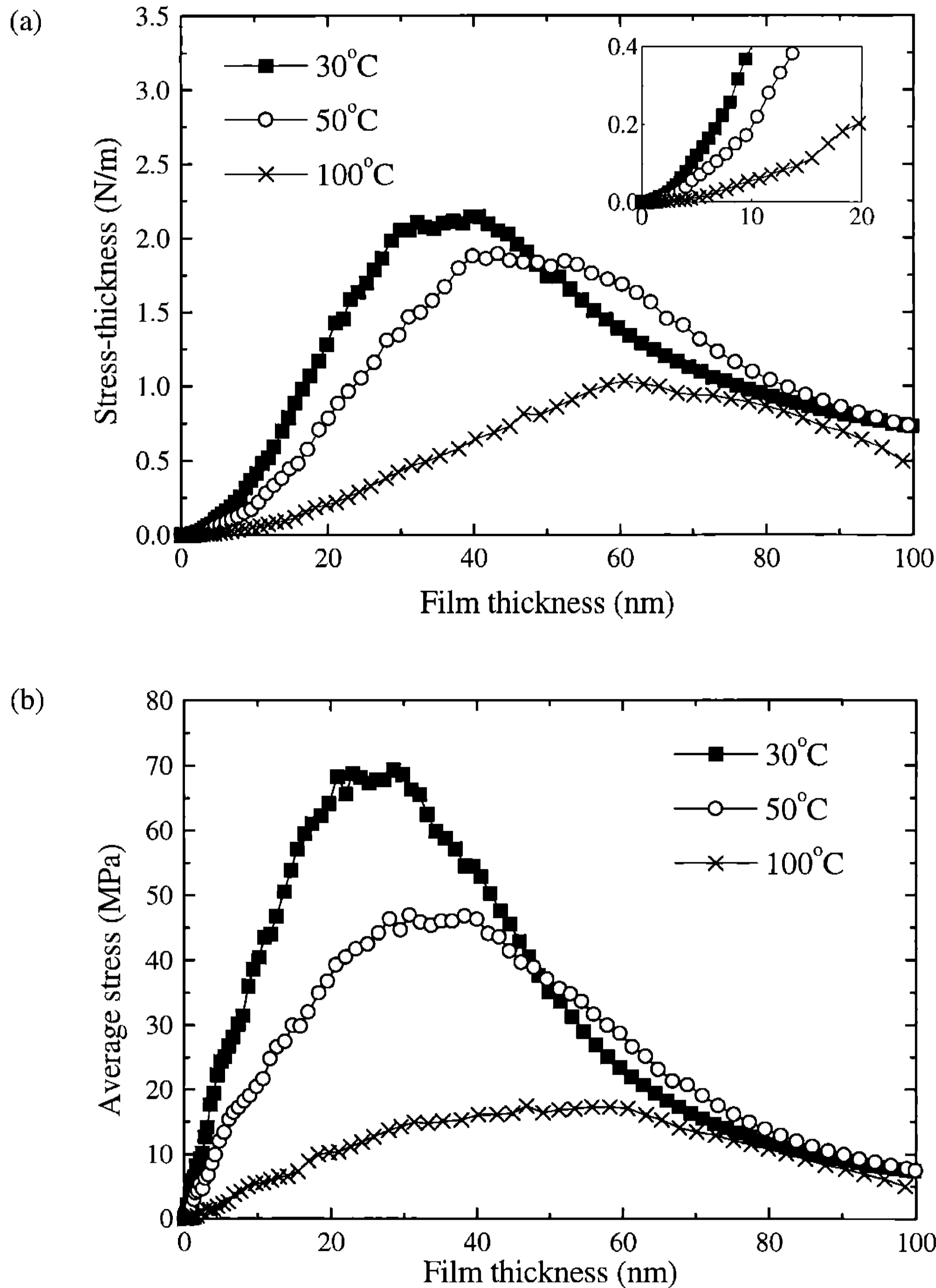

Figure 4-27: Simulation of Ag thin films with traction at the film-substrate interface during deposition at different temperatures showing, (a) stress-thickness product versus film thickness, and (b) average stress versus film thickness. Stress generation was modeled using the FEM approach, while stress relaxation was assumed to occur via a microstructure-dependent diffusion mechanism.

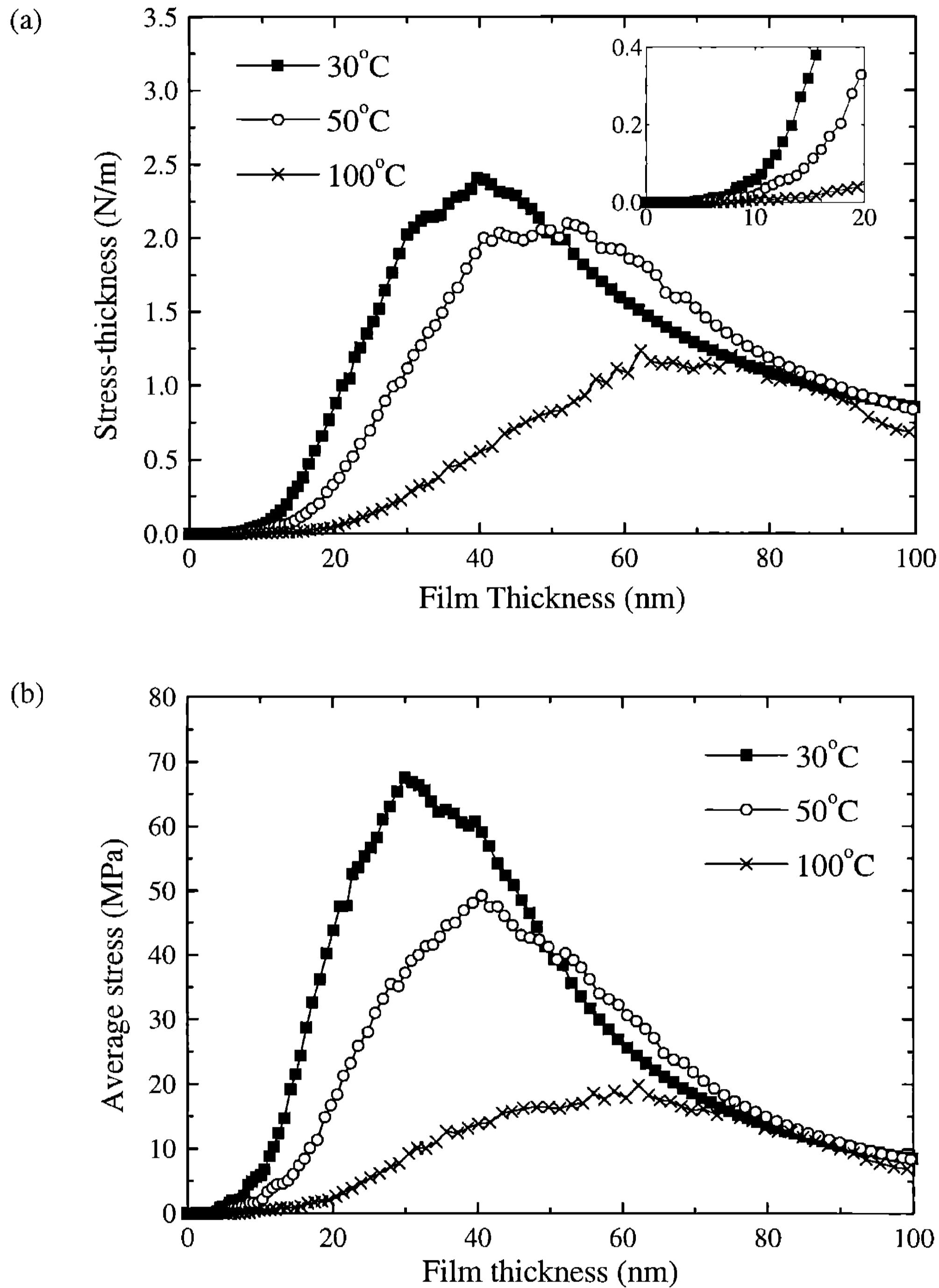

Figure 4-28: Simulation of Ag thin films with partial sliding at the film-substrate interface during deposition at different temperatures showing, (a) stress-thickness product versus film thickness, and (b) average stress versus film thickness. Impingements between island clusters with an area less than A_{crit} were assumed to not generate tensile stress during coalesence due to island sliding.

Even once numerous grain boundaries had formed, as seen in Fig. 3-3 for a 12 nm Ag film deposited at 30°C, the measured stress-thickness in the film was still very low. Because the stress relaxation mechanism is strongly dependent on the island size, the tensile stress generated as a result of the initial coalescence are expected to be relaxed very quickly. However, even with a microstructure-dependent stress relaxation mechanism, the simulated stress-thickness for the case of island-substrate traction was appreciable before a thickness of even 10 nm. If sliding of the island was assumed in the simulation, the onset of the tensile stress generation was retarded during the early stage of growth until a greater thickness, as shown in Fig. 4-28. The average stress increased dramatically as the film approached a percolated structure for which sliding is inhibited.

The second feature to consider is that the magnitude of the maximum tensile stress-thickness decreased, and the film thickness coinciding with the maximum increased, with increasing deposition temperature. For all deposition temperatures, the maximum tensile stress-thickness occurred when the film was in the late channel stage just before continuity, as confirmed using SEM. Since continuity occurred at larger film thicknesses with increasing deposition temperature as shown in Fig. 4-9, the average grain size at continuity is larger at higher deposition temperatures, as confirmed by TEM. Similar trends were observed for the Ag films deposited at different deposition rate, as shown in Fig. 3-5. The magnitude of the maximum tensile stress-thickness decreased, and the film thickness coinciding with the maximum increased, with decreasing deposition rate. Film continuity occurred at larger film thicknesses, as shown in Fig. 3-6, with correspondingly larger grain size for decreasing deposition rate, as confirmed by TEM. Based on the FEM results for island coalescence stress in Fig. 4-15, the magnitude of the maximum tensile stress should decrease with increasing grain size. However, predicting the relative magnitudes of the maximum stress-thickness also requires consideration of the influence of stress relaxation.

The simulation, which accounted for both tensile stress generation and relaxation, reproduced the experimental trends of a decreasing maximum tensile stress-thickness that occurred at larger film thicknesses with increasing deposition temperature. With an activation energy of 0.3 eV and an appropriate pre-exponential factor, the simulation was also able to reproduce the measured stress-thickness with a factor of two for all

deposition temperatures. If an activation energy of 0.6 eV was used, as reported by Kobrinsky and Thompson for diffusive stress relaxation in continuous Ag films [Kobr 98], the simulation produced the same qualitative trends with deposition temperature, but using a value of 0.3 eV gave better agreement with the experimental results.

The third feature of the stress-thickness versus thickness curves to be considered is the observed temperature dependence of the negative slope region immediately following film continuity. Since the zipping mechanism for tensile stress generation becomes inactive once the film achieve continuity, the subsequent decrease in the stress-thickness may be due in part to stress relaxation. As can be seen from Fig. 3-7, the slope of the curves just after continuity suggests that the rate of stress relaxation decreased with increasing deposition temperature. Even though diffusion increases rapidly with increasing temperature, the proposed stress relaxation mechanism is also strongly dependent on the microstructural scale, which also depends on the deposition temperature. As shown in Fig. 4-9, the film thickness coinciding with continuity increased with increasing deposition temperature. Therefore, films deposited at higher temperature had slower relaxation rates after continuity because of the strong thickness dependence of the stress relaxation rate. As shown in Figs. 4-27 and 4-28, the simulation reproduces the lower postcontinuity stress relaxation rate observed at higher deposition temperatures using the same activation energy (0.3 eV), which also correctly reproduced the maximum tensile stress-thickness dependence with deposition temperature.

One last feature of the experimentally measured curves that has not been addressed here is the compressive stress observed at large thicknesses. Compressive stress during island-type growth is typically attributed to the Laplace pressure induced by surface stresses [Aber 94, Camm 00]. While the tensile stresses resulting from island coalescence are relaxed by diffusion of matter down the grain boundaries, the diffusive mechanism cannot fully relax the compressive stress imposed by the substrate, as shown schematically in Fig. 4-25(d). Consequently, once the tensile stress near the grain boundaries has relaxed, the compressive stress within the interior of the grain will still be present and may explain the compressive stress observed in the thicker continuous films. Two experimental trends observed in Chapter 3 would seem to support such a mechanism. For lower deposition rates of Ag grown at room temperature as shown in

Fig. 3-5, the instantaneous stress (i.e. slope of the stress-thickness versus thickness curve) after film continuity is larger. The larger grain sizes in the films deposited at the lower deposition rates would tend to decrease the stress relaxation rate, according to Eq. 4.28, however the slower deposition rate allows more time for stress relaxation during growth. In addition, the instantaneous stress during deposition of Cu after growth interrupts, as shown in Fig. 3-13, also increases with decreasing deposition rate. One important difference between the Ag and Cu data is that the initial 25 nm of the Cu film was deposited at 0.1 nm/sec and established the grain size prior to decreasing the deposition rate. The increased time for stress relaxation at lower deposition rates would eliminate more of the tensile stress resulting from island coalescence and "expose" more of the compressive regions that cannot be relaxed by the diffusive stress relaxation.

However, other experimental evidence seems to contradict the importance of a diffusive stress relaxation mechanism during thin film growth. For instance, no initial compressive stress was observed during the island stage of growth of Ag but a compressive stress regime was observed at large film thickness. Also, during growth interrupts of Cu as shown in Fig. 3-11, a large tensile rise is observed that evolves over time and eventually plateaus at a constant stress level. The origin of the tensile rise during growth interrupts is discussed in detail in Chapter 5. After the initial tensile rise, the stress should have decreased in the compressive direction with time, rather than increasing and reaching a plateau, if the proposed diffusive stress relaxation mechanism was active during the growth interrupt. The experimental evidence for the *a*-Ge films deposited at room temperature is even more compelling. During growth interrupts of *a*-Ge films deposited at room temperature, as shown in Fig. 3-16, no change in stress is observed over time periods comparable to the deposition time. However, a net compressive stress is observed at large film thicknesses, as seen in Fig. 3-15, without any evidence of stress relaxation during the growth interrupts.

4.6 Summary and conclusions

Models for stress generation and relaxation have been compared to *in situ* measurements of stress during UHV deposition of thin films that grow by the Volmer-Weber mechanism. To emulate a realistic microstructure during growth, a computer

simulation was developed to model the process of film growth through continuous nucleation of islands that grow to impingement, and eventually form a continuous polycrystalline film. The simulation allowed for the calculation of stress evolution using the analytical models with a microstructure that changes as the film thickness increases.

Comparison of the stress evolution for Ag and Al growth indicates that Ag films during the island stage of growth do not support stress in contrast to Al films that support stress from the very onset of deposition. The primary difference in their behavior was attributed to shear occurring at the Ag-SiO_2 interface, which is suppressed at the much stronger Al-SiO_2 interface. The initial compressive stress behavior of Al during the island stage of growth was modeled as a size-dependent lattice contraction due to a Laplace pressure. Using the film growth simulation with a model for calculating the compressive stress as a function of island size, the simulation was able to qualitatively reproduce the early stress behavior as a function of film thickness for the Al film deposition. However, the gross overprediction of the magnitude of the compressive stress indicates that significant relaxation of the compressive stress is occurring during deposition.

Several different approaches were considered for modeling the tensile stress generation resulting from island coalescence. For comparison with previous analytical results, FEM was used to model the island coalescence process for a plane-strain geometry. By minimizing the sum of the positive strain energy and the associated reduction in interfacial energy, the equilibrium configuration resulting from island coalescence was calculated as a function of island radius. The magnitude of the average tensile stress calculated using FEM was more consistent with experimental measurements than the stresses calculated using the simple Hoffman analysis or the Nix-Clemens crack-closure model. In addition, a simple analytical treatment of the island zipping process was developed using average strains to calculate the strain energy resulting from grain boundary formation. Even using a series of assumptions that tend to result in an overestimation of the island coalescence stress, the analytical model predicts stresses closer to the FEM results than those of the Nix-Clemens model. From additional FEM calculations, the magnitude of the island coalescence stress was found to decrease dramatically with decreasing island contact angle.

By using the contact-angle dependent FEM results and assuming perfect island-substrate traction, the simulation was in reasonable agreement with the stress-thickness measurements of Al over the range of thicknesses prior to film continuity. If perfect island-substrate traction was assumed during the Ag film deposition, the simulation predicts the onset of an appreciable tensile stress at a much earlier film thickness than observed experimentally in Ag. By including a critical area criterion for island sliding in the simulation, the simulation produced stresses in general agreement with the measured stress-thickness data of Ag prior to film continuity.

In order to study the kinetics of stress evolution during deposition, Ag films were deposited at different temperatures. Using the FEM results for stress generation and a microstructure-dependent stress relaxation model, the simulation reproduced the qualitative trends in stress with film thickness observed experimentally. The magnitude of the measured maximum stress-thickness decreased, and occurred at a larger film thickness, with increasing deposition temperature. These observations are consistent with the tensile stress generation model for a grain size that increases with increasing deposition temperature, as observed in TEM micrographs. The same correlation of a larger average grain size resulting in a smaller maximum tensile stress at a greater film thickness was observed for Ag deposited at different rates at room temperature. The slope of the measured stress-thickness curves at different temperatures indicate that once the film is continuous, the stress relaxation rate decreased with increasing deposition temperature. Although the proposed stress relaxation mechanism is thermally activated, the slower relaxation rate after continuity reflects the strong film-thickness dependence of the stress relaxation mechanism as captured by the simulation results.

During deposition of the Al, Ag, Cu, and *a*-Ge films considered in this thesis, a generic stress evolution from compressive to tensile and then back to compressive stress was observed with increasing film thickness. The long-term compressive stress behavior was attributed to the diffusive stress relaxation of the tensile stress near the grain boundary resulting from island zipping. A region of compressive stress due to the Laplace pressure, which is located towards the center of the grain and near the island-substrate interface, cannot be relaxed by the diffusive creep mechanism. Experimentally, a larger instantaneous compressive stress for continuous films was observed in Ag and

Cu deposited at slower deposition rates, for which more time was available for tensile stress relaxation. However, other experimental evidence indicates that diffusive stress relaxation is not the dominant mechanism resulting in the compressive stress at large film thickness. During growth interrupts of a-Ge, no evidence of a tensile stress relaxation was measured over time scales comparable to the deposition time even though the same compressive-tensile-compressive behavior was observed during continuous deposition. In addition, growth interrupts of continuous Cu films showed a slow tensile rise that plateaud at a constant stress value, rather than a tensile stress relaxation as expected for a diffusive relaxation mechanism. The origin of the compressive instantaneous stress for all films and the reversible tensile rise behavior for the high mobility films will be addressed in Chapter 5 in terms of a non-equilibrium thin film growth model.

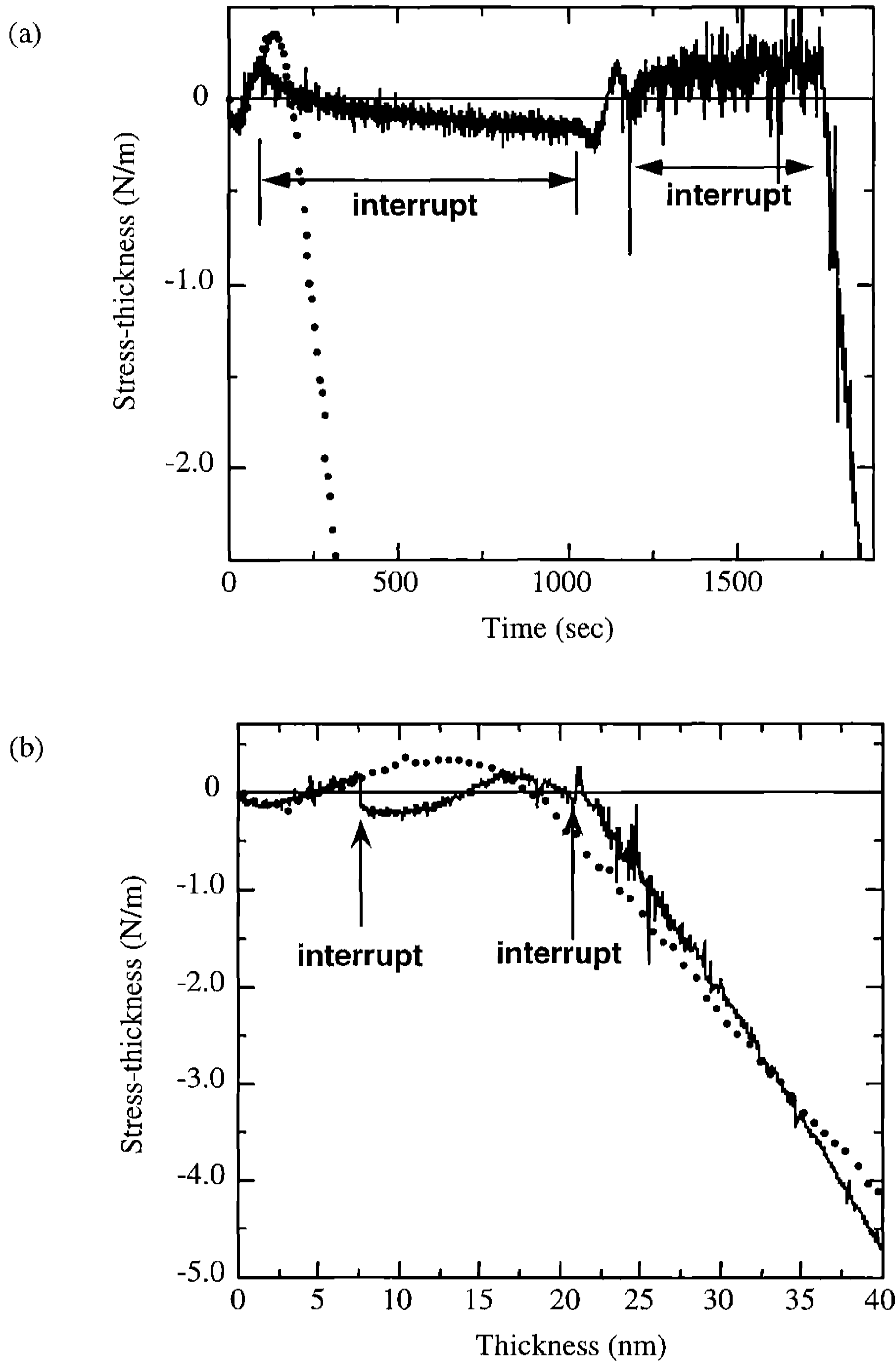

Figure 3-17: Growth interrupt behavior for a-Ge grown at 270°C showing (a) stress-thickness versus time, and (b) stress-thickness versus film thickness. The solid line is for growth with interrupts, while the dots are uninterrupted growth data. The arrows in (a) indicate the thickness at which the interrupts occurred. The measurements were performed at SNL by JAF and SJH.

Stress and Structure Evolution During Volmer-Weber Growth of Thin Films

by

Steven Craig Seel

Submitted to the Department of Materials Science and Engineering in Partial Fulfillment of the Requirements for the Degree of

Doctor of Philosophy

at the

MASSACHUSETTS INSTITUTE OF TECHNOLOGY

March 2002
[June 2002]

© Massachusetts Institute of Technology 2002. All rights reserved.

Author..
Department of Materials Science and Engineering
March 14, 2002

Certified by..
Carl V. Thompson
Stavros Salapatas Professor of Materials Science and Engineering
Thesis Supervisor

Accepted by..
Harry L. Tuller
Chairman, Department Committee on Graduate Students

ARCHIVES

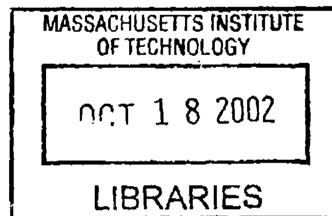

V.2

Chapter 5

Discussion of stress evolution during growth interrupts

5.1 Introduction

For the Al, Ag, Cu, and *a*-Ge films considered in this thesis, after the maximum in the tensile stress coincident with reaching film continuity, further thickening of the film results in a decreasing stress that becomes net compressive for an increasing film thickness. No consensus exists in the literature as to the correlations between the evolving microstructure and the measured stress behavior for continuous films during thin film deposition. To elucidate the kinetics of stress evolution during growth, several researchers have studied the evolution of stress as a function of time after interruptions of growth for continuous films [Aber 85, Shul 96, Flor 01]. For materials deposited at low homologous temperatures (T_{dep}/T_{melt}), only negligible changes in stress are observed during growth interrupts, as shown in section 3.4.3 for *a*-Ge deposited at room temperature. However for film deposited at higher homologous temperatures, a tensile rise in the stress is observed when growth is interrupted, as shown for Cu in section 3.4.2. In addition, the tensile rise is reversible in that the stress reverses back to the behavior observed before the growth interrupt when growth is resumed. No models exist in the literature that attempt to give a quantitative explanation for the reversible tensile rise behavior.

The stress evolution during deposition in the compressive regime at large film thicknesses and the stress behavior during growth interrupt will be modeled in terms of the non-equilibrium surface morphology that develops during deposition. The evolution of the grain shape at the film surface during deposition is modeled as the competition between the deposition-induced film roughening and diffusion-driven smoothing. For the resulting non-equilibrium grain shapes, the in-plane compressive stress resulting from excess surface stress is calculated using finite element method solutions and correlated to the measured compressive stress during deposition at large thicknesses.

During a growth interrupt when the deposition flux is eliminated, surface diffusion drives the grain shape towards equilibrium with an associated time-dependent decrease in the compressive stress that appears as a tensile rise as observed experimentally during growth interrupts for films deposited at high homologous temperatures. When deposition is resumed, the surface morphology again assumes a non-equilibrium shape that results in compressive stress generation. The model predictions will be compared to the experimentally observed behavior for thin film stress evolution during growth interrupts.

5.2 Experimental evidence for non-equilibrium film growth

The kinetics of surface growth processes has been the focus of considerable experimental [Gimz 85, Chia 91, He 92, Pala 94, Thom 94, Mayr 99] and theoretical research [Kard 86, Mazo 88, Raib 00]. Under conditions of restricted atomic mobility, the development of a non-equilibrium surface morphology during thin film growth is controlled by the competition between deposition-induced kinetic roughening and diffusion-driven smoothing. In order to study far-from-equilibrium surface morphologies, films are typically deposited at low homologous temperatures or metallic alloy films are used that remain amorphous when deposited near room temperature. The morphology of the film surface can been studied using a variety of techniques which either directly or indirectly measure some metric of surface roughness. Scanning tunneling microscopy (STM) provides height versus position data that can be acquired *in situ* after deposition. From the STM images, both the root-mean-square roughness σ_{rms} and the height-difference distribution function $G(R)$ can be calculated as:

$$\sigma_{rms} = \sqrt{\left\langle \left[h(x,y) - \langle h(x,y) \rangle \right]^2 \right\rangle}$$
$$G(R) = \left\langle \left| h(\vec{r}) - h(\vec{r}+\vec{R}) \right|^2 \right\rangle_{r,R} \tag{5.1}$$

where $\vec{r} = (x, y)$ and $<>_{r,R}$ denotes the average over all pairs of points, separated horizontally by a distance R. Alternatively, specular reflection (angle of incidence equal to the angle of reflection) of x-rays from surfaces yields information about the root-mean-square roughness, while the diffuse component of the x-ray scattering is related to the height-difference distribution function. Other techniques such as low-energy electron diffraction [He 92] and gas adsorption isotherms [Chia 91] can provide similar roughness information.

In these experimental papers, the goal was to study the fractal nature of the surface roughness, however other pertinent information can be gleaned from their data. For surfaces with self-affine (i.e. fractal) roughness, the height-difference distribution function scales as $G(R) \propto R^{2H}$, where $0<H<1$ is referred to as the roughness exponent [Thom 94]. The scaling of the self-affine roughness saturates at a characteristic horizontal cutoff, or correlation length ξ, at which distance significant deviation from the power-law behavior occurs. The correlation length ξ is approximately equal to the average grain size at the film surface as observed in both crystalline materials [Pala 94, Thom 94] and amorphous materials [Mayr 01]. Therefore, the value of the height-difference distribution function $G(R)$ at $R=\xi$ provides information about the grain shape at the surface. To an approximation, the square root of $G(R)$ equals the average height difference between the peak height at the center of the grain and the valley height at the grain boundary. The scaling of $G(R=\xi)$ with film thickness provides important information about the non-equilibrium grain shape during thin film growth.

The surface morphology of 100 nm-thick Ag films deposited at 90 K were studied *ex situ* using STM [Gimz 85]. After deposition, pyridine was purposefully adsorbed on the film surface to stabilize the rough surface by preventing smoothing due to surface diffusion upon warming to room temperature. Deep trench-like grooves were observed at

the grain boundaries between grains, even though, as the authors comment, surface smoothing probably occurred even with the pyridine adsorption. In another series of studies, Ag films of different thickness were deposited by thermal evaporation at room temperature and studied by STM [Pala 94] and x-ray reflectivity [Thom 94]. Even at room temperature, self-affine scaling of the surface roughness was observed indicating that surface diffusion of Ag is clearly limited at room temperature and results in non-equilibrium growth conditions. The correlation length ξ was found to increase with increasing film thickness, in agreement with a grain size that scales with the film thickness [Lita 99, Knor 95, Thom 90]. The value of $G(R=\xi)$ was found to increase with increasing film thickness indicating an increasing height difference between the center of the grain and the height at the grain boundary. Growth experiments have also been performed for amorphous metallic alloys deposited at room temperature and studied using *ex situ* STM [Mayr 99]. An increasing correlation length ξ with film thickness was found to correlate with an increasing amorphous cluster size at the film surface. In addition, the value of $G(R=\xi)$ was found to increase with increasing film thickness, similar to the metallic film experiments.

In summary, non-equilibrium growth has been observed experimentally in many systems, even for Ag deposited at room temperature. A model for non-equilibrium growth during thin film deposition is described in the following section.

5.3 Non-equilibrium thin film growth model

5.3.1 Partial differential equation (PDE) describing thin film growth

During e-beam and thermal evaporation, the flux of atoms is essentially normal to the substrate surface provided the distance between the source and substrate is sufficiently large and the substrate is relatively small [Ohri 92]. As the evaporant atoms approach the film surface, they are deflected or "steered" towards the surface due to interatomic forces. This "steering" phenomenon has been studied by molecular dynamics simulations which indicate that deflection of the low energy evaporant atoms, with kinetic energies on the order of 0.1 eV, are strongly attracted to the potential well represented by the film surface, with an energy on the order of eV's, at a distance of

approximately 1 nm [Sand 92]. Experimentally, steering has been attributed as the origin of increased roughness in grazing incidence deposition [Dijk 99]. If steering of the deposited atoms is considered, the local growth rate of a surface h_t due to the deposition flux J depends on the surface curvature K [Mazo 88, Srol 88, Raib 00]:

$$h_t = J + bJK = J - bJ\, h_{xx}\left(1+h_x^2\right)^{-3/2}, \tag{5.2}$$

where $h(x,t)$ is the one-dimensional surface profile as a function of position and time and b is the "steering" interaction distance which is approximately 1 nm [Sand 92]. It should be noted that Mazor *et al.* and Srolovitz *et al.* did not include the steering mechanism in their analysis, but rather considered a finite-atom size effect resulting in an equation of the same form as Eq. 5.2. Without surface diffusion, those areas with the high positive curvature grow faster than those with lower or negative curvature resulting in a surface that increases in roughness with increased deposition time.

Surface diffusion is driven by difference in chemical potential μ, which in this case are due to differences in curvature [Mull 57]. The velocity of the surface normal to itself due to surface diffusion is given by $v_\perp = -D_e \nabla_s^2 K$, where D_e is the effective surface diffusivity and ∇_s designates the surface gradient. The effective diffusivity is given by $D_e = D_s \gamma_s \Omega^{4/3}/K_B T$, where D_s is the surface diffusivity, γ_s is the surface energy, Ω is the atomic volume, K_B is the Boltzmann constant and T is the temperature in Kelvin. In Cartesian coordinates, the velocity of the surface profile h_t due to surface diffusion is given by [Mazo 88, Srol 88]:

$$h_t = -D_e \left\{\left(1+h_x^2\right)^{-1/2}\left[h_{xx}\left(1+h_x^2\right)^{-3/2}\right]_x\right\}_x. \tag{5.3}$$

By combining Eqs. 5.2 and 5.3, the final evolution equation of the film surface can be expressed under the combined action of surface diffusion and a constant deposition rate with steering effects [Mazo 88, Srol 88, Raib 00].

The boundary conditions for the PDE are defined in terms of the geometry of the grain at the film surface. The one-dimensional surface profile of the grain $h(x,t)$ is

assumed to be symmetric in that a mirror plane of symmetry exists at the center of grain, as shown in Fig. 5-1. At the point where the grain boundary intersects the surface, a groove is formed such that an angle ϕ exists between the grain surface and the plane of the substrate, as shown in Fig. 5-1, whose equilibrium value is determined by Young's equation:

$$\phi = 2\,sin^{-1}\left(\frac{\gamma_{gb}}{2\gamma_s}\right), \tag{5.4}$$

where γ_{gb} and γ_s are the grain boundary and surface energies, respectively. For metals, $\gamma_s/\gamma_{gb} \approx 1/3$ so that ϕ is approximately 20 degrees. The initial condition (i.e. $h(x,0)$) for the PDE is the surface profile of the continuous film immediately following the island

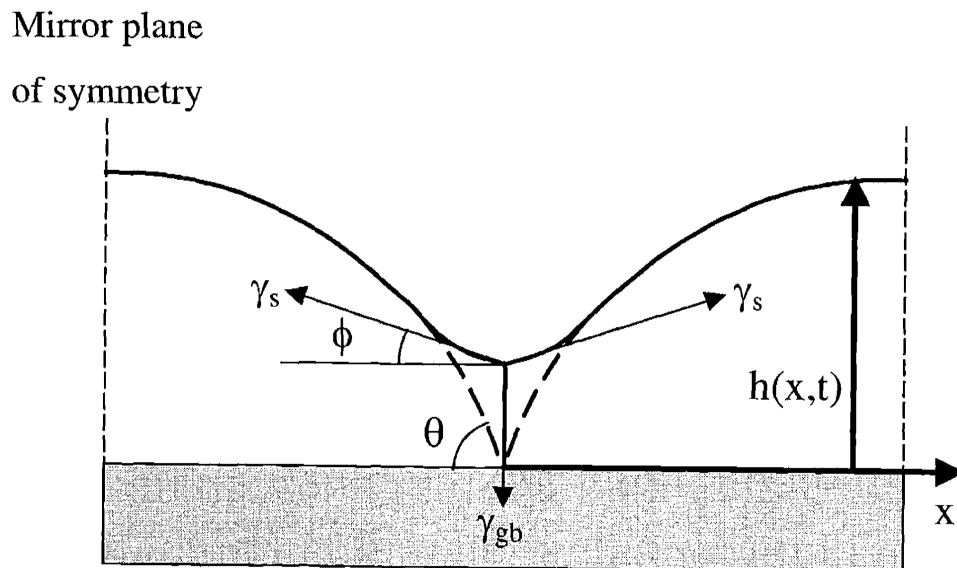

Figure 5-1: Surface morphology of the film before and after island coalescence. Prior to coalescence, the islands have a circular cap cross-section (dashed line) with an island-substrate contact angle θ. After coalescence, the balance between the surface energy γ_s and grain boundary energy γ_{gb} result in an angle ϕ between the grain surface and the plane of the substrate.

coalescence process, as shown in Fig. 5-1. Prior to island coalescence, the islands are assumed to have a circular cap cross-sectional shape with island-substrate contact angle θ. After island coalescence, the grains have are deformed due to the island zipping process and the grain surface forms an angle ϕ with the plane of the substrate at the grain boundary, as described above in terms of the boundary conditions.

5.3.2 Modeling thin film growth of low-mobility materials

Low mobility materials tend to grow with columnar grain structures with an average grain size that increases through the thickness of the film, as shown in Fig. 1-2 [Mouc 69, Thor 77, Grov 84]. Grain boundary motion occurs at the surface of the growing film where high energy adatoms are mobile, but not in the bulk of the film where atoms at grain boundaries are immobile. The grain boundaries at the surface move in response to the grain boundary curvature in the plane of the film so that the average in-plane grain radius $\langle r \rangle$ evolves with film thickness as:

$$\langle r \rangle \cong C\, h^{1/2}, \tag{5.5}$$

where C is a constant and h is the film thickness. Although the thickness dependence of the amorphous cluster size at the surface of the a-Ge was not studied, materials such as amorphous Cu-Ti films [Geye 98] and amorphous Zr-Al-Cu films [Mayr 01] exhibit a cluster-like surface morphology whose length scale increased with film thickness in general agreement with Eq. 5.5.

For low mobility materials, surface diffusion is very slow at room temperature so any change in the surface morphology due to diffusion according to Eq. 5.3 can effectively be ignored. However as noted previously, surface diffusion of adatoms during deposition must be somewhat appreciable in order for the grain size to increase with increasing film thickness. Therefore, the evolution of the film surface due to a deposition flux is dictated by the growth equation given by Eq. 5.2. The simplest surface morphology to consider is a film composed of hemispherical-capped grains with in-plane radius r that increase as $h^{1/2}$ as shown in Fig. 5-2(a). For a hemispherical-capped grain

(a) hemispherical cap grains

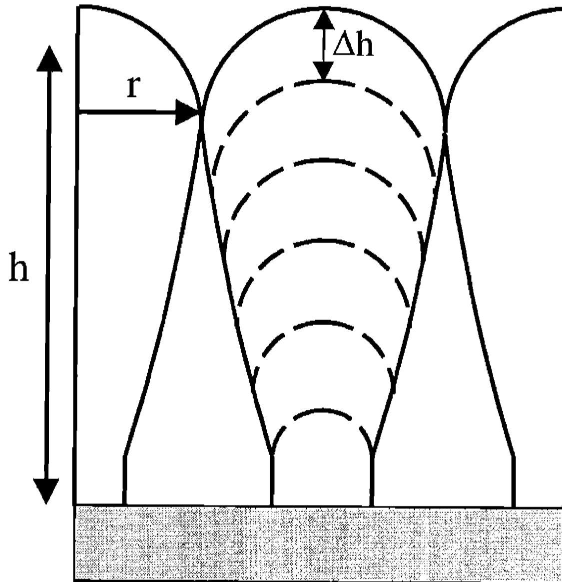

(b) grains with grain boundary angle ϕ

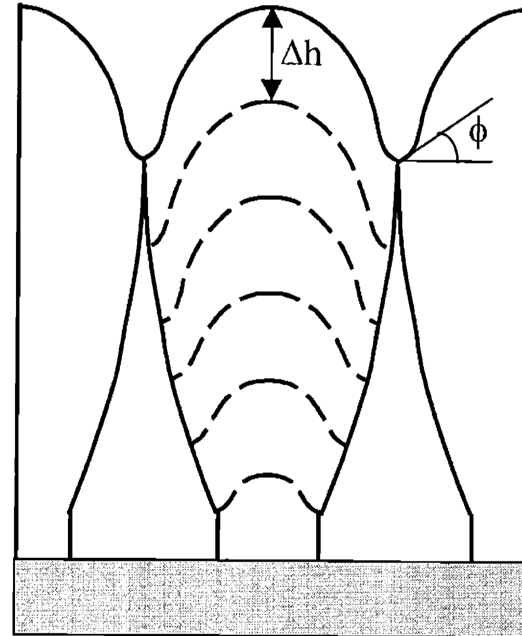

Figure 5-2: Schematic of the surface morphology evolution with deposition for (a) hemispherical cap grains that increase in height by Δh linearly with time of deposition, and (b) grains with angle ϕ between the grain surface and the plane of the substrate that increase in height Δh faster at the center of grain than at the grain boundary due differences in curvature. The in-plane grains radius r is shown to increase with the film thickness h as $h^{1/2}$.

with constant curvature across the surface, the second term on the right-hand side of Eq. 5.2 is constant so that the flux of material at every point across the surface is the same. So to an approximation, the grain surface remains hemispherical in shape with increasing film thickness as shown in Fig. 5-2(a).

If however, the angle ϕ at the grain boundary between the grain surface and the plane of the substrate is less than 90 degrees, the boundary condition is more similar to that as shown in Fig. 5-1. In this case, the curvature at the center of the grain is greater than that near the grain boundary so that the second term on the right-hand side of Eq. 5.2 is not longer constant for every point across the surface. Instead, the center of the grain

will increase in thickness faster than at the grain boundary where the curvature is lower. Furthermore, the center of the grain will grow faster and faster as the curvature will continuously increase with increasing film thickness at the center of the grain, as shown schematically in Fig. 5-2(b). The numerical solution of the PDE given by Eq. 5.2 is inherently unstable because of the compounded increase in curvature at the center of the grain with time. Instead, a simple analogy can be considered by defining a constant $r_{\Delta K}$ equal to the rate of increase in the difference in the curvatures between that at the center of the grain and at the grain boundary. If the difference in curvature $\Delta K = K_{center} - K_{gb}$ is compounded continuously during deposition, then the difference in curvature will increase as $\Delta K(t) = \Delta K_0 exp(r_{\Delta K}t)$, where K_0 is the difference in curvature at time equal to zero and t is time. Time equal to zero is the time at which the film becomes continuous after island coalescence. The difference in height between the center of the grain and at the grain boundary at time equal to zero is given by $h_{cap,0}$. The difference in height will increase by Δh_{cap} in a time Δt according to $\Delta h_{cap} = bJ(K_{center}-K_{gb})\Delta t$, as can be seen from Eq. 5.2. Therefore, the difference in height between the center of the grain and at the grain boundary $h_{cap}(t)$ will increase with time as:

$$h_{cap}(t) = h_{cap,0} + bJ\,K_0\int_0^t exp(\,r_{\Delta K}\,t\,)dt = h_{cap,0} + \frac{bJ\,K_0\left[exp(\,r_{\Delta K}\,t\,) - 1\right]}{r_{\Delta K}}. \qquad (5.6)$$

For nominal values of $r_{\Delta K}$, h_{cap} will increase exponentially with time such that the aspect ratio of the grain cap, given by h_{cap}/r where r is the in-plane grain radius at the surface, will also increase exponentially. As the aspect ratio of the grain cap increases, the curvature at the center of the grain will become very large such that surface diffusion due to curvature may mitigate the exponential increase in the grain cap aspect ratio.

For small values of $r_{\Delta K}$, $\exp(r_{\Delta K}t)$ is approximately equal to $1+r_{\Delta K}$ so that Eq. 5.6 reduces to $h_{cap}(t) = h_{cap,0} + bJK_0t$ so that the grain cap height increases linearly with time. In this case, Jt is the increase in film thickness since the time that the film becoming continuous due to island coalescence so that $Jt = h-h_0$, where h is the total film thickness and h_0 is the film thickness at which the film became continuous. To further simplify Eq.

5.6, the approximations are taken that $h_{cap,0}= h_0$ and that $h_0 >> b$ so that the evolution of h_{cap} with film thickness can be expressed as:

$$h_{cap}(h) \approx h_0 + b\,K_0\,h \tag{5.7}$$

By assuming a value of b= 1 nm [Sand 92] and using h_0= 5 nm for a-Ge (the film thickness coincident with the tensile stress-thickness peak in Fig. 3-15), the only unknown quantity is K_0, the initial difference in curvature between the center of the grain and the curvature at the grain boundary. Since the film surface is assumed to approach the grain boundary at a relatively shallow angle ϕ as shown in Fig. 5-2(b), the curvature of the surface near the grain boundary is low, or perhaps even negative, but will be assumed to be approximately zero so that $K_{gb}= 0$. The film surface at the center of the grain immediately after island coalescence is approximately a hemispherical cap so that $K_{center} \approx 1/h_0$ and therefore $K_0= K_{center}-K_{gb} \approx 1/h_0$. By combining Eq. 5.5 and Eq. 5.7, the aspect ratio of the grain cap $AR_{cap} = h_{cap}/r$ as a function of film thickness is approximately given by $AR_{cap} = h_{cap}/(Ch^{1/2})$, which at large film thicknesses reduces to $AR_{cap}= [b/Ch_0]h^{1/2}$ so that the aspect ratio continuously increases with film thickness.

Two cases for surface morphology evolution during deposition were considered in this section. In the first case shown in Fig. 5-2(a), the grain surface was assumed to remain as a hemispherical cap whose height is equal to the in-plane grain radius at the surface. In the second case, the grain surface was assumed to approach the grain boundary at an angle ϕ as shown in Fig. 5-2(b). Due to the difference in the curvature at the center of the grain and the lower curvature at the grain boundary, the center of the grain was shown to increase in thickness faster than at the grain boundary. For this case, the aspect ratio of the grain cap increases with increasing film thickness. As will be shown in section 5.4, the excess surface stress associated with the grain cap surface area results in a compressive stress, whose magnitude depends on the aspect ratio of the grain cap.

5.3.3 Modeling thin film growth of high-mobility materials

For high mobility materials, the average in-plane grain size, which spans the thickness of the film, scales with the film thickness as a result of grain growth during deposition [Lita 99, Knor 95, Thom 90]. Grain boundary diffusivity must be appreciable at room temperature in order for grain growth in the bulk of the film to occur during deposition. Surface diffusivity would also be expected to be considerable at room temperature, although the calculated diffusivity at room temperature using experimentally determined values ranges over greater than 10 orders of magnitude [Neum 72]. For Ag deposited at room temperature, self-affine scaling of the surface roughness was observed indicating that surface diffusion of Ag is clearly limited at room temperature [Pala 94, Thom 94]. With only limited surface diffusion at room temperature, non-equilibrium growth conditions should lead to an evolution of the surface morphology with increasing film thickness, similar to that described in section 5.3.2 for low-mobility materials. The scaling behavior described in the previous section will be slightly modified since in high mobility materials, the grain size scales with the film thickness.

Two scenarios for the evolution of the film surface morphology during deposition will be considered, similar to the discussion in section 5.3.2 for low-mobility film. In the first case, the grain cap is assumed to remain as a spherical cap with an in-plane grain radius that increases linearly with film thickness. In the second case, the grain surface is assumed to approach the grain boundary at an angle ϕ as shown in Fig. 5-2(b). Due to the difference in the curvature at the center of the grain and the lower curvature at the grain boundary, the center of the grain increases in thickness faster than at the grain boundary. For the growth law of the grain cap height given by Eq. 5.6, the aspect ratio of the grain cap increases exponentially with time, however surface diffusion will tend to mitigate the exponential growth, especially for higher melting points materials. As will be shown in section 5.4, the excess surface stress associated with the grain cap surface area results in a compressive stress, whose magnitude depends on the aspect ratio of the grain cap.

5.4 Compressive stress generation in continuous films

5.4.1 Finite element method (FEM) modeling of compressive stress generation

In section 5.3, the grain shape at the film surface was shown to evolve during deposition with increasing film thickness. The geometry of the grain cap at the surface can be grossly characterized by the aspect ratio equal to the height of the grain cap divided by the in-plane grain radius at the film surface. For convenience, the grain cap will be modeled using finite element methods (FEM) as an ellipsoid with radius r and grain cap height h_{cap} as shown in Fig. 5-3 for a film of thickness h. The free surface of

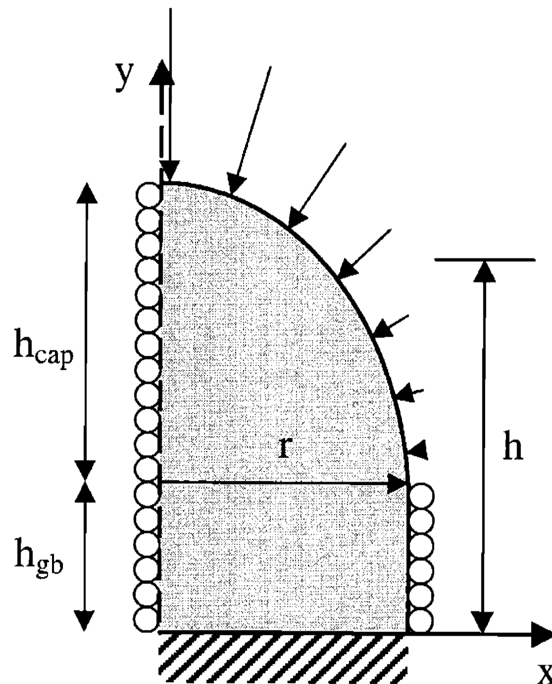

Figure 5-3: FEM axisymmetric representation of a grain with in-plane radius r, average film thickness h, and an ellipsoidal grain cap. The aspect ratio of the grain cap is equal to h_{cap}/r where h_{cap} is the height of the grain cap. The x-axis represents the grain-substrate interface where traction is imposed. The y-axis is a rotational axis of symmetry along which sliding is allowed. Sliding along the grain boundary of height h_{gb} is also allowed. The arrowed lines along the grain surface represent the local pressure proportional to the local mean curvature.

the grain has an excess energy equal to the surface area times the surface energy, or more accurately the surface stress. Moving the surface of the grain cap towards the local centers of curvature reduces the excess energy of the system by decreasing the surface area. The local pressure difference between the inside and outside of the grain surface is proportional to the local geometric mean curvature of the surface, as shown schematically in Fig. 5-3. In the FEM calculations, displacements were imposed at the film surface proportional to the local pressure and which result in the same boundary conditions at the surface as applying the corresponding pressure. Decreasing the surface area to reduce the surface energy results in a compressive stress in the volume of the grain and an associated increase in strain energy. The balance between the surface energy reduction and the increase in strain energy produces an energy-minimizing surface shape with an associated average compressive stress within the grain. The pressure acting at the surface of the grain results in an in-plane compressive stress, as shown in Fig. 5-4. The horizontal components of the pressure (in the x-direction) acting on opposing surfaces of the grain cap produce an in-plane compressive stress σ_x in the grain cap, while the vertical components of the pressure (in the y-direction) produce a stress σ_y in the volume of the grain. The in-plane Poisson expansion due to the vertical stress σ_y is prevented in the volume of the grain bounded by grain boundary due to the symmetric boundary conditions resulting in an additional component of the in-plane compressive stress σ_x.

FEM calculations were performed for several different geometries to test the influence of the aspect ratio of the grain cap (h_{cap}/r) and the aspect ratio of the entire grain (h/r). For each geometry, the energy-minimizing grain cap shape was determined and the resulting in-plane compressive stress was calculated as a function of the in-plane grain radius, as shown in Fig. 5-5. The elastic constants for Cu were used in the FEM calculation with Youngs modulus E= 127.7 GPa and Poisson ratio ν=0.34 [Simm 71], although the trends observed in Fig. 5-5 will apply in general for a-Ge.

As can be seen in Fig. 5-5 for all curves, the average equilibrium compressive stress decreases in magnitude with increasing in-plane grain size. For a given island geometry, the ratio of the grain cap surface area to grain volume decreases with increasing grain size. Since the energy reduction due to the decrease in surface area must

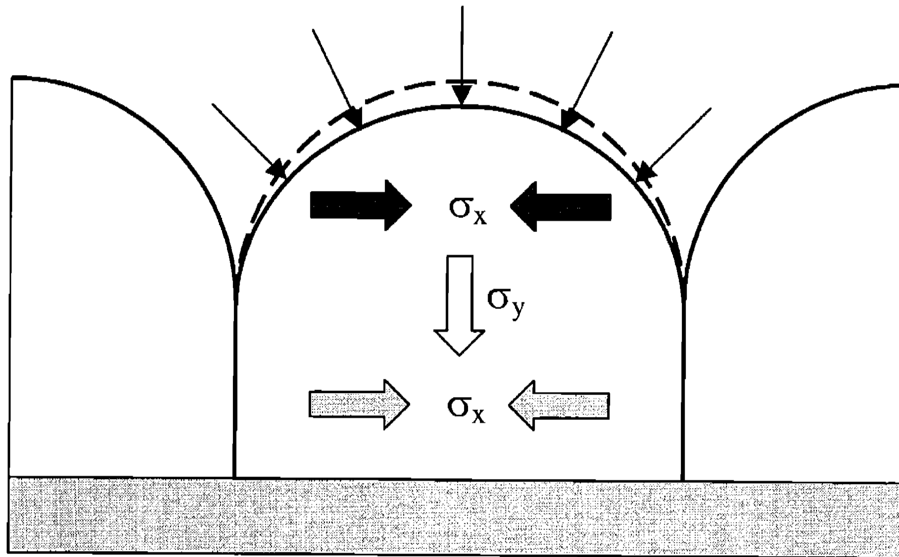

Figure 5-4: Schematic diagram showing the origin of the in-plane compressive stress σ_x in the grain due to the action of a reduction in the grain cap surface area. The dark gray block arrows indicate the in-plane stress in the grain cap due to the horizontal components of the "pressure" acting on the opposite surfaces of the grain cap. The symmetric boundary conditions at the grain boundaries prevent a Poisson expansion due to σ_y, which therefore results in an in-plane compressive stress σ_x in the lower portion of the grain as indicated by the light gray block arrows.

balance with the volumetric strain energy at equilibrium, the equilibrium compressive stress decreases in magnitude with increasing grain size. For a given grain cap aspect ratio, for example as shown in Fig. 5-5(a), the average equilibrium compressive decreases in magnitude with increasing grain aspect ratio h/r. For a given island radius and grain cap aspect ratio, the grain cap surface area is a constant while the total volume of the grain increases linearly with film thickness, so that the influence of the surface becomes negligible at an infinite film thickness under these restricted conditions. Finally as can be seen by comparing the curves in Fig. 5-5, the average equilibrium compressive stress increases in magnitude with increasing grain cap aspect ratio for a given grain radius and

(a)

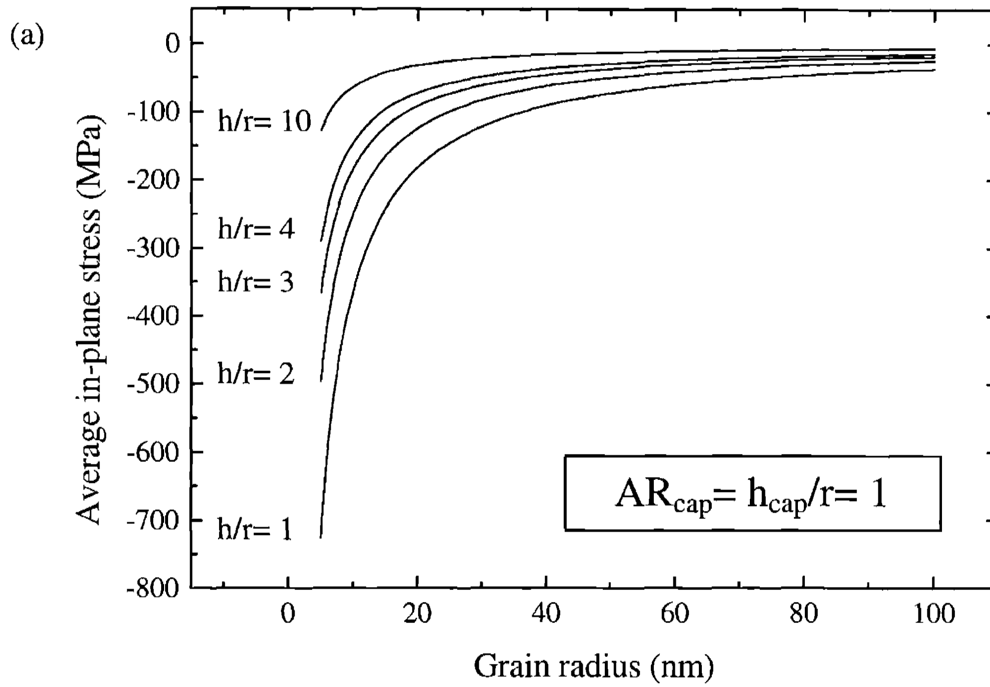

(b)

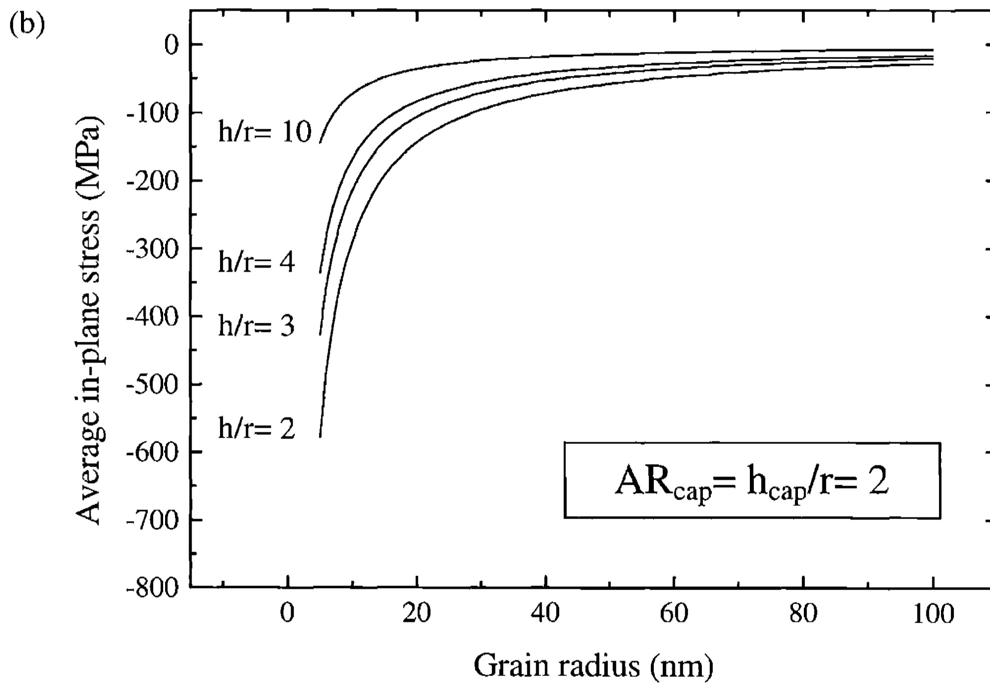

Figure 5-5: <continued on next page>

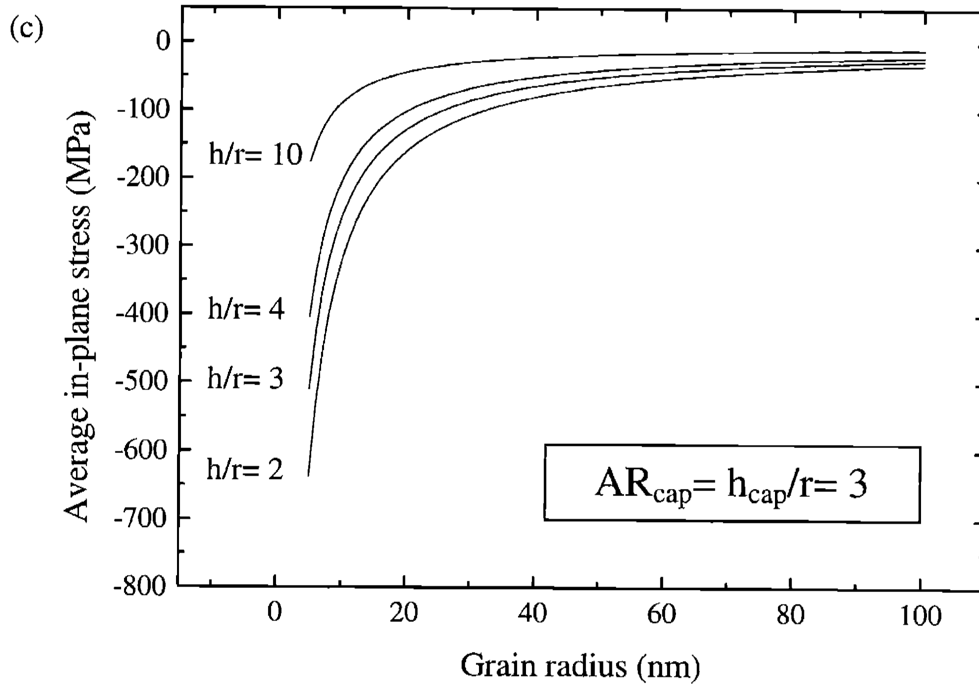

Figure 5-5: FEM calculations of the average in-plane stress as a function of the in-plane grain radius r for grain cap aspect ratios of (a) AR_{cap}= 2, (b) AR_{cap}= 4, and (c) AR_{cap}= 6. For each figure with different grain cap aspect ratio, the aspect ratio of the entire grain h/r was also varied.

grain aspect ratio. The FEM results for compressive stress generation as a function of grain geometry are compared in the next section to the measured stress evolution during deposition of continuous a-Ge and Cu films.

5.4.2 FEM model comparison to measured compressive stress evolution

In section 5.3.2, the thin film growth of low-mobility materials such as a-Ge was considered. For such materials, the average grain radius r increases with film thickness h as $h^{1/2}$. Although the thickness dependence of the amorphous cluster size at the surface of the a-Ge was not studied, materials such as amorphous Cu-Ti films [Geye 98] and amorphous Zr-Al-Cu films [Mayr 01] exhibit a cluster-like surface morphology, similar in appearance to grains in polycrystalline films, with a cluster length scale that increases with film thickness and whose size is smaller than the film thickness. From the stress

measurement during deposition of a-Ge shown in Fig. 3-15, the thickness at which the film becomes continuous is approximately 5 nm, coincident with the tensile peak in the stress thickness curve. If the island shape just prior to coalescence is assumed to be hemispherical, then the island radius is approximately equal to the film thickness and the constant C is Eq. 5.5 can be estimated as $C= r/h^{1/2}= 1 \text{ X } 10^5 \text{ m}^{1/2}$.

If the surface morphology of the a-Ge film is assumed to be composed of hemispherical caps during deposition, as shown in Fig. 5-2(a), then the aspect ratio of the "grain" cap is always equal to 1 during deposition. Figure 5-5(a) can therefore be used to estimate the compressive stress generation during deposition with a cluster radius at the surface that evolves as $Ch^{1/2}$. The calculated stress-thickness versus film thickness curve during deposition estimated for a thickening continuous a-Ge film is shown in Fig. 5-6(a) using the FEM results from Fig. 5-5(a) to estimate the compressive stress. The calculated stress-thickness curve demonstrates a decreasing stress-thickness with increasing film thickness as observed experimentally for a-Ge (see Fig. 3-15). However rather than a constant compressive instantaneous stress with increasing film thickness as observed experimentally, the instantaneous stress in the calculated stress-thickness curve decreases with increasing film thickness.

If the surface morphology of the a-Ge film is assumed to be composed of amorphous clusters with "grain" caps that evolve during deposition as shown in Fig. 5-2(b), then the aspect ratio of the caps increases exponentially during deposition. If the cluster radius at the surface is again assumed to evolve as $Ch^{1/2}$ but with an aspect ratio that increases linearly (rather than exponentially) with film thickness, the calculated compressive stress generation during deposition can be estimated using the FEM results in Fig. 5-5. The calculated stress-thickness versus film thickness curve is shown in Fig. 5-6(b) using a linear growth rate of the grain cap aspect ratio that best fits the data. The calculated stress-thickness curve demonstrates a compressive instantaneous stress that slightly decreases with increasing film thickness in better agreement with the experimental data for a-Ge than Fig. 5-6(a). The instantaneous stress (i.e. slope of the stress-thickness versus thickness curve) for the calculated curve in Fig. 5-6(b) is

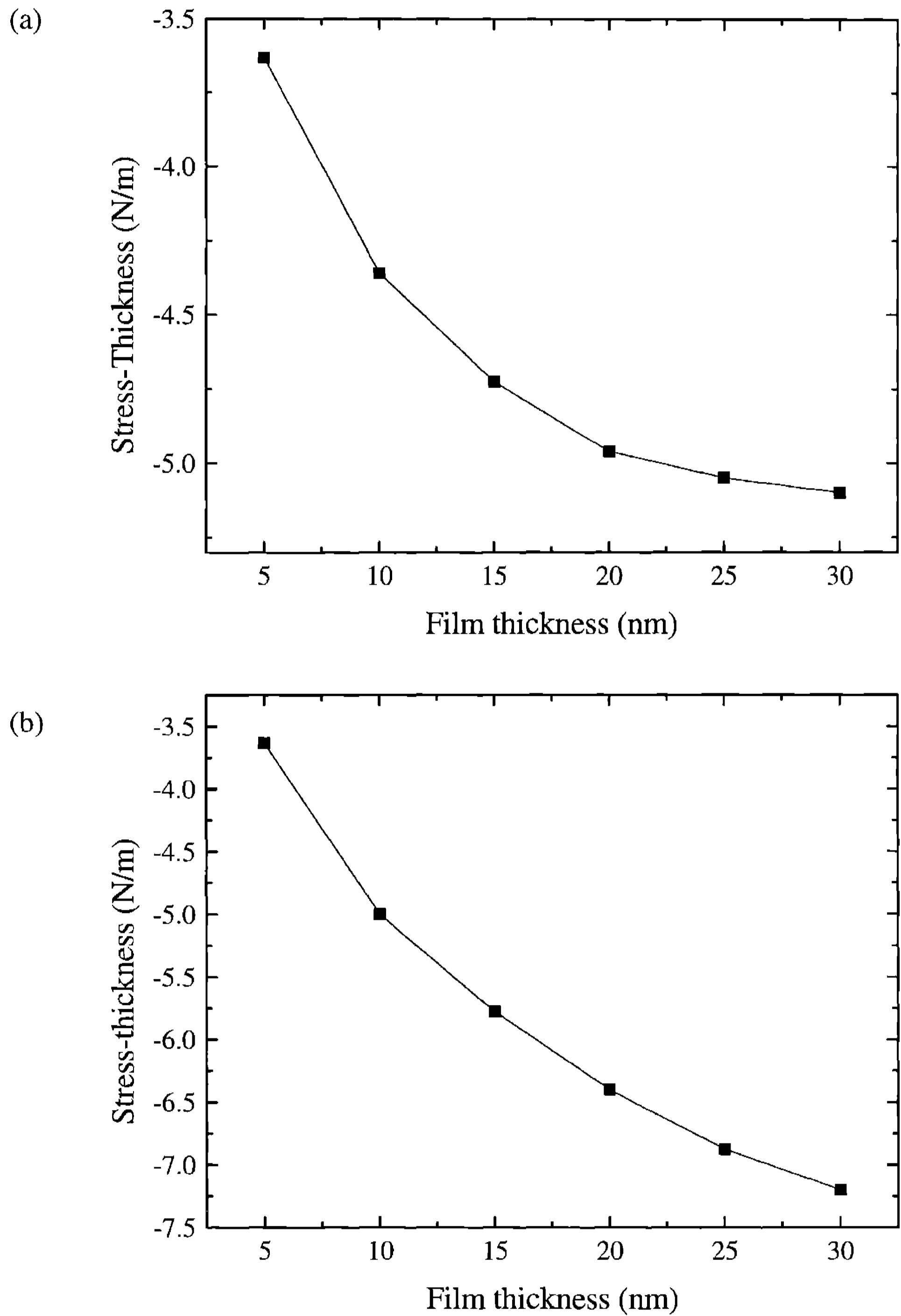

Figure 5-6: Calculated compressive stress generation during thin film deposition of a continuous *a*-Ge film for (a) a cluster cap shape at the surface that remains hemispherical during deposition (see Fig. 5-2(a)), and (b) a cluster cap shape that increases in aspect ratio linearly during deposition (see Fig. 5-2(b)). The average cluster size at the surface was assumed to increase as $h^{1/2}$.

approximately one-third of the value measured experimentally for a-Ge (see Fig. 3-15). However a direct comparison is difficult because the elastic constants for Cu were used in the FEM results shown in Fig. 5-5.

In section 5.3.3, the thin film growth of high-mobility materials such as Cu was considered. For such materials, the average grain radius r increases linearly with the film thickness h. From the stress measurement during deposition of Cu shown in Fig. 3-10, the film thickness at which the film becomes continuous is approximately 10 nm, coincident with the tensile peak in the stress thickness curve. The in-plane grain radius will be assumed to equal the film thickness during deposition. If the surface morphology of the Cu film is assumed to be composed of hemispherical grain caps during deposition, as shown in Fig. 5-2(a), then the aspect ratio of the grain cap is always equal to 1 during deposition. Therefore, the calculated stress-thickness versus film thickness curve during deposition can be estimated for a thickening continuous Cu film using the FEM results in Fig. 5-5(a) for a constant grain aspect ratio h/r and grain cap aspect ratio equal to 1. The calculated stress-thickness as a function of film thickness is a constant because the magnitude of the compressive stresses in Fig. 5-5(a) scales with the inverse of the grain size, which scales linearly with the film thickness. The magnitude of the constant stress-thickness therefore depends on the scaling of the grain size with the film thickness.

If however, the surface morphology of the Cu film has grain caps that evolve during deposition as shown in Fig. 5-2(b), then the aspect ratio of the caps increases exponentially during deposition. If the in-plane grain radius is again assumed to evolve linearly with film thickness ($h/r=2$) but with an aspect ratio that increases linearly (rather than exponentially) with film thickness, the calculated compressive stress generation during deposition can be estimated using the FEM results in Fig. 5-5. The calculated stress-thickness versus film thickness curve for Cu is shown in Fig. 5-7 using a linear growth rate of the grain cap aspect ratio that best fits the data. The calculated stress-thickness curve demonstrates a decreasing stress-thickness with increasing film thickness, in agreement with the measured data for Cu (see Fig. 3-10). In addition, the instantaneous stress (i.e. slope of the stress-thickness versus thickness curve) in the calculated curve is constant with increasing film thickness but only approximately one-fifth of the value measured experimentally for Cu.

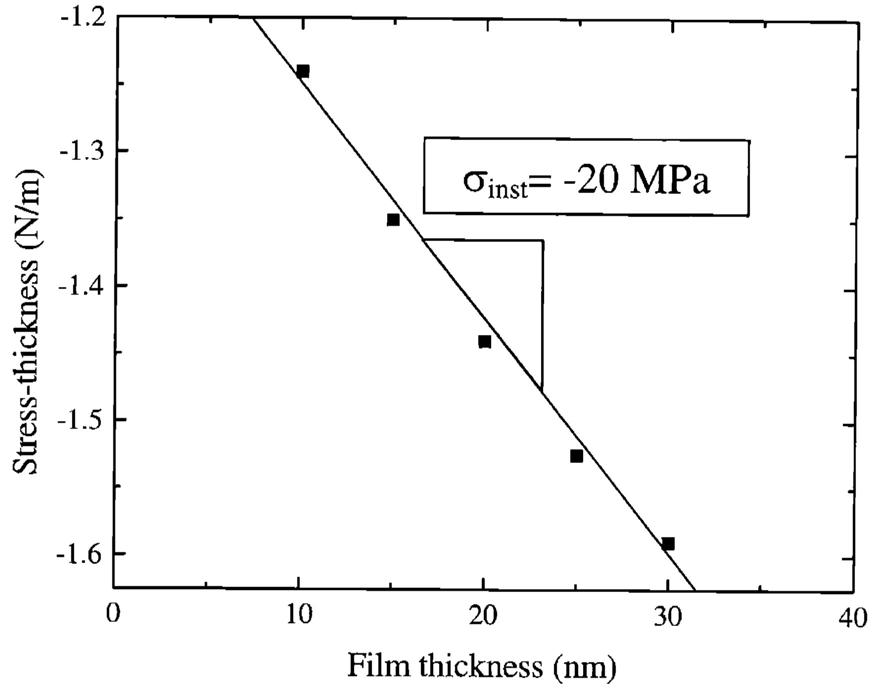

Figure 5-7: Calculated compressive stress generation during thin film deposition of a continuous Cu film for a grain cap shape that increases in aspect ratio linearly during deposition (see Fig. 5-2(b)). The in-plane grain radius was assumed to increase linearly with film thickness.

5.4.3 Discussion

To maintain a constant instantaneous stress with increasing film thickness, the ratio of the surface area to grain volume must remain constant during deposition since the equilibrium compressive stress is calculated by balancing the surface energy reduction associated with the grain cap surface area and the strain energy in the volume of the grain. Since the volume of the film increases linearly with the film thickness h, the surface area must increase as $h^{3/2}$ to maintain a constant surface area to volume ratio. If the aspect ratio of the grain cap increases linearly with increasing film thickness, the surface area of the cluster cap increases quickly enough with increasing film thickness to maintain a constant instantaneous stress as can be seen from Fig. 5-7. As the grain cap aspect ratio increases with film thickness, the curvature of the surface also becomes greater and curvature-driven diffusion should eventually prevent further increases in the

aspect. However, the in-plane grain radius is also increasing with increasing film thickness so that the diffusion distances become larger at greater film thicknesses, and therefore the aspect ratio can increase with increasing film thickness.

The magnitude of the instantaneous stress calculated using the FEM results is smaller than that observed experimentally for both *a*-Ge and Cu. In order for the instantaneous stress to be larger, the compressive stresses must be greater at larger film thicknesses. In order for the compressive stress to be larger, the grain cap aspect ratio must continuously increase with increasing film thickness. However at very large film thicknesses, this compressive stress effect should become negligible, as the influence of any surface phenomena should not affect the bulk stress in the volume of the material. Although no reports exist in the literature for *in situ* stress measurements of very thick films deposited by physical vapor deposition, 1 μm-thick W films deposited by chemical vapor deposition (CVD) have been shown to exhibit a turnover from compressive stress to tensile stress at large film thicknesses [Leus 93].

According to the compressive stress generation model described above, the magnitude of the compressive stress should decrease with decreasing deposition rate or increasing deposition temperature. For either a decreasing deposition rate or higher temperature, the surface morphology should be closer equilibrium because surface diffusion is more effective in decreasing the curvature at the surface. For Ag deposited at different deposition temperature as shown in Fig. 3-7, the instantaneous stress decreases with increasing deposition temperature in agreement with the compressive stress generation model, however the interpretation of these results is difficult because changing the deposition temperature also strongly affects the grain size during deposition. For Cu deposited at different deposition rate as shown in Fig. 3-13, the compressive instantaneous stress *increases* with decreasing deposition rate contrary to the prediction of the compressive stress generation model. The observation of a greater rate of compressive stress generation with decreasing deposition rate is somewhat surprising, but has been confirmed by other researcher [Flor_2 02] and cannot be explained within the framework of our model for compressive stress generation.

In order to validate the model for compressive stress generation due to non-equilibrium thin film surface morphology evolution, the surface structure must be

monitored during growth using an *in situ* technique such as light scattering spectroscopy [Chas 98] or x-ray reflectivity [Chas 97].

5.5 Stress behavior during growth interrupts

When film growth of high-mobility materials is interrupted, a tensile rise in the stress is observed over time, as shown for Cu in Fig. 3-11. The initial rate of the tensile rise increase is slower and the time to reach an equilibrium stress value increases with increasing film thickness, as shown for Cu in Fig. 3-12. When growth is resumed, the stress-thickness decreases and assumes the value that existed before the growth interrupt so that the observed tensile rise behavior is reversible. The growth interrupt behavior can be understood in terms of the compressive stress generation model described in the previous section.

During deposition, a non-equilibrium surface structure develops because surface diffusion cannot keep up with the changes in the surface morphology due to the deposition flux. However during a growth interrupt, the deposition flux stops and diffusion can smooth out the surface of the film. As the aspect ratio of the grain cap surface decreases, the magnitude of the compressive stress decreases (see Fig. 5-5) which appears as a tensile rise, as observed experimentally for Cu in Fig. 3-12. The initial rate of the tensile rise is much faster than at later times because the curvature-driven diffusion slows down with time as the surface becomes smoother. In addition, the rate of the tensile rise increase is slower for growth interrupts performed at larger film thicknesses (see Fig. 3-12) because the grain sizes are larger and the diffusion distances are greater. Figure 3-12 shows that in Cu the magnitude of the rise in the tensile stress (after long enough times for the stress to equilibrate) is nominally independent of the film thickness, however in Fig. 3-14 the magnitude of the rise in the tensile stress decreases with decreasing deposition rate. At slower deposition rates, surface diffusion has more time to smooth out the non-equilibrium surface morphology that develops due to the deposition flux. Consequently, the magnitude of the tensile rise during growth interrupts should decrease with decreasing deposition rate according to the compressive stress generation model described in the last section. However as mentioned previously, the model does not correctly predict the influence of the deposition rate on the compressive stress

behavior during deposition. Finally, when growth is resumed after a growth interrupt, a non-equilibrium surface morphology quickly develops again resulting in the same compressive stress behavior observed before the growth interrupt.

For the *a*-Ge films deposited at room temperature, no observable change in stress occurs during growth interrupts over time scales comparable to the time to deposit the film (see Fig. 3-16). Because surface diffusion in low-mobility materials at room temperature is negligible, the non-equilibrium surface morphology remains unchanged when deposition is interrupted. However for *a*-Ge films deposited at 270°C as shown in Fig. 3-17, a rise in the tensile stress is observed during growth interrupts presumable due to faster surface diffusion at elevated temperature.

5.6 Discussion of other models in the literature

Several other models have been proposed in the literature as to the origin of the compressive stress at large film thicknesses. Abermann first suggested that the long-term compressive stress is a continuation of the compressive that develops during the initial island stage of growth [Aber 85, Camm 00, Flor 01], however the tensile stress generation due to island coalescence masks the compressive stress that developed during the island stage of growth. As mentioned in Chapter 4, if diffusive stress relaxation of the tensile stress at grain boundaries occurs after reaching film continuity, the early compressive stress can be umasked and the film will become net compressive again. However, the lack of any observable tensile stress relaxation during growth interrupts indicates that diffusive stress relaxation is not significant. In addition, a compressive stress after film continuity is observed for *a*-Ge for which any significant stress relaxation is improbable. Spaepen has suggested that extra atoms may be incorporated into the film at adjacent compressive surface ledges resulting in a compressive stress in the film [Spae 00], however the validity of such a mechanism is difficult to prove. Recently, another mechanism for compressive stress generation in continuous films was proposed as the flux-driven incorporation of excess atoms into grain boundaries [Flor 02, Chas 02]. The argument states that during growth, the deposition flux produces an overpressure greater than the equilibrium vapor pressure of the film material resulting in an increased chemical potential of the atoms at the surface. The excess chemical potential drives the

surface atoms to the lower chemical potential at the grain boundary until the chemical potentials at the surface and grain boundary are balanced. The excess incorporation of atoms into the grain boundary creates a compressive stress during deposition. Unfortunately, the details of the model are not yet published and have been discussed only in a review [Flor 02]. However, this mechanism cannot explain the compressive stress observed in *a*-Ge for which surface and grain boundary diffusion are negligible.

The reversible tensile rise behavior during growth interrupts has also been explored in the literature. Abermann suggested that the tensile rise is the result of film densification due to grain growth, however the reversible nature of the tensile rise rules out grain growth [Aber 85, Chau 72]. Spaepen has suggested that the reversible tensile rise behavior is the result of the creation and annihilation of compressive-type surface ledges resulting in a change in the surface stress. During a growth interrupt, the elimination of compressive-type ledges results in an apparent tensile rise for which diffusion over long distance must occur so that the time scale of the tensile rise is long. When growth is resumed, the nucleation of new ledges is a local process that occurs quickly and explains the relatively fast return to the compressive behavior observed prior to the growth interrupt. The model for excess incorporation of atoms into grain boundaries during growth has also be used to explain the reversible tensile rise behavior. When the growth flux is terminated, the surface chemical potential decreases below that of the grain boundary so that the atoms flow back out onto the surface, relieving the compressive stress due to the excess atoms at the grain boundary. When growth is resumed, the chemical potential at the surface increases and the compressive stress in the film is established again. Again, the details of the models have not yet been published as necessary for a critical review of the mechanism.

Chapter 6

Conclusions and future work

6.1 Conclusions and summary

In this thesis, the correlations between thin film formation by the Volmer-Weber mechanism and the associated evolution of thin film stress during deposition was studied. Towards that end, a new electrical technique for the *in situ* measurement of stress during deposition was developed using piezoresistive microcantilever devices, also referred to as piezocantilevers. In our study of stress evolution during Cu deposition, the piezocantilevers were found to give quantitatively similar results to those found in the literature using cantilever deflection techniques such as differential capacitance and laser deflectometery. However, the origin of a systematic measurement artifact during the initial couple nanometers of deposition has not yet been resolved. The advantages of the piezocantilever devices over other measurement techniques include insensitivity to mechanical vibration, no optical or mechanical alignment necessary, and a potentially greater measurement sensitivity due to the very thin silicon microcantilever substrates. In addition, the piezocantilever devices can be used to measure stress in thin films during chemical vapor deposition (CVD) due to cantilever lengthening, which is not possible with the cantilever deflection techniques if the film is deposited on both sides of the cantilever.

In all experiments considered in this thesis, thin films that grow by the Volmer-Weber mechanism were deposited by electron-beam evaporation (e-beam) in ultrahigh

vacuum (UHV) onto oxidized silicon substrate. The data presented for the Al, Ag, and amorphous Ge (*a*-Ge) films were collected by our collaborators Jerrold A. Floro and Sean J. Hearne at Sandia National Labs (SNL). The stress measurements for Cu were made using the piezocantilever devices. During deposition of the Al, Ag, Cu, and *a*-Ge films considered in this thesis, a generic stress evolution from an initial compressive stress to a maximum tensile stress coinciding with film continuity and then back to compressive stress was observed with increasing film thickness. The differences in behavior resulting from varying deposition conditions and materials systems provided a tool by which to understand and model the stress-structure relationship during thin film deposition.

In order to model the evolving microstructure during growth, a computer simulation of thin film growth by the Volmer-Weber mechanism was developed. By inputting the experimentally determined average grain size in the continuous film and the island contact angle, the simulation was able to capture the measured evolution of substrate coverage versus film thickness *during* deposition. The film growth simulation allowed modeling of microstructure-, temperature-, and time-dependent stress generation and relaxation mechanisms using a realistically evolving microstructure during thin film growth.

During the island stage of film growth, no significant stress was measured during the deposition of Ag, in contrast to Al films that supported stress from the very onset of deposition. Stress relaxation due to shear was more prevalent at the weakly bonded Ag-SiO_2 interface than for the much stronger Al-SiO_2 interface. The initial compressive stress behavior of Al during the island stage of growth was modeled as a size-dependent lattice contraction due to a Laplace pressure. Using the film growth simulation with a model for calculating the compressive stress as a function of island size, the simulation was able to qualitatively reproduce the early stress behavior as a function of film thickness for the Al film deposition. However, the magnitude of the calculated compressive stress indicates that significant relaxation of the compressive stress must occur during deposition.

The tensile stress resulting from island coalescence was modeled analytically and using finite element methods (FEM). The magnitude of the average tensile stress calculated using FEM was more consistent with experimental measurements than the

stresses calculated using the simple Hoffman analysis or the Nix-Clemens crack-closure model. A simple analytical treatment of the island zipping process was developed using average strains to calculate the strain energy resulting from grain boundary formation. Even using a series of assumptions that tend to result in an overestimation of the island coalescence stress, the analytical model predicts stresses closer to the FEM results than those of the Hoffman analysis and the Nix-Clemens model. For the hemispherical geometry, the FEM results were very similar in magnitude to the plane strain geometry and in agreement within a factor of 2 with the Freund-Nix model of island coalescence using Hertzian contant with attractive forces. In addition, the magnitude of the island coalescence stress calculated by FEM was found to decrease dramatically with decreasing island contact angle.

Using the contact-angle-dependent FEM results and assuming perfect island-substrate traction, the film growth simulation qualitatively reproduced the stress-thickness measurements of Al over the range of thicknesses prior to film continuity. If perfect island-substrate traction was assumed during the Ag film deposition, the simulation predicts the onset of an appreciable tensile stress at a much earlier film thickness than observed experimentally in Ag. By including a critical area criterion for island sliding in the simulation, the simulation produced stresses in general agreement with the measured stress-thickness data of Ag prior to film continuity.

Using the FEM results for island coalescence stress and a microstructure-dependent stress relaxation model, the simulation reproduced the qualitative trends in stress with film thickness observed experimentally for Ag deposited at different temperatures. The magnitude of the measured maximum stress-thickness decreased, and occurred at a larger film thickness, with increasing deposition temperature, consistent with the tensile stress generation model for a grain size that increases with increasing deposition temperature, as observed by TEM. The same correlation of a larger average grain size resulting in a smaller maximum tensile stress at a greater film thickness was observed for Ag deposited at different rates at room temperature. As the continuous films thickened, the slope of the measured stress-thickness curves for Ag indicated that the stress relaxation rate decreased with increasing deposition temperature. Although the proposed stress relaxation mechanism is thermally activated, the slower relaxation rate

after continuity reflects the strong film-thickness dependence of the stress relaxation mechanism as captured by the simulation results.

The stress evolution during deposition in the compressive regime at large film thicknesses and the stress behavior during growth interrupt were modeled in terms of a non-equilibrium surface morphology that develops during deposition. The evolution of the grain shape at the film surface during deposition was modeled as the competition between the deposition-induced film roughening and diffusion-driven smoothing. For the resulting non-equilibrium grain shapes, the in-plane compressive stress resulting from excess surface stress is calculated using finite element method (FEM) solutions. The stress-thickness versus film thickness curves calculated using the non-equilibrium growth conditions and the FEM calculation of compressive stress demonstrate a decreasing compressive stress-thickness with increasing film thickness, in agreement with the experimental stress measurements of continuous *a*-Ge and Cu films during deposition. However, the magnitude of the calculated instantaneous stress was smaller than measured experimentally by more than a factor of 3.

The non-equilibrium growth model was also used to explain the stress behavior during growth interrupts of low-mobility materials such as *a*-Ge and high mobility materials such as Cu. During a growth interrupt when the deposition flux is eliminated, surface diffusion drives the grain shape towards equilibrium with an associated time-dependent decrease in the compressive stress that appears as a tensile rise, as observed experimentally during growth interrupts of Cu. No such tensile is observed experimentally for *a*-Ge because surface diffusion at room temperature is negligible. When deposition is resumed, the surface morphology again assumes a non-equilibrium shape that results in compressive stress generation similar to that observed before the growth interrupt. The reversible nature of the surface morphology evolution due to non-equilibrium growth conditions explains the reversible tensile rise behavior in high mobility materials.

6.2 Future work

6.2.1 Piezocantilevers

Although the measurement sensitivity of the piezocantilever devices is nominally equivalent to that of the MOSS system, the sensitivity could be improved by a factor of 20 by simple changes to the design and fabrication. Because of limitations of the grind and polish procedure to thin the (110) device wafer, the cantilever thickness had to be greater than 20 μm. With the increasing interest in MEMS applications over the past few years, custom wafer vendors can now create bonded wafer pairs with a 5 μm-thick (110) device wafer bonded to a 500 μm-thick (100) handle wafer. By decreasing the silicon microcantilever thickness from 20 μm to 5 μm, the measurement sensitivity could be increased by a factor of 4. In terms of the design, a boron doping concentration at the surface of 10^{20} B/cm^3 was chosen to avoid the temperature dependence the piezoresistive coefficient. At a doping concentration of 10^{18} B/cm^3, the piezoresistive coefficients are larger by a factor of 5, which corresponds to an increase in the measurement sensitivity by a factor of 5. By choosing the lower doping concentration, the temperature dependence of the piezoresistive coefficients would have to be calibrated. However over the 5°C temperature excursions that typically occur during thin film deposition, the piezoresistive coefficients only change by a couple percent. The increased measurement sensitivity would allow, for instance, the study of the stress behavior at very early times during the island stage of thin film growth when the measured stress-thickness is near the resolution of the current devices.

Because the piezocantilever technique monitors thin film stress by an electrical measurement, no mechanical or optical alignment is necessary unlike the differential capacitance and laser deflectometery methods, respectively. Changing the temperature of the deposition chamber during thin film stress measurements throws off the alignment, and therefore concurrent thermal cycling and stress measurements are not feasible for the differential capacitance and laser deflectometery methods. Using the piezocantilever devices, *in situ* thermal cycling of a thin film after deposition is possible and would allow for the study of the effect of post-deposition grain growth on the stress in the film, without breaking vacuum.

For all cantilever techniques used to measure thin film stress, the cantilever must be free to deflect. Therefore during chemical vapor deposition (CVD), both the front and backside of the cantilever are coated with the deposited material. If a uniform layer of material is deposited on both sides of the cantilever, a zero net cantilever curvature will result and cantilever deflection technique for measuring thin film stress during deposition will be useless. It should be noted that several reports exist in the literature of measuring CVD thin film stress, however the issue discussed above was not addressed [Leus 93, Nest 99, Hear 99, Shel 01]. Even though the cantilever does not deflect due to the stress in the CVD film, the cantilever does lengthen resulting in a stress in the substrate. The piezocantilever devices, which monitor the stress in the substrate, could therefore be used to measure stress during CVD deposition.

6.2.2 Compressive stress during island stage of thin film growth

The dramatic difference in the compressive stress behavior of the Al and Ag films during the island stage of thin film growth was attributed to the strength of the island-substrate interface. The weakly-bonded Ag-SiO_2 interface allowed for easy stress relaxation resulting in nominally zero stress at low film thickness, whereas a significant compressive stress was observed for the more strongly-bonded Al-SiO_2 system during the same stage of thin film growth. Copper would be a ideal candidate for study because the problem of interface strength between Cu and various underlayers has been carefully studied due to the recent introduction of Cu as an interconnect material. For instance, Cu is known to adhere poorly to Si_3N_4 [Bagc 96] and much better to materials such as Ta and TiN [Lane 00]. Unfortunately, varying the underlayer material also affects the grain size and texture of Cu films [Ziel 95].

In order to better model the compressive stress evolution during the island stage of growth, the kinetics of the stress relaxation process must be studied in more detail. The relative magnitudes of compressive stress generation and stress relaxation depend on both the thin film growth rate and the deposition temperature. At a higher deposition rate, less time elapses during a finite increase in the film thickness and therefore less stress relaxation can occur. Increasing the deposition rate also produces a higher island nucleation density and correspondingly smaller island sizes at a given film thickness. In

terms of the Cammarata model for compressive stresses in islands (see section 4.3.4.1), the higher deposition rate results in a smaller lock-down radius. However since the islands are also smaller for a higher deposition rate, the net influence on the compressive stress with increasing deposition rate is inconclusive (see Eq. 4.7). In terms of the compressive shell model (see section 4.3.4.2), less stress relaxation and smaller island sizes with increasing deposition rate produces a larger compressive stress at a given film thickness. Increasing the deposition temperature results in a smaller island nucleation density and correspondingly larger island sizes at a given film thickness. If the stress relaxation mechanism is a thermally-activated process, such as diffusion or dislocation glide through obstacles, the rate of stress relaxation should increase with increasing deposition temperature. In terms of the compressive shell model, faster stress relaxation and larger island sizes with increasing deposition temperature produces a smaller compressive stress at a given film thickness. At least for the compressive shell model, these trends with changing deposition rate and temperature would support the origin of the compressive stress in islands.

The nature of the compressive stress relaxation mechanism can also be explored by performing growth interrupts during the island stage of thin film growth at different thicknesses and temperatures. By varying the film thickness for different growth interrupts, the island size can be changed and the dependence of the microstructural length scale on the stress relaxation mechanism can be determined. By varying the deposition temperature, the activation energy of the stress relaxation mechanism can be studied. Unfortunately, increasing the temperature causes island coarsening so that the island size at a given film thickness is larger and coarsening will occur during the growth interrupt. If the microstructural and temperature dependencies of the compressive stress relaxation mechanism are known, the stress relaxation rate can be more accurately modeled. With an accurate model for the stress relaxation, the models for compressive stress generation can be thoroughly compared against experimental data. However, it should be noted that extremely good measurement sensitivity is required for these types of measurements since the stress-thickness during the island stage of growth is relatively small compared to the noise in the measurement technique.

6.2.3 Film growth simulation

The current version of the film growth simulation assumes conditions of a constant nucleation rate and a constant radial growth velocity of growing islands. The simulation was shown to match the experimentally measured evolution of substrate coverage versus film thickness during deposition. However, the simulation does not conserve volume consistent with a constant deposition rate, especially at low substrate coverage. To conserve volume during deposition in the simulation, the material not associated with the growth of existing island must be involved in the nucleation of new islands. For the expected critical nucleation size of only a couple atoms, the simulation must be able to track an extremely large number of islands during growth. In addition, island coarsening should be implemented to agree with the observed increasing island size with film thickness. Coarsening due to curvature-driven grain boundary motion both before and after film continuity should be included to emulate the experimentally observed grain growth during deposition.

6.2.4 Tensile stress generation during grain boundary formation

The absolute magnitude and exact nature of tensile stress generation resulting from island coalescence is still a matter of debate. One issue that has been addressed in this research using the film growth simulation is the influence of an increasing island size during deposition on the evolution of tensile stress generation with increasing film thickness. An ideal experimental verification of the models would involve the coalescence of a periodic array of islands with a known size, which could be created by photolithography and pattering of a continuous film. A continuous single crystal film would be ideal since no grain boundaries exist but a polycrystalline film may suffice. A higher temperature anneal would transform the islands from a square or hexagonal cross-sectional shape after patterning to the more realistic spherical cap shape. The high temperature anneal may eliminate the grain boundaries if a polycrystalline film is used, but may also results in unwanted island coarsening. After patterning and the high temperature anneal, further deposition will cause the periodic array of islands to coalesce at a known film thickness. The magnitude of the resulting tensile stress can be correlated to the island size at impingement and compared to the predictions from the various

models. If the magnitude of tensile stress increases after the film thickness coinciding with the initial island coalescence, then the model for continuous island coalescence stress generation with increasing film thickness [Shel 01, Flor 02] would be validated.

Molecular dynamics (MD) simulations can also be used to study the proposed mechanism of tensile stress generation resulting from island coalescence [Taka 02]. The nearly instantaneous process of grain boundary formation caused by island straining can be captured in the timescale of a MD simulation. Rather than a continium-based mechanical model for island coalescence, as discussed in section 4.4.5.2, island coalescence in the MD simulation should occur "naturally" as a result of the interatomic forces between islands. For the simplest case of two coalescing spheres, the MD results can be compared to the FEM predictions and Hertzian-contact model of Fruend and Chason considered in Chapter 4.

6.2.5 Stress behavior of continuous films during deposition and growth interrupts

The instantaneous stress (i.e. slope of the stress-thickness versus film thickness curve) after film continuity for the Al, Ag, Cu and *a*-Ge films is compressive. To study the origin of the compressive instantaneous stress, the microstructural and temperature dependence of the compressive stress generation mechanism must be examined. The average grain size for a given film thickness can be controlled by varying the initial deposition rate in that slower deposition rates results in larger grains. After deposition of a continuous film of a given film thickness and average grain size controlled by the initial deposition rate, the deposition rate can be varied and the correlation with the measured instantaneous stress can be studied without the added complication of a grain size dependency. Alternatively, the initial deposition rate can be varied to provide continuous films with different average grains sizes at a given film thickness, and the measured instantaneous stress can be correlated to different microstructural scales for the same subsequent deposition rate. The temperature dependency of the instantaneous stress can also be studied using a similar methodology. After deposition of a continuous film at a given film thickness, the sample can be annealed at a high enough temperature to promote profuse grain growth and then brought back to lower temperatures. At several

lower temperatures, at which grain growth will no longer occur after the high temperature anneal, the dependence of the instantaneous stress with temperature can be studied without the grain size changing due to grain growth. The photolithographically defined samples, as discussed previously, would also be useful since a film with a monodispersed grain size, which is also resistant to grain growth with increasing temperature, can be artificially constructed to test the grain size and temperature dependence of the instantaneous stress.

In Chapter 6, the evolving film surface morphology due to non-equilibrium growth conditions was ascribed as the source of the constant compressive instantaneous stress observed in continuous film during deposition. Direct evidence of an evolving surface structure with concurrent stress measurements during deposition would validate the model, without relying on indirect evidence from results in the literature. The morphology of the film surface during growth can be monitored by *in situ* techniques such as light scattering spectroscopy [Chas 98] and x-ray reflectivity [Chas 97]. Any morphological changes in surface structure can also be examined during growth interrupts. Alternatively, *in situ* resistance measurements may provide indirect evidence of the evolution of the grain cap shape during deposition and growth interrupts.

Also in Chapter 6, the partial differential equation (PDE) describing the evolution of the surface morphology during deposition was described in terms of curvature-driven surface diffusion and a deposition flux with steering effects. The PDE was used to provide intuition about the evolution of the surface morphology of the film during growth. To provide better quantitative confirmation of the modeling, the PDE should be solved numerically using finite difference techniques. However, the non-linear terms and higher-order derivatives make numerical solutions of such a PDE difficult. Preliminary work using a Level-set method to numerically solve the PDE are underway [Frie 02] and agree in general with the non-equilibrium structures proposed in Chapter 6.

Appendix A

Piezocantilever design and fabrication

A.1 Cleanroom fabrication

The piezocantilever devices were fabricated in the Microsystem Technology Laboratories (MTL) facilities at MIT. Two different cleanrooms were used that will be referred to in the process flow. The Integrated Circuit Laboratory (ICL) is a class 10 cleanroom and the Technology Research Laboratory (TRL) is a class 100 cleanroom. The machines used to fabricate the piezocantilever device will be given along with the recipes for each machine. Any problems encountered during the development phase will be mentioned along with the process modifications required to fix them. Also note that the procedure described below may not be compatible with current MTL policy, which evolves as user needs arise and as new equipment is added to the facility.

Before any cleanroom processing could begin, the silicon wafers had to be purchased with certain specifications and chrome masks for photolithography had to be designed and fabricated by an outside vendor. The eight photolithography masks used in the process were designed using KIC, a freeware mask layout tool available for both Windows and UNIX at ftp.srware.com/pub. The mask will be referred to by three letter abbreviations as follows:

ALI	alignment mask	CCO	contact cut mask
PHO	phosphorus implant mask	MET	metallization mask
BOR	boron implant mask	CVD	CVD passivation mask
BSE	backside etch mask	FSE	frontside etch mask

The layout for each individual mask layer is given in Fig. A-1. All of the masks are dark-field masks, except for the MET mask, which is a clear-field mask. In addition, the BSE mask is mirror imaged since this mask is used on the backside of the wafer but aligned to features on the frontside of the wafer. Since the final die size is 10 mm X 10 mm after dicing the wafer into pieces, the size of the devices is limited to 9.4 mm X 9.4 mm to leave "streets" between the die for the width of the die saw cut (see Fig. A-2). The through-wafer etch processing used for the micromachining of the cantilevers makes the wafers very fragile and susceptible to breaking, especially if the holes intersect with the outer edge of the wafer. Consequently, the die pattern does not cover the entire 5" chrome mask and is limited to an area smaller than the 4" wafer as shown in Fig. A-2.

The specifications for the silicon wafers used for the device and handle wafers must be determined before any processing can occur. The cleanroom facilities at MIT utilize equipment manufactured to handle 4-inch silicon wafers, which have a nominal thickness of around 500 μm. The device wafer from which the 20-μm-thick cantilevers are fabricated is a (110) silicon wafer of standard thickness and double-side polished (DSP). The handle wafer that acts as the supporting structure for the thinned (110) wafer is a DSP (100) silicon wafer with a low (i.e. less than 2 μm) total thickness variation across the wafer. The handle wafer must be a smooth on both the front and back surface (i.e. double-side polished) because the frontside is bonded to the device wafer and photolithography must be done on the backside.

One issue with the (110) wafer did arise as a result of a lack of familiarity on the vendor's part in dealing with (110) silicon wafers. The usual (100) silicon wafer has one primary flat on the outer edge that provides information about the in-plane orientation of the wafer. For a (100) DSP wafer, the frontside and backside are indistinguishable both in appearance and in terms of the crystallographic orientation because of the four-fold symmetry along the [100] axis. Unfortunately, the same is not true for a (110) wafer with one primary flat along a [111] direction because only two-fold symmetry exists along the [110] axis. Consequently, Laue x-ray diffraction were performed on each wafer to determine the in-plane orientation of the wafer. The in-plane orientation of the wafers is critical in the design of the piezocantilever devices because of the crystallographic asymmetry of the piezoresistive coefficients.

BSE +
FSE +
PAS +
MET +
CCO +
ARS +
BOR +
ALI

Figure A-1: (a) The ALI mask used to create the alignment mark in the 0.2 μm-thick thermal oxide. The features shown above are enlarged by approximately a factor of ten relative to the other mask in Fig. A.1 to see the detail better. Note that a couple of the labels used in the alignment marks, which correspond to other masks, have been changed. The "ARS" label corresponds to the PHO mask, and the "PAS" label corresponds to the CVD mask.

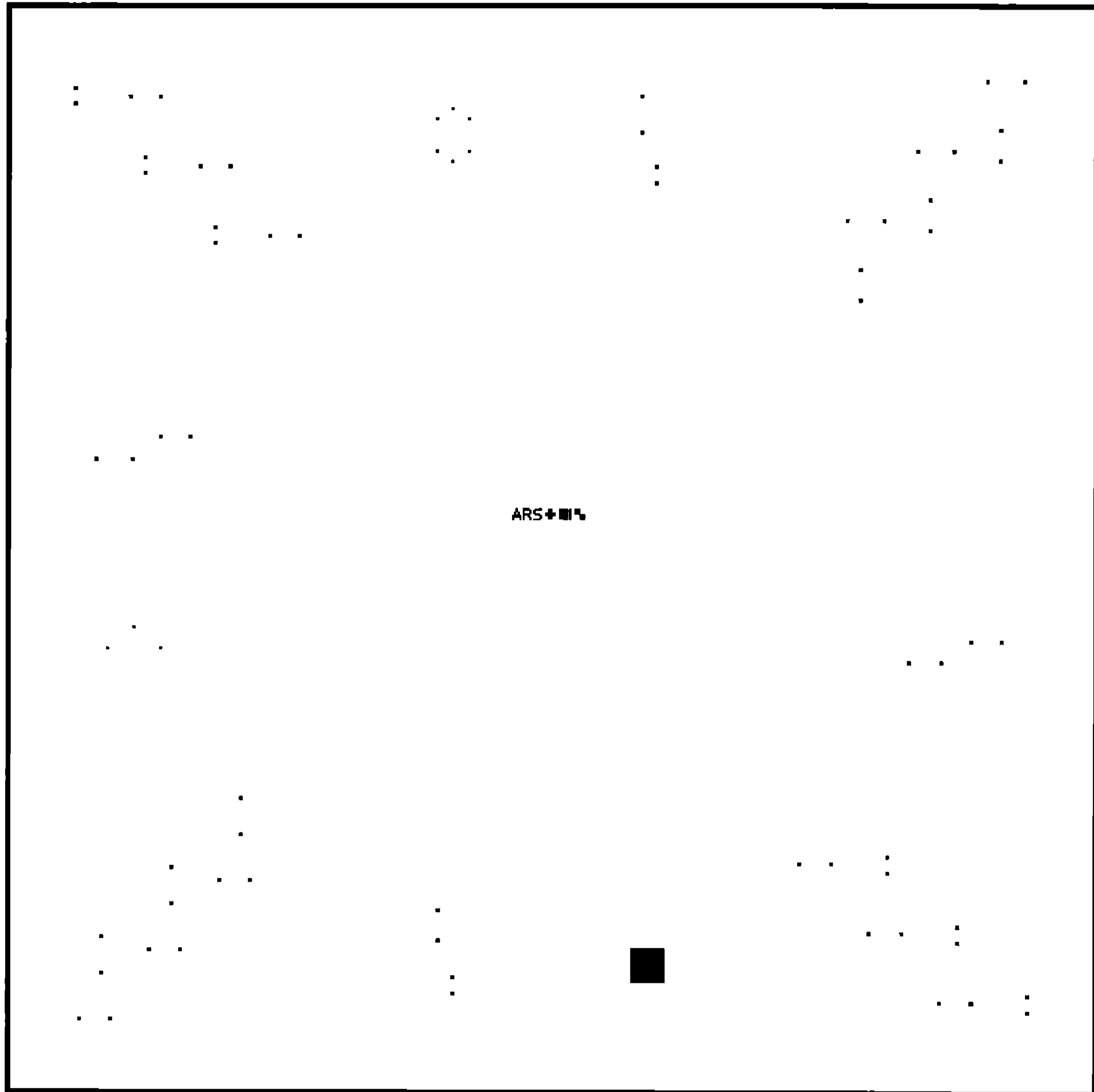

Figure A-1: (b) The PHO mask used for the phosphorous implant of n++ contacts. The original design was to use arsenic for the contacts, and hence the ARS alignment mark label, but the phosphorous implant was significantly less expensive.

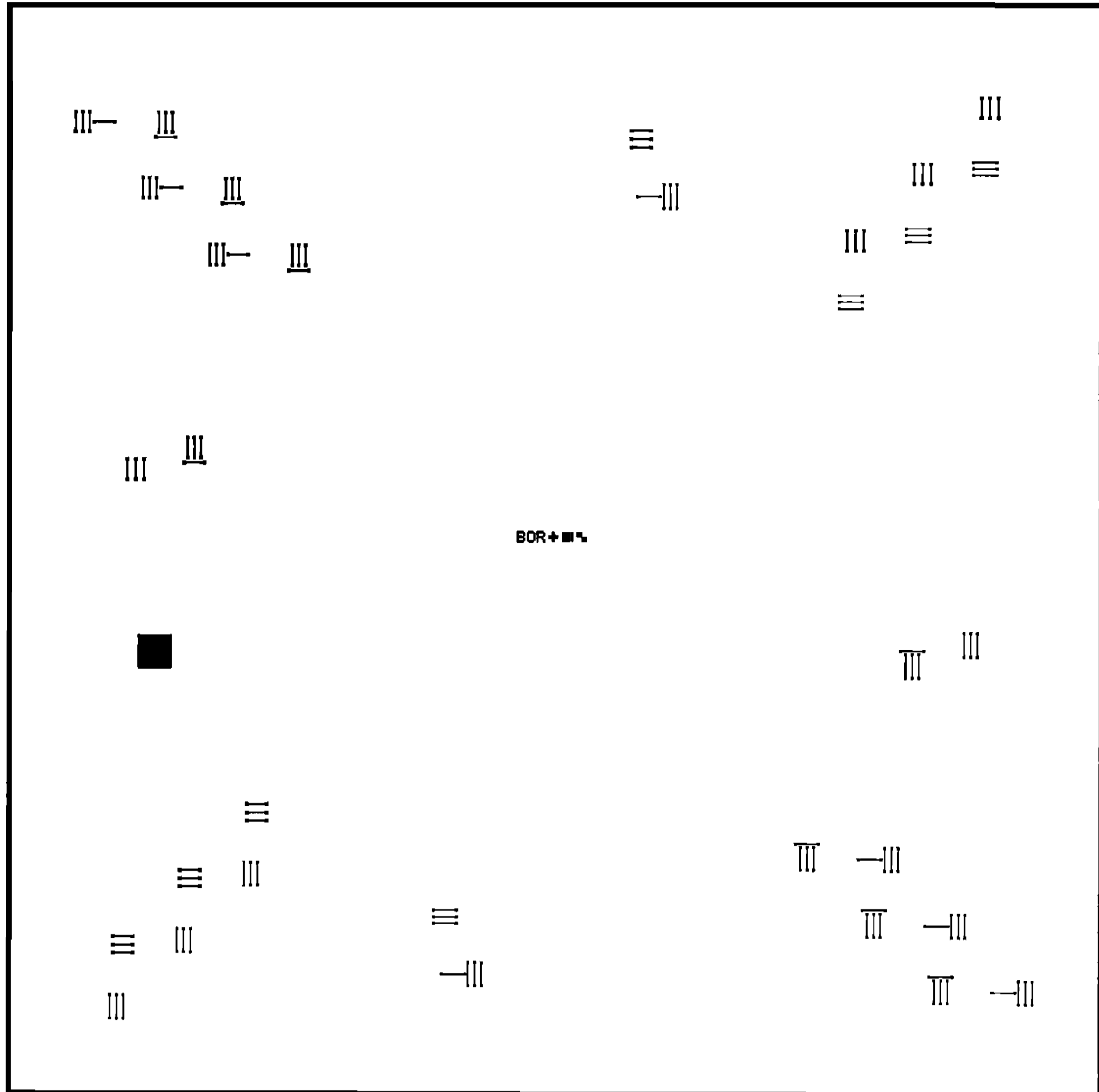

Figure A-1: (c) The BOR mask used for the boron implant of the resistors.

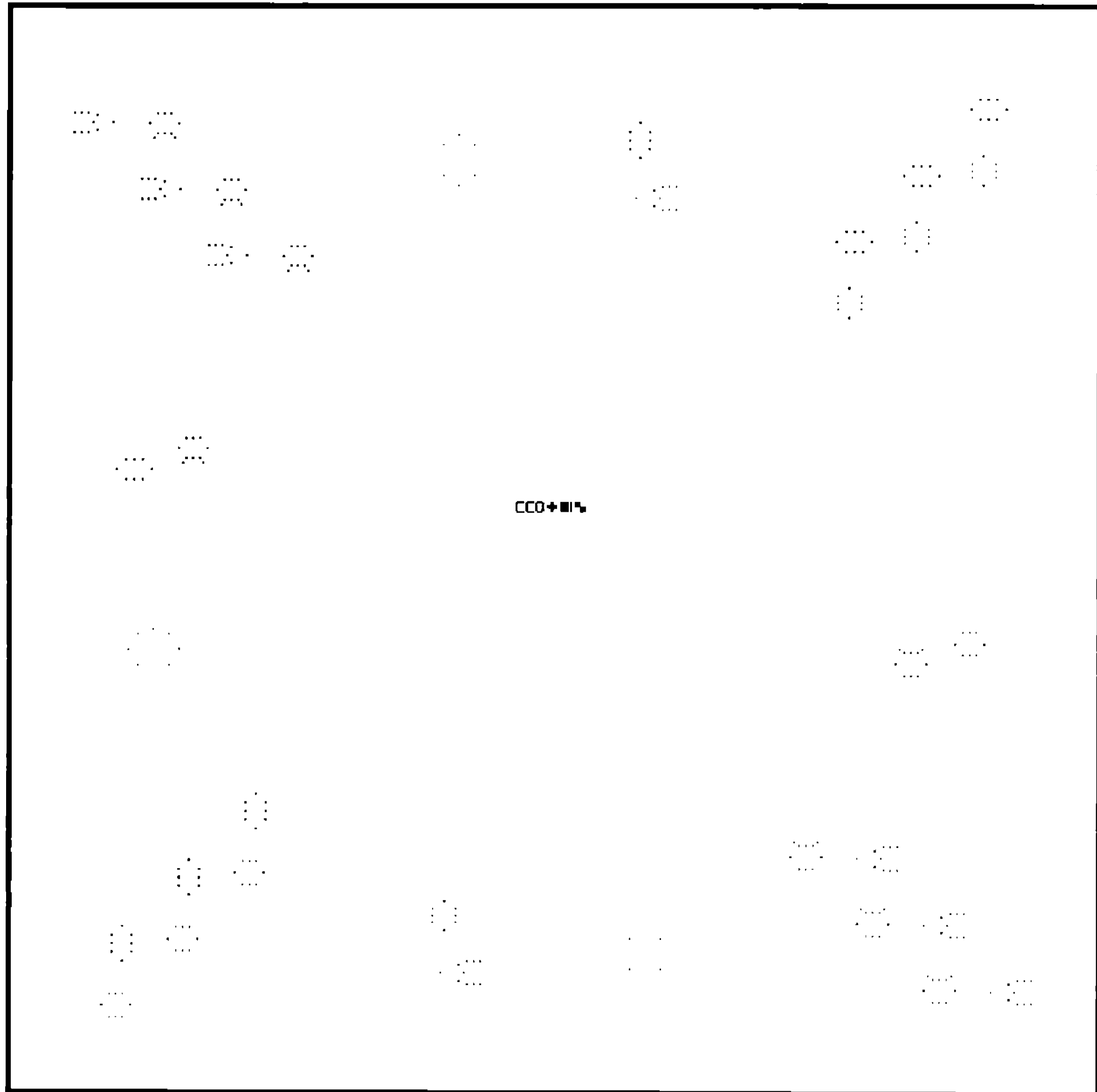

Figure A-1: (d) The CCO mask used to create the contacts through to 0.2 μm-thick thermal oxide to the implanted regions in the silicon.

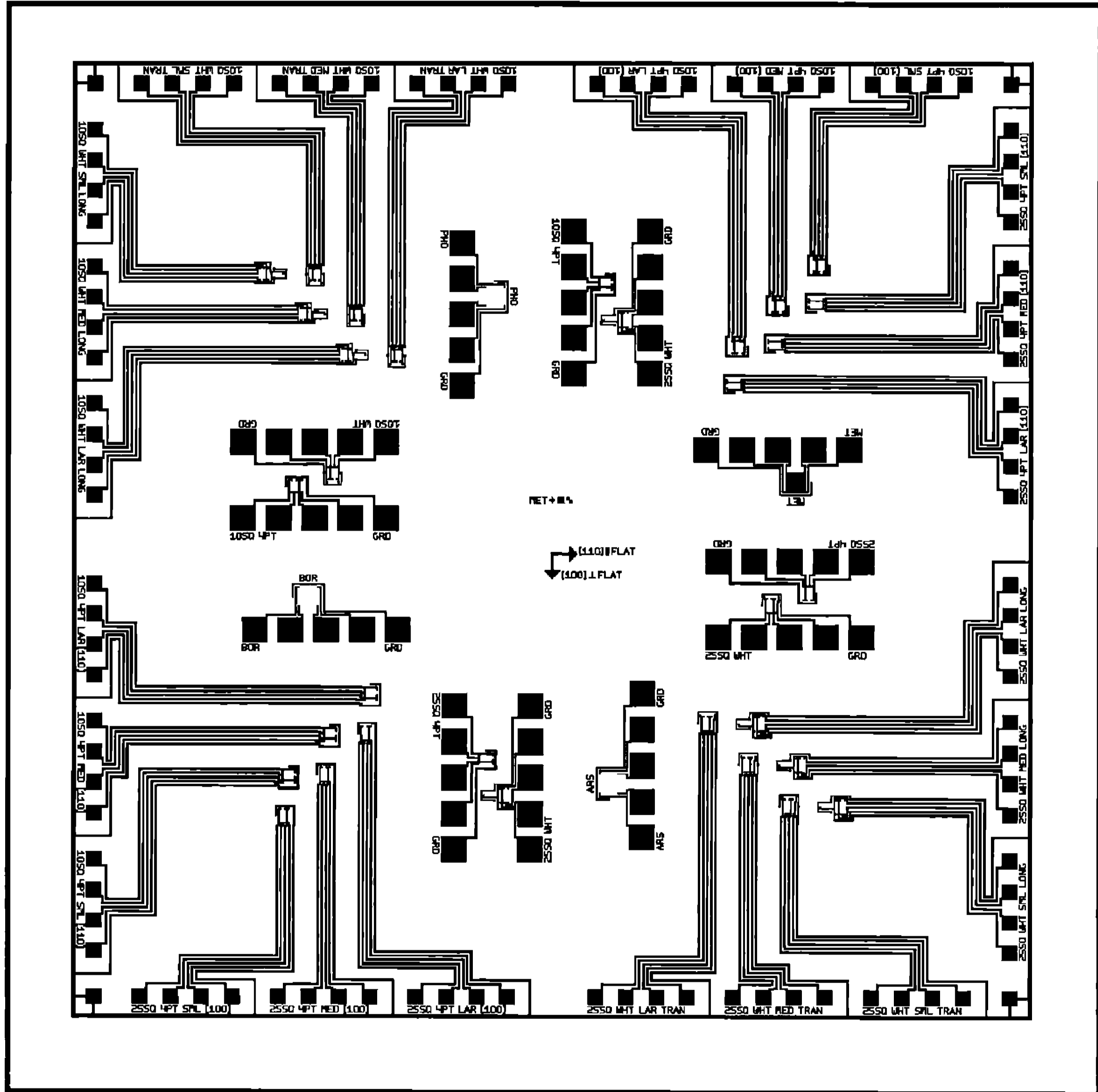

Figure A-1: (e) The MET mask for the aluminum metallization. The squares near the edges of the pattern are the bond pads. Gold wire bonding connects the bond pads on the die to the gold bond pads on the ceramic packaging.

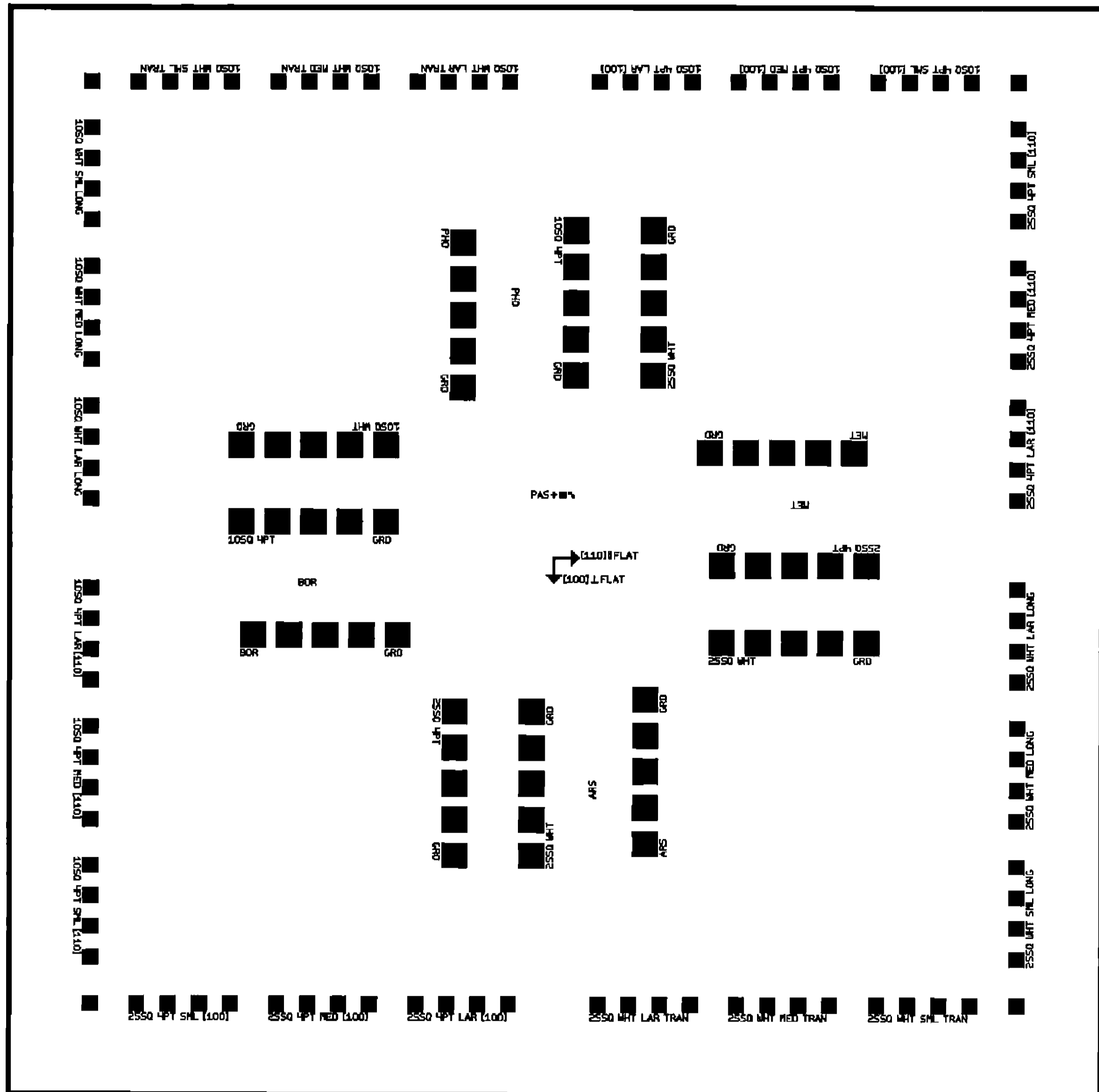

Figure A-1: (f) The CVD mask used to pattern the CVD oxide to expose the aluminum bond pads. Note that the name of the mask was changed from PAS to CVD in the alignment mark labels.

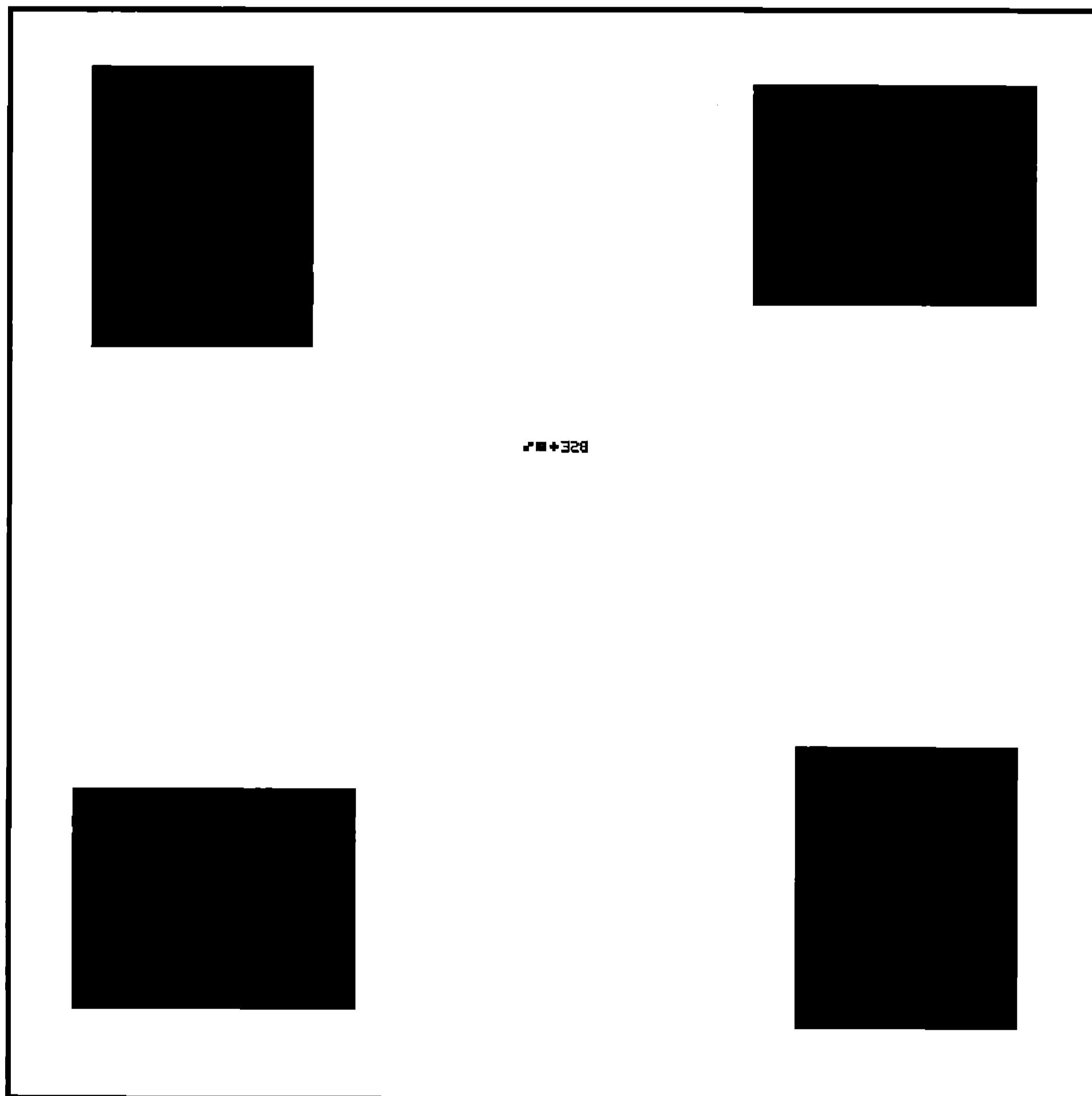

Figure A-1: (g) The BSE mask used to etch through the entire wafer thickness of the handle wafer. Note that the pattern is mirrored relative to the other mask layers because the mask is used on the backside of the wafer but aligned to marks on the front.

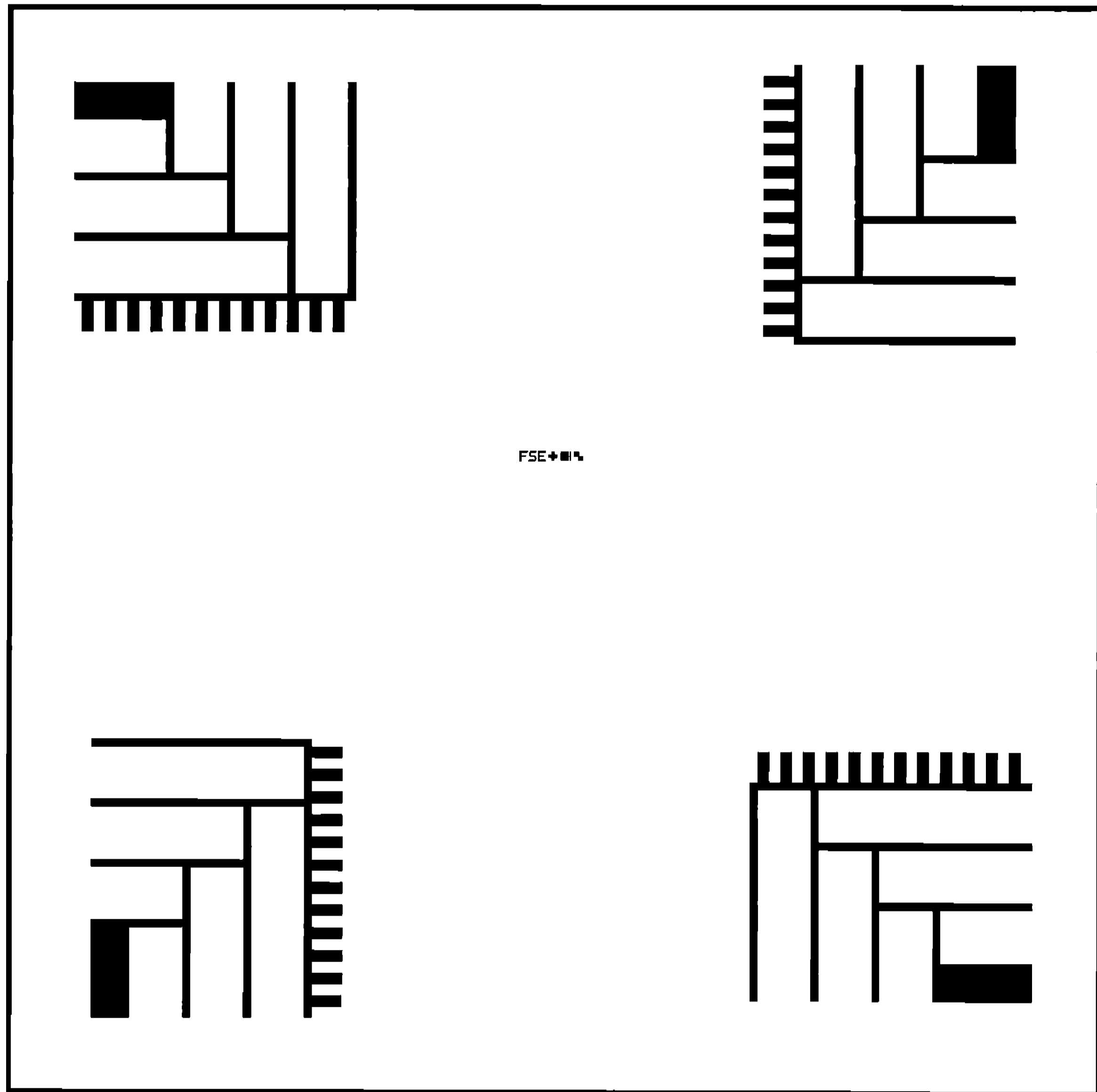

Figure A-1: (h) The FSE mask used to etch through the device wafer silicon to release the cantilevers. There are four sets of six cantilevers shown above.

(a) individual die

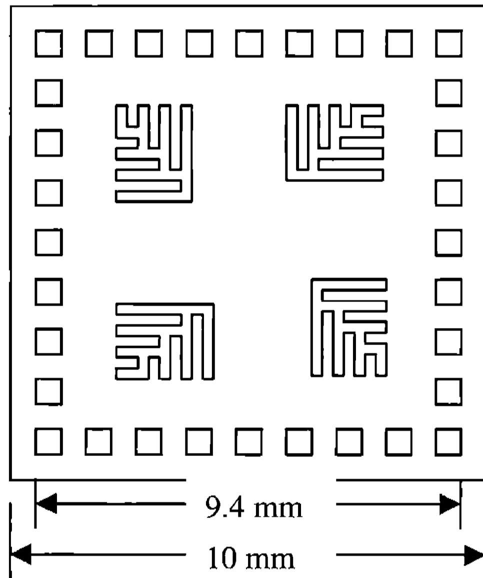

(b) die pattern on wafer

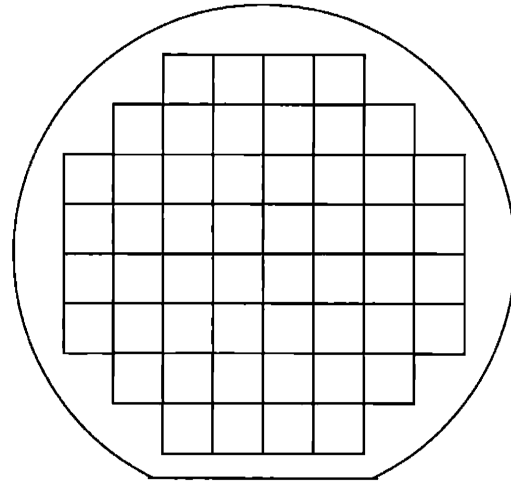

Figure A.2: (a) Schematic of an individual die showing aluminum bond pads around the outside edge and four groups of six cantilevers. (b) The die are patterned across the chrome masks so as not to intersect with the edges of the silicon wafer.

Prior to wafer bonding, a 1-μm-thick oxide was thermally grown on the handle wafer by a sequence of dry-wet-dry oxidation steps in an 1100°C furnace. The processing steps using the MTL facilities are given below:

Step	Description	Machine
1	RCA clean	ICL rca
2	1 μm thermal oxide recipe G0224 1100°C Dry oxidation, 20 minutes Wet oxidation, 120 minutes Dry oxidation, 20 minutes	ICL tubeA3
3	Measure oxide thickness middle, left, right, top, bottom 1.0075, 1.0071, 1.0085, 1.0082, 1.0072 avg. 1.008um	TRL nanospec

Prior to wafer bonding, both sets of wafers were RCA cleaned to remove all particles on the surface and to create the hydroxyl radical on the surfaces that promote bonding. Immediately after the RCA clean, the device wafer and handle wafer were contacted face-to-face at room temperature and then permanently bonded by annealing at 1100°C in N_2 for 75 minutes. The processing steps are given below:

Step	Description	Machine
4	RCA clean	TRL rca
5	Contact wafers	homemade Teflon chuck
6	Bonding anneal 1100°C for 1 hr N_2 ambient	TRL tubeA2

Figure 2-18 shows infrared images of bonded wafers for a "perfect" bond (left) and a bond with an interface bubble (right) presumably due to a trapped particle. To achieve a final device wafer thickness of 20 μm, the device wafer was mechanically ground to about a 30-μm thickness then reduced to the final thickness by chemical mechanical polishing to eliminate sub-surface damage due to grinding. The choice of a low thickness variation handle wafer was chosen because the handle wafer is the reference plane for the grind and polish procedure. Two external vendors, Disco Hi-Tec and Semiconductor Processing, were employed for the grind and polish procedure, respectively. The bonded wafer stack now consists of a 500-μm thick (100) handle wafer bonded to a 20-μm thick (110) device wafer with a 1 μm-thick thermal oxide at the bond interface (see Fig. 2-19).

The bonding procedure was performed using a homemade Teflon chuck to align and contact the wafers in air. Even within the confines of a class 100 cleanroom, particles are occasionally trapped between the wafers prior to bonding, as seen in Fig. 2-2-18(b). During the grind and polish procedure, pieces of silicon break off when the bubbles fracture causing the entire wafer to break. Newer facilities within MTL, namely the EV bonder, contact the wafers under vacuum and would have reduced the incidence of trapped particles between the bonded wafers.

Upon reintroduction of the thinned wafer into MTL, a rigorous cleaning procedure was required to remove particles and contamination. The standard cleaning procedure is given below:

Step	Description	Machine
7	DI rinse	TRL acidhood, yellow-dot tank
8	Piranha clean 3:1 H_2SO_4:H_2O_2 15 min	TRL acidhood, yellow-dot tank
9	DI rinse	TRL acidhood, yellow-dot tank
10	Piranha clean	TRL acidhood, green-dot tank
11	Dump rinse	TRL acidhood
12	50:1 HF:H_2O dip	TRL acidhood, green-dot tank
13	Dump rinse	TRL acidhood
14	Spin rinse dryer	TRL srd

The standard cleaning procedure will be utilized later and assumed to follow the same procedure as described above, unless otherwise noted. After the cleaning procedure, a 0.2-μm-thick oxide was thermally grown on the bonded wafer. The processing steps are given below:

Step	Description	Machine
15	RCA clean	TRL rca
16	0.2 μm thermal oxide 1000°C Dry oxidation, 20 minutes Wet oxidation, 25 minutes Dry oxidation, 20 minutes	TRL tubeA2
17	Measure oxide thickness middle, left, right, top, bottom 0.2160, 0.2154, 0.2281, 0.2157, 0.2151 avg. 0.2180 μm	TRL nanospec

The oxide layer reduces the amount of damage to the silicon during ion implantation and provides an insulating layer on the top surface of silicon wafer.

Alignment marks, shown in Fig A-3, were etched in the oxide layer using the ALI mask. The crosses in the alignment marks are used during each successive mask

(a) dark-field alignment marks

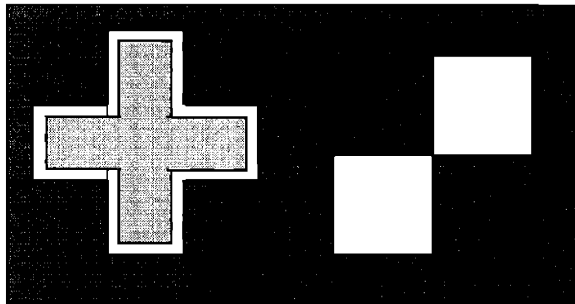

(c) exposure and develop marks

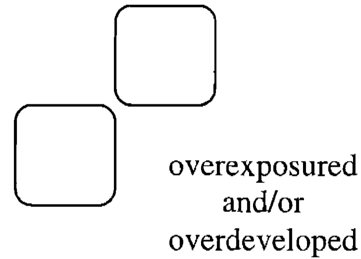

(b) clear-field alignment marks

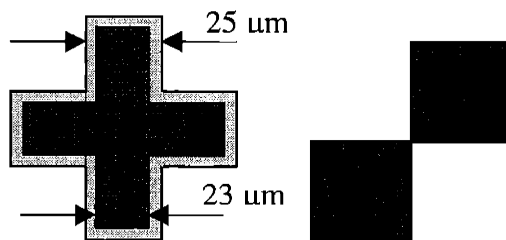

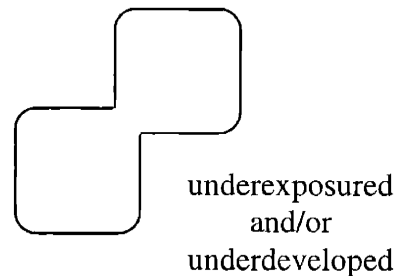

Figure A-3: Schematic of the types of alignment marks used for (a) dark-field masks, and (b) clear-field masks. The patterned etch on the wafer is shown in light gray, while the chrome mask features are shown in dark gray. The touching square pattern is inspected after the expose and develop steps to aid in the photolithography processing.

alignment, whereas the touching squares are inspected after the exposure and development steps. If the squares are not touching, then the exposure time and/or the development time was too long. The alignment marks were created from the beginning of processing since the successive ion implantation steps do not create any physical features on the wafers. The standard photolithography procedure is given below:

Step	Description	Machine
18	HMDS (adhesion promotor) 5 sec	TRL HMDS
19	Coater (1 μm photoresist) OCG resist (dispenser #1)	TRL coater

	500 rpm for 8 sec during resist dispense	
	850 rpm for 6 sec during resist spread	
	3000 rpm for 30 sec during final spread	
20	Prebake resist	TRL prebake
	30 min at 90°C	
21	Alignment and exposure	TRL ksaligner2
	ALI mask	
	55 sec exposure	
22	Develop	TRL photo-wet-l
	OCG 1:1 developer	
	~2 min in developer	
23	DI rinse	TRL photo-wet-l
24	Spin rinse dryer	TRL srd
25	Postbake resist	TRL postbake
	30 min at 120°C	

The standard photolithography procedure will be utilized later and assumed to follow the same procedure as described above, unless otherwise noted. One modification to the standard photolithography procedure was made during this step to coat the backside of the wafer with resist to protect the oxide during the subsequent BOE etch. The standard procedure for a front and backside photoresist is as follows:

Step	Description	Machine
19a	Coater (1 μm photoresist)	TRL coater
	backside of wafer	
	OCG resist (dispenser #1)	
	500 rpm for 8 sec during resist dispense	
	850 rpm for 6 sec during resist spread	
	3000 rpm for 30 sec during final spread	
20a	Prebake resist	TRL prebake
	15 min at 90°C	
19b	Coater (1 μm photoresist)	TRL coater
	frontside of wafer	
	OCG resist (dispenser #1)	
	500 rpm for 8 sec during resist dispense	
	850 rpm for 6 sec during resist spread	
	3000 rpm for 30 sec during final spread	
20b	Prebake resist	TRL prebake
	25 min at 90°C	

Note that the standard coater step using a stainless steel chuck, but a rubber gasket chuck should be used for the front and backside photoresist to reduce scratching of the frontside

surface. After the photolithography step, the areas of thermal oxide not covered by photoresist were etched through to the underlying silicon using buffered oxide etch (BOE). The processing steps are given below:

Step	Description	Machine
26	BOE etch of oxide	TRL acidhood
	0.1 μm/min etch rate of thermal oxide in BOE	
	2.5 min etch for 0.2 μm thermal oxide	
27	Remove photoresist	TRL acidhood
	piranha etch (3:1 H_2SO_4:$H_2 0_2$)	
	15 min	

Three ion implantation steps were performed to create the electrical components in the top surface of the (110) device wafer. The ions were implanted through the 0.2 μm oxide layer to reduce the amount of damage to the silicon. The dose and energy for the ion implantation must be adjusted accordingly to take into account that some fraction of the implanted material will remain in the oxide layer. The concentration profiles of the implanted species were calculated using SUPREM, a one-dimensional simulation tool for semiconductor processing. Photoresist was used as the implant mask and the appropriate thickness of resist was chosen to statistically allow only 0.001% of the incident dose to penetrate the resist.

The first implant was a blanket phosphorous implant to create a uniform n-type region in the top surface of the (110) silicon device layer that was diffused to a depth of about 2 μm by a long drive-in anneal at 1100°C. This implant would not have been necessary if n-type (110) wafer had been available from the wafer vendor. The phosphorous ion implantation was performed at an accelerating voltage of 150 kV with a dose of 2×10^{13} cm^{-2}. After the return of the wafer from the ion implantation vendor, a standard cleaning process (see step 7-14 above) was performed to bring the wafers back into the cleanroom. A summary of the processing steps above is given below:

Step	Description	Machine
28	P ion implantation	Ion Implant Services
	Energy: 150 kV	
	Dose: 2×10^{13} cm^{-2}	
29	Standard cleaning process	TRL acidhood

For the remaining two ion implantations, only selected areas of the wafers were implanted by masking the surface of the wafer with patterned photoresist. The second implant was a phosphorous implant to create n++ contacts to the original phosphorous implant for good ohmic contact. In order to mask the implant, a photoresist layer of 1.3 μm was used instead of the 1 μm in the standard lithography procedure (see steps 18-25) and the PHO mask was used during exposure. The phosphorous ion implantation was performed at an accelerating voltage of 150 kV with a dose of 8 X 10^{14} cm^{-2}. Upon return of the wafers from the ion implant vendor, a standard cleaning process (see steps 7-14 above) was performed to bring the wafers back into the cleanroom and to remove the photoresist. A summary of the processing steps is given by:

Step	Description	Machine
30	Standard photolithography 1.3 μm resist PHO mask	TRL
31	P ion implantation Energy: 150 kV Dose: 8 X 10^{14} cm^{-2}	Ion Implant Services
32	Standard cleaning process	TRL acidhood

The last implant was a selected-area boron implant to create the boron resistors within the top surface of the (110) silicon. In order to mask the implant, a photoresist layer of 1.3 μm was used instead of the 1 μm in the standard lithography procedure (see steps 18-25) and the BOR mask was used during exposure. The boron ion implantation was performed at an accelerating voltage of 50 kV with a dose of 1 X 10^{16} cm^{-2} to give a surface concentration of 10^{20} B/cm^3. For such a high dose, the wafer must be water-cooled during ion implantation to avoid overheating the photoresist. Upon return of the wafers from the ion implant vendor, a standard cleaning process (see steps 7-14 above) was performed to bring the wafers back into the cleanroom and to remove the photoresist. Unfortunately, the photoresist was overheated during the ion implantation even with the water cooling of the wafer. Several oxygen plasma ash operations along with piranha strips had to be performed to remove the overheated photoresist. A summary of the processing steps is given below:

Step	Description	Machine
33	Standard photolithography 1.3 μm resist BOR mask	TRL
34	B ion implantation Energy: 50 kV Dose: 1×10^{16} cm^{-2}	Ion Implant Services
35	Standard cleaning process	TRL acidhood

A short anneal for 30 min at 1000°C was performed to activate both the boron and n++ phosphorous implanted species. The processing steps are given below:

Step	Description	Machine
36	RCA clean	TRL rca
37	Activation anneal 1000°C for 30 min N_2 ambient	TRL tubeA2

A cross-section of the bonded wafer and a top view of the wafer surface after the ion implantation steps are shown in Figure 2-19.

Contacts through the 0.2-μm-thick insulating oxide layer are made to the phosphorous and boron regions by selective etching of the oxide in BOE. The processing steps are given below:

Step	Description	Machine
38	Standard photolithography CCO mask	TRL
39	BOE etch of oxide 5.0 min etch	TRL acidhood

The usual etch rate for thermal oxide in BOE is about 0.1 μm/min, but the high concentration of boron in the oxide was found to decrease the etch rate by approximately a factor of two. A 0.3 μm-thick blanket film of Al was deposited by sputter deposition and then patterned to create the metal interconnects between the silicon layer and bond pads, which provide large areas of Al for wire bonding. A short sinter anneal for 30 min at 400°C was found to be suitable to create good ohmic contact with the boron region

without "spiking" through to the n-type phosphorous layer. The processing steps are given below:

Step	Description	Machine
40	Pre-metal clean	ICL pre-metal
	piranha clean in blue-dot tank	
	blue-dot dump rinse	
	piranha clean in green-dot tank	
	green-dot dump rinse	
	30 sec 50:1 HF:DI dip	
	green-dot dump rinse	
	spin rinse dry	
41	Sputter 0.3 μm Al	ICL endura
42	Standard photolithography	TRL
43	Etch Al	TRL acidhood
	PAN etch at 40°C	
	0.2 μm/min etch rate of Al	
44	Remove photoresist	TRL asher
45	Sinter anneal of Al	TRL tubeA3
	400°C for 30min	
	N_2 ambient	

Next, a 0.5 μm-thick passivating oxide layer was grown over the entire surface of the wafer by chemical vapor deposition of silicon dioxide at 400°C. The passivating oxide was then patterned with photoresist and selectively removed from above the aluminum bond pads. Whereas BOE etches both oxide and Al, a special product called Pad Etch 1, an acetic acid based etch, removes oxide and only slowly etches the underlying Al. The etch rate in Pad Etch 1 is 0.25 μm/min for the CVD oxide and less than 0.05 μm/min for Al. The processing steps are given below:

Step	Description	Machine
46	0.5 μm CVD oxide	ICL concept1
47	Measure oxide thickness	TRL nanospec
	middle, left, right, top, bottom	
	0.4466, 0.4471, 0.4469, 0.4702, 0.4671	
	avg. 0.4680 μm	
48	Standard photolithography step	TRL
	front and backside resist	
	CVD mask	
49	Etch CVD oxide over bond pads	TRL acidhood

Pad Etch 1
0.5 μm CVD oxide at 0.25 μm/min etch rate
total etch time 2.5 min

A cross-section of the bonded wafers and a top view of the wafer surface after the oxide passivation step are shown in Figure 2-20.

The next sequence of steps use silicon micromachining techniques to create the 20-μm-thick cantilevers from the continuous (110) device wafer. Deep etches into the backside and frontside of the wafer require special photolithography techniques and processing tools. The etches are performed using a deep reactive ion etching (DRIE) system manufactured by STS. The deep etching is achieved through a series of etch and passivation cycles. The SF_6-based etch chemistry isotropically etches the silicon. After each etch cycle, a C_4F_8–based passivation cycle forms a protective polymer layer on the sidewalls that inhibits further etching by the SF_6. By repeated etch-passivation cycles, features can be etched through the entire wafer thickness with relatively good control of the dimensions of the feature through the thickness.

The photolithography procedure is significantly modified for use in the DRIE etcher. The resist layer must be much thicker than the standard resist to withstand the long etch times and severe etch chemistry. The etch selectivity is approximately 100:1 Si:photoresist etch rate so at least a 5 μm resist layer is required to etch through a 500 μm-thick wafer. The STS machine uses backside wafer cooling to prevent overheating of the resist during machine operation, and since through-wafer etching is desired, the 4" wafer must be mounted on a 6" handle wafer. The thick resist photolithography steps and procedure for wafer mounting are given in detail below.

The first DRIE process was to etch through the entire 500-μm thickness of the 4" (100) handle wafer in selected areas. The 1 μm-thick inter-wafer oxide acts as the etch stop layer for the DRIE process. The etch selectivity is approximately 180:1 $Si:SiO_2$ etch rate for thermal oxide. In addition, the backside of the bonded wafer still has the 0.2-μm thick thermal oxide deposited very early in processing. Once the thick resist is exposed and developed, the oxide will be etched and acts as a masking material itself if the thick resist is overetched during DRIE. The thick resist photolithography process for the backside etch process is given below:

Step	Description			Machine
50	HMDS (adhesion promoter)			TRL HMDS
	5 sec			
51	Backside thick resist			TRL coater
	rubber gasket chuck			
	thick resist (dispenser #3)			
	dispense	1750rpm	12sec	
	spread	2000rpm	60sec	
	edgebead	5000rpm	3sec	
52	Prebake resist			TRL prebake
	60 min at 90°C			
53	Photolithography			TRL EV1
	backside optics			
	BSE mask			
	22 sec exposure			
54	Develop			TRL photo-wet-l
	MIF440 developer			
	2 min develop time			
55	Frontside resist			TRL coater
	rubber-gasket chuck			
	1 μm OCG resist			
56	Postbake resist			TRL prebake
	30 min at 90°C (thick resist recipe)			
57	Etch backside oxide			TRL acidhood
	BOE for 2 min			

During the edgebead spin (see step 51), a cleanroom cotton swab soaked in acetone was used to remove the "comet tails" on the outside edge of the wafer. Next the patterned wafer was mounted using photoresist onto a 6" handle wafer. In the STS DRIE, the backside wafer cooling acts on the 6" wafer, so the mounting photoresist is the heat diffusion path away from the 4" wafer being etched to the 6" handle wafer. However, the photoresist outgases during heating so a venting path must exist between the 4" wafer and the 6" handle wafer. The "target" mount pattern of photoresist on the 6" handle wafer is shown in Fig. A-4. The mount pattern was created by first coating the entire wafer with thick resist, then while the wafer was still spinning in the coater, all of the resist except

(a) thick resist target mount pattern

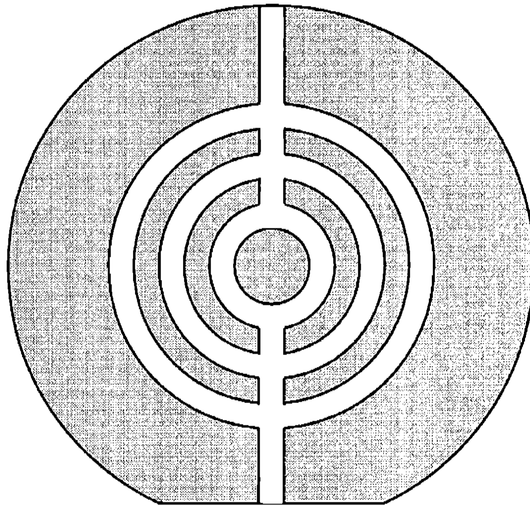

(b) after mounting 4" wafer

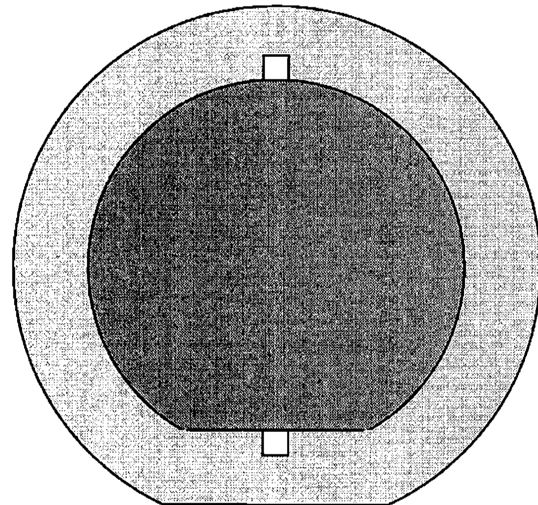

Fig. A.4: (a) Target mount pattern of thick photoresist (gray) on the 6" handle wafer. The cleared areas provide a vent path for the resist, which outgases due to heating during the DRIE etch. (b) After mounting the 4" wafer, the long vent path should be painted over with resist to leave only a small vent near the top and bottom.

the smallest inner circle was removed using an acetone squirt bottle. Starting from the outside edge and moving the dispenser arm inward, resist was applied on the wafer leaving a torus of uncoated wafer to act as the vent path. The above steps were repeated until several vent tori were created. Then using a fabwipe damp with acetone, two vent paths were created along radii of the wafer as shown in Fig. A-4. After mounting the 4" wafer on the handle wafer, a cleanroom cotton swab was used to paint thick resist on the vent path leaving only a small area of unexposed silicon on the handle wafer. The "target" mount procedure is given below:

Step	Description		Machine
58	Thick resist target mount		TRL coater
	6" handle wafer		
	thick resist (dispenser #3)		
	dispense	1750rpm	

	acetone 1750rpm	
59	Mount 4" wafer on 6" handle wafer	
60	Prebake resist	TRL prebake
	20 min at 90°C	

Prior to loading the mounted wafer in the STS, the backside of the handle wafer was scraped clean with a razor to remove any incidental resist that would interfere with the gasket seal used for the backside wafer cooling in the STS. The wafer was rotated after every hour of etching in the STS to minimize any asymmetry of the etch rate profile in the chamber. As mentioned previously, the inter-wafer oxide was the etch stop for the DRIE process and was visible as a color change from gray silicon to blue oxide under a microscope. Prior to dismounting the wafer, the exposed inter-wafer oxide was removed using BOE. The 4" wafer was dismounted from the handle wafer by soaking in acetone. The backside etch process is given below:

Step	Description	Machine
61	DRIE backside	TRL sts2
	mit69a recipe	
	rotate wafer every hour	
	160 μm/hr etch rate	
62	Remove inter-wafer oxide	TRL acidhood
	BOE etch in ultrasonic bath	
63	Dismount 4" wafer from handle	TRL solvent-nonau
	acetone soak for 24-48 hrs	

When using the BOE at the bottom of a deeply etched feature, bubbles form which prevent further etching. The bubbles can be dislodged by either manually tapping the wafer on the bottom the etch container or by placing the etch container in an ultrasonic bath. Care must be taken to operate the ultrasonic bath at lower power or the resist will tend to spall off the surface of the wafer.

After the backside DRIE step, four 20-μm-thick membranes of (110) silicon approximately 2 mm X 2 mm in size have been created in each 10 mm X 10 mm die. From each 2 mm X 2 mm membrane, six cantilevers are fabricated as can be seen in Fig. 2-17. To protect the membranes from breaking when using vacuum chuck equipment (e.g. the coater and aligner), special blue tape found in TRL was attached to the backside

of the wafer to seal the back surface. The same thick resist photolithography (see steps 50-56) was done except using the FSE mask on the frontside of the wafer. The protective OCG resist (see step 55) cannot be applied using the coater because the deep etch holes prevent even spreading of the resist. Instead, an atomizer was used to spray resist on the backside of the wafer. The wafer was "target" mounted to another 6" handle wafer using the same pattern as shown in Fig. A-4. Since only 20 μm of silicon are etched in the final DRIE process to release the cantilevers, the etch time was much shorter than the full wafer DRIE etch. The processing steps to release the cantilevers are given below:

Step	Description			Machine
64	HMDS (adhesion promoter)			TRL HMDS
	5 sec			
65	Tape backside of wafer			
66	Frontside thick resist			TRL coater
	rubber gasket chuck			
	thick resist (dispenser #3)			
	dispense	1750rpm	12sec	
	spread	2000rpm	60sec	
	edgebead	5000rpm	3sec	
67	Prebake resist			TRL prebake
	60 min at 90°C			
68	Photolithography			TRL EV1
	backside optics			
	FSE mask			
	22 sec exposure			
69	Develop			TRL photo-wet-l
	MIF440 developer			
	2 min develop time			
70	Remove tape from backside of wafer			
71	Backside resist			TRL solvent-nonau
	atomizer spray OCG resist			
72	Postbake resist			TRL prebake
	30 min at 90°C (thick resist recipe)			
73	Thick resist target mount			TRL coater
	6" handle wafer			
	thick resist (dispenser #3)			
	dispense	1750rpm		
	acetone	1750rpm		
74	Mount 4" wafer on 6" handle wafer			
75	Prebake resist			TRL prebake
	20 min at 90°C			
76	DRIE frontside			TRL sts2

mit69a recipe
total etch time ~15 min

77 Dismount 4" wafer from handle — TRL solvent-nonau
acetone soak for 24-48 hrs

A cross-section of the bonded wafer with released cantilevers is shown in Fig 2-21. After thoroughly cleaning the dismounted wafer in acetone, both the front and backside of the wafer were coated with OCG resist using the atomizer. The resist will mostly protect the wafer from the silicon dust created during the die saw operation.

A.2 Improvement on the piezocanitlever design

From a practical standpoint, the design and processing of the piezocantilever devices can be improved in several ways:

1. By using n-type (110) silicon wafers, the first phosphorous implant would not have been necessary and would have eliminated several processing steps.
2. The yield of the wafer bonding process could have been improved by using commercial wafer bonding equipment that contacts the wafers in vacuum rather than in air, which reduces the incidence of trapped particles between wafers.
3. The measurement sensitivity of the devices could have been improved by a factor of 4 by reducing the (110) silicon microcantilever thickness from 20 μm to 5 μm. Rather than grinding and polishing, a bonded wafer pair with a 5 μm-thick (110) silicon device wafer with a 500 μm-thick (100) handle wafer can be purchased from custom wafer vendors.
4. The measurement sensitivity of the devices could have been improved by a factor of 5 by reducing the boron implant concentration from 10^{20} B/cm^3 to 10^{18} B/cm^3. For the 5°C temperature variation typically observed during deposition, the piezoresistive coefficients only decrease by a couple percent at 10^{18} B/cm^3 doping, while they are nominally independent of temperature at 10^{20} B/cm^3.
5. The number of devices produced per wafer could have been improved by a factor of 10 by decreasing the die size from 10 mm X 10 mm to about 3 mm X 3 mm. Each 10 mm X 10 mm die has approximately 24 microcantilevers, but only 2 are

used per deposition and each die can only be used once. In addition, half of the cantilevers are useless because the cantilever tip-deflection calibration can only be used for the cantilevers fabricated along the [110]-direction.

In terms of operation of the piezocantilever devices, several improvements must also be considered:

1. Although preliminary testing indicates that electrical noise from the e-gun source is not causing the spurious initial tensile rise in the measurements (see section 3.4), better shielding of the cabling could eliminate that problem and decrease the amount of noise in the data.
2. The temperature calibration is currently a time-consuming effort because of the crude setup for controlling the temperature. A programmable furnace that could cycle the temperature while concurrent calibration measurements are collected would alleviate the tedious nature of the temperature calibration, which must be performed both before and after thin film deposition.

Appendix B

Simulation of Volmer-Weber Growth of thin films

The thin film growth simulation models the island nucleation and growth processes occurring during deposition of films that grow by the Volmer-Weber mechanism. Thin film growth was modeled in a two-dimensional simulation with periodic boundary conditions by tracking the nucleation and growth of circles. The simulation calculates the intersection between growing circles and the resulting boundary, which represent grain boundary formation between coalescing islands. Triple points are formed at the intersection of three boundaries within an ensemble of three islands. Eventually, the film is fully continuous and said to be composed of grains, rather than islands. With the ability to reproduce a realistically evolving microstructure, models for stress generation and relaxation that depend on size and time can be implemented and compared to experimental results.

The simulation is written in C code and compiled using gcc with the aid of a Makefile. The program requires an input file with a name of the following format: <BASENAME>.inp. BASENAME is also used as the suffix for <BASENAME>.out, the calculated output of the program, and <BASENAME>.ps, the Postscript graphics output file. The usage of the compiled executable is of the form: <EXECUTABLE> <BASENAME>.inp. The format of a sample input file is given below:

****

```
Seed
8
NumberGrains
200
RealRadius
20.0e-9
DepRate
0.2e-9
ContactAngle
80
SurfaceStress
1.4
LockDownRadius
0.0e-9
YoungModulus
87.3e9
PoissonRatio
0.354
DeltaGamma
2.532
ClusterAreaCrit
20000e-18
Temperature
323
PreExpFactor
2.5e-20
ActivationEnergy
0.3
Graphics
0.6
```

****

For brevity, only simple identifications for the input values are supplied in the input file. A full description of the inputs is given in the source code describing their use in the simulation and the expected units. The Makefile used to create the executable "grow" is given below:

****

```
# MAKEFILE

CC     = gcc
FLAGS  = -g -Wall -pedantic
INCL   = -I/.
LIBS   = -lm

.c.o:  ; $(CC) -c $(FLAGS) $(INCL) $*.c

OBJ_NUC=      main.o \
              allocate.o \
              nucleate.o \
              intersection.o \
              boundary.o \
              contact.o \
              stress.o \
              graphics.o \
              auxiliary.o
```

```
grow:  $(OBJ_NUC)
       $(CC) $(FLAGS) $(INCL) $(OBJ_NUC) -o grow $(LIBS)

clean:
       rm -f *.o core
```

****

As can be seen above, there are 10 different C code files required to compile the executable as well as three header files not listed above. The first header file, defines.h, lists several constants used in the simulation:

****

```
/* defines.h */

/* Maximum amount of allocatable RAM in MB */
#define RAM_MAX          256

#define MAXSIDES         30
#define DUPL_FRAC        0.30
#define TOL1             1e-5
#define TOOCLOSE         0.001
#define TOOSMALL3        1e-3
#define PI               3.14159265358979323846264338327950
```

****

Another header file, struct.h, list the structures used in the simulation:

****

```
/* struct.h */

/* Structure of island/grain information */
typedef struct
{ double x, y;                  /* x,y nucleation coordinate */
  double r;                     /* island radius */
  double t;                     /* time of nulceation */
  int    numpoint;              /* number of intersection points */
  int    point[MAXSIDES];       /* intersection point indexed to point struct
*/
  int    numbound;              /* number of boundary points */
  int    bound[200*MAXSIDES];   /* boundary points indexed to bound struct */
  int    numcontact;            /* number of contact points */
  int    contact[2*MAXSIDES];   /* contact pnts indexed to contact struct */
  double area;                  /* in-plane area of island/grain */
  float  stress;                /* calculated stress in grain */
  float  stress_comp;           /* calculated comp. stress in grain */
  int    delete;                /* flag for island coarsening */
} grain_struct;


/* Structure of intersection point information
** Point of intersection between two circles (island/grains)
*/
typedef struct
{ double x, y;         /* x,y coordindate of intersection point */
  double t;            /* time intersection point formed */
  int    cw;           /* next point in cw direction around island */
```

```
  int    ccw;           /* next point in ccw direction around island */
  int    grain[2];      /* two grains involved with intersection point */
  double theta;         /* angle between int. point and nucl. point of island */
} point_struct;

/* Structure of boundary point information
** Boundary points are the evenly spaced points that form the grain
** boundary between intersection and/or triple points around the
** island/grain
*/
typedef struct
{
  double x1,y1;         /* x,y coordinate of boundary point */
  double x2,y2;         /* x,y coord of next boundary point in ccw direction */
} bound_struct;

/* Structure of contact point information
** Two contact points are formed the first time two island contact
*/
typedef struct
{
  float t;                /* time contact formed */
  int   grain;            /* grain#1 associated with island contact */
  int   grain_contact;    /* grain#2 associated with island contact */
  int   point[2];         /* intersection points on either side of contact */
  float length;           /* length of grain boundary between ints. points */
  float radius;           /* radius of grain#1 */
  float z0;               /* zipping height due to island coalescence */
  float height;           /* height of grain boundary */
  float theta;            /* angle btwn contact point & nucl. point of grain#1 */
  float stress;           /* zipping stress associated with coalescence */
  float area;             /* grain boundary area */
} contact_struct;
```

****

The final header file, external.h, lists the external global variables and external procedures called within main.c.

****

```
/* external.h */

/* The main structures used in the simulation (see struct.h) */
grain_struct *grain;
point_struct *point;
bound_struct *bound;
contact_struct *contact;

/*
** The scaling factor for the simulation relates simulation dimension
** to real dimensions:
** radius_real= scaling*radius_simulation
*/
float  scaling;

/*
** The lateral growth rate of the growing island in the simulation
** g0= dep_rate_real*geom/scaling
*/
float  g0;
```

```
/* Dimensions of entire simulation field of grains */
double xmin, xmax, ymin, ymax;
double xsize, ysize;

/* Simulation time in seconds */
float  t;
/* Current total number of grains including those due to PBC */
int    ng;

int long numbound;

/* allocate.c */
extern int  allocate_memory(int, float);

/* nucleate.c */
extern void nucleate_island(float *);

/* intersection.c */
extern void island_intersection(int *);
extern void organize_intersection_points();
extern void draw_island_boundary();

/* contact.c */
extern void new_contacts(int *);
extern void update_contacts(int);
extern void stress_contacts(int, float, float, float, float, float);

/* auxiliary.c */
extern double calc_grain_area(int);
extern int inbound(double, double);

/* coarsen.c */
extern void island_coalesce(int, int, double);
extern void island_coalesce_noshift(int, int, double);

/* graphics.c */
extern void ps_write(FILE *, int);

/* stress.c */
extern void laplace_pressure(float, float, float);
extern void stress_relax_coble(float, float, float, float);
extern void film_stress_relax_coble(float, float, float, float);


**********************************************
```

The main procedure, main.c, handles several initial operations including:

(1) Opens the input and output files.

(2) Reads in the values from the input file used in the simulation.

(3) Allocates memory for the main structures in the program.

Within the main timestep loop in main.c, several operations are performed including:

(1) Attempts a single nucleation of a new island.

(2) Increases the radius of existing island according to the deposition rate.

(3) Determines any new intersections between growing island.

(4) Calculates boundary between islands that have intersected.

(5) Calculate stress due to island coalescence.

(6) Calculate stress relaxation due to surface coble creep.

(7) Calculate compressive stress due to Laplace pressure.

(8) Calculate average stress for the entire film.

The main.c code was written so as to parse the operations into simple procedure calls and to keep the flow of the program as simple as possible.

****

```
/*  main.c */

#include <stdio.h>
#include <math.h>
#include <stdlib.h>
#include "defines.h"
#include "struct.h"
#include "external.h"

int main(int argc, char *argv[])
{
  char   basename[50];       /* input file basename */
  char   filename[100];      /* file name plus io directory */
  char   text[80];           /* dummy text string */
  FILE   *fin;               /* pointer to input file */
  FILE   *fout;              /* pointer to outfule file */
  FILE   *fps;               /* pointer to graphics file */

  /* Parameter read from input file */
  int    seed;               /* seed for random number generator, rand() */
  int    number_grains;      /* desired number grains in final structure */
  float  radius_real;        /* final grain size from input file */
  float  dep_rate_real;      /* deposition rate in m/sec */
  int    contact_angle;      /* island-substrate contact angle, degrees */
  float  ca;                 /* island-substrate contact angle, radians */
  float  gamma;              /* surface stress of island, J/m2 */
  float  r_lock;             /* lock-down radius used in comp stress calc */
  float  E;                  /* Young's modulus of film material, Pa */
  float  nu;                 /* Poisson ratio of film material, unitless */
  float  dg;                 /* 2*gamma_surface - gamma_gb, J/m2 */
  float  cluster_area_crit;  /* island sliding criteria */
  float  temperature;        /* deposition temperature in K */
  float  pre_exp;            /* Pre-exp factor to surface coble creep */
  float  q_act;              /* Activation energy to surface coble creep */
  float  graphics_coverage;  /* Substrate coverage at which to do graphics */

  /* Relate real dimensions and rate to simulation growth conditions */
  float  geom;               /* geometric factor for spherical-cap island */
  float  g0_i_ratio;         /* lateral growth rate to nucleation rate ratio */
  float  dep_rate;           /* deposition rate in simulation */
  float  size;               /* estimated average grain size in simulation */

  /* film thickness during deposition */
  float  thickness;
  /* fractional substrate coverage */
  float  coverage;
```

```
/* Random time between nucleation attempts */
float  time_step;

/* Used to check if graphics dumped yet */
int gdump;

/* Track number of intersection and contact points */
int numpoint;
int numcontact;
int numcontact_old;

double area;
double stress_comp;
double stress_tensile;
double stress;
int    ng_inbound;

float  h_begin, h_final, h_step;

float  sim_radius;

int i;


if (argc!=2) {
  printf("USAGE:  ./grow results/BASENAME\n");
  printf("where results/BASENAME.inp must have the correct format\n");
  exit(0);
}

/*  Read in name of input file in results directory */
sprintf(basename, "%s", argv[1]);
sprintf(filename, "%s.inp", basename);

if((fin=fopen(filename,"r"))==NULL) {
  printf("\nError opening input file %s\n", filename);
  exit(0);
}

/* Use in basename to create output file pointers */
sprintf(filename, "%s.out", basename);

if((fout=fopen(filename,"w"))==NULL) {
  printf("\nError opening output file %s\n", filename);
  exit(0);
}

sprintf(filename, "%s.ps", basename);

if((fps=fopen(filename,"w"))==NULL) {
  printf("\nError opening graphics output file %s\n", filename);
  exit(0);
}

/*
** Read simulation parameters from input file
*/

/* Random seed */
fgets(text,80,fin);
fscanf(fin, "%d", &seed);
fgets(text,80,fin);  fgets(text,80,fin);
```

```
/* Total number of grains once continuous film */
fscanf(fin, "%d", &number_grains);
fgets(text,80,fin);  fgets(text,80,fin);

/* Average grain radius once continuous (meters) */
fscanf(fin, "%f", &radius_real);
fgets(text,80,fin);  fgets(text,80,fin);

/* Deposition rate (meter/sec) */
fscanf(fin, "%f", &dep_rate_real);
fgets(text,80,fin);  fgets(text,80,fin);

/* Contact angle (degrees) */
fscanf(fin, "%d", &contact_angle);
fgets(text,80,fin);  fgets(text,80,fin);
/* Convert contact angle from degrees to radians */
ca= PI*contact_angle/180.0;

/* Surface stress (J/m2) */
fscanf(fin, "%f", &gamma);
fgets(text,80,fin);  fgets(text,80,fin);

/* Lock-down radius (meters) */
fscanf(fin, "%f", &r_lock);
fgets(text,80,fin);  fgets(text,80,fin);

/* Young's modulus of film material (Pa) */
fscanf(fin, "%f", &E);
fgets(text,80,fin);  fgets(text,80,fin);

/* Poisson ratio of film material (unitless) */
fscanf(fin, "%f", &nu);
fgets(text,80,fin);  fgets(text,80,fin);

/* Delta gamm = 2*gamma_surface - gamma_gb (J/m2) */
fscanf(fin, "%f", &dg);
fgets(text,80,fin);  fgets(text,80,fin);

/* Critical cluster area (m^2) */
fscanf(fin, "%f", &cluster_area_crit);
fgets(text,80,fin);  fgets(text,80,fin);

/* Deposition temperature (K) */
fscanf(fin, "%f", &temperature);
fgets(text,80,fin);  fgets(text,80,fin);

/* Pre-exponential to surface coble creep */
fscanf(fin, "%f", &pre_exp);
fgets(text,80,fin);  fgets(text,80,fin);

/* Activation energy for surface coble creep (eV) */
fscanf(fin, "%f", &q_act);
fgets(text,80,fin);  fgets(text,80,fin);

/* Graphics at specified substrate coverage
** If graphics are not desired, set above 1.0
*/
fscanf(fin, "%f", &graphics_coverage);
fclose(fin);

printf("# INPUT FILE DATA:\n");
printf("# Seed:              %d\n", seed);
printf("# Number of grains:  %d\n", number_grains);
```

```
printf("# Real radius:       %e A\n", 1e10*radius_real);
printf("# Deposition rate:   %f nm/s\n", 1e9*dep_rate_real);
printf("# Contant angle      %d degrees\n", contact_angle);
printf("# Surface stress:    %f J/m2\n", gamma);
printf("# Lock-down radius:  %f nm\n", 1e9*r_lock);
printf("# Young's modulus    %f GPa\n", 1e-9*E);
printf("# Poisson ratio      %f\n", nu);
printf("# Delta gamma        %f\n", dg);
printf("# Crit. clust. area  %f\n", cluster_area_crit);
printf("# Temperature        %f\n", temperature);
printf("# Pre exponential    %e\n", pre_exp);
printf("# Activation energy  %f\n", q_act);

/* Assign seed for pseudo-random number generator, rand(). */
srand((unsigned int) (seed));

/* Read C.V. Thompson, JMR 14, 3164 (1999) */
/* The final average grain radius can be estimated as:
** radius= 0.602*g_i_ratio^(1/3)
** where g_i_ratio is the lateral growth rate/nucleation rate ratio.
**
** The scaling factor for the simulation relates simulation dimension
** to real dimensions:
** radius_real= scaling*radius_simulation
**
** From Thompson 1999, the lateral growth rate of an isolated island
** is the deposition rate time a geometric factor:
** dep_rate= g/geom;
**
** The real deposition rate supplied as an input to the simulation
** is therefore given by:
** dep_rate_real= (g_sim/geom)*scaling
**
** The choosen time step (shown later) gives a constant nucleation rate
** of one new nuclei per unit exposed area per unit time.
** I_sim= 1
**
** Combining the following three expressions from above:
** radius_real= scaling*radius_sim
** radius_sim= 0.602(g_sim/I_sim)^(1/3)
** g_sim= dep_rate_real*geom/scaling
**
** radius_real= scaling*0.362*(dep_rate_real*geom/(I_sim*scaling))^(1/3)
** radius_real= 0.602*(scaling^2*dep_rate_real*geom/(I_sim))^1/3
**
** Rearranging the above equation to solve for scaling:
** scaling= (radius_real/0.602)^(3/2)*(I_sim/dep_rate_real*geom)^(1/2)
*/

geom= 1.0;
geom *= pow(sin(ca),3.0);
geom *= 1.0/pow(1.0 - cos(ca),2.0);
geom *= 1.0/(2.0 + cos(ca));
scaling= pow((radius_real/0.602),1.5)*sqrt(1.0/(dep_rate_real*geom));
g0= dep_rate_real*geom/scaling;
g0_i_ratio= g0;

/* Calculate deposition rate for simulation */
dep_rate= g0/geom;

/* Use average grain size to calculate size of substrate. */
size= 2*0.602*pow(g0_i_ratio,(1.0/3.0));
xmin= 0.0; ymin= 0.0;
```

```
xmax= sqrt(number_grains)*size;
ymax= sqrt(number_grains)*size;
xsize= xmax-xmin;
ysize= ymax-ymin;

printf("# SIZE OF GRAINS %f\n", size);
printf("# xsize x ysize  %f x %f\n", xsize, ysize);
printf("# dep rate %f nm/s\n", dep_rate*scaling*1e9);
printf("# g0 %f\n", g0);

/* Allocate memory for structure arrays */
if ( allocate_memory(number_grains, size) == 0)
  exit(0);

/* Initialize to zero:
** number of grains (ng)
** time (t)
** film thickness
** fractional substrate coverage
** variable to check if graphics dumped yet
*/
ng= 0;
t= 0.0;
thickness= 0.0;
coverage= 0.0;
numcontact= 0;
gdump= 0;

/* Convert to scaling dimensions */
cluster_area_crit *= 1.0/(scaling*scaling);

while (coverage < 0.99) {

  /* Do graphics dump at specified coverage */
  if ((coverage > graphics_coverage) && !(gdump)) {
    ps_write(fps, ng);
    gdump= 1;
  }

  /*
  ** (1) Increment time step of simulation
  ** (2) Attempt to nucleate new island
  */
  nucleate_island(&time_step);

  /*
  ** At begining of new timestep:
  ** (1) Calculate radius of island (ignoring intersections)
  ** (2) Initialize number of intersection points to zero
  ** (3) Initialize number of boundary points to zero
  */
  for (i=0; i<ng; i++) {
    grain[i].r= g0*(t-grain[i].t);
    grain[i].numpoint= 0;
    grain[i].numbound= 0;
  }

  /* Determine intersection points between island */
  island_intersection(&numpoint);

  /* Organize intersection point in a CCW fashion around island */
  organize_intersection_points();
```

```
    /* Create boundary points between intersection points */
    draw_island_boundary();

    /* Calculate area of islands/grains */
    for (i=0; i<ng; i++) {
      grain[i].area= calc_grain_area(i);
      if (grain[i].area < TOL1)
       grain[i].area = TOL1;
    }

    /* Determine new contacts between island
    ** numcontact_added= numcontact_new - numcontact_old
    */
    numcontact_old= numcontact;
    new_contacts(&numcontact);

    /* Update old contact points */
    for (i=0; i<numcontact_old; i++)
      update_contacts(i);

    /* Calculate zipping stress for new contact points */
    for (i=numcontact_old; i<numcontact; i++)
      stress_contacts(i, ca, E, nu, dg, cluster_area_crit);

    /* Calculate Laplace pressure for all island */
    laplace_pressure(ca, gamma, r_lock);

    /* Stres relaxation */
    stress_relax_coble(time_step, temperature, pre_exp, q_act);

    /* Area averaged stress */
    stress_tensile= 0;
    stress_comp= 0;
    area= 0;
    ng_inbound= 0;

    for (i=0; i<ng; i++) {

      if (inbound(grain[i].x, grain[i].y)) {
       area += grain[i].area;
       stress_comp += grain[i].area*grain[i].stress_comp;
       stress_tensile  += grain[i].area*grain[i].stress;
       ng_inbound++;
      }
    }

    coverage= area/(xsize*ysize);
    thickness += dep_rate*time_step*coverage;
    stress_comp *= 1.0/area;
    stress_tensile *= 1.0/area;

    fprintf(fout, "%f %f %f %f %f %f %f\n", t, 1e9*scaling*thickness,
stress_comp*1e-6, stress_comp*scaling*thickness, 0.5*stress_tensile*1e-6,
stress_tensile*scaling*thickness, coverage);
  }

  h_step= thickness/200.0;
  h_begin= thickness + h_step;
  h_final= 3.0*thickness;
  time_step= h_step/dep_rate;

  for (thickness=h_begin; thickness<h_final; thickness +=h_step) {
```

```
    t +=time_step;
    film_stress_relax_coble(time_step, temperature, pre_exp, q_act);

    /* Area averaged stress */
    stress_tensile= 0;
    stress_comp= 0;
    area= 0;
    ng_inbound= 0;

    for (i=0; i<ng; i++) {

      if (inbound(grain[i].x, grain[i].y)) {
       area += grain[i].area;
       stress_comp += grain[i].area*grain[i].stress_comp;
       stress_tensile  += grain[i].area*grain[i].stress;
       ng_inbound++;
      }
    }
    coverage= area/(xsize*ysize);
    stress_comp *= 1.0/area;
    stress_tensile *= 1.0/area;

    fprintf(fout, "%f %f %f %f %f %f %f\n", t, 1e9*scaling*thickness,
stress_comp*1e-6, stress_comp*scaling*thickness, 0.5*stress_tensile*1e-6,
stress_tensile*scaling*thickness, coverage);
  }
}
```

****

The allocate.c code calculates the approximate memory usage for the size of the simulation specific in the input file and limits the total memory usage to 256MB. After checking the memory usage, the memory for the main structures used in the simulation is allocated.

****

```
/* allocate.c */

#include <stdio.h>
#include <math.h>
#include <stdlib.h>
#include "defines.h"
#include "struct.h"

extern grain_struct *grain;
extern point_struct *point;
extern bound_struct *bound;
extern contact_struct *contact;

int allocate_memory(int number_grains, float size)
{
    /* Estimations of the the maximum size for array declaration */
  int    maxgrains;
  int    maxpoints;
  int    maxbound;
  int    maxbounds;
  int    maxcontacts;
```

```
  /* Calculate total memory usage of allocated structures */
  int     ram_mb;

  /* Estimate size of arrays */

  /* PBC mirror copies of the structure around central structure.
  ** The 3X3 array of mirror copied structure gives 9*number grains
  ** The factor of 2 in front is for a margain of safety
  */
  maxgrains= 2*(9*number_grains);

  /* Each island impinges with on average 6 grains
  ** The extra 100 if for a margin of safety
  */
  maxpoints= 6*maxgrains + 100;

  /* Each island forms a grain boundary with on average 6 grains
  ** The distance between boundary points is never less than TOOCLOSE
  ** Each island must be alloted the max number of possible boundary points
  */
  maxbound = 6*size/TOOCLOSE;
  maxbounds= maxbound*maxgrains;

  /* Each island impinges with on average 6 grains
  ** The extra 100 if for a margin of safety
  */
  maxcontacts= 6*maxgrains + 100;

  printf("# maxgrain    %d\n", maxgrains);
  printf("# maxpoint    %d\n", maxpoints);
  printf("# maxbound    %d\n", maxbound);
  printf("# maxbounds   %d\n", maxbounds);
  printf("# maxcontacts %d\n", maxcontacts);

  ram_mb= 0;
  ram_mb += (int) maxgrains*sizeof(grain_struct);
  printf("# Using %.0f MB of RAM\n", ram_mb/1.0e6);
  ram_mb += (int) maxpoints*sizeof(point_struct);
  printf("# Using %.0f MB of RAM\n", ram_mb/1.0e6);
  ram_mb += (int) maxbounds*sizeof(bound_struct);
  printf("# Using %.0f MB of RAM\n", ram_mb/1.0e6);
  ram_mb += (int) maxcontacts*sizeof(contact_struct);
  printf("# Using %.0f MB of RAM\n", ram_mb/1.0e6);
  ram_mb *= 1.0e-6;

  /* Allocate memory */
  grain= (grain_struct *) malloc(maxgrains*sizeof(grain_struct));
  point= (point_struct *) malloc(maxpoints*sizeof(point_struct));
  bound= (bound_struct *) malloc(maxbounds*sizeof(bound_struct));
  contact= (contact_struct *) malloc(maxcontacts*sizeof(contact_struct));

  if (ram_mb < RAM_MAX)
    return(1);
  else {
    printf("%d MB of RAM allocated greater than %d MB limit.\n", ram_mb,
RAM_MAX);
    return(0);
  }
}
```

****

The nucleate.c code increments the timestep and attempts to nucleate a new island at a random position on the substrate. If the random position is already occupied by an existing island, then the nucleation attempt fails. If nucleation is successful, the new nucleus position is copied and translated in a 3X3 array to create the periodic boundary conditions, where only the middle array element is used to calculate results in the simulation.

****

```
/* nucleate.c */

#include <stdio.h>
#include <math.h>
#include <stdlib.h>
#include "defines.h"
#include "struct.h"

extern grain_struct *grain;
extern point_struct *point;
extern bound_struct *bound;
extern contact_struct *contact;

extern float t;
extern int ng;
extern float g0;
extern float scaling;
extern double xmax, ymax;


/* nucleate */
void new_grain(double, double);

void nucleate_island (float *time_step)
{
  /* Random position on substrate for nucleation attempt */
  double xx, yy;
  /* Distance between existing island and position of nulceation attempt */
  double dx, dy, r;
  /* If random nucleation position not contained within existing island */
  int    okay;
  int    i;

  /* Random time between nucleation attempts */
  *time_step = 2.0*((1+rand())/(double)(1.0+RAND_MAX)) / (xmax*ymax);

  /* Increase total simulation by time step */
  t += *time_step;
  /* Random position for current nucleation attempt */
  xx = rand()/(double)(RAND_MAX) * xmax;
  yy = rand()/(double)(RAND_MAX) * ymax;

  /* Check that new nucleation site outside any existing islands. */
  okay = 1;
  for (i=0; i<ng && okay; i++) {
    r= g0*(t - grain[i].t);
    dx= grain[i].x - xx;
    dy= grain[i].y - yy;
    if ( (dx*dx + dy*dy) < (r*r) )
```

```
      okay= 0;
  }

  /*
    If okay then record the new nuclei.  Duplicate the nuclei
    eight times (once for each direction from the center rectangle).
  */
  if (okay) {
    new_grain(xx,      yy-ymax);
    new_grain(xx,      yy);
    new_grain(xx,      yy+ymax);
    new_grain(xx-xmax,yy-ymax);
    new_grain(xx-xmax,yy);
    new_grain(xx-xmax,yy+ymax);
    new_grain(xx+xmax,yy-ymax);
    new_grain(xx+xmax,yy);
    new_grain(xx+xmax,yy+ymax);
  }
}

void new_grain(double x, double y)
{
  grain[ng].t= t;
  grain[ng].x= x;
  grain[ng].y= y;

  grain[ng].area= 0;
  grain[ng].delete= 0;
  grain[ng].numcontact= 0;
  grain[ng].stress= 0;

  ng++;
}
```

****

The file intersection.c contains code related to the calculation of the intersection points between intersecting island.

****

```
/*  intersection.c */

#include <stdio.h>
#include <math.h>
#include <stdlib.h>
#include "defines.h"
#include "struct.h"

extern grain_struct *grain;
extern point_struct *point;
extern bound_struct *bound;
extern contact_struct *contact;

extern float t;
extern float g0;
extern int ng;
extern double xmin, xmax, ymin, ymax;
extern int long numbound;
```

```
/* auxiliary.c */
extern int meet (double, double, double, double, double);

/* intersection.c */
int  same_point(int, int);
void circle_intersect(int, int, double *, double *);
int  find_triple(int, int, int, int *, double, double, double, int *);
int  hyper(double, double, double, double, double, double, double,
                 double, double, double *, double *, double *);
double tp_grain_angle(int, int, int);

/* boundary.c */
extern int drawhyp(int, int, int, int);
extern int draw_circle_full(int);
extern int draw_circle(int, int, int);

void island_intersection(int *numpoint) {

  double xi, yi, ri;
  double xj, yj, rj;
  double xk, yk, rk;
  int    near[MAXSIDES*10];
  double xci[2], yci[2];
  int    intersect;
  int    i, j, k, p, nn, jj, kk;

  /* The "points" are those which results from the intersection of
  ** two circles.  Since the circles grow each timestep, they must be
  ** recalculated each timestep, so initialize numpoint to zero.
  */
  *numpoint= 0;

  /* Determine which grains intersect. */
  for (i=0; i<ng; i++) {
    /* Store data for current grain, i */
    xi= grain[i].x;  yi= grain[i].y;  ri=grain[i].r;

    /* Generate a list of possible neighbors. */
    nn= 0;
    for (j=0; j<ng; j++) {
      if (j != i) {
       xj= grain[j].x;  yj= grain[j].y;  rj= grain[j].r;
       if ( meet(xi, yi, xj, yj, ri+rj) )
         near[nn++]= j;
      }
    }

    /* Find new points of intersection of grains */
    for (jj=0; jj<nn; jj++) {
      j= near[jj];
      /* Determine the x,y coords of the two points of intersection
      ** of the grain, i, and the neighboring grain, j.
      */
      circle_intersect(i,j,xci,yci);
      /* Determine if any other grains have intersected the x,y coord
      ** of the intersection point.  If no other intersections are
      ** found, then the point is recorded.  These type of points will
      ** move each timestep and are therefore recalculated each timestep.
      ** If the point is intersected, the point must be part of a triple
      ** point.
      */
      for (p=0; p<2; p++) {
       intersect= 0;
```

```
      /* loop for the kth neighbor */
      for (kk=0; kk<nn; kk++) {
        k = near[kk];
        if (k != j) {
          xk = grain[k].x;  yk = grain[k].y;  rk = grain[k].r;
          if ( meet(xk,yk,xci[p],yci[p],rk) )
            intersect= 1;
        }
      }
      if (!intersect) {
        point[*numpoint].x= xci[p];
        point[*numpoint].y= yci[p];
        point[*numpoint].t= t;
        point[*numpoint].grain[0]= j;
        point[*numpoint].grain[1]= j;
        point[*numpoint].theta= atan2(yci[p]-yi,xci[p]-xi);
        point[*numpoint].cw= p % 2;
        point[*numpoint].ccw= (p+1) % 2;
        grain[i].point[grain[i].numpoint++]= (*numpoint)++;
      }
      else {
        find_triple(i,jj,nn,near,xci[p],yci[p],t,numpoint);
      }
     }
    }
  }  /* loop for ith grain */
}

void organize_intersection_points() {

  int    pt;
  double theta0, theta1, thetac;
  int    grn;
  int    i, j, k, l, m;

  numbound= 0;
  /* Now organize the points around each grain */
  for (i=0; i<ng; i++) {
    /*
    **  Determine ccw direction of grains around triple points.
    **  If grain0 and grain1 equal, then only circle intersection point.
    */
    for (j=0; j<grain[i].numpoint; j++) {
      pt= grain[i].point[j];
      if (point[pt].grain[0] != point[pt].grain[1]) {
       theta0= tp_grain_angle(i, pt, point[pt].grain[0]);
       theta1= tp_grain_angle(i, pt, point[pt].grain[1]);

       if (theta0 < theta1) {
         grn= point[pt].grain[0];
         point[pt].grain[0]= point[pt].grain[1];
         point[pt].grain[1]= grn;
       }
      }
    }

    /* Sort intersection points around grain */
    for (j=1; j<grain[i].numpoint; j++) {
      pt= grain[i].point[j];
      thetac= point[pt].theta;
      m= 0;
      while ( (thetac>point[grain[i].point[m]].theta) && m<j) m++;
      for (l=j; l>m; l--)
```

```
        grain[i].point[l]= grain[i].point[l-1];

       grain[i].point[m]= pt;
     }

     /* Remove any duplicate points */
     for (j=0; j<grain[i].numpoint-1; j++)
       if ( same_point(grain[i].point[j], grain[i].point[j+1]) ) {
        for (k=j; k<grain[i].numpoint-1; k++)
          grain[i].point[k]= grain[i].point[k+1];
        grain[i].numpoint--;
        j--;
       }
  }
}

void draw_island_boundary()
{
  int    pt_start, pt_stop;
  int    i, j, k;

  for (i=0; i<ng; i++) {

    /* No intersection points then still a circular island */
    if (grain[i].numpoint == 0)
      draw_circle_full(i);
    /* Traverse intersection points around grain and calculate the length
    ** of the grain boundary and the grain size.
    */
    for (j=0; j<grain[i].numpoint; j++) {
      pt_start= grain[i].point[j];

      if (j<grain[i].numpoint-1)
       pt_stop= grain[i].point[j+1];
         else
           pt_stop= grain[i].point[0];

      k= point[pt_start].grain[0];

      if (same_point(pt_start,pt_stop) ) {
       /* printf("DUPLICATE POINTS IN STRUCTURE?\n"); */
       continue;
      }

      if ( (point[pt_start].ccw==1) && (point[pt_stop].cw==1) ) {
       drawhyp(i,k,pt_start,pt_stop);
      }
      if ( (point[pt_start].ccw==0) && (point[pt_stop].cw==0) )
       draw_circle(i,pt_start,pt_stop);
    }
  }
}


int same_point(int p1, int p2)
{
  double x1, y1, x2, y2;
  double distance;

  x1= point[p1].x;    y1= point[p1].y;
  x2= point[p2].x;    y2= point[p2].y;
  distance= sqrt( (x2-x1)*(x2-x1) + (y2-y1)*(y2-y1) );
  if (distance < TOL1)
```

```
    return(1);
  else
    return(0);
}

void circle_intersect(int i, int j, double *xci, double *yci)
{
  double x1, y1, r1;
  double x2, y2, r2;
  double r3;
  double theta1, theta2, theta3;
  double theta;
  double dx_prime, dy_prime;
  double dx, dy;
  double dc[2][2];

  x1= grain[i].x;    y1= grain[i].y;    r1= grain[i].r;
  x2= grain[j].x;    y2= grain[j].y;    r2= grain[j].r;

  r3= sqrt( (x1-x2)*(x1-x2) + (y1-y2)*(y1-y2) );

  /* l:m:s r1:r2:r3 */
  if ( (r1>r2) && (r2>r3) && (r1>r3) ) {
    theta1= acos( (r2*r2 + r3*r3 - r1*r1)/(2*r2*r3) );
    theta2= asin( (r2/r1)*sin(theta1) );
    theta3= asin( (r3/r1)*sin(theta1) );
  }

  /* l:m:s r1:r3:r2 */
  if ( (r1>r2) && (r2<r3) && (r1>r3) ) {
    theta1= acos( (r2*r2 + r3*r3 - r1*r1)/(2*r2*r3) );
    theta2= asin( (r2/r1)*sin(theta1) );
    theta3= asin( (r3/r1)*sin(theta1) );
  }

  /* l:m:s r2:r1:r3 */
  if ( (r1<r2) && (r2>r3) && (r1>r3) ) {
    theta2= acos( (r1*r1 + r3*r3 - r2*r2)/(2*r1*r3) );
    theta1= asin( (r1/r2)*sin(theta2) );
    theta3= asin( (r3/r2)*sin(theta2) );
  }

  /* l:m:s r2:r3:r1 */
  if ( (r1<r2) && (r2>r3) && (r1<r3) ){
    theta2= acos( (r1*r1 + r3*r3 - r2*r2)/(2*r1*r3) );
    theta1= asin( (r1/r2)*sin(theta2) );
    theta3= asin( (r3/r2)*sin(theta2) );
  }

  /* l:m:s r3:r1:r2 */
  if ( (r1>r2) && (r2<r3) && (r1<r3) ) {
    theta3= acos( (r1*r1 + r2*r2 - r3*r3)/(2*r1*r2) );
    theta1= asin( (r1/r3)*sin(theta3) );
    theta2= asin( (r2/r3)*sin(theta3) );
  }

  /* l:m:s r3:r2:r1 */
  if ( (r1<r2) && (r2<r3) && (r1<r3) ) {
    theta3= acos( (r1*r1 + r2*r2 - r3*r3)/(2*r1*r2) );
    theta1= asin( (r1/r3)*sin(theta3) );
    theta2= asin( (r2/r3)*sin(theta3) );
  }
```

```
  /* components of distance to intersection of circles */
  dx_prime= r1*cos(theta2);
  dy_prime= r1*sin(theta2);

  /* calculate direction cosine rotation matrix */
  theta= atan2(y2-y1,x2-x1);
  dc[0][0]= cos(theta);
  dc[0][1]= sin(theta);
  dc[1][0]= -sin(theta);
  dc[1][1]= cos(theta);

  /* already in rotated coordinate system, so transform back */
  dx= dc[0][0]*dx_prime - dc[1][0]*dy_prime;
  dy= dc[0][1]*dx_prime - dc[1][1]*dy_prime;
  xci[0]= x1+dx;
  yci[0]= y1+dy;

  dx= dc[0][0]*dx_prime + dc[1][0]*dy_prime;
  dy= dc[0][1]*dx_prime + dc[1][1]*dy_prime;
  xci[1]= x1+dx;
  yci[1]= y1+dy;

  /*
  printf("theta: %f %f %f %f\n", theta1, theta2, theta3, theta);
  printf("%f %f %f %f %f %f %f\n", x1, y1, r1, x2, y2, r2, r3);
  printf("%f %f %f %f %f\n", theta, dx_prime, dy_prime, dx, dy);
  printf("%f %f %f %f\n", xci[0], yci[0], xci[1], yci[1]);
  */
}

int find_triple(int i, int jj, int nn, int *near, double xci, double yci,
double t, int *numpoint)
{
  int j, k, kk, nt, m, mm;
  double xi, yi, ri, ti;
  double xj, yj, rj, tj;
  double xk, yk, rk, tk;
  double xn, yn, tn;
  double xm, ym, rm, tm;
  double rch;
  int    ntrip;
  double xp[2],yp[2],tp[2];
  double bound_x, bound_y;
  int    okay;

  bound_x= DUPL_FRAC*xmax;
  bound_y= DUPL_FRAC*ymax;

  xi= grain[i].x;   yi= grain[i].y;   ri= grain[i].r;   ti= grain[i].t;

  j= near[jj];
  xj= grain[j].x;   yj= grain[j].y;   rj= grain[j].r;   tj= grain[j].t;

  /* loop for the kth neighbor */
  for (kk=0; kk<nn;kk++) {
    k= near[kk];
    if (k != j) {
      xk= grain[k].x;   yk= grain[k].y;   rk= grain[k].r;   tk= grain[k].t;
      if ( meet(xk,yk,xci,yci,rk) ) {

        /*
        ** Determine the number, position, and formation time of triple
         ** points associated with the three grains.  Alert user if no
```

```
       ** triple points were found.
       */

       ntrip = hyper(xi,yi,ti,xj,yj,tj,xk,yk,tk,xp,yp,tp);

       /*
      ** Process each triple point found. In particular check to see that
       ** the triple point is a valid triple point and not erroneous due to
       ** edge effects.  Also check to make sure that no other grain could
       ** have grown to the triple point before the three grains we have
       ** found to form the triple point.
       */


       for (nt=0;nt<ntrip;nt++) {
         xn = xp[nt];    yn = yp[nt];     tn= tp[nt];
         if ( (xn < xmin-bound_x) || (yn < ymin-bound_y) ||
              (xn > xmax+bound_x) || (yn > ymax+bound_y) )
          {  /* printf("Triple out of bounds.\n"); */ }
         else if (tn > t)
           {  /* printf("Triple point time too large %d %d %f %f.\n", i, j,
tn, \
                t); */ }
         else {
           /*
          ** Check to see that no other grain has reached the triple
           ** point first.
           */
           okay = 1;
           for (mm=0;mm<nn;mm++) {
            m = near[mm];
            if ( (m != j) && (m != k)) {
             xm = grain[m].x;  ym = grain[m].y;
             rm = grain[m].r;  tm = grain[m].t;
             rch = g0 * (tn - tm);
             if (rch>0.0 && meet(xn,yn,xm,ym,rch) ) {
               okay = 0;
             }
            }
          }

           /* If okay=1 we have found a triple point. */
           if (okay == 1) {
             /* Record triple point information */
             point[*numpoint].x= xn;
             point[*numpoint].y= yn;
             point[*numpoint].t= tn;
             point[*numpoint].grain[0]= j;
             point[*numpoint].grain[1]= k;
             point[*numpoint].theta= atan2(yn-yi,xn-xi);
             point[*numpoint].ccw= 1;
             point[*numpoint].cw= 1;
             grain[i].point[grain[i].numpoint++]= (*numpoint)++;

           } /* if valid triple point */
         }  /* if triple in bounds   */
       }  /* loop over triples found   */
     }  /* if jth and kth could meet      */
   }  /* loop for kth neighbor              */
 }
 return(1);
}
```

```
/*
Subroutine to calculate the intersection points of two hyperbolae.
These represent the boundaries between grains 1 and 2 and
grains 1 and 3, when they grow circularly, nucleated at different
times.
*/
int hyper(double x1, double y1, double t1, double x2, double y2,
          double t2, double x3, double y3, double t3,
          double *xp, double *yp, double *tt)
{

  double aa1,aa2,bb1,bb2,w1,w2,den,aaa,bbb,ccc,ddd,at,bt;
  double ct,f2,root,cc1,cc2,g2;

  g2 =  g0*g0;
  aa1 = 2.*(x2-x1);
  aa2 = 2.*(x3-x1);
  bb1 = 2.*(y2-y1);
  bb2 = 2.*(y3-y1);

  w1 = x2*x2-x1*x1+y2*y2-y1*y1+g2*(t1*t1-t2*t2);
  w2 = x3*x3-x1*x1+y3*y3-y1*y1+g2*(t1*t1-t3*t3);
  den = bb2*aa1 - bb1*aa2;

  if (den == 0.0) {
    printf("Special case:  Three points in straight line.\n");
    return(0);
  }

  if (aa1 == 0.0) {
    /* Special case of x1 = x2 */
    aaa = w1/bb1;
    bbb = -2.*g2*(t1-t2)/bb1;
    ccc = (w2-bb2*aaa)/aa2;
    ddd = (-2.*g2*(t1-t3) - bb2*bbb)/aa2;
  }
  else {
    aaa = (w2*aa1-w1*aa2)/den;
    bbb = 2.*g2*((t3-t1)*aa1 + (t1-t2)*aa2)/den;
    ccc = (w1-bb1*aaa)/aa1;
    ddd = (-2.*g2*(t1-t2) - bb1*bbb)/aa1;
  }

  at = g2 - ddd*ddd - bbb*bbb;
  bt = 2.*(-t1*g2-ccc*ddd+x1*ddd-aaa*bbb+y1*bbb);
  ct = t1*t1*g2-(ccc-x1)*(ccc-x1)-(aaa-y1)*(aaa-y1);

  if (at == 0.0) {
    /* Special case of a=0; bt*T+c*T=0  */
    printf("Special case, t is not quadratic.\n");
    tt[0] = -ct/bt;
    cc1 = w1 - 2.*g2*(t1-t2)*tt[0];
    cc2 = w2 - 2.*g2*(t1-t3)*tt[0];
    yp[0] = (cc2*aa1-cc1*aa2)/den;

    if (aa1 == 0.0) xp[0] = (cc2-bb2*yp[0])/aa2;
    else xp[0] = (cc1-bb1*yp[0])/aa1;

    return (1);
  }

  f2 = bt*bt - 4.*at*ct;
  if (f2 < 0.0) {
```

```
    /* Handle the special case of imaginary roots. */
    printf("Special case:  imaginary roots.\n");

    /*  Return to program if error was from roundoff. */
    if (fabs(f2/(bt*bt)) > 0.001) return(0);
    else {
      root = 0.0;
      printf("Continued with root = 0.\n");
    }
  }
  else root = sqrt(f2);


  tt[0] = (-bt+root)/(2.*at);
  if (tt[0] < t3) return(0);

  cc1 = w1 - 2.*g2*(t1-t2)*tt[0];
  cc2 = w2 - 2.*g2*(t1-t3)*tt[0];
  yp[0] = (cc2*aa1-cc1*aa2)/den;
  if (aa1 == 0.0)
    xp[0] = (cc2 - bb2*yp[0])/aa2;
  else
    xp[0] = (cc1 - bb1*yp[0])/aa1;

  tt[1] = (-bt-root)/(2.*at);
  if (tt[1] < t3) return(1);

  cc1 = w1 - 2.*g2*(t1-t2)*tt[1];
  cc2 = w2 - 2.*g2*(t1-t3)*tt[1];
  yp[1] = (cc2*aa1-cc1*aa2)/den;
  if (aa1 == 0.0)
    xp[1] = (cc2 - bb2*yp[1])/aa2;
  else
    xp[1] = (cc1 - bb1*yp[1])/aa1;
  return(2);
}

double tp_grain_angle(int g1, int pt, int g2)
{
  double x1, y1;
  double xj, yj;
  double x2, y2, x2_new, y2_new;
  double theta;
  double dc[2][2];

  x1= grain[g1].x;    y1= grain[g1].y;
  xj= point[pt].x;    yj= point[pt].y;
  theta= atan2(yj-y1,xj-x1);
  dc[0][0]= cos(theta);
  dc[0][1]= sin(theta);
  dc[1][0]= -sin(theta);
  dc[1][1]= cos(theta);

  x2= grain[g2].x;
  y2= grain[g2].y;
  x2_new= dc[0][0]*(x2-xj) + dc[0][1]*(y2-yj);
  y2_new= dc[1][0]*(x2-xj) + dc[1][1]*(y2-yj);

  theta= atan2(y2_new,x2_new);

  return(theta);
}
```

****

The file boundary.c contains procedure to calculate the boundary points. The boundary points are evenly spaced points between intersection and/or triple points that constitute the edges of an island/grain.

****

```
/* boundary.c */

/* contact.c */

#include <stdio.h>
#include <math.h>
#include <stdlib.h>
#include "defines.h"
#include "struct.h"

extern grain_struct *grain;
extern point_struct *point;
extern bound_struct *bound;
extern contact_struct *contact;

extern float t;
extern int ng;
extern float scaling;
extern int long numbound;
extern double xmin, xmax, ymin, ymax;
extern float g0;

float xcursor, ycursor;

/* boundary.c */
int move_to(double, double);
int draw_to(double, double, int);

/*
Subroutine to draw the hyperbola that forms the boundary
between two grains which nucleate at different times.
This is done by a simplified method, developed Dec. 1984,  which
uses a transformation of coordinates to align the local axes,
(u,v), with the hyperbola.

x1,y1,t1        specifies the first nucleus
xn1,yn1,tn1     specifies the first triple point node
x2,y2,t2        specifies the second nucleus
xn2,yn2,tn2     specifies the second triple point node
*/
int drawhyp(int g1, int g2, int p1, int p2)
{
  double x1, y1, t1, x2, y2, t2;
  double xn1, yn1, tn1, xn2, yn2, tn2;
  double dx,dy,dr,ct,xc,yc,st,un1,vn1,un2,vn2;
  double a,b,c,b2,v,u,dv,x,y,xx,yy;
  int i,points;

  x1= grain[g1].x;   y1= grain[g1].y;   t1= grain[g1].t;
  x2= grain[g2].x;   y2= grain[g2].y;   t2= grain[g2].t;

  xn1= point[p1].x;   yn1= point[p1].y;   tn1= point[p1].t;
  xn2= point[p2].x;   yn2= point[p2].y;   tn2= point[p2].t;
```

```
  /* Find the parameters for the coordinate transformation.   */
  dx = x2 - x1;
  dy = y2 - y1;
  dr = sqrt(dx*dx + dy*dy);
  ct = dx/dr;
  st = dy/dr;
  xc = (x1 + x2)/2.;
  yc = (y1 + y2)/2.;

  /*  Transform the coordinates of the triple point nodes. */
  un1 =   (xn1-xc)*ct + (yn1-yc)*st;
  vn1 = -(xn1-xc)*st + (yn1-yc)*ct;
  un2 =   (xn2-xc)*ct + (yn2-yc)*st;
  vn2 = -(xn2-xc)*st + (yn2-yc)*ct;

  /*  Specify the hyperbola. */
  a = 0.5 * g0 * (t2-t1);
  c = 0.5 * dr;
  b2 = c*c - a*a;
  b = sqrt(b2);

  /*
  ** Determine the number of segment points we need to keep
  ** the segment point spacing close to the desired spacing.  Don't
  ** allow there to be zero segment points as GB_INIT will barf.
  ** The "points" variable is actually equal the number of segment
  ** points plus 1.
  */
  if (TOOCLOSE > TOOSMALL3) {
    points = fabs(vn2-vn1) / TOOCLOSE;
    if (points < 2) points = 2;
  }
  else
    points = 8;

  /* Tell where to start */
  move_to(xn1,yn1);

  /* Increment over values of v to draw the segment. */
  dv = (vn2-vn1)/( (double)(points) );
  v = vn1;
  for (i=0;i<points-1;i++) {
    v = v + dv;
    u = a * sqrt(1. + v*v/b2);
    x = u*ct - v*st + xc;
    y = u*st + v*ct + yc;

    draw_to(x,y,g1);

    xx = x;  yy = y;
    if (x < xmin) xx = x + (xmax-xmin);
    if (x > xmax) xx = x - (xmax-xmin);
    if (y < ymin) yy = y + (ymax-ymin);
    if (y > ymax) yy = y - (ymax-ymin);
  }

  /* Tell where to stop */
  draw_to(xn2,yn2,g1);

  return(1);
}
```

```
int draw_circle_full(int g)
{
  double xn, yn, rn;
  int    points;
  double theta, dt;
  double dx, dy;
  double x, y;
  int    i;

  xn= grain[g].x;        yn= grain[g].y;       rn= grain[g].r;

  points= 2*PI*rn / TOOCLOSE;
  if (points < 2) points= 2;

  /* Tell where to stop */
  move_to(xn+rn,yn);

  dt= 2*PI/( (double)(points) );
  theta= 0;
  for (i=0; i<points; i++) {
    dx= rn*cos(theta);
    dy= rn*sin(theta);
    x= xn+dx;
    y= yn+dy;

    draw_to(x,y,g);
    theta += dt;
  }

  /* Tell where to stop */
  draw_to(xn+rn,yn,g);

  return(1);
}

int draw_circle(int g, int p0, int p1)
{
  double xn, yn, rn;
  double x0, y0, theta0;
  double x1, y1, theta1;
  double dc[2][2];
  double dtheta;
  double arc_length;
  int    points;
  double theta, dt;
  double dx_prime, dy_prime;
  double dx, dy;
  double x, y;
  int    i;

  xn= grain[g].x;   yn= grain[g].y;   rn= grain[g].r;
  x0= point[p0].x;  y0= point[p0].y;  theta0= point[p0].theta;
  x1= point[p1].x;  y1= point[p1].y;  theta1= point[p1].theta;

  /* calculate direction cosine rotation matrix */
  dc[0][0]= cos(theta0);
  dc[0][1]= sin(theta0);
  dc[1][0]= -sin(theta0);
  dc[1][1]= cos(theta0);

  dtheta= theta1- theta0;
  if (dtheta < 0)
    dtheta += 2*PI;
```

```
  arc_length= dtheta*rn;

  points= arc_length / TOOCLOSE;
  if (points < 2) points= 2;

  /* Tell where to stop */
  move_to(x0,y0);

  dt= (dtheta)/( (double)(points) );
  theta= 0;
  for (i=0; i<points-1; i++) {
    dx_prime= rn*cos(theta);
    dy_prime= rn*sin(theta);
    dx= dc[0][0]*dx_prime + dc[1][0]*dy_prime;
    dy= dc[0][1]*dx_prime + dc[1][1]*dy_prime;
    x= xn+dx;
    y= yn+dy;

    draw_to(x,y,g);
    theta += dt;
  }

  /* Tell where to stop */
  draw_to(x1,y1,g);

  return(1);
}

int move_to(double x, double y)
{
  xcursor = x;  ycursor = y;
  return(1);
}

int draw_to(double x, double y, int i)
{
  bound[numbound].x1 = xcursor;
  bound[numbound].y1 = ycursor;
  bound[numbound].x2 = x;
  bound[numbound].y2 = y;
  grain[i].bound[grain[i].numbound++]= numbound++;

  xcursor=x;  ycursor=y;
  return(1);
}
```

****

The file contact.c contain code related to calculation of the impingement between two islands. Intersection points are recalculated every timestep since the intersection points change position when the islands grow in size. The contact point stores information about the first contact between two islands. When the two island impingement, the island coalescence model described in Chapter 4 is used to calculate the resulting tensile stress generation.

****

```
/* contact.c */

#include <stdio.h>
#include <math.h>
#include <stdlib.h>
#include "defines.h"
#include "struct.h"

extern grain_struct *grain;
extern point_struct *point;
extern bound_struct *bound;
extern contact_struct *contact;

extern float t;
extern int ng;
extern float scaling;
extern int long numbound;

/* auxiliary.c */
extern int inbound(double, double);

/* contact.c */
float gb_length(int);
float zip_height(int, int, float, float, float);
float height(int, int);
float cluster_area(int);


void new_contacts(int *numcontact)
{

  int pt_start, pt_stop;
  int ct;
  int found;
  int i, j, k, m;

  /* Determine if new contact points */
  for (i=0; i<ng; i++) {

    /* Only process those grains that are inbounds */
    if (inbound(grain[i].x, grain[i].y)) {

      /* Search intersection points to see if new contact points */
      for (j=0; j<grain[i].numpoint; j++) {
       pt_start= grain[i].point[j];

       if (j<grain[i].numpoint-1)
         pt_stop= grain[i].point[j+1];
       else
         pt_stop= grain[i].point[0];
       k= point[pt_start].grain[0];

       if ( (point[pt_start].ccw==1) && (point[pt_stop].cw==1) ) {
         found= 0;
         for (m=0; m<grain[i].numcontact; m++) {
           if (contact[grain[i].contact[m]].grain_contact == k) {
             found= 1;
             ct= grain[i].contact[m];
           }
         }
         if (!found) {
           contact[*numcontact].t= t;
           contact[*numcontact].grain= i;
```

```
          contact[*numcontact].grain_contact= k;
          contact[*numcontact].point[0]= pt_start;
          contact[*numcontact].point[1]= pt_stop;

          grain[i].contact[grain[i].numcontact++]= (*numcontact)++;

        }
        if (found) {
          contact[ct].point[0]= pt_start;
          contact[ct].point[1]= pt_stop;
        }
      }
    }
  }
 }
}

void update_contacts(int ct)
{
  int i, k;

  i= contact[ct].grain;
  k= contact[ct].grain_contact;

  contact[ct].length= gb_length(ct);
  contact[ct].height= height(i,k);
  contact[ct].radius= sqrt(grain[i].area/PI);
}

float gb_length(int ct)
{
  int    grn;
  double x1, y1;
  double x2, y2;
  double xb, yb;
  float  distance;
  float  length;
  int    start, stop;
  int    i;

 grn= contact[ct].grain;
  x1= point[contact[ct].point[0]].x;
  y1= point[contact[ct].point[0]].y;
  x2= point[contact[ct].point[1]].x;
  y2= point[contact[ct].point[1]].y;

  start= stop= -1;
  for (i=0; i<grain[grn].numbound; i++) {
    xb= bound[grain[grn].bound[i]].x1;
    yb= bound[grain[grn].bound[i]].y1;
    distance= sqrt((xb-x1)*(xb-x1)+(yb-y1)*(yb-y1));
    if (distance < TOL1)
      start= i;
    distance= sqrt((xb-x2)*(xb-x2)+(yb-y2)*(yb-y2));
    if (distance < TOL1)
      stop= i;
  }

  length= 0;
  if (start < stop)
    for (i=start; i<stop; i++) {
      x1= bound[grain[grn].bound[i]].x1;
      y1= bound[grain[grn].bound[i]].y1;
```

```
      x2= bound[grain[grn].bound[i]].x2;
      y2= bound[grain[grn].bound[i]].y2;
      length+= sqrt((x2-x1)*(x2-x1)+(y2-y1)*(y2-y1));
    }
  else {
    for (i=start; i<grain[grn].numbound; i++) {
      x1= bound[grain[grn].bound[i]].x1;
      y1= bound[grain[grn].bound[i]].y1;
      x2= bound[grain[grn].bound[i]].x2;
      y2= bound[grain[grn].bound[i]].y2;
      length+= sqrt((x2-x1)*(x2-x1)+(y2-y1)*(y2-y1));
    }
    for (i=0; i<stop; i++) {
      x1= bound[grain[grn].bound[i]].x1;
      y1= bound[grain[grn].bound[i]].y1;
      x2= bound[grain[grn].bound[i]].x2;
      y2= bound[grain[grn].bound[i]].y2;
      length+= sqrt((x2-x1)*(x2-x1)+(y2-y1)*(y2-y1));
    }
  }
  return(length);
}

float zip_height(int g1, int g2, float ca, float E, float dg)
{
  float r0, r1, r2;
  float z0_r1, z0_r2;
  float y0_r1, y0_r2;
  float z0_r1_min;
  float min;
  float se1_unit, se2_unit, se;
  float egb;
  float etot;
  int   i, steps;

  if ( (grain[g1].area < TOL1) || (grain[g2].area < TOL1) )
    return(0);

  r0= 100e-10;
  r1= scaling*sqrt(grain[g1].area/PI);
  r2= scaling*sqrt(grain[g2].area/PI);

  steps= 1000;
  min= 0;
  z0_r1_min= 1.0;

  for (i=1; i<steps; i++) {
    z0_r1= (1.0/steps)*i;
    y0_r1= 1.0 - sqrt(1.0/(sin(ca)*sin(ca))-pow(z0_r1+cos(ca)/sin(ca),2.0));
    z0_r2= z0_r1*r1/r2;
    y0_r2= 1.0 - sqrt(1.0/(sin(ca)*sin(ca))-pow(z0_r2+cos(ca)/sin(ca),2.0));
    se1_unit= E*0.2576*pow(y0_r1, 2.0);
    se2_unit= E*0.2576*pow(y0_r2, 2.0);
    se= se1_unit*r1*r1 + se2_unit*r2*r2;
    egb= dg*z0_r1*r1;
    etot= se-egb;
    /* printf("%f %e %e %e\n", z0_r1, se, egb, etot); */
    if (etot<min) {
      min= etot;
      z0_r1_min= z0_r1;
    }
  }
  return(z0_r1_min*r1/scaling);
```

```
}

float height(int i, int j)
{
  double x1, y1, r1;
  double x2, y2, r2;
  double r3;
  double theta1, theta2, theta3;
  double h;

  x1= grain[i].x;   y1= grain[i].y;   r1= grain[i].r;
  x2= grain[j].x;   y2= grain[j].y;   r2= grain[j].r;

  r3= sqrt( (x1-x2)*(x1-x2) + (y1-y2)*(y1-y2) );

  /* l:m:s r1:r2:r3 */
  if ( (r1>r2) && (r2>r3) && (r1>r3) ) {
    theta1= acos( (r2*r2 + r3*r3 - r1*r1)/(2*r2*r3) );
    theta2= asin( (r2/r1)*sin(theta1) );
    theta3= asin( (r3/r1)*sin(theta1) );
  }

  /* l:m:s r1:r3:r2 */
  if ( (r1>r2) && (r2<r3) && (r1>r3) ) {
    theta1= acos( (r2*r2 + r3*r3 - r1*r1)/(2*r2*r3) );
    theta2= asin( (r2/r1)*sin(theta1) );
    theta3= asin( (r3/r1)*sin(theta1) );
  }

  /* l:m:s r2:r1:r3 */
  if ( (r1<r2) && (r2>r3) && (r1>r3) ) {
    theta2= acos( (r1*r1 + r3*r3 - r2*r2)/(2*r1*r3) );
    theta1= asin( (r1/r2)*sin(theta2) );
    theta3= asin( (r3/r2)*sin(theta2) );
  }

  /* l:m:s r2:r3:r1 */
  if ( (r1<r2) && (r2>r3) && (r1<r3) ){
    theta2= acos( (r1*r1 + r3*r3 - r2*r2)/(2*r1*r3) );
    theta1= asin( (r1/r2)*sin(theta2) );
    theta3= asin( (r3/r2)*sin(theta2) );
  }

  /* l:m:s r3:r1:r2 */
  if ( (r1>r2) && (r2<r3) && (r1<r3) ) {
    theta3= acos( (r1*r1 + r2*r2 - r3*r3)/(2*r1*r2) );
    theta1= asin( (r1/r3)*sin(theta3) );
    theta2= asin( (r2/r3)*sin(theta3) );
  }

  /* l:m:s r3:r2:r1 */
  if ( (r1<r2) && (r2<r3) && (r1<r3) ) {
    theta3= acos( (r1*r1 + r2*r2 - r3*r3)/(2*r1*r2) );
    theta1= asin( (r1/r3)*sin(theta3) );
    theta2= asin( (r2/r3)*sin(theta3) );
  }

  /* components of distance to intersection of circles */
  h= fabs(r1*cos(theta2));

  return(h);
}
```

****

The file stress.c contains procedure related to the calculation stress in the island including:

(1) tensile stress generation due to island coalescence

(2) compressive stress generation due a Laplace pressure

(3) stress relaxation due to surface coble creep

****

```
/* stress.c */

#include <stdio.h>
#include <math.h>
#include <stdlib.h>
#include "defines.h"
#include "struct.h"

extern grain_struct *grain;
extern contact_struct *contact;
extern float scaling;
extern float g0;
extern float t;
extern int ng;

/* auxiliary.c */
extern int inbound(double, double);

/* contact.c */
extern float height(int, int);

/* stress.c */
float cluster_area(int);

void stress_contacts(int ct, float ca, float E, float nu, float dg, float
cluster_area_crit)
{
  float z0_r, y0_r;
  float stress_tensile;
  int i, k;

  i= contact[ct].grain;
  k= contact[ct].grain_contact;

  contact[ct].z0= zip_height(i,k,ca,E,dg);
  contact[ct].length= gb_length(ct);
  contact[ct].height= height(i,k);
  contact[ct].radius= sqrt(grain[i].area/PI);

  z0_r= contact[ct].z0/contact[ct].radius;
  y0_r= 1.0 - sqrt(1.0/(sin(ca)*sin(ca)) - pow(z0_r + cos(ca)/sin(ca), 2.0));
  stress_tensile= 0.5*(E/(1.0-nu*nu))*pow(y0_r, 1.3892);

  if ( (cluster_area(i) > cluster_area_crit) &&
       (cluster_area(k) > cluster_area_crit) )
    grain[i].stress += stress_tensile;
  else
    grain[i].stress += 0.0;
}
```

```
void laplace_pressure(float ca, float gamma, float r_lock)
{

  float comp_prefactor;
  float radius;
  int   i;

  /* Laplace Pressure
  ** Since radius changing each timestep, must recalculate stress for
  ** each grain.
  **
  ** Two models for the origin of compressive stress resulting from
  ** the Laplace pressure.  The first says simply that the compressive
  ** stress in an island is given by:
  ** stress= -gamma/radius
  ** The other model assumes that an island can easily slide when very
  ** small, but above a critical size the island attaches to the
  ** substrate with a certain lattice parameter.  As the island grows
  ** larger, the equilibrium lattice parameter dictated by the Lapalce
  ** pressure increases.  However the newly added material assumes the
  ** lattice parameter of the existing material.  Consequently, the
  ** material is under a compressive stres since the lattice parameter
  ** is smaller than the equilibrium lattice parameter:
  ** stress= gamma(1/radius - 1/radius_lock)
  **
  ** For gamma= 1.5 and radius_lock= 50, both models give similar results.
  */

  comp_prefactor= 4.0*gamma*sin(ca);
  comp_prefactor *= 1.0/(1.0 - cos(ca));
  comp_prefactor *= 1.0/(2.0 + cos(ca));

  for (i=0; i<ng; i++) {

    radius= scaling*sqrt(grain[i].area/PI);
    if (radius < 5e-10)
      radius= 5e-10;
    grain[i].stress_comp= -0.5*comp_prefactor/radius;


    /* if (radius > r_lock)
        grain[i].stress_comp= comp_prefactor*(1/radius - 1/r_lock);
      else
        grain[i].stress_comp= 0;
    */

  }
}

void stress_relax_coble(float time_step, float temperature, float pre_exp,
float q_act)
{
  float ht;
  float length;
  int   ct;
  float stress_relax;
  int   i,j;

  for (i=0; i<ng; i++) {
    if (inbound(grain[i].x, grain[i].y)) {

      ht= 0;
```

```
      length= 0;
      for (j=0; j<grain[i].numcontact; j++) {
       ct= grain[i].contact[j];
       if (contact[ct].height > contact[ct].z0)
         ht += contact[ct].height;
           else
            ht += contact[ct].z0;
       if (contact[ct].length > 2*contact[ct].z0)
         length += contact[ct].length;
           else
             length += 2*contact[ct].z0;
      }

      if (grain[i].numcontact > 0) {
       ht *= 1.0/grain[i].numcontact;

       stress_relax  = 1.0/pow(ht,3.0);
       stress_relax *= 1.0/pow(scaling,3.0);
       stress_relax *= pre_exp;
       stress_relax *= exp(-q_act*1.602e-19/(1.381e-23*temperature));
       stress_relax *= grain[i].stress;
       stress_relax *= time_step;

       if (stress_relax > grain[i].stress)
         grain[i].stress= 0;
       else
         grain[i].stress -= stress_relax;
      }
    }
  }
}

void film_stress_relax_coble(float time_step, float temperature, float pre_exp,
float q_act)
{
  float ht;
  float length;
  int   ct;
  float radius;
  float stress_relax;
  int   i, j, k;


  for (i=0; i<ng; i++) {
    grain[i].r= g0*(t-grain[i].t);

    if (inbound(grain[i].x, grain[i].y)) {

      ht= 0;
      length= 0;
      for (j=0; j<grain[i].numcontact; j++) {
       ct= grain[i].contact[j];
       k= contact[ct].grain_contact;
       contact[ct].height= height(i,k);
       contact[ct].radius= sqrt(grain[i].area/PI);
       radius= 0.5*(contact[ct].radius + sqrt(grain[k].area/PI));
       if (contact[ct].height > contact[ct].z0)
         ht += contact[ct].height;
           else
             ht += contact[ct].z0;
       length += contact[ct].length;
      }
```

```
      if (grain[i].numcontact > 0) {
       ht *= 1.0/grain[i].numcontact;

       stress_relax  = 1.0/pow(ht,3.0);
       stress_relax *= 1.0/pow(scaling,3.0);
       stress_relax *= pre_exp;
       stress_relax *= exp(-q_act*1.602e-19/(1.381e-23*temperature));
       stress_relax *= grain[i].stress;
       stress_relax *= time_step;

       if (stress_relax > grain[i].stress)
         grain[i].stress= 0;
          else
            grain[i].stress -= stress_relax;
      }
    }
  }
}


float cluster_area (int grn)
{
  int   *cluster_list;
  int   num_cl, num_cl_last;
  float area;
  int   ct;
  int   found1, found2;
  int   i, j, k;

  if (grain[grn].numcontact==0)
    return (grain[grn].area);

  cluster_list= (int *) malloc(ng*sizeof(int));

  num_cl= 0;
  cluster_list[num_cl++]= grn;

  num_cl_last= 0;
  while (num_cl_last < num_cl) {
    num_cl_last= num_cl;
    for (i=0; i<num_cl; i++) {
      grn= cluster_list[i];
      for (j=0; j<grain[grn].numcontact; j++) {
       ct= grain[grn].contact[j];

       found1= found2= 0;
       for (k=0; k<num_cl; k++) {
         if ( (contact[ct].grain == cluster_list[k]) )
           found1= 1;
         if ( (contact[ct].grain_contact == cluster_list[k]) )
           found2= 1;
       }

       if (!found1)
         cluster_list[num_cl++]= contact[ct].grain;
       if (!found2)
         cluster_list[num_cl++]= contact[ct].grain_contact;
      }
    }
  }

  area= 0.0;
  for (i=0; i<num_cl; i++)
```

```
    area += grain[cluster_list[i]].area;

  free(cluster_list);
  return(area);
}
```

****

The file graphics.c contains the procedure to create a Postscript dump of the film structure. Only the middle array element of the film structure is displayed so that the edges of the structure exhibit periodic boundary conditions.

****

```
/* graphics.c */

#include <stdio.h>
#include <stdlib.h>
#include <math.h>
#include <time.h>
#include "defines.h"
#include "struct.h"

#define MAXLINE          400
#define UNIT             144
#define TOOCLOSE2        0.5
#define XM               4
#define YM               4
#define LINEWIDTH        0.5
#define MARGIN           0.5
#define HEADER           "%!%!PS-Adobe"
#define FONT             "Courier"
#define SIZEFONT         16

extern grain_struct *grain;
extern int long numbound;

/* auxiliary.c */
extern int  inbound(double, double);

extern grain_struct *grain;
extern bound_struct *bound;

extern double xmin,xmax,ymin,ymax;
extern double xsize,ysize,xcursor,ycursor;


void ps_write (FILE *f, int ng)
{
  double x, y;
  int xmpts, ympts;
  int margx, margy;
  float ax, ay;
  float bx, by;
  float tooclx, toocly;
  float xpscurr1, ypscurr1;
  float xsized2, ysized2;
  int i, j, counter;

  /* initialization of the postscript coordinates of the page */
```

```
xmpts = XM*UNIT;
ympts = YM*UNIT;
margx = (int) (MARGIN*UNIT);
margy = (int) (MARGIN*UNIT);
xsized2= xsize/2.0;
ysized2= ysize/2.0;

/* defines the coordinates transformation */
ax = (xmpts-2*margx)/xmax;
bx = margx;
ay = (ympts-2*margy)/ymax;
by = margy;
tooclx = TOOCLOSE2/ax;
toocly = TOOCLOSE2/ay;

/* header of the postscript file */
fprintf (f,"%s\n",HEADER);
fprintf (f,"initgraphics\n");
fprintf (f,"newpath\n");
fprintf (f,"0 setlinecap\n");
fprintf (f,"%.2f setlinewidth\n",LINEWIDTH);
fprintf (f,"0.8 setgray\n");

for (i=0; i<ng; i++) {
  counter = MAXLINE;
  for (j=0; j<grain[i].numbound; j++) {

    x = bound[grain[i].bound[j]].x1;
    y = bound[grain[i].bound[j]].y1;
    if ( inbound(x,y)) {
     xpscurr1 = ax*x+bx;
     ypscurr1 = ay*y+by;
     counter++;

     if (counter > MAXLINE) {
       counter= 0;
       fprintf (f,"stroke\n");
       fprintf (f, "%.1f %.1f moveto\n", xpscurr1, ypscurr1);
     }
     else
       fprintf (f, "%.1f %.1f lineto\n", xpscurr1, ypscurr1);
    }
  }
  fprintf (f,"fill\n");
  fprintf (f,"stroke\n");
}

fprintf (f,"0.0 setgray\n");

for (i=0; i<ng; i++) {
  counter = MAXLINE;
  for (j=0; j<grain[i].numbound; j++) {

    x = bound[grain[i].bound[j]].x1;
    y = bound[grain[i].bound[j]].y1;

    if ( inbound(x,y)) {
     xpscurr1 = ax*x+bx;
     ypscurr1 = ay*y+by;
     counter++;

     if (counter > MAXLINE) {
       counter= 0;
```

```
          fprintf (f, "stroke\n");
          fprintf (f, "%.1f %.1f moveto\n", xpscurr1, ypscurr1);
        }
        else
          fprintf (f, "%.1f %.1f lineto\n", xpscurr1, ypscurr1);

        if (j==grain[i].numbound-1) {
          x = bound[grain[i].bound[j]].x2;
          y = bound[grain[i].bound[j]].y2;
          xpscurr1 = ax*x+bx;
          ypscurr1 = ay*y+by;
          fprintf (f, "%.1f %.1f lineto\n", xpscurr1, ypscurr1);
        }
      }
    }
    fprintf (f,"stroke\n");
  }

  /* draws the frames */
  fprintf (f,"0.0 setgray\n");
  fprintf (f,"1 setlinewidth\n");
  fprintf (f,"%d %d moveto\n",margx,margy);
  fprintf (f,"%d %d lineto\n",xmpts-margx,margy);
  fprintf (f,"%d %d lineto\n",xmpts-margx,ympts-margy);
  fprintf (f,"%d %d lineto\n",margx,ympts-margy);
  fprintf (f,"%d %d lineto\n",margx,margy);
  fprintf (f,"stroke\n");

  /* prints the simulation parameters */
  /* fprintf (f,"/%s findfont %d scalefont setfont\n",FONT,SIZEFONT);
  fprintf (f,"%d %.1f moveto\n",margx, ympts+0.5*UNIT);
  fprintf (f,"(G_I_ratio: %f  Delta: %.2f  Seed: %d) show\n", g_i_ratio, delta,
seed);
  fprintf (f,"%d %.1f moveto\n",margx, ympts+0.25*UNIT);
  fprintf (f,"(Average grain size: %f) show\n", d_avg);
  */
  fprintf (f,"showpage\n");
  fclose (f);
}
```

****

The last file, auxiliary.c, contains a few extraneous procedure called throughout the program.

****

```
/* auxiliary.c */

#include <stdio.h>
#include <math.h>
#include <stdlib.h>
#include "defines.h"
#include "struct.h"

extern grain_struct *grain;
extern point_struct *point;
extern bound_struct *bound;
extern contact_struct *contact;

extern float t;
```

```
extern int ng;
extern double xmin, xmax, ymin, ymax;

int inbound(double x, double y)
{
  float boundx, boundy;

  boundx= 0.0*xmax;
  boundy= 0.0*ymax;

  if (x>xmax+boundx) return(0);
  if (x<xmin-boundx) return(0);
  if (y>ymax+boundy) return(0);
  if (y<ymin-boundy) return(0);
  return(1);
}

double calc_grain_area(int grn)
{
  int i;
  double x1, y1, x2, y2;
  double area;

  area= 0;
  for (i=0; i<grain[grn].numbound; i++) {
    x1= bound[grain[grn].bound[i]].x1;
    y1= bound[grain[grn].bound[i]].y1;
    x2= bound[grain[grn].bound[i]].x2;
    y2= bound[grain[grn].bound[i]].y2;
    area += x1*y2 - y1*x2;
  }

  area *= 0.5;

  return(area);
}

/*
This routine determines if the distance r is greater than
the separation between points x1,y1 and x2,y2.
*/
int meet(double x1, double y1, double x2, double y2, double r)
{
  if ( ((x1-x2)*(x1-x2) + (y1-y2)*(y1-y2)) > r*r )
    return(0);

  return(1);
}


*****************************************************
```

Appendix C

Texture Development Due to Grain Growth in FCC Thin Films

C.1 Introduction

Normal grain growth is a coarsening process driven by the reduction of grain boundary energy. Grain growth in thin films can also be driven by orientation-dependent driving forces such as surface- [$Vook_2$ 65, Made 72, Thom 85] and interface-energy anisotropy [Thom 90, Ziel 94] and strain-energy-density anisotropy [Vook 65, Thom 93, Flor 94, Ziel 94]. Grains with low combined surface and interface energy and strain energy density have an energetic advantage and grow to eliminate higher energy grains. This leads to an evolution in the distribution of orientations in the film during grain growth.

Stresses are often generated in thin films during deposition and as a result of post-deposition processing. Compressive or tensile intrinsic stresses are generated during deposition at the deposition temperature and arise from a variety of mechanisms [Doer 88, Koch 94]. Extrinsic stresses result from differential thermal expansion between film and substrate when the temperature is changed from the deposition temperature. Since a thin film is constrained in its macroscopic dimensions by a substrate, grain growth will also induce a tensile stress as excess grain boundary volume is eliminated [Chau 72]. For films under a non-zero state of stress, the anisotropy of elastic properties and orientation-

dependent yielding generate differences in strain energy density that can drive orientation evolution during grain growth [Vook 65, Sanc 92, Flor 94].

Surface- and interface-energy anisotropy and strain-energy-density anisotropy do not in general favor the growth of grains with the same crystallographic orientations, i.e. textures. The orientation favored during grain growth minimizes the sum of these orientation-dependent driving forces. The magnitudes of the driving forces due to surface- and interface-energy anisotropy and strain-energy-density anisotropy are influenced by the characteristics and processing conditions of the film, for example the film thickness and deposition temperature.

The influence of deposition temperature and film thickness on texture evolution during grain growth has been investigated for Ag and Cu thin films deposited on thick oxidized silicon substrates. The results for $Ag/SiO_2/Si$ and $Cu/SiO_2/Si$ are presented in the form of texture maps, which relate deposition temperature and film thickness to the relative volume fraction of (111), (100), and random orientations for as-deposited films as well as films annealed at high temperature to promote further grain growth. In addition, $Ag/SiO_2/Si$ samples were annealed at high temperature in a four-point bending jig to produce strain in addition to the thermal strain generated during heating.

C.2 Driving forces for grain growth

Grain growth in thin films rapidly results in a columnar microstructure in which the grain boundaries traverse the thickness of the film [Thom 90]. Subsequent grain growth occurs primarily through grain boundary motion in the plane of the film and can be modeled as a quasi two-dimensional process. In this case, the growth of a grain of radius r can be described in the mean-field approximation as [Thom 93]

$$\frac{dr}{dt} = \mu\left(\gamma_{gb}\left(\frac{1}{\bar{r}} - \frac{1}{r}\right) + \frac{\Delta\gamma}{h} + \Delta W_{\varepsilon}\right), \qquad \text{(C.1)}$$

where $\Delta\gamma = \left(\bar{\gamma}_s - \gamma_s\right) + \left(\bar{\gamma}_i - \gamma_i\right)$, and

$$\Delta W_{\varepsilon} = \overline{W_{\varepsilon}} - W_{\varepsilon} ,$$

and where h is the film thickness, μ is the average grain boundary mobility, γ_{gb} is the average grain boundary energy, and $\bar{r}$ is the average grain radius in the film. The average surface and interface energies are $\bar{\gamma}_s$ and $\bar{\gamma}_i$, and the surface and interface energies for this specific grain are given by γ_s and γ_i. The average strain energy density stored in the film is $\overline{W}_\varepsilon$, while the strain energy density of this particular grain is W_ε.

The first term in Eq. C.1, $\mu\gamma_{gb}\left(\frac{1}{\bar{r}}-\frac{1}{r}\right)$, accounts for normal grain growth driven by minimization of local in-plane boundary curvature, which, in turn, favors the growth of larger than average grains. Curvature-driven grain growth can, in principle, be texture selective if grain boundary energies or mobilities are non-uniform and depend on grain orientation. With uniform grain boundary energies, in-plane-curvature-driven grain growth can lead to the development of texture when nucleation and growth leads to as-deposited films with grain sizes correlated with grain orientations. In such films, curvature-driven grain growth favors orientations represented by grains with an average grain size larger than the overall average grain size in the film.

The second term in Eq. C.1 represents surface- and interface-energy-driven grain growth. Grains with low surface and interface energies grow preferentially to grains with high combined surface and interface energies. For fcc metals, (111) planes are close-packed and minimize the energy of a free surface. As a result, (111) textured grains will have the lowest surface energy, γ_s. When the interaction between the film and the substrate is weak, such as in the case of Ag or Cu deposited on amorphous SiO_2, the interface energy of (111) textured grains is expected to be low as well. Therefore, (111) textured grains are favored during grain growth when surface- and interface-energy anisotropy is the dominating texture-dependent driving force.

The third term in Eq. C.1 represents the effect of strain-energy-density anisotropy on grain growth. Grains with low strain energy densities will grow in preference to grains with high strain energy densities. In elastically deformed films, strain-energy-density anisotropy results from the anisotropy of the stiffness tensor. The degree of elastic anisotropy is reflected by the anisotropy factor $A = 2c_{44}/(c_{11}-c_{12})$, where the c_{ij}'s are the

coefficients of the stiffness matrix for the material. Elastically isotropic materials have an anisotropy factor of 1. The anisotropy factors for Ag and Cu are 3.01 and 3.19, respectively, and therefore have anisotropic elastic properties. Thin films on thick substrates are approximately in a state of plane stress [Röll 76, Doer 88]. When subjected to a biaxial strain, elastically deformed grains with texture (hkl) have a strain energy density given by

$$W_{\varepsilon} = M_{hkl}\varepsilon^{2} \qquad \text{(C.2)}$$

where M_{hkl} is an orientation-dependent biaxial modulus derived from the stiffness tensor for the material [Muri 77, Nix 89]. The plane stress and biaxial strain assumptions underlying Eq. C.2 are valid for films where grain sizes are larger than the film thickness and when the strain in the film is equibiaxial. For materials with an anisotropy factor greater than 1, including Ag and Cu and all cubic metals (except Mo), grains with (100) texture have the lowest elastic strain energy density of all orientations and (111) grains have the highest elastic strain energy density [Röll 76]. Therefore, when elastic strain energy density is the dominant orientation-dependent driving force for grain growth in these films, (100) grains will grow preferentially. However when the combined intrinsic and extrinsic stresses exceed the elastic limit, yielding will result in a decrease in the stress in the film. The yield stress of individual grains in a columnar polycrystalline film has been shown to depend on grain texture, grain diameter, and film thickness [Frue 87, Nix 89, Sanc 92, Thom 93].

C.3 Stress in Thin Films

As-deposited thin films are often subject to intrinsic stresses generated during all stages of film formation and thickening [Doer 88, Koch 94]. The magnitude and sign of the stress depend not only on the material but also the deposition method. For evaporated fcc metals deposited at or below room temperature, the intrinsic strain ε_i after deposition typically evolves to a biaxial strain of order 0.1% or less [Aber 90, Shul 96, Flor 01]. The extrinsic biaxial strain due to differential thermal expansion in annealed films is

$$\varepsilon_{th} = \int_{T_{dep}}^{T_{anneal}} (\alpha_s(T) - \alpha_f(T))dT \cong (\alpha_s - \alpha_f)(T_{anneal} - T_{dep}) = \Delta\alpha\Delta T \ , \qquad \text{(C.4)}$$

where α_s and α_f are the thermal expansion coefficients of the substrate and the film, respectively, and T_{dep} and T_{anneal} are the deposition and anneal temperatures, respectively. For the combinations of films and substrate studied in this paper, $\alpha_f > \alpha_s$ and $T_{anneal} > T_{dep}$ so ε_{th} is always compressive.

Stresses can also be generated after deposition during the grain growth process. Since the macroscopic dimensions of the film are fixed by the substrate, grain growth will always induce a tensile stress as excess grain boundary volume is eliminated [Chau 71, Doer 88]. When the microstructure of the film is columnar, this densification strain is biaxial and is given by

$$\varepsilon_d = \Delta a\left(\frac{1}{d_0} - \frac{1}{d}\right) \qquad \text{(C.5)}$$

where Δa is the free volume per unit grain boundary area, d_0 is the average grain size of the as-deposited film and d is the final average grain size of the film. In addition to the thermal and densification stresses, stress relaxation can arise in films subjected to thermal anneals from rearrangement of line defects within the film and recombination of line and point defects [Gard 88, Volk 94].

C.3 Experimental Technique

Continuous polycrystalline films were electron beam evaporated in an ultra high vacuum environment onto oxidized silicon substrates. The base pressure in the deposition chamber was of order 1 X 10^{-9} Torr prior to deposition and typically rose by an order of magnitude during deposition. The deposition rates were 1 nm/sec for both the Ag and Cu films. The deposition temperature and the final film thickness were systematically varied between –150°C and 25°C and 0.1 to 1.0 μm, respectively. The substrate temperature was monitored during deposition and did not increase by more than 10°C during deposition.

The orientation distribution was measured *ex situ* for the as-deposited films and for films annealed in vacuum or in a reducing ambient at approximately $0.5T_{melt}$ (400°C for Ag and 450°C for Cu) using x-ray texture analysis. Those samples deposited below room temperature had to be warmed to room temperature to perform the *ex situ* texture analysis. X-ray pole figure data was acquired using the <111> Bragg reflections in the Schultz geometry by tilting the sample as it is rotated about its normal [Schu 49, Cull 78, ASTM 96]. The background intensity was collected under identical scan conditions but at a Bragg angle two degrees smaller than the (hkl) reflection of interest, and subsequently subtracted from the raw data. A correction factor for geometric defocusing error was determined using a random powder sample of sufficient thickness that transmission of x-rays through the sample is negligible [Cher 52]. The net effect of tilting the specimen is an apparent change in the Bragg angle towards lower diffraction values for one half of the specimen and towards higher values for the other half of the specimen resulting in a widening of the diffraction peak. Consequently, part of the diffracted intensity may not be received by the detector and therefore the measured intensity is expected to decrease with increasing tilt angle. The defocusing correction factor $R_{defocus}$ as a function of the tilt angle α equals the intensity of the random powder sample at different α divided by the intensity measured at α=0. In addition, an absorption correction is necessary because the x-ray penetration depth exceeded the film thickness so that the volume of material that diffracts, and correspondingly the diffraction intensity, increases with increasing tilt angle α [Schu 49]. The absorption correction factor R_{abs} as a function of α equals:

$$R_{abs} = \frac{I(\alpha)}{I(\alpha = 0)} = \frac{1 - exp[-2\mu h/(sin(\theta)cos(\alpha))]}{1 - exp[-2\mu h/sin(\theta)]}, \quad \text{(C.1)}$$

where μ is the absorption coefficient of the film material, h is the film thickness, and θ is the Bragg diffraction angle. For Cu K-α radiation at a wavelength of 1.5418Å, the absorption coefficient μ for Ag is 228700 m^{-1} and for Cu is 40700 m^{-1} [ASTM 96].

For films on amorphous substrates, the azimuthal coordinate is not relevant as the orientation dependent driving forces for grain growth are determined solely by the texture

of grains and not by the in-plane orientation of grains with respect to the substrate. The data was integrated with respect to the azimuthal coordinate and then normalized so that the fiber texture plot is shown as normalized intensity as a function of the tilt angle.

C.4 Experimental Results

Figure C-1(a) is a <111> fiber texture plot for a 1.0 μm-thick Ag film deposited at 25°C onto an oxidized silicon substrate. Typical Ag films consist of (111), (100) and random texture components, however (211) and (511) peaks due to secondary twinning have been observed by other researchers [Dutt 71, Gard 81, Gitt 85, Grie 99]. Note that the random texture component determined from the pole figure data is undetectable using standard Bragg-Brentano diffraction techniques. As shown in Fig. C-1(b), the texture components of the 1.0 μm-thick film changed following the 1 hr anneal at 400°C and resulted in stronger (111) and (100) textures with a smaller random texture component. Figure C-2 is a compilation of the texture components of as-deposited Ag films and after a 1 hour anneal at 400°C for systematically varied deposition temperature and final film thickness. The bold values indicate an increase while italic values indicate a decrease in the texture component upon annealing. For the as-deposited Ag films, the volume fraction of (111) grains, in general, decreased with increasing film thickness and lower deposition temperature, while the (100) and random volume fractions increased with increasing film thickness and lower deposition temperature. After annealing of the Ag films at 400°C, the (111) volume fraction, in general, increased for thinner films deposited at higher temperatures, while the (100) volume fraction increased for thicker films deposited at lower temperatures. In addition, the random volume fraction typically decreased after the high temperature anneal but almost always constituted a larger volume fraction than the (100) texture component.

Figure C-3(a) is a <111> fiber texture plot for a 1.0 μm-thick Cu film deposited at 25°C onto an oxidized silicon substrate. Typical Cu films consist of (111), (100), (110) and random texture components, consistent with reports by other authors [Trac 93, Ziel 94]. As shown in Fig. C-3(b), the texture components of the 1.0 μm-thick film changed following the 1 hr anneal at 450°C and resulted in stronger (111) texture with a smaller

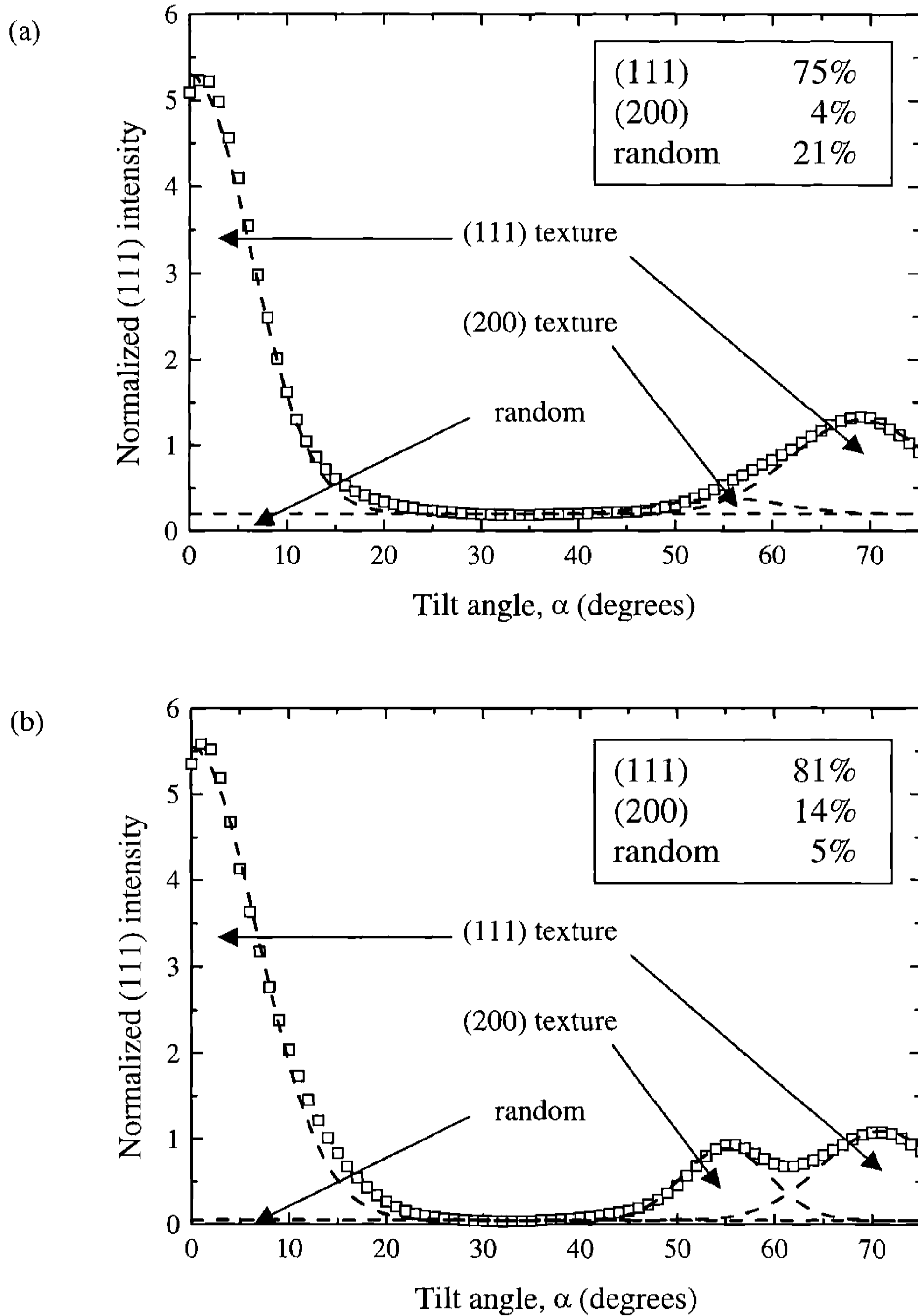

Figure C-1: (a) (111) fiber texture plot for an as-deposited 1.0 μm-thick Ag film deposited at room temperature on an oxidized silicon substrate, and (b) after a 1 hr anneal at 400°C at 1 X 10^{-9} Torr. The Ag film exhibits (111), (200) and random texture components.

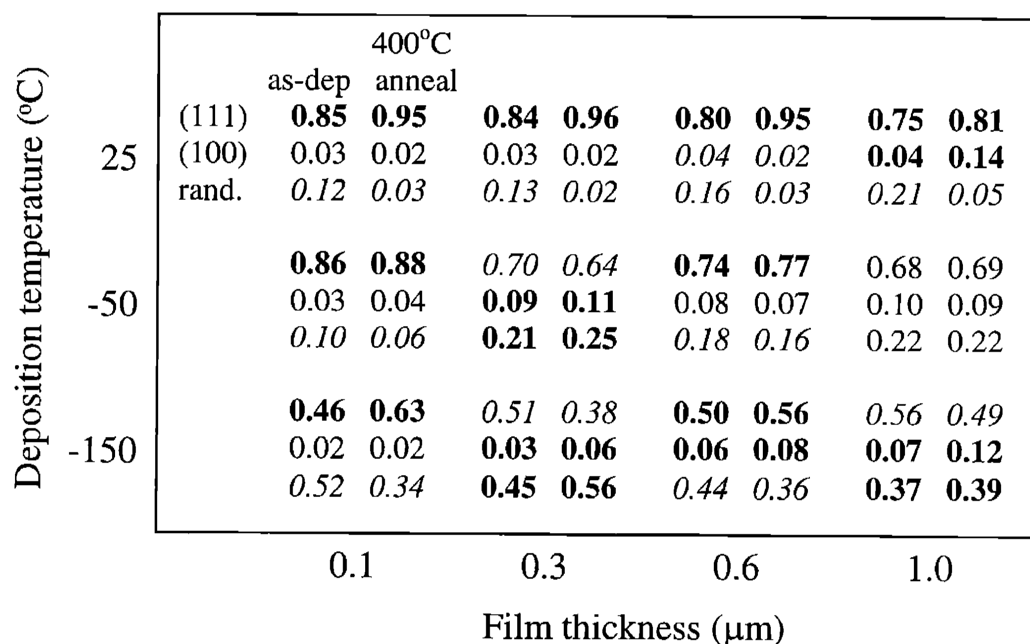

Deposition temperature (°C)		0.1 as-dep	0.1 400°C anneal	0.3 as-dep	0.3 400°C anneal	0.6 as-dep	0.6 400°C anneal	1.0 as-dep	1.0 400°C anneal
25	(111)	**0.85**	**0.95**	**0.84**	**0.96**	**0.80**	**0.95**	**0.75**	**0.81**
	(100)	0.03	0.02	0.03	0.02	*0.04*	*0.02*	**0.04**	**0.14**
	rand.	*0.12*	*0.03*	*0.13*	*0.02*	*0.16*	*0.03*	*0.21*	*0.05*
-50	(111)	**0.86**	**0.88**	*0.70*	*0.64*	**0.74**	**0.77**	0.68	0.69
	(100)	0.03	0.04	**0.09**	**0.11**	0.08	0.07	0.10	0.09
	rand.	*0.10*	*0.06*	**0.21**	**0.25**	*0.18*	*0.16*	0.22	0.22
-150	(111)	**0.46**	**0.63**	*0.51*	*0.38*	**0.50**	**0.56**	*0.56*	*0.49*
	(100)	0.02	0.02	**0.03**	**0.06**	**0.06**	**0.08**	**0.07**	**0.12**
	rand.	*0.52*	*0.34*	**0.45**	**0.56**	*0.44*	*0.36*	**0.37**	**0.39**

Film thickness (μm)

Figure C-2: Compilation of the (111), (100) and random texture components of as-deposited Ag films and after a 1 hour anneal at 400°C for systematically varied deposition temperature and final film thickness. The bold values are textures that strengthened following the 400°C anneal, while italic values indicate texture components that weakened.

(100) and random texture component. Figure C-4 is a compilation of the texture components of as-deposited Cu films and after a 1 hr anneal at 450°C for systematically varied deposition temperature and final film thickness. The bold values indicate an increase while italic values indicate a decrease in the texture component upon annealing. Films deposited at −150°C delaminated from the substrate during deposition as evidence by additional Cu deposition in delaminated regions. Since only the sample stage was cooled to −150°C during deposition, preferential gas adsorption probably contaminated the substrate surface and interfered with adhesion of the Cu film. For the as-deposited Cu films, the (111) volume fraction is approximately 80% and independent of the film

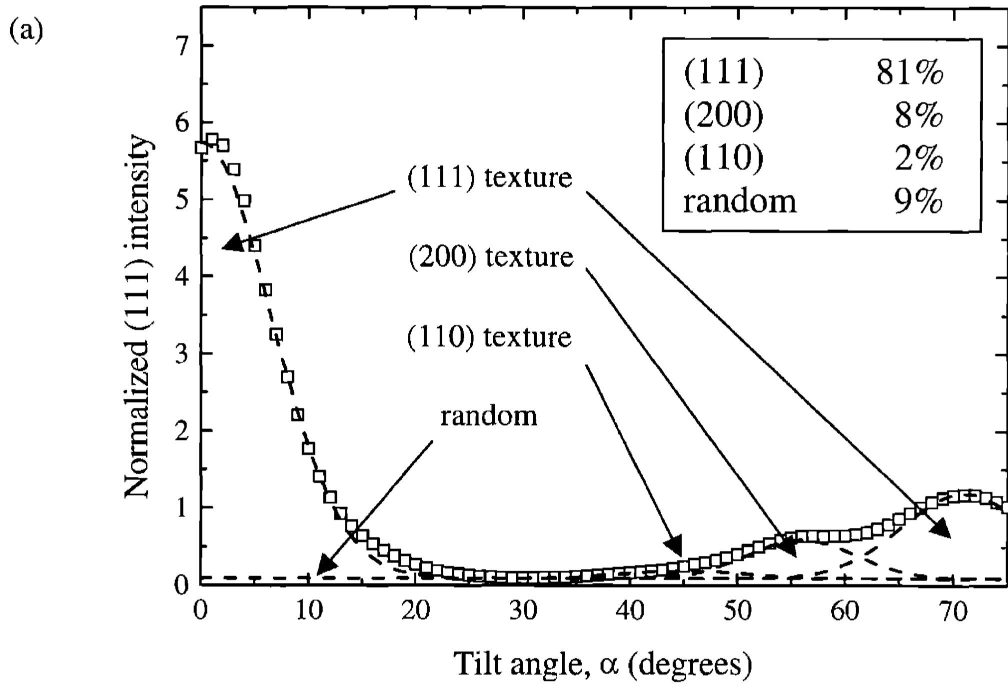

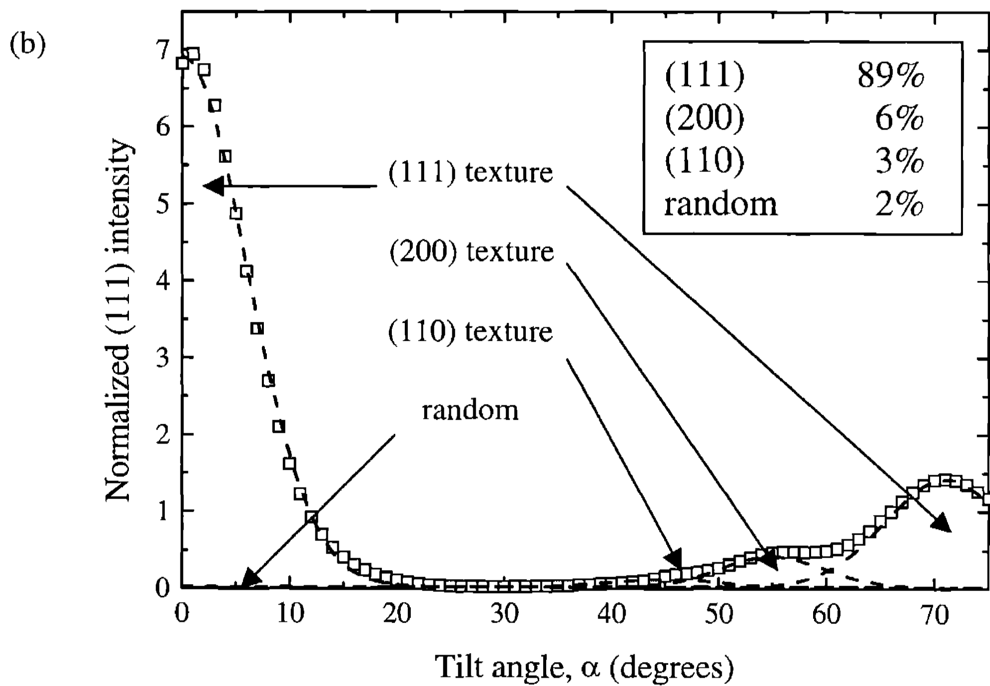

Figure C-3: (a) (111) fiber texture plot for an as-deposited 1.0 μm-thick Cu film deposited at room temperature on an oxidized silicon substrate, and (b) after a 1 hr anneal at 450°C at 1 X 10^{-9} Torr. The Cu film exhibits (111), (200), (110) and random texture components.

Deposition temperature (°C)		0.1 as-dep	0.1 450°C anneal	0.3		0.6		1.0	
25	(111)	**0.79**	**0.87**	**0.86**	**0.93**	**0.82**	**0.84**	**0.81**	**0.89**
	(200)	*0.04*	*0.02*	0.03	0.03	**0.05**	**0.09**	*0.08*	*0.06*
	(110)	0.06	0.07	0.03	0.02	0.02	0.02	0.02	0.03
	rand.	*0.11*	*0.04*	*0.08*	*0.02*	*0.11*	*0.05*	*0.09*	*0.02*
-50		**0.81**	**0.83**	**0.78**	**0.82**	**0.83**	**0.88**	**0.83**	**0.87**
		0.02	**0.05**	0.05	0.04	0.04	0.05	0.03	0.02
		0.12	*0.07*	0.07	0.06	*0.06*	*0.02*	0.06	0.06
		0.07	*0.05*	*0.10*	*0.08*	*0.07*	*0.05*	*0.07*	*0.05*

Film thickness (μm)

Figure C-4: Compilation of the (111), (200), (110) and random texture components of as-deposited Cu films and after a 1 hour anneal at 450°C for systematically varied deposition temperature and final film thickness. The bold values are texture components that strengthened following the 450°C anneal, while italic values indicate a weakening of the texture component following the high temperature anneal.

thickness and deposition temperature. Following the high temperature anneal, the (111) texture tended to strengthen at the expense of a decreasing random texture component, while the (100) and (110) textures were relatively unchanged.

Figure C-5 is a <111> fiber texture plot for a 0.6 μm-thick Ag film deposited at 25°C onto an oxidized silicon substrate. Also shown in Fig. C-5 are texture plots of the Ag film after annealing at 400°C for 1 hr in forming gas (80:20 N_2/H_2) alone (dashed line) and with an additional 0.2% compressive strain applied during heating using a four-point bending apparatus (dash-dot line). The magnitude of the thermal strain due to differential thermal expansion between the Ag film and Si substrate is approximately 0.6% compressive strain. For the 0.6 μm-thick Ag film shown in Fig. C-5 and additional 0.1, 0.3, and 1.0 μm-thick Ag films (not shown), the applied compressive strain results in a slight strengthening of the (111) texture upon annealing.

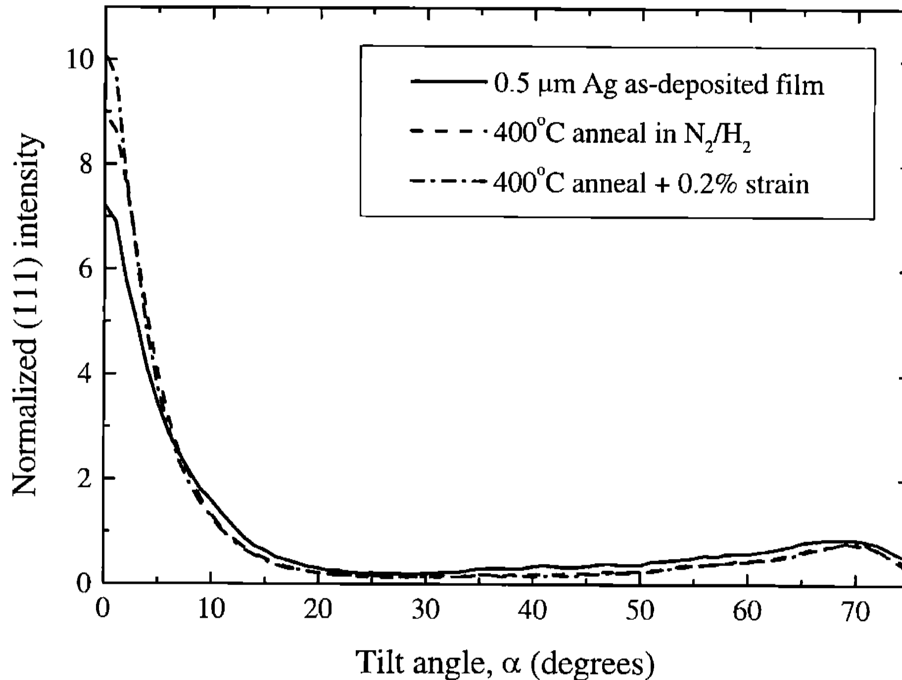

Figure C-5: A (111) fiber texture plot of a 0.6 μm-thick Ag film deposited at room temperature on an oxidized silicon substrate for the as-deposited film (solid line), after annealing at 400°C in forming gas (80:20 N_2/H_2) alone (dashed line) and with an additional 0.2% compressive strain applied during annealing using a four-point bending apparatus (dash-dot line). The additional compressive strain results in a slight strengthening of the (111) texture.

The microstructures of the Ag and Cu films in the as-deposited state and following the high temperature anneal were examined by transmission electron microscopy (TEM). The TEM micrographs indicate that grain growth occurred during deposition and/or upon annealing at room temperature as evidence by a bimodal grain size distribution in the as-deposited films. The abnormally large grains were typically (111) or (100) grains as confirmed by selected area diffraction and by inspection of the relative orientation of intersecting stacking faults or twins in the grains (i.e. perpendicular intersections in (100) grains and 60° intersections in (111) grains). The grain sizes of the non-abnormal grains were difficult to determine in the as-deposited films because of the very small grain sizes and highly-defective grain structures, especially for the films

deposited below room temperature. Following the high temperature anneal, the average grain size increased by approximately an order of magnitude and was approximately 2 to 3 times the film thickness with a less prevalent occurrence of abnormal grains.

In order to understand the contribution of strain-energy-density anisotropy to texture evolution during grain growth, the average stress was measured as a function of temperature for $Ag/SiO_2/Si$ films deposited at room temperature. Curvature data was acquired in a temperature range of 25°C to 350°C with a Tencor FLX-2320 and converted to stress using Stoney's equation [Nix 89]. Figure C-6 shows the stress-temperature relationship in a film thermally cycled three times at atmospheric pressure in an H_2/N_2 reducing gas environment. The difference between the first thermal cycle and the subsequent cycles results from stress relaxation mechanisms and from grain growth, which occurs primarily during the first heating cycle. Figure C-6 shows that the film yields at stresses between -50 and -100 MPa during the first heating cycle, after a change in temperature of less than 100°C.

C.5 Discussion

For the both the $Ag/SiO_2/Si$ and $Cu/SiO_2/Si$ systems, the (111) texture is dominant in the as-deposited films at all thicknesses and deposition temperatures. In the as-deposited Ag films, the (111) texture is stronger for thinner films deposited at higher temperatures, while the random and (100) textures are stronger for thicker films deposited at lower temperatures. The observation of a strong (111) texture in fcc metallic films has been well documented for a variety systems [$Vook_2$ 65, Made 72, Thom 85]. The evidence of an increasing (100) texture with increasing film thickness has previously been observed for Ag films deposited on glass using *ex situ* x-ray diffraction [Gitt 85]. The observation of a stronger (100) texture for thicker films deposited below room temperature has also been reported for Cu films deposited on glass by *in situ* x-ray diffraction [Vook 65].

As mentioned previously, grain growth occurred during deposition and/or as a result of annealing at room temperature as evidence by the TEM observations of abnormally large grains in the as-deposited films. Grain growth during thin film

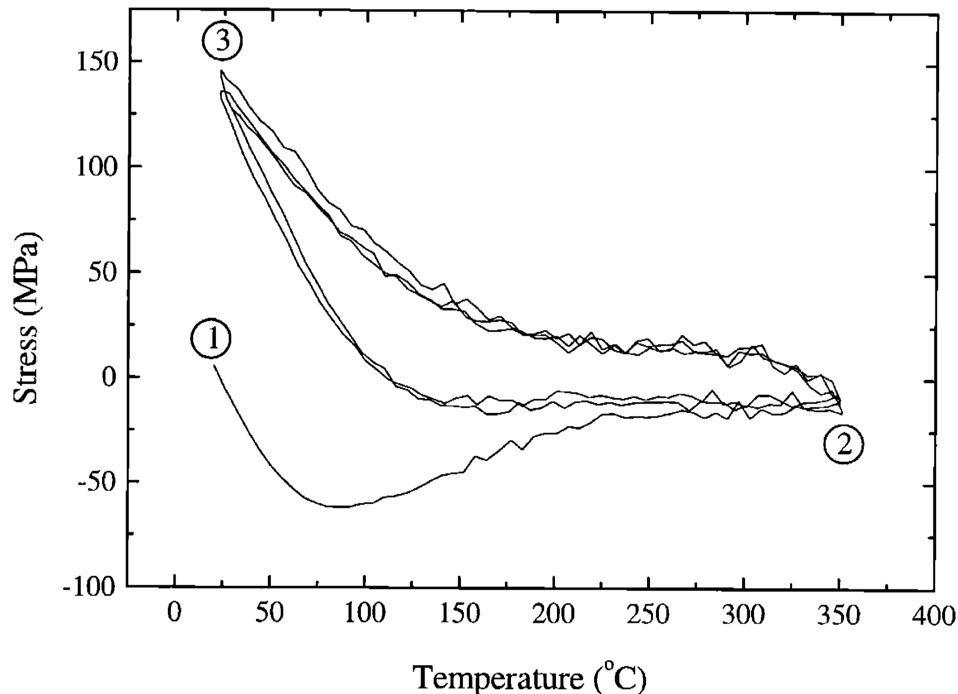

Figure C-6: Stress versus temperature measurement during annealing of a 0.5 μm-thick Ag film on oxidized Si in an H_2/N_2 reducing gas ambient. Three thermal cycles were performed in the sequence 1-2-3-2-3-2-3 at a heating/cooling rate of 6°C/min. Grain growth occurred primarily during the first heating.

deposition has been observed using *in situ* TEM for Ag and Au films, for which the final grain sizes were larger than the initial island spacing [Pash 64, Pash 65]. Grain growth during deposition and/or as a result of room temperature annealing has also been inferred from *ex situ* microscopy of films of different thicknesses [Aber 85, Lita 99]. Reflected high energy electron diffraction (RHEED) studies of Ag during deposition onto glass showed a random texture in discontinuous film that developed towards a (111) texture once the film became continuous, presumably due to orientation-selected grain growth [Kaka 73, Gard 81]. The development of a stronger (100) texture upon heating of Cu films deposited on glass from a deposition temperature of -190°C to room temperature has been observed using *in situ* x-ray diffraction and attributed to orientation-selective grain growth [Vook 65].

The texture trends for the $Ag/SiO_2/Si$ system in the as-deposited state can be understood in terms of the driving forces for grain growth. As described earlier, strain-energy-density anisotropy, which favors the (001) texture, is greater for thick films under larger stresses, while the surface- and interface-energy anisotropy, which favors the (111) texture, is dominant for small thicknesses at low stresses. The detailed interplay of surface, interface, and strain energies and the effects of grain-size-dependent yielding as well as other effects such as grain-boundary-groove-induced grain growth stagnation can be analyzed using computer simulations of grain growth [Care 96].

The magnitude of the strain energy density driving force for grain growth ΔW_ε is determined by the strain state of the film, the elastic constants for the film, and on the yield stress of each grain. For films deposited below room temperature, differential thermal expansion between the Ag or Cu film and the silicon substrate results in compressive strains upon heating to room temperature. The magnitude of the thermal strain in the film at room temperature increases with decreasing deposition temperature. For Cu films deposited at $-190^{\circ}C$, texture evolution has been observed using *in situ* x-ray diffraction upon heating toward room temperature beginning at temperatures below $0^{\circ}C$, presumably due to orientation-selective grain growth [Vook 65]. Since grain boundary mobility only become sufficiently large above $0^{\circ}C$ to allow grain growth, the thermal strain present in the film during grain growth at room temperature increases with decreasing deposition temperature resulting in the favored growth of (100) grains, as shown in Fig. C-2 for the $Ag/SiO_2/Si$ system. The lack of a more dominant (100) texture in the $Cu/SiO_2/Si$ system for thicker films deposited at lower temperatures, as shown in Fig. C-4, is unexpected and in disagreement with previous work [Vook 65].

The evolution of texture following the high temperature anneals of the Ag and Cu films is less dramatic than the differences in texture due to the initial deposition conditions. The expectation given the strain-energy-density driving force for grain growth would be the prevalence of an increasing (100) texture during a high temperature anneal of thick films deposited at lower temperatures. However as shown in Fig. C-6, plastic deformation decreases the stress in the film at higher temperatures resulting a smaller elastic strain energy density in the film. Therefore, only a modest increase in the (100) texture was observed upon high temperature annealing of the thick Ag films

deposited at lower temperatures, and no apparent favored growth of the (100) texture in the Cu films. Furthermore, the additional compressive strain imposed during the high temperature anneal with the four-point bending apparatus did not result in any additional (100) grain growth, as shown in Fig. C-5, because of plastic deformation at high temperatures resulting in a smaller stress in the film.

C.6 Conclusions

The influence of deposition temperature and film thickness on texture evolution during grain growth has been investigated for Ag and Cu thin films deposited on thick oxidized silicon substrates. For the as-deposited Ag films, the volume fraction of (111) grains, in general, decreased with increasing film thickness and lower deposition temperature, while the (100) and random volume fractions increased with increasing film thickness and lower deposition temperature. After annealing of the Ag films at 400°C, the (111) volume fraction, in general, increased for thinner films deposited at higher temperatures, while the (100) volume fraction increased for thicker films deposited at lower temperatures. The results for the Ag/SiO_2/Si system are consistent with orientation-dependent grain growth resulting in a (111) texture for thinner films at low stresses due to surface- and interface-energy reduction, and the favored growth of (100) textures for thicker films under large thermal stresses due to strain-energy-density minimization. However, similar trends were not observed for the Cu/SiO_2/Si system in disagreement with previous research [Vook 65]. Finally, the expectation of increased (100) grain growth due to additional compressive strain imposed during the high temperature anneal by a four-point bending apparatus was not observed. From stress measurements during thermal cycling of Ag films, plastic deformation at high temperatures decreases the stress in the film at high temperatures and weakens the preferential growth of (100) grains due to strain-energy-density minimization.

References

[Aber 90] R. Abermann, "Measurement of the intrinsic stress in thin metal films", Vacuum **41**, 1279 (1990).

[Aber 86] R. Abermann and R. Koch, "In situ study of thin film growth by internal stress measurement under ultrahigh vacuum conditions: silver and copper under the influence of oxygen", Thin Solid Films **142**, 65 (1986).

[Aber 85] R. Abermann and R. Koch, "The internal stress in thin silver, copper and gold films", Thin Solid Films **129**, 71 (1985).

[Aber 84] R. Abermann and H.P. Martinz, "Internal stress and structure of evaporated chromium and MgF_2 films and their dependence on substrate temperature", Thin Solid Films **115**, 185 (1984).

[Aber 78] R. Abermann, R. Kramer and J. Mäser, "Structure and internal stress in ultra-thin silver films deposited on MgF_2 and SiO substrates", Thin Solid Films **52**, 215 (1978).

[Apai 79] G. Apai, J.F. Hamilton, J. Stohr, and A. Thompson, "Extended x-ray absorption fine structure of small Cu and Ni clusters: binding-energy and bond-length changes with cluster size", J. Appl. Phys. **43**, 165 (1979).

[ASTM 96] ASTM Designation E81-96: Standard test method for preparing quantitative pole figures (1996).

[Bagc 96] A. Bagchi and A.G. Evans, "Measurements of the debond energy for thin metallization lines on dielectrics", Thin Solid Films **286**, 203 (1996).

[Baue 94] E. Bauer, "Low energy electron microscopy", Rep. Prog. Phys. **57**, 895 (1994).

[Bran 73] W.A. Brantley, "Calculated elastics constants for stress problems associated with semiconductor devices", J. Appl. Phys. **44**, 534 (1973).

[Camm 00] R.C. Cammarata, T.M. Trimble, and D.J. Srolovitz, "Surface stress model for intrinsic stresses in thin films" J. Mater. Res. **15**, 2468 (2000).

[Camm 94] R.C. Cammarata, "Surface and interface stress effects in thin films", Prog. Surf. Sci. **46**, 1 (1994).

[Care 96] R. Carel, C.V Thompson, and H.J. Frost, "Computer simulation of strain energy effects vs. surface and interface energy effects on grain growth in thin films", Acta Metall. **44**, 2479 (1996).

[Chas 02] E. Chason, B.W. Sheldon, L.B. Freund, J.A. Floro and S.J. Hearne, Phys. Rev. Lett., submitted for publication (2002).

[Chas 98] E. Chason, M.B. Sinclair, J.A. Floro, J.A. Hunter and R.Q. Hwang, "Spectroscopic light scattering for real-time measurements of thin film and surface evolution", Appl. Phys. Lett. **72**, 3276 (1998).

[Chas 97] E. Chason and T.M. Mayer, "Thin film and surface characterization by specular X-ray reflectivity", Crit. Rev. Sol. St. and Mat. Sci. **22**, 1 (1997).

[Chau 72] P. Chaudhari, "Grain growth and stress relief in thin films", J. Vac. Sci. Technol. **9**, 520 (1972).

[Cher 52] W.P. Chernock and P.A. Beck, "Analysis of certain errors in the x-ray reflection method for quantitative determination of preferred orientations", J. Appl. Phys. **23**, 341 (1952).

[Chia 91] R. Chiarello, V. Panella and J. Krim, "X-ray reflectivity and adsorption isotherm study of fractal scaling in vapor-deposited films", Phys. Rev. Lett. **67**, 3408 (1991).

[Chiu 93] C.-H. Chiu and H. Gao, "Stress singularities along a cycloid rough surface", Int. J. Solids Structures **30**, 2983 (1993).

[Cull 78] B. D. Cullity, *Elements of X-Ray Diffraction* (Addison-Wesley, Reading MA, 1978).

[D'Heu 70] F.M. D'Heurle, "Aluminum films deposited by RF sputtering", Metall. Trans. **1**, 725 (1970).

[Dijk 99] S. Dijken, L.C. Jorritsma and B. Poelsema, "Steering-enhanced roughening during metal deposition at grazing incidence", Phys. Rev. Lett. **82**, 4038 (1999).

[Doer 88] M.F. Doerner and W.D. Nix, "Stress and deformation processes in thin films on substrates", CRC Crit. Rev. Sol. St. Mat. Sci. **14**, 225 (1988).

[Dolj 72] F.A. Doljack and R.W. Hoffman, "The origins of stress in thin nickel films", Thin Solid Films **12**, 71 (1972).

[Dutt 71] P.K. Dutta and H. Wilman, "Crystal growth and orientations in vacuum-condensed silver films and their systematic dependence on the residual air

pressure, film thickness, rate of deposition and substrate temperature", Appl. Phys. **3**, 839 (1971).

[Eato 97] W.P. Eaton and J.H. Smith, "Micromachined pressure sensors: review and recent developments", Smart Materials and Structures **6**, 530 (1997).

[Eise 01] C. Eisenmenger-Sittner, "Surface evolution of polycrystalline Al films deposited on amorphous substrates at elevated temperatures", J. Appl. Phys. **89**, 6085 (2001).

[Fan 88] W.C. Fan, J. Strozier, and A. Ignatiev, "Island formation of aluminum on the graphite (0001) surface: LEED and AES study", Surf. Sci. **195**, 226 (1988).

[Flin 87] P.A. Flinn, D.S. Gardner, and W.D. Nix, "Measurement and interpretation of stress in aluminum-based metallization as a function of thermal history", IEEE Trans. Electron Devices **34**, 689 (1987).

[$Flor_2$ 02] J.A. Floro, Sandia National Laboratories, NM, unpublished research (2002).

[Flor 02] J.A. Floro, E. Chason, R.C. Cammarata, and D.J. Srolovitz, "Physical origins of instrinsic stress in Volmer-Weber thin films", MRS Bulletin **27**, 19 (2002).

[Flor 01] J.A. Floro, S.J. Hearne, J.A. Hunter, P. Kotula, E. Chason, S.C. Seel, and C.V. Thompson, "The dynamic competition between stress generation and relaxation mechanisms during coalescence of Volmer-Weber thin films", J. Appl. Phys. **89**, 4886 (2001).

[Flor 97] J.A. Floro, E. Chason, S.R. Lee, R.D. Twesten, R.Q. Hwang, and L.B. Freund, "Real-time stress evolution during $Si_{1-x}Ge_x$ Heteroepitaxy: Dislocations, Islanding, and Segregation", J. Elec. Mat. **26**, 969 (1997).

[Flor 94] J.A. Floro, C.V. Thompson, R. Carel, and P.D. Bristowe, "Competition between strain and interface energy during epitaxial grain growth in Ag films on Ni(001)", J. Mater. Res. **9**, 2411 (1994).

[Freu 01] L.B. Freund and E. Chason, "Model for stress generated upon contact of neighboring islands of the surface of a substrate", J. Appl. Phys. **89**, 4866 (2001).

[Frie 02] C.A. Friesen, Department of Materials Science and Engineering, MIT, unpublished research (2002).

[Fros 87] H.J. Frost and C.V. Thompson, "The effect of nucleation conditions on the topology and geometry of two-dimensional grain structures", Acta Metall. **35**, 529 (1987).

[Gao 99] H. Gao, L. Zhang, W.D. Nix, C.V. Thompson and E. Arzt, "Crack-like grain-boundary diffusion wedges in thin metal films", Acta. Mater. **47**, 2865 (1999).

[Gard 88] D.S. Gardner and P.A. Flinn, "Mechanical stress as a function of temperature in aluminum films", IEEE Trans. Elec. Dev. **35**, 2160 (1988).

[Gard 81] T.M. Gardiner and M.H.B. Stiddard, "The growth and orientation of vapour-deposited thin films of silver on glass", Thin Solid Films **77**, 335 (1981).

[Geye 98] U. Geyer, U. von Hülsen, and H. Kopf, "Internal interfaces and intrinsic stress in thin amorphous Cu-Ti and Co-Tb films", J. Appl. Phys. **83**, 3065 (1988).

[Ghan 68] S.K. Ghandi, *The theory and practice of microelectronics* (Wiley, New York, 1968).

[Gimz 85] J.K. Gimzewski, A. Humbert, J.G. Bednorz and B. Reihl, "Silver films condensed at 300 and 90 K: Scanning tunneling microscopy of their surface topography", Phys. Rev. Lett. **55**, 951 (1985).

[Gitt 85] A. Gittis and D. Dobrev, "Development of textures during the growth of silver films condensed in vacuum on glass", Thin Solid Films **130**, 335 (1985).

[Grie 99] J. Greiser, D. Muller, P. Mullner, C.V. Thompson and E. Arzt, "Growth of giant grains in silver thin films", Scripta Mat. **41**, 709 (1999).

[Grig 66] C.W.B. Grigson and D.B. Dove, J. Vac. Sci. Tech. **3**, 120 (1966).

[Grov 84] C.R.M. Grovenor, H.T.G. Hentzell and D.A. Smith, "The development of grain structure during growth of metallic films", Acta Metall. **32**, 773 (1984).

[Gumb 91] P. Gumbsch and M. Daw, "Interface stresses and their effects on the elastic moduli of metallic multilayers", Phys. Rev. B **44**, 3934 (1991).

[He 92] Y.-L. He, H.-N. Yang, T-M. Lu and G.-C. Wang, "Measurements of dynamic scaling from epitaxial growth front: Fe film on Fe(001)", Phys. Rev. Lett. **69**, 3770 (1992).

[Hear 99] S. Hearne, E. Chason, J. Han, J.A. Floro, J. Figiel, J. Hunter, H. Amano and I.S.T. Tsong, "Stress evolution during metalorganic chemical vapor deposition of GaN", Appl. Phys. Lett. **74**, 356 (1999).

[Henr 98] C.R. Henry, "Growth, structure and morphology of supported metal clusters studied by surface science techniques", Cryst. Res. Technol. **33**, 1119 (1998).

[Hill 65] M. Hillert, Acta Metall. **13**, 227 (1965).

[Hoff 76] R.W. Hoffman, "Stress in thin films: the relevance of grain boundaries and impurities", Thin Solid Films **34**, 185 (1976).

[Kaka 73] K.K. Kakati and H. Wilman, "The development of oriented crystal growth during condensation of gold, silver and copper films in vacuum, and its systematic dependence on the residual gas pressure and adsorption, and the film thickness, atomic mobility and chemical reactivity", J. Phys. D. **6**, 1307 (1973).

[Kand 91] Y. Kanda, "Piezoresistance effect of silicon", Sensors and Actuators A **28**, 83 (1991).

[Kand 82] Y. Kanda, "A graphical representation of the piezoresistive coefficients in silicon", IEEE Trans. On Electron Devices **ED-29**, 4 (1982).

[Kard 86] M. Kardar, G. Parisi, and Y.C. Zhang, "Dynamic scaling of growing interfaces", Phys. Rev. Lett. **56**, 889 (1986).

[Knor 95] D.B. Knorr and D.P. Tracy, "A review of microstructure in vapor deposited copper thin films", Mat. Chem. Phys. **41**, 206 (1995).

[Kobr 01] M.J. Kobrinsky, "Inelastic Behavior of FCC Metallic Structures with Reduced Dimensionality", Ph.D. dissertation, Massachusetts Institute of Technology, Cambridge, Department of Materials Science and Engineering, 2001.

[Kobr 98] M.J. Kobrinsky and C.V. Thompson, "The thickness dependence of the flow stress of capped and uncapped polycrystalline Ag thin films", Appl. Phys. Lett. **73**, 2429 (1998).

[Koch 94] R. Koch, "The intrinsic stress of polycrystalline and epitaxial thin metals films", J. Phys: Condens. Matter **6**, 9519 (1994).

[Koch 86] R. Koch and R. Abermann, "Microstructural changes in vapor-deposited silver, copper and gold films investigated by internal stress measurements", Thin Solid Films **140**, 217 (1986).

[Koch 85] R. Koch and R. Abermann, "On the influence of thermal effects on interval stress measurements during and after deposition of silver, gold, and copper films", Thin Solid Films **129**, 63 (1985).

[Koch 82] R. Koch, H. Leonard, and R. Abermann, "The influence of O_2, H_2, H_20, N_2, $C0$ and CH_4 on the structure of thin silver films investigated by ultrahigh vacuum internal stress measurements", Thin Solid Films **89**, 117 (1982).

[Kino 67] K. Kinosita, K. Maki, and K. Takeuchi, "Coalescence of islands in its relation to stress buildup in very thin metal films", Proceedings of the Second Colloquium on Thin Films, 118 (1967).

[Klok 68] E. Klokholm and B.S. Berry, "Intrinsic stress in evaporated metal films", J. Electrochem. Soc. **115**, 823 (1968).

[Knor 94] D.P. Tracy and D.B. Knorr, "Texture and microstructure of thin copper films", J. Elec. Mat. **22**, 611 (1993).

[Lane 00] M. Lane, R.H. Dauskardt, N. Krishna and I. Hashim, "Adhesion and reliability of copper interconnects with Ta and TaN barrier layers", J. Mater. Res. **15**, 203 (2000).

[Lekh 68] S.G. Lekhnitskii, *Anisotropic Plates* (Gordon and Breach Science Publishers, 2nd edition, 1968).

[Leus 93] G.J. Leusink, T.G.M. Oosterlaken, G.C.A.M. Janssen and S. Radelaar, "The evolution of growth stresses in chemical vapor deposited tungsten films studied by in situ wafer curvature measurements", J. Appl. Phys. **74**, 3899 (1993).

[Linn 96] R. Linnemann, T. Gotszalk, I.W. Rangelow, P. Dumania, and E. Oesterschulze, "Atomic force microscopy and lateral force microscopy using piezoresistive cantilevers", J. Vac. Sci. Technol B **14**, 856 (1996).

[Lita 99] A.E. Lita and J.E. Sanchez, "Characterization of surface structure in sputtered Al films: Correlation to microstructure evolution", J. Appl. Phys. **85**, 876 (1999).

[Made 72] S. Mader, R. Feder, and P. Chaudhari, "Recrystallization of (001) oriented gold films into (111) orientation", Thin Solid Films **14**, 63 (1972).

[Mae 99] K. Mae, V.V. Moshchalkov, and Y. Bruynseraede, "Intensity profile along the RHEED streaks for various thin film surface morphologies", Thin Solid Films **340**, 145 (1999).

[Maki 69] K. Maki, Y. Nakjima, and K. Kinosita, "Stress in vacuum-deposited films of Ag, Au, and Cu", J. Vac. Sci. Tech. **6**, 622 (1969).

[Mans 90] M. Mansfield and R.J. Needs, "Surface energy and stress of lead (111) and (110) surfaces", Phys. Rev. B **43**, 8829 (1990).

[Mark 94] L.D. Marks, "Experimental studies of small particles structures", Rep. Prog. Phys. **57**, 603 (1994).

[Mart 90] R.E. Martinez, W.M. Augustyniak and J.A. Golovchenko, "Direct measurement of crystal surface stress", Phys. Rev. Lett. **64**, 1035 (1990).

[Mayr 01] S.G. Mayr and K. Samwer, "Model for intrinsic stress formation in amorphous thin films", Phys. Rev. Lett. **87**, 36105 (2001).

[Mayr 99] S.G. Mayr, M. Moske, and K. Samwer, "Identification of key parameters by comparing experimental and simulated growth of vapor-deposited amorphous $Zr_{65}Al_{7.5}Cu_{27.5}$ films", Phys. Rev. B **60**, 16950 (1999).

[Mays 68] C.W. Mays, J.S. Vermaak, and D. Kuhlmann-Wilsdorf, "On surface stress and surface tension: II. Determination of the surface stress of gold", Surf. Sci. **12**, 134 (1968).

[Mazo 88] A. Mazor, D.J. Srolovitz, P.S. Hagan, and B.G. Bukiet, "Columnar growth in thin films", Phys. Rev. Lett. **60**, 424 (1988).

[Mouc 69] B.A. Mouchan, and A.V. Demichisin, Fiz. Met. **28**, 83 (1969).

[Muri 77] M. Murikami and P. Chaudhari, "Thermal strain in lead thin films. I. Dependence of the strain on crystal orientation", Thin Solid Films **46**, 109 (1977).

[Murr 75] L.E. Murr, *Interfacial Phenomena in Metals and Alloys* (Addison-Wesley, Reading, MA, 1975).

[Need 90] R.J. Needs and M.J. Godfrey, "Surface stress of aluminum and jellium", Phys. Rev. B **42**, 10933 (1990).

[Need 89] R.J. Needs and M. Mansfield, "Calculations of the surface stress tensor and surface energy of the (111) surfaces of iridium, platinum and gold", J. Phys.: Condens. Matter **1**, 7555 (1989).

[Nest 99] D.C. Nesting, J. Kouvetakis, S. Hearne, E. Chason and I.S.T. Tsong, "Real-time monitoring of structure and stress evolution of boron films

grown on Si(100) by ultrahigh vacuum chemical vapor deposition", J. Vac. Sci. Tech. A **17**, 891 (1999).

[Neum 72] G. Neumann and G.M. Neumann, *Surface Self-Diffusion of Metals* (Bay Village, OH, Diffusion Information Center, 1972).

[Nix 99] W.D. Nix and B.M Clemens, "Crystallite coalescence: A mechanism for intrinsic tensile stresses in thin films", J. Mater. Res. **14**, 3467 (1999).

[Nix 89] W.D. Nix, "Mechanical properties of thin films", Met. Trans. A **20**, 2217 (1989).

[Nye 85] J.F. Nye, *Physical properties of crystals: their representation by tensors and matrices* (Oxford University Press, New York, 1985).

[Ohri 92] M. Ohring, *The Materials Science of Thin Films* (Academic Press, Boston, 1992).

[Pala 94] G. Palasantzas and J. Krim, "Scanning tunneling microscopy study of the thick film limit of kinetic roughening", Phys. Rev. Lett. **73**, 3564 (1994).

[Pash 65] D.W. Pashley and M.J. Stowell, "Nucleation and growth of thin films as observed in the electron microscope", J. Vac. Sci. Tech. **3**, 156 (1965).

[Pash 64] D.W. Pashley, M.J. Stowell, M.H. Jacobs, and T.J. Law, "The growth and structure of gold and silver deposits formed by evaporation inside an electron microscope", Philos. Mag. **10**, 127 (1964).

[Pogo 01] V.V. Pogosov and V.P. Kurbatsky, "Density-functional theory of elastically deformed finite metallic system: work function and surface stress", J. Exp. and Theoretical Phys. **92**, 304 (2001).

[Raib 00] M. Raible, S.G. Mayr, S.J. Linz, M. Moske, P. Hänggi, and K. Samwer, "Amorphous thin film growth: Theory compared with experiment", Europhys. Lett. **50**, 61 (2000).

[Rein 97] B. Reinker, M. Moske, and K. Samwer, "Kinetic roughening of amorphous $Zr_{65}Al_{7.5}Cu_{27.5}$ films investigated *in situ* with scanning tunneling microscopy", Phys. Rev. B. **56**, 9887 (1997).

[Röll 76] K. Röll, "Analysis of stress and strain distribution in thin films and substrates"J. Appl. Phys. **47**, 3223 (1976).

[Royl 79] L.M. Roylance and J.B. Angell, "A batch fabricated silicon accelerometer", IEEE Trans. Electron Devices **26**, 1911 (1979).

[Sanc 92] J.E. Sanchez, Jr. and E. Arzt, "Effects of grain orientation on hillock formation and grain growth in aluminum films on silicon substrates", Scripta Metall. Mater. **27**, 285 (1992).

[Sand 92] D.E. Sander, D.M. Halstead and A.E. DePristo, "Metal/metal homoepitaxy on FCC(111) and FCC(001) surfaces: deposition and scattering from small islands", J. Vac. Sci. Technol. A **10**, 1986 (1992).

[Sche 90] A.J. Schell-Sorokin and R.M. Tromp, "Mechanical stress in (sub)monolayer epitaxial films", Phys. Rev. Lett. **64**, 1039 (1990).

[Schu 49] L.G. Schultz, J. Appl. Phys. **20**, 1030 (1949).

[Seel 00] S.C. Seel, C.V. Thompson, S.J. Hearne, and J.A. Floro, "Tensile stress evolution during deposition of Volmer-Weber thin films", J. Appl. Phys. **88**, 7079 (2000).

[Shel 01] B.W. Sheldon, K.H.A. Lau and A. Rajamani, "Intrinsic stress, island coalescence, and surface roughness during the growth of polycrystalline films", J. Appl. Phys. **90**, 5097 (2001).

[Shul 96] A.L. Shull, "Measurements of stress during deposition of copper and silver thin films and multilayers", Harvard University, Cambridge, MA, Division of Applied Sciences (1996).

[Simm 71] G. Simmons and W. Wang, *Single crystal elastic constants and calculated aggregate properties: a handbook* (MIT Press, second edition, 1971).

[Smal 94] M.K. Small and W.D. Nix, "Calculation of the [111]-texture dependence of the elastic biaxial modulus", *Materials Research Society Symposium Proceedings* **343**, 561 (1994)

[Smit 54] C.S. Smith, "Piezoresistance effect in germanium and silicon", Phys. Rev. **94**, 42 (1954).

[Soll 85] C. Solliard and M. Flueli, "Surface stress and size effects on the lattice parameter in small particles of gold and platinum", Surf. Sci. **156**, 487 (1985).

[Spae 00] F. Spaepen, "Interfaces and stresses in thin films", Acta Mater. **48**, 31 (2000).

[Srol 88] D.J. Srolovitz, A. Mazor and B.G. Bukiet, "Analytical and numerical modeling of columnar evolution in thin films", J. Vac. Sci. Technol. A **6**, 2371 (1988).

[Ston 09] G.G. Stoney, "The tension of metallic films deposited by electrolysis", Proc. R. Soc. London **A32**, 172 (1909).

[Su 93] C.M. Su and M. Wuttig, "In situ mechanical relaxation of Cu films growing on a Si substrate", Appl. Phys. Lett. **63**, 3437 (1993).

[Taka 02] A.R. Takahashi, Dept. of Materials Science and Engineering, MIT, unpublished research (2002).

[Thom 99] C.V. Thompson, "On the grain size and coalescence stress resulting from nucleation and growth processes during formation of polycrystalline thin films", J. Mater. Res. **14**, 3164 (1999).

[Thom 98] C.V. Thompson, "Grain growth in polycrystalline thin films of semiconductors", Interface Science **6**, 85 (1998).

[Thom 95] C.V. Thompson and R. Carel, "Texture development in polycrystalline thin films", Mater. Sci. Eng. B **32**, 211 (1995).

[Thom 94] C. Thompson, G. Palasantzas, Y.P. Feng, S.K. Shina, and J. Krim, "X-ray-reflectivity study of the growth kinetics of vapor-deposited silver films", Phys. Rev. B **49**, 4902 (1994).

[Thom 93] C. V. Thompson, "Texture evolution during grain growth in polycrystalline films", Scripta Metall. et Mat. **28**, 167 (1993).

[Thom 90] C.V. Thompson, "Grain growth in thin films", Annu. Rev. Mat. Sci. **20**, 245 (1990).

[$Thom_2$ 90] C.V. Thompson, J.A. Floro and H.I. Smith, "Epitaxial grain growth in thin metal films", J. Appl. Phys. **67**, 4099 (1990).

[Thom 85] C.V. Thompson, "Secondary grain growth in thin films of semiconductors: theoretical aspects", J. Appl. Phys. **58**, 763 (1985).

[Thom 84] C.V. Thompson and H.I. Smith, "Surface-energy-driven secondary grain growth in ultrathin (<100 nm) films of silicon", Appl. Phys. Lett. **44**, 603 (1984).

[Thor 89] J.A. Thorton, "Stress related effects in thin films", Thin Solid Films **171**, 5 (1989).

[Thor 77] J.A. Thornton, "High rate thick film growth", Annu. Rev. Mater. Sci. **7**, 239 (1977).

[Thou 93] M.D. Thouless, "Effect of surface diffusion on the creep of thin films and sintered arrays of particles", Acta Metall. Mater. **41**, 1057 (1993).

[Thur 90] G. Thurner and R. Abermann, "Internal stress and structure of ultrahigh vacuum evaporated chromium and iron films and their dependence on substrate temperature and oxygen partial pressure during deposition", Thin Solid Films **192**, 277 (1990).

[Timo 34] S. Timoshenko, *Theory of Elasticity* (McGraw-Hill Book Company, New York, 1934).

[Tort 91] M. Tortonese, R.C. Barrett, and C.F. Quate, "Atomic resolution with an atomic force microscope using piezoresistive detection", Appl. Phys. Lett. **62**, 834 (1991).

[Toul 70] Y.S. Touloukian, R.K. Kirby, R.E. Taylor, and P.D. Desai. *Thermophysical Properties of Matter. Thermal Expansion. Metallic Elements and Alloys*, (IFI/Plenum, New York, 1970).

[Town 87] P.H. Townsend, D.M. Barnett, and T.A. Brunner, "Elastic relationships in layered composite media with approximation for the case of thin films on a thick substrate", J. Appl. Phys. **62**, 4438 (1987).

[Trac 93] D.P. Tracy and D.B. Knorr, "Texture and microstructure of thin copper films", J. Elec. Mat. **22**, 611 (1993).

[Tuft 63] O.N. Tufte and E.L. Stelzer, "Piezoresistive properties of silicon diffused layers", J. Appl. Phys. **34**, 313 (1963).

[Turl 92] J.F. Turlo, Ph. D. thesis, Stanford University, Stanford, CA, 1992.

[Vena 84] J.A. Venables, G.D.T. Spiller and M. Hanbucken, "Nucleation and growth of thin films", Rep. Prog. Phys. **47**, 399 (1984).

[Venk 92] R. Venkatraman and J.C. Bravman, "Separation of film thickness and grain boundary strengthening effects in Al thin films on Si", J. Mat. Res. **7**, 2040 (1992).

[Volk 94] C. A. Volkert, C. F. Alofs, and J. R. Liefting, "Deformation mechanisms of Al films on oxidized Si wafers", J. Mat. Res. **9**, 1147 (1994).

[Vook 65] R.W. Vook and F. Witt, "Structure and annealing behavior of metal films deposited on substrates near 80°K: I. Copper films on glass", J. Vac. Sci. Tech. **2**, 49 (1965).

[$Vook_2$ 65] R.W. Vook and F. Witt, "Structure and annealing behavior of metal films deposited on substrates near 80°K: II. Gold films on glass", J. Vac. Sci. Tech. **2**, 243 (1965).

[Wass 72] H.J. Wasserman and J.S. Vermaak, "On the determination of the surface stress of copper and platinum", Surf. Sci. **32**, 168 (1972).

[Wass 70] H.J. Wasserman and J.S. Vermaak, "On the determination of a lattice contraction in very small silver particles", Surf. Sci.. **22**, 164 (1970).

[Wilc 69] J.D. Wilcock, D.S. Campbell, and J.C. Anderson, "The internal stress in evaporated silver and gold films", Thin Solid Films **3**, 13 (1969).

[Wina 91] D. Winau, R. Koch, A. Fuhrmann and K.H. Rieder, "Film growth studies with intrinsic stress measurement: Polycrystalline and epitaxial Ag, Cu, and Au films on mica(001)", J. Appl. Phys. **70**, 3081 (1991).

[Wind 92] H. Windischmann, "Intrinsic stress in sputter-deposited thin films", Crit. Rev. Sol. St. Mat. Sci. **17**, 547 (1992).

[Wolt 81] J. Woltersdorf, A.S. Nepijko, and E. Pippel, "Dependence of lattice parameters of small particles on the size of the nuclei", Surf. Sci. **106**, 64 (1981).

[Ziel 95] E.M. Zielinski, R.P. Vinci and J.C. Bravman, "Effects of barrier layer and processing conditions on thin film Cu microstructure", J. Elec. Mat. **24**, 1485 (1995).

[Ziel 94] E.M. Zielinski, R.P. Vinci, and J.C. Bravman, "Effects of barrier layer and annealing on abnormal grain growth in copper thin films", J. Appl. Phys. **76**, 4516 (1994).